
# THE COMPARTMENTALIZATION OF A DEEPWATER FOLD AND THRUST BELT IN THE LEVANT

**OLUCHUKWU NWOSU**

**Submitted in partial fulfilment of the requirement for the degree of Ph.D.**

**Cardiff University**

**Dec 2013**

**DECLARATION**

This work has not been submitted in substance for any other degree or award at this or any other university or place of learning, nor is being submitted concurrently in candidature for any degree or other award.

Signed …… (Candidate) Date ……

**STATEMENT 1**

This thesis is being submitted in partial fulfillment of the requirements for the degree of ……(insert MCh, MD, MPhil, PhD etc, as appropriate)

Signed …… (Candidate) Date ……

**STATEMENT 2**

This thesis is the result of my own independent work/investigation, except where otherwise stated.

Other sources are acknowledged by explicit references. The views expressed are my own.

Signed …… (Candidate) Date ……

**STATEMENT 3**

I hereby give consent for my thesis, if accepted, to be available for photocopying and for inter-library loan, and for the title and summary to be made available to outside organisations.

Signed …… (Candidate) Date ……

**STATEMENT 4: PREVIOUSLY APPROVED BAR ON ACCESS**

I hereby give consent for my thesis, if accepted, to be available for photocopying and for inter-library loans **after expiry of a bar on access previously approved by the Academic Standards & Quality Committee.**

Signed …… (Candidate) Date ……

# SUMMARY

This research project used 3D seismic data located in deep water fold and thrust belt in the Levant Basin eastern Mediterranean, to investigate the nature and kinematics of compartmentalized thrust related folds. The principal aim is to better understand thrust related fold development and interactions in compressional settings.

The fold and thrust belt in the Levant Bain is mainly comprised of overlapping thrust faults of similar and opposing dips segmented or bounded by conjugate sets of strike slip faults. Detailed interpretation and analysis of the 3D geometry of the structures revealed that thrust faulting is an early process in the development of the thrust and fold pair, thrust interact with each other, and strike slip faults along strike. A preliminary end member interaction of thrust faults and strike slip faults is proposed based on observation of their bounding or segmenting pattern.

The concept of fault interaction was mainly developed from the investigation of the propagation of thrust fault compartmentalised by strike slip faults. This involves a combination of kinematic analysis which includes fault displacement and shortening profiles, and the patterns of syn kinematic sediments above fold limb. Kinematic data suggests that strike slip faults are acting as barriers to thrust fault propagation. Similar barrier to fault propagation are observed between overlapping thrust faults within a single fold formed by the linkage of smaller thrust folds. The results showed that the faults are restricted as they link and transfer displacement. In addition to the propagation of thrust faults, vertical distribution of fault displacement suggests that they ramp up from detachment, this agrees with the classical models of thrust propagation folds.

# ACKNOWLEDGEMENT

Firstly, I am humbly grateful to the **ALMIGHTY GOD** for his kindness and tender mercies towards me and keeping me alive all throughout my time in the University. If it wasn't for God who was on my side, I wouldn't have been alive to even start the PhD in the first place. God is my provider, protector, fortress and my lord in whom I trust.

I wish to express my sincere gratitude to my parents, Sir and Lady Johnson Nwosu, for their sincere and valuable guidance, financial support and encouragement extended to me. Many thanks to my brothers, Chinedu, Paul and Chikodi for their immeasurable financial and spiritual support. My family has been my inspiration all though the PhD programme.

I am deeply grateful to my supervisor, Professor Joseph Cartwright, who not only financed the major part of my PhD, but also gave me the opportunity to undertake this research.I learned a lot through his passion for geology, numerous discussions about structural geology and valuable advice on writing up the thesis. The project greatly benefited from his patience, knowledge and guidance. I will forever be grateful and indebted to him; he is one of the very few that have sown so greatly into my endeavours.

I am also thankful to my co-supervisor Dr Tiago Alves, and Dr David James for their constructive comments on my work. A big thank you to Gwen for her technical support. More also, a special thanks go to my friends in 3D lab; Chris wild and Ben Manton (my house mates), and Dan Morgan for proof reading my thesis, Bledd Davis, Pete Bird, Tuvie Omeru and Hamood Alhabis for secretly drinking and partying with me once in a while. My thanks are further extended to other members of 3D lab in room 1.59 Duate Soares, Matino foschi, David Gamboa, Kamaldeen Omasanya, we really became like a family towards the end of my write-up.

I would also like to thank my friends in my church for their immeasurable prayers and spiritual support. Pastor Dave Prichard and his family, (Ben, Jess, Bonny, Ivy) never stopped praying for me. I also appreciate Paul, Jade, Bunmi, Olu, and John for their laying hands on me during special prayers. More also a special thanks to Ada and Tony Emezie, who would always encourage me to attend evening home fellowships.

The last but the least, I appreciate the kind support and encouragement from my lovely fiance' Chinwe Ogbonna, who stayed strong and believed in me accomplishing this phase of my life, God bless you richly.

# TABLE OF CONTENT

# LIST OF FIGURES

**CHAPTER ONE. INTRODUCTION**



## CHAPTER TWO. METHODS

## CHAPTER THREE. GEOLOGY

## CHAPTER FOUR. STRUCTURES IN GAL C

## CHAPTER FIVE. THE INTERACTION BETWEEN THRUST FAULTS AND STRIKE SLIP FAULTS

## CHAPTER SIX. THE SEGMENTATION AND PROPAGATION OF A SINGLE FOLD

## CHAPTER SEVEN. DISCUSSION

# CHAPTER ONE

## 1 INTRODUCTION

### 1.1 BACK GROUND STUDY

Deepwater fold and thrust belts are commonly formed in association with major gravity deformational systems in passive continental margins (Morley and Guerin 1996). Within these continental margin gravity driven systems, an up dip extensional domain is invariably paired with a down dip contractional domain, in which there are distinctive suites of folds and duplicated thrust faults and thrust related microscopic structures, which are collectively termed deep water fold and thrust belts (Rowan *et al.* 2004). They are one of the main focus for hydrocarbon exploration (Rowan et al. 2004), due to their potential to host large oil and gas reserves with thrust-related anticlines representing the principal trapping structure or fault planes which are preferred conduits for fluid migration from deepwater source rocks (Ingram *et al.* 2004; Cooper 2007).

Up until the middle of the 19$^{th}$ century, thrust faults were studied based on outcrop geology. This restricts their detailed description due to incomplete outcrop exposure. This field based approach has led to a number of failed attempts to analyze their structural style and development. Deepwater fold and thrust belts are characterized by complex structural style and they have proven difficult to explore largely due to the unavailability of good quality seismic imaging. However, following the improvement of seismic interpretation in the late 20$^{th}$ century, deepwater fold and thrust belts have been continuously expanding fields of geological investigation due to the stimulus for further exploration provided by recent discoveries, the improved demand for gas, and improved access to promising areas (Meneses-Rocha and Yurewicz 1999).

Considerable research efforts have been expended on the structural analysis of deepwater fold and thrust belt in the past two decades, starting with the pioneering studies in the deepwater Nigeria (Damuth 1994; Cohen and McClay 1996; Morley and Guerin 1996; McClay *et al.* 1998), Brazil

(Cobbold *et al.* 1996), Gulf of Mexico (Trudgill *et al.* 1999). These studies have shown the common occurrence of thrust related folds in deepwater fold and thrust belt. Three main types of thrust-related folds are now generally recognised : (1) fault bend folds (Rich 1934; Suppe 1983), (2) fault propagation folds and (3) fault detachment folds (Jamison 1987). Other types such as fault break folds, fault drag folds (Dahlström 1970), and fault displacement folds (Wickham 1995) have also been identified. Most of these studies were based on two-dimensional descriptions of exposed outcrop and two dimensional seismic lines. Three-dimensional analysis of thrust-related fold structures are limited to a few recent studies in which thrust systems in deep water setting have been described using high resolution three dimensional seismic data (Corredor *et al.* 2005; Briggs *et al.* 2006; Higgins *et al.* 2007; Higgins *et al.* 2009). These researchers used kinematic observations and displacement distance analysis to define and differentiate the various styles of thrusting (Corredor et al. 2005; Briggs et al. 2006), displacement transfers styles (Higgins et al. 2007), interaction between folding and coeval sedimentation (Shaw *et al.* 2004; Clark and Cartwright 2009) .

However, other than that documented by Higgins et al (2007), (2009), there has been little work addressing the compartmentalization of thrust-related folds. These studies Higgins *et al* (2007), (2009) made it clear that a fold could appear simple on map view but can be internally segmented. The fold presented in their study contain numerous thrust faults of similar and opposing dip, link and transfer displacement through transfer zones with fold creating a central structural culmination and causing fold vergence to vary along strike (Higgins et al. 2009). These linkage types vary in spatial extents and have distinctive different styles (type 1, 2 and 3) based on their antithetic relationship (Higgins et al. 2007). This thesis expands on the knowledge of fold compartmentalization, and thus faults interactions by understanding a specific analysis folds compartmentalized by thrust faults, and strike slip faults.

Deformation in the contractional domain of the Levant Basin is complex compared to other toe thrust belts which are developed at the leading edge of a gravity driven continental margins such as

offshore Brazil, Gulf of Mexico, and offshore Nigeria (Cobbold et al. 1996; McClay et al. 1998; Trudgill et al. 1999; Corredor et al. 2005). The Basin is mainly deformed by thrust faults and associated folds, and conjugate strike slip faults, associated with complex tectonic interactions involving the combination of gravitational collapse and subsequent basinward spreading of the Nile Cone along with the tilting induced collapse of the Levant Margin (Loncke *et al*., 2006; Gradmann et al., 2005; Cartwright and Jackson, 2008). Other far field tectonic boundaries have also been stipulated to influence deformation in the study area, these include; the butreesing effects of the Eratosthenes Seamount (Mascle *et al.* 2001), and (3) the Cyprus Subduction Trench (Netzeband *et al.* 2006c).

The combination of the results presented in this thesis with those of previous works (Bertoni and Cartwright 2006; Netzeband et al. 2006c; Cartwright *et al.* 2012) allows an integrated understanding of the complex deformation governing the distal domain of the Levant Basin. This study only focuses on deformation in the passive margin of the Levant, however, similar techniques used here, may also be applied in describing other fold and thrust belts.

## 1.2 AIMS

The main aims of this thesis are:

1. To explore the inter-relationships between thrust faults, thrust related folds and strike slip faults
2. To describe and explain the three dimensional geometries and propagation of thrust related folds.
3. Examine the factors influencing the slip distribution on thrusts faults with a specific focus of structural compartmentalization.
4. To describe and explain the relationship between displacement on thrust faults, and shortening.

## 1.3 OVERVIEW OF THRUST SYSTEMS

### 1.3.1 Thrust Fault Systems.

A thrust system is defined as a zone of closely related thrust faults that are geometrically, kinematically and mechanically linked (Hills and Hills 1972). The intricate and inter-related combination of thrust faults and folds are conventionally referred to as thrust related folds (Willis 1893; Suppe 1983; Williams and Chapman 1983; DeCelles and Giles 1996; Sherkati *et al.* 2005). These structures are generally formed by the accommodation of horizontal shortening of bedding surface, older strata in the hangingwall moves over younger strata in the footwall (Figure 1.1).

Thrust systems occur at all scales from millimetres to kilometres in regions that are dominated by compressional tectonics. They can thus develop in a wide variety of environments, which includes those that occur in Accretionary prisms which developed in sub-duction zone e.g Barbados Prism (Platt *et al.* 1985), Foreland fold and thrust belt e.g Canadian Rocky Mountains (Bond and Kominz 1984) and toe thrust belts associated with gravity driven systems such as the NigerDelta (Damuth 1994). Foreland fold and thrust belts have been the most intensely studied due to their significant volume of both petroleum and coal reserves such as the Cordilleran belt in western Canada (Van der Flier-Keller and Goodarzi 1992).

Thrust faults generally cutup the stratigraphic section in the form of a staircase trajectory made up of alternating flats and ramps (McClay 1992a; McClay et al. 1998) (Figure 1.2a). The thrust fault separates the deformed hangingwall from the footwall and commonly root into zone of shear parallel to the stratification called a detachment or decollement (Burchfiel *et al.* 1989; Baby *et al.* 1992) . Zones of detachment are usually lithological units and are typically weak or incompetent layer such as overpressure shale or salt (Morley and Guerin 1996; Morley *et al.* 2011) . The competency of the detachment may influence the style of detachment (Morley and Guerin 1996). Thrust faults ramp through zones of competent lithology. Those that reach the surface are termed emergent and those that do not propagate to the surface are termed blind faults (Berger and Johnson 1982).

### 1.3.2 Styles of Thrust Deformation

The style of deformation of thrust systems is one of the main factors which influences the distribution of oil and solid mineral reserves in fold and thrust belts (Morley and Guerin 1996; Cooper 2007). The style of thrusting and fold mainly depends on whether the system is a thick or thin skin deformation, the nature or competency of the detachment layer, and whether or not the fold is buried (Morley et al. 2011).

The style of thrusting and folding which involves both the sedimentary cover and basement is known as thick-skinned deformation (Coward 1983), an example is the Laramide Uplift (Cross 1986). In this case, the basal detachment of the majority of the faults is within the basement. The thick-skin style contrasts with the thin-skin style in which the sedimentary cover is independently deformed of the underlying crust, examples include the NigerDelta (Corredor et al. 2005), Canadian Rock Mountains (Price 1981). Tracing the thrust back into the hinterland, basement rocks become involved in the thrust sheet, which may have been transported in a thin-skinned manner. In some cases both structural styles coexist such as in the Rocky Mountain Cordillera were thick-skinned styles are found in the interior and thin- skinned in the external part (Hamilton 1988).

Fault dip and shape depends on the competency of detachment layer. Faults which detached within salt layers, tend to be listric and are characterized to have a wedge like geometry at the detachment front (Davis and Engelder 1985b; Tonghe 1999), while those detached at more competent or hard layers, such basement tend to be steeply dipping (Pfiffner 2006) (Figure 1.1 b).

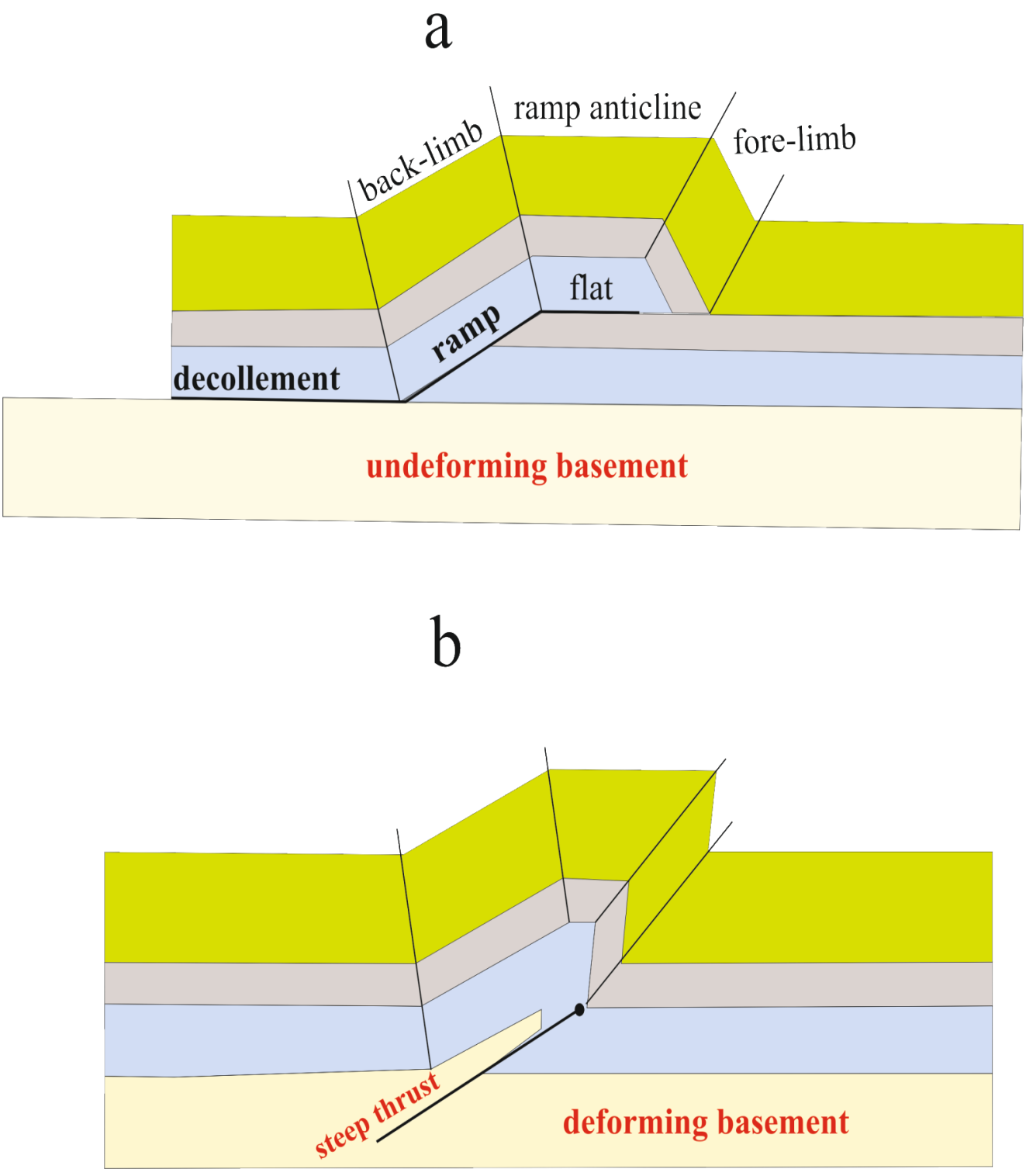


Figure 1.1: Styles of Deformation (a) Thin- skinned (b) Thick- skinned.

Detachment thickness have also been observed to influence fault displacement (Briggs et al. 2006; Morley et al. 2011). Thrust faults which detach at thick detachment layer tend to increase in displacement towards the detachment layer whilst those that sole into thinner layers are characterized by decreases in displacement down dip (Briggs et al. 2006). Detachment folds are most likely to form over thick incompetent detachment layer compared to fault propagation folds (Mitra 2002). Other parameters which may also affect the style of thrusting include the burial of thrust faults and folds by either post or syn-sedimentary deposits (Storti and Poblet, 1997), and interactions of thrusting with other fault related structures (Ellis and Dunlap 1988).

### 1.3.3 Thrust Related Fold

Folding and thrust faulting are inter-dependent and/or competing processes that have been described using several models (Suppe 1983; Jamison 1987). However, the timing relationship between thrusting and folding has not been fully understood. In modelling simple thrust- related folding it is assumed that both processes (folding and faulting) are contemporaneous (Rich 1934; Suppe 1983). It has been shown by Willis (1893) that folds can be a primary structure to faults such as the fault break folds and spreading thrusts, while the shear thrust faults indicate faults with limited folding.

In recent studies, three end members of thrust- related folds have been identified (Figure 1.2). (1) fault bend fold (2) fault propagation fold and (3) Detachment fold. These end members have most commonly been accepted in structural geology (Rich 1934; Suppe 1983; Jamison 1987).

#### *1.3.3.1 Fault bend fold*

Fault bend folds are commonly called ramp folds (Figure 1.2 b). They develop when the hanging wall of a thrust fault is transported from the decollement zone, ramping up through competent layers and becoming flat at a higher stratigraphical incompetent layer, in the form of a step like trajectory. Fault bend folds were first described by Rich (1934) in his account of the evolution of the Pine Mountain Thrust of the Appalachians, where he observed that the dominant style of the structure consisted of

symmetric anticlines. This example of a thrust- related fold was later modelled using both the volume conversation concept (Suppe 1983) as well as variation in forelimb and backlimb thickness (Jamison 1987).

Fault bend folds progressively change shape in complex ways as they develop and are characterized to have a ramp bounded by upper and lower detachment zones. Folds form as a result of the movement of the hanging wall through the ramp region so that fore limb of the fold is always located towards the foreland side of the of the ramp. The limbs of the fold are thought to grow in a self-similar manner by hinge migration so that dip angles of the limb remains constant (Suppe, 1983). Geometrically, they are asymmetric, the fore limb can be shorter than back limb, but are less gently dipping compared to those of fault propagation fold (Jamison 1987). The inter-limb and upper ramp angle of the fault controls the thickness of the forelimb (Jamison 1987).

### 1.3.4 Fault propagation fold

In fault propagation folding the upper tip position has a direct association with the folding unlike the case of fault bend fold where folding is a consequence of ramping up of the thrust fault. The fold is mainly asymmetric: the front limb is steeper than back limb (Figure 1.2 d). The mechanism of this fold type was first described by William and Chapman (1983) using vertical displacement distribution. The geometries and kinematics have been modelled and studied using kink band in details by Suppe (1983), and Jamison (1987). A simple kink band model of a fault propagation fold shows that the back limbs of fault propagation folds develop by hinge migration while the fore limbs by either limb rotation or limb migration (Suppe 1983). The fore limbs are generally steeply dipping while back limbs dip almost parallel to footwall (Suppe and Medwedeff 1990). However, the vast majority of thrust related folds do not exhibit kink-type hinges, and instead exhibit a smooth curvature.

Fault propagation folds can laterally show changes from open fold geometry to tight folds (Mitra 1990). Such geometric changes have been observed in the Turner Valley anticline in Canada (Gallup 1951) and the Niger Delta (Higgins et al. 2007; Higgins et al. 2009) .

The mechanism of synchronous and inter-dependent faulting requires continuous folding of the layers above the fault tip. Splay faults may develop close to the tip of the principal fault forming a trishear zone as modelled by Erslev (1991). Trishear propagation folds have also been observed and described in the Niger Delta (Mueller *et al.* 2005; Briggs et al. 2006).

Furthermore, fault propagation folds may be tight and the fault may propagate along the syncline, because this requires a relatively small synclinal bend in the thrust fault (Mitra 1990). The translation of the fold through the synclinal bend may result in the formation of an additional backlimb panel. Alternatively, minor faults or splay faults may develop through the forelimb of the fold, leaving the synclinal axis in the footwall of the principal thrust fault, such as those in the Taipei Thrust, western Taiwan (Suppe 1985). Fault propagation folding has also been documented to change to fault bend folding, especially where the tip of the fault reaches an upper incompetent layer (Mitra 1990). This translation of thrust- related fold types may suggest that fault bend folds with steeply dipping forelimb were initially growing as fault propagation folds. A good example of this evolutionary sequence has been presented in the Willis Mountain anticline (Perry 1979)

#### *1.3.4.1 Detachment fold*

A simplified detachment fold is shown in Figure 1.2 f. This fold type was introduced by Jamison (1987) in the course of modelling the fault propagation fold (Suppe 1983). They are simply defined as folds with no ramp above an incompetent layer where deformation is concentrated exclusively above the detachment. The best examples of thrust detachment folds are found in the Canadian Rocky Mountains (Jamison 1997), Western China fold thrust belt (Tonghe 1999), Southern Pyrenees (Storti and Poblet 1997b).

Detachment folds are characterized by fold amplitude, the height between the crest of the fold and surface of the undeformed sedimentary section (arbitrary surface). They grow above a weak layer such as salt which flows like liquid (Morley and Guerin 1996). They grow in amplitude, the deformed layer has to be folded or shortened in order to maintain constant bed length, which could be kinematically

impossible without a detachment. Examples of detachment above mobile units have been documented in the southern Pyrenees (Hardy *et al.* 1996) and the Appalachians (Wiltschko and Chapple 1977). Detachment folds have also been reported to develop above less mobile substrate, a typical example is found in the Wyoming thrust and fold belt (Groshong and Epard 1994). These cases are less common, they require deformation in the core so that growing fold within the anticline is filled in order to remain balance (Nemcok *et al.* 2009).

Fold detachment folds may subsequently translate into forelimbs, similar to fault break thrusts, described by (Willis 1893) in the Appalachians, and also along back limb thrusts as those described by (Rowan 1997) in the Mississippi Fan fold and thrust belt . Such structures are termed thrust detachment folds (Mitra 2002; Mitra *et al.* 2006).

Similar to thrust propagation folds, some thrust detachment folds can have their forelimb steeper than their back limb. Both fault types (propagation thrust and detachment thrust) are characterized by poor seismic expression because of their steep forelimbs and complex geometries. One of the main differences between fault propagation folds and decollement folds is in the geometry of their syn-kinematic sedimentary package above their limbs and crest (Storti and Poblet 1997b). Fault detachment folds usually have their growth units more steeply dipping than their pre-growth unit, while fault propagation folds are characterized by growth units, consistent flat lying panels which conform to those of the pre-growth units.

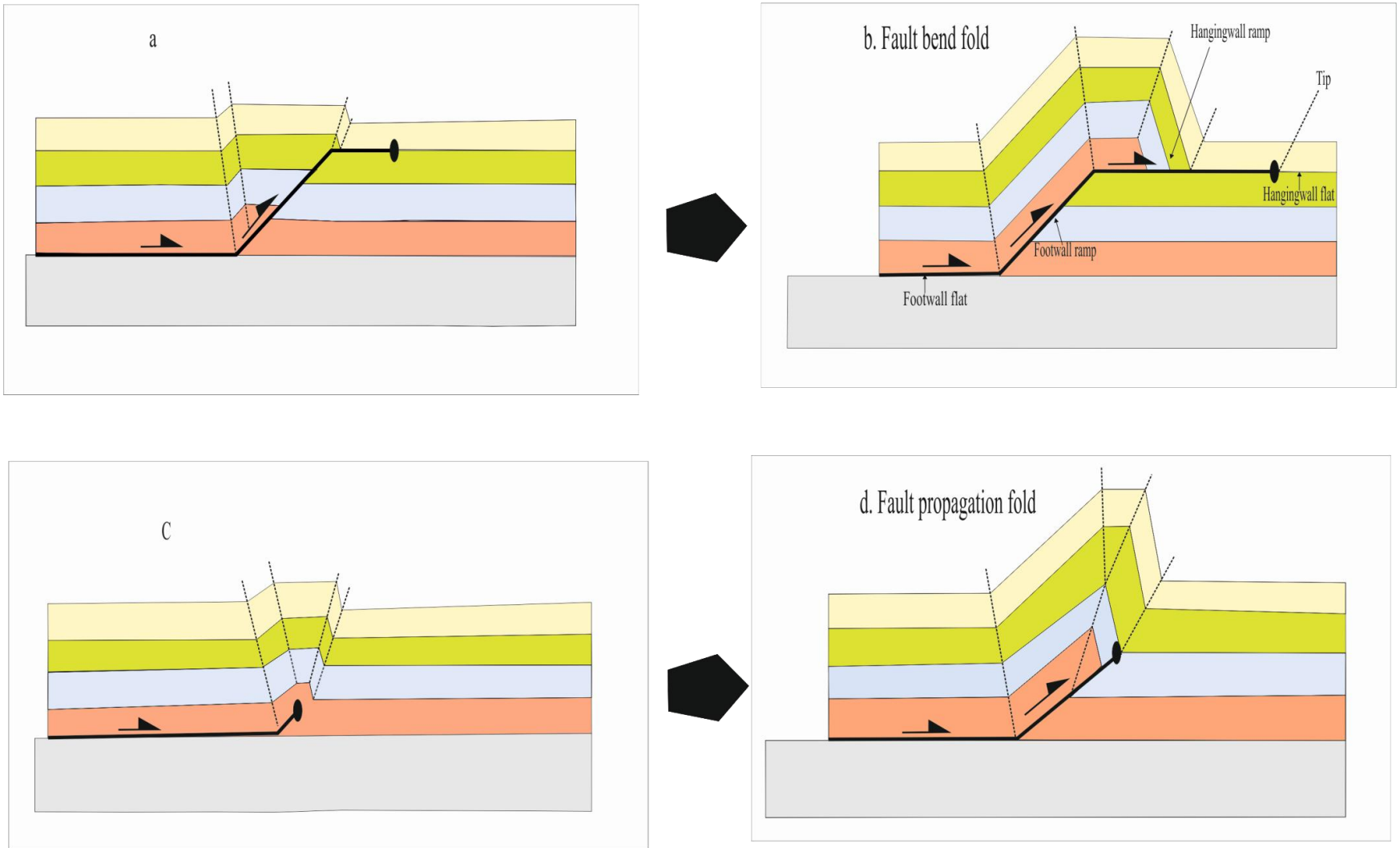


Figure 1.2: The 3 main end member thrust related folds. (a, b) Fault Bend Fold. (c, d) Fault propagation fold. (e, f) Detachment fold.

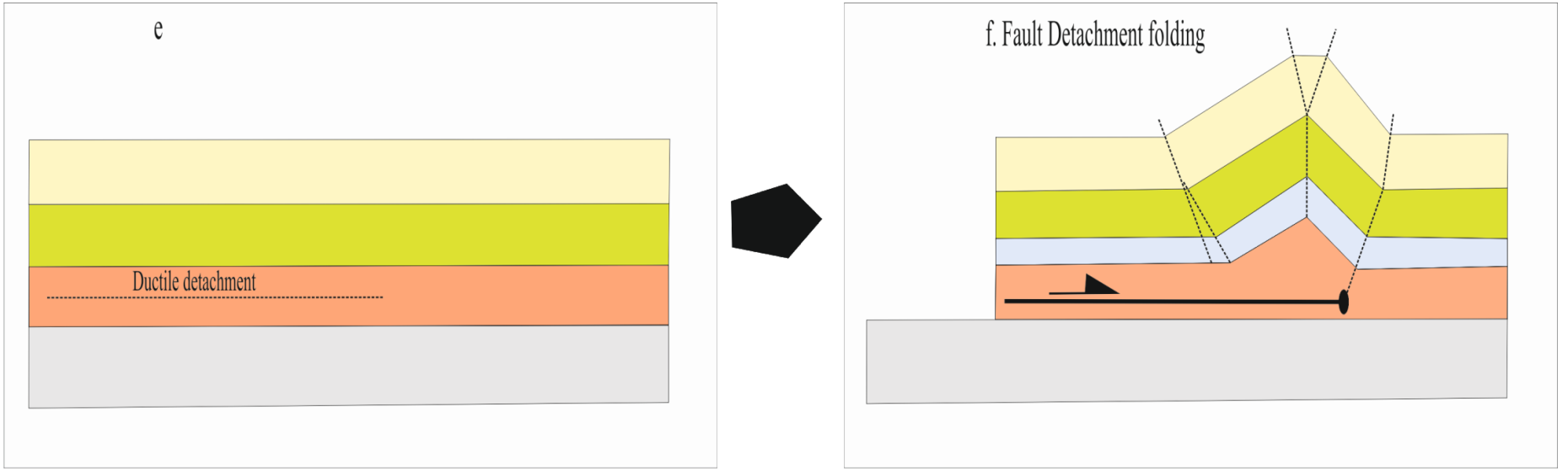


Figure 1.3: The 3 main end member thrust related folds. (a, b) Fault Bend Fold. (c, d) Fault propagation fold. (e, f) Detachment fold.

### 1.3.5 Duplex and Imbricate Structures

The term duplex was introduced by Dahlstrom (1970) to describe the Canadian rocky mountains. Although the earliest examples of duplex structures have long been described in cross sections through the Highlands of Scotland (Peach *et al.* 1907). The kinematic development of a duplex with parallel floor and roof thrusts, and uniform horse geometry was first modelled by Boyer and Elliott (1982). They used a sequence of fault bend anticlines and a progression of thrusting from hinterland to foreland similar to those observed in field studies and seismic sections (Rich 1934; Bally *et al.* 1970; Stearns 1978; Corredor et al. 2005).

Imbricate faults refer to a fault system made up of severally closely spaced faults in echelon arrangement. Each of the faults dies out up section by transferring displacement to their associated folds at tip or by distributing it among several splays. Some of the faults may climb directly to the surface (Elliott 1976) . Imbricate and duplex structures are very difficult to differentiate and in most cases, both structures co-exist. The main difference between imbricate and duplex systems is that duplex structures have a major site of roof detachment and the displacement at the roof of an imbricate system is relatively small (Mitra 1986).

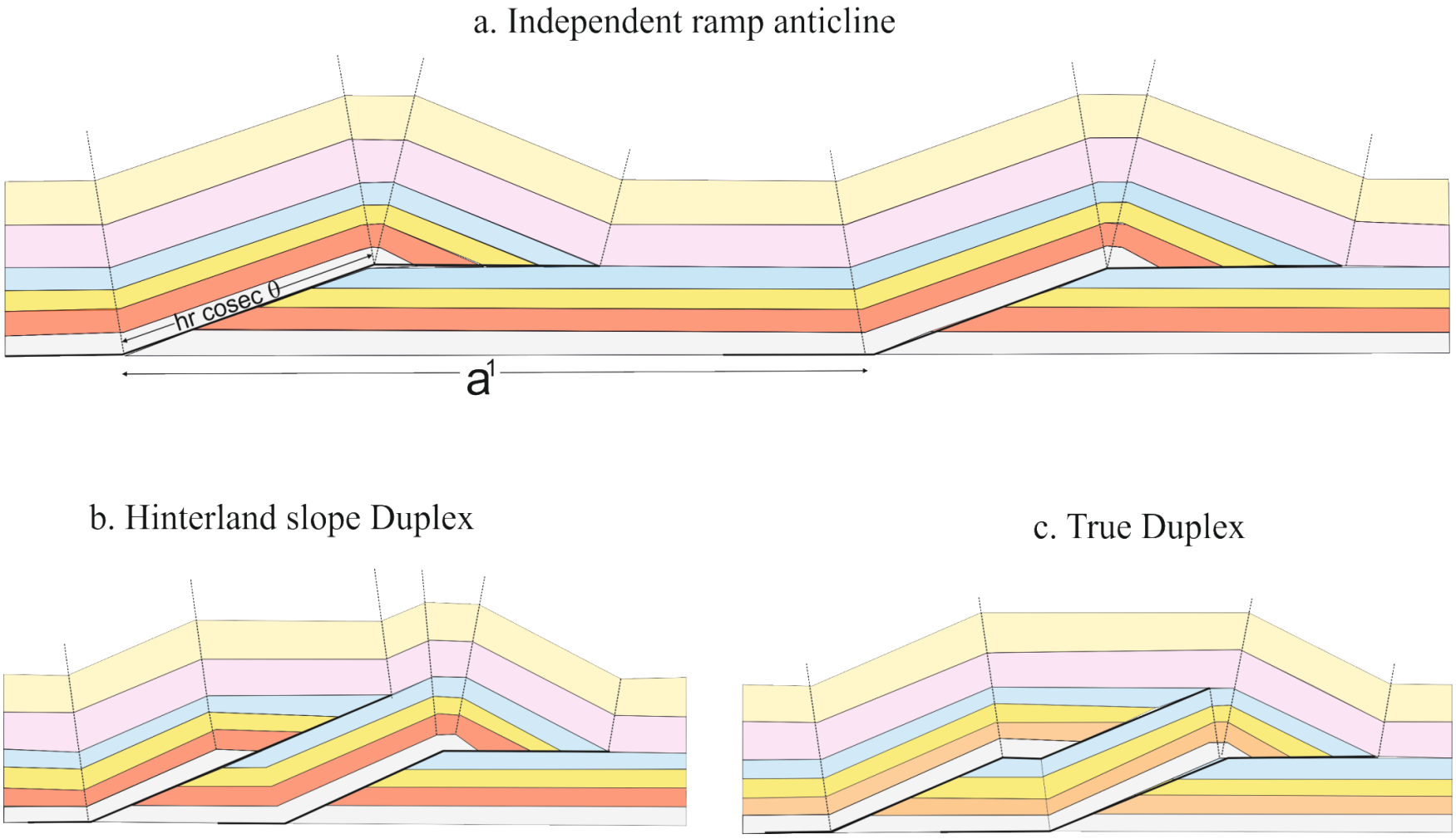


Figure 1.4: Geometric classes of duplex structures consisting of systems of ramp anticline. Final spacing between ramps is denoted as a1, while ramp length is hr cosecθ . After (Mitra) 1986.

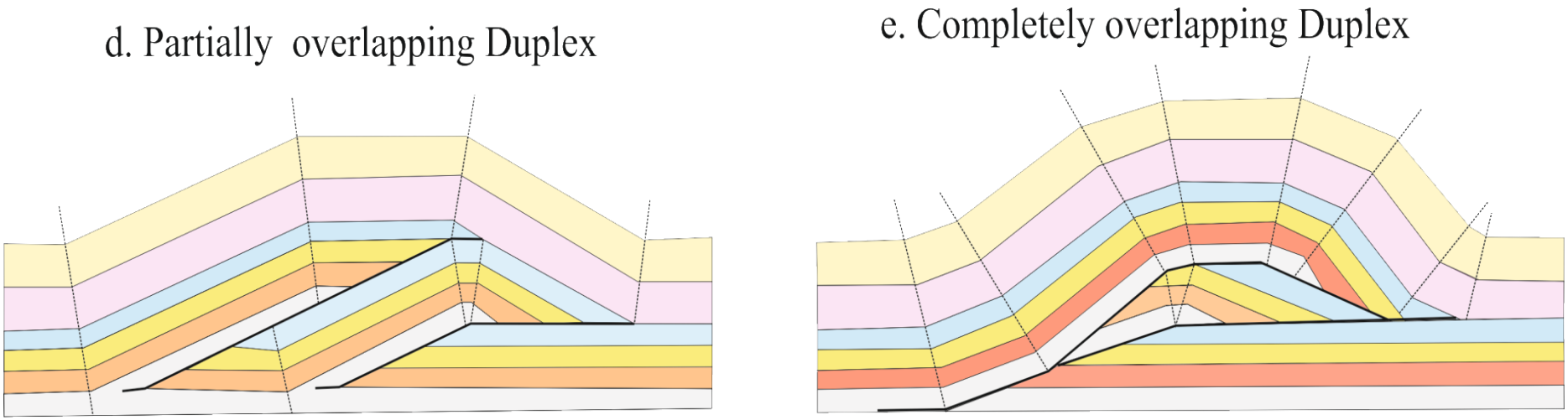


Figure 1.5: Geometric classes of duplex structures consisting of systems of ramp anticline. Final spacing between ramps is denoted as a1, while ramp length is hr cosecθ . After (Mitra) 1986.

### 1.3.6 Classification of Duplex and Imbricate Systems

Duplex and imbricate thrust systems vary from simple to complex geometry. The simplest thrust system consists of a simple fault bend fold with a floor thrust, a roof thrust and a series of imbricate faults connecting the roof and floor thrusts (Boyer and Elliott 1982). Complex duplex geometries display systems of hybrid folds with similar characteristics to fault propagation folds and fault bend folds (Suppe and Medwedeff 1984). Three main classes of duplex structures have been classified based on ramp angle, spacing between individual thrust faults and their relative displacements (Mitra 1986 Figure 1.3); (1) independent ramp anticline (2) true duplexes and (3) overlapping ramp anticline.

#### *1.3.6.1 Independent Ramp Anticline and Hinterland Slopping Duplexes*

The final spacing between the thrust faults is much higher than their relative displacement for independent ramp anticline (Figure 1.3 a). The overall shape between the fault anticline is synclinal in form. The geometry of the syncline is dependent on the relative displacements of the thrust faults (Mitra 1986). Hinterland sloping duplexes are formed where the spacing between the thrust faults is small so that at the contact between horses, the roof thrust slopes towards the hinterland (Figure 1.3 b)

#### *1.3.6.2 True Duplex*

This is similar to a type of duplex modelled by Boyer and Elliott (1982). A true duplex is characterized by a parallel floor and roof thrust at the contact of the adjacent horses (Mitra 1986). In some cases, the spacing between the anticlines is almost equal the ramp length (Figure 1.3 c), although in certain conditions (such as the rate of shortening), the spacing could be larger or smaller than their relative displacements.

#### *1.3.6.3 Overlapping ramp anticline*

These structures are characterized by anticlines that partially or completely overlap the fault ramp. The partially overlapping type consists of duplexes with roof thrusts dipping towards

the foreland (Figure 1.3 d). Whereas the completely overlapping type mainly has spacing between faults larger than ramp (Figure 1.3 e). In some cases spacing is less than zero, resembling an anticlinal stack with adjacent horses (Boyer and Elliott 1982) or an antiformal stack (McClay 1992a).

## 1.4 FAULT INTERACTIONS

Faults interact when displacement is transferred between pairs of faults or modified by another medium. The term displacement transfer was first used by Dahlstrom (1970), when he observed that as one fault dies out it reassigned its role of shortening and displacement to another fault. Displacement transfer occurs between relay faults (Huggins *et al.* 1995), intersecting faults(Tearpock and Bischke 1991), cross-cutting faults (Manighetti 2001), echelon faults (Dahlstrom 1970) and, faults and folds (such as a tip propagation fold) (Williams and Chapman 1983). This section focuses on the main types of fault- fault interaction in terms of displacement transfer.

### 1.4.1 Relay Faults

Faults are said to have a relay pattern (Figure 1.4) when displacement is transferred between the faults without intersecting (Larsen 1988; Peacock and Sanderson 1995). The zones of overlap where displacement is transferred from one fault to another is termed relay zone or soft linkage (Walsh and Watterson 1991; McClay and Khalil 1998) .This zone has been defined as a type of overlapping zone where the faults bounding the zone dip in the same direction and are kinematically related (Huggins et al. 1995), sub-horizontally layered rocks will contain a relay ramp or synthetic transfer zone (Boyer and Elliott 1982; Larsen 1988). Relay ramps can be offset by minor faults connecting the original faults and only the hangingwall of the principal faults can be completely disconnected from the footwall as has been observed in some extensional settings (Morley *et al.* 1990; Trudgill and Cartwright 1994). Displacement distribution geometry of relay faults tends to be asymmetric, having

very high gradient across zones of overlap (Huggins et al. 1995), this asymmetry has been observed in normal faults (Larsen 1988) and thrust faults (Higgins et al. 2009).

In thrust- related fault systems, relay zones have been described and characterized into types 1, 2 and 3 by Higgins ( 2007) based on their pattern of linkage or branch line relative to the depth of overlapping zone (Figure 1.4 a-f). Type 1 linkage occurs when overlapping zones occur at a shallow horizon above the branch line forming the pop up structure and convoluted hanging wall- hanging wall (Hw-Hw) within the zone of shortening transfer (Figure 1.4 a and b). In type 2 linkage, the overlap may form at deeper horizon below the branch line; this creates distinctive tight fold and an undeformed corridor of footwall – footwall (Fw-Fw) at the transfer zone (Figure 1.4 c and d). Type 3 linkage is characterized by cross cutting faults (Figure 1.4 E and F), so that both faults are present above and below the branch line. Strata above the cross cutting line form a distinctive convoluted Hw-Hw transfer fold while those below the line form an indirect undeformed Fw-Fw corridor (Higgins et al. 2007).

Relay zones are relevant to the growth and scaling relationship of both isolated faults and fault arrays (Cartwright *et al.* 1995), hydrocarbon trapping potential (Larsen 1988) and pore fluid migration (McGrath and Davison 1995).

### 1.4.2 Branching Faults

Fault are said to branch when they intersect at point (Figure 1.4 g-h). The line of intersection is termed branch line Boyer and Elliott (1982). Faults that intersect are said to be hard linked (Walsh and Watterson 1991). Displacement between the principal and branch fault is transferred (Barnett *et al.* 1987) or conserved (Groshong 2006) at branch lines. The interfering fault can merge or link with the principal fault to form a through- going segments (Boyer and Elliott 1982; Childs *et al.* 1995; Higgins et al. 2007).

### 1.4.3 Splay Faults

Faults generally link or bifurcate into a series of minor faults known as splays (Boyer and Elliott 1982; Needham *et al.* 1996b). Splays mainly occur at the extremities of the principal faults and they die out along strike at tip lines. Splay faults transfer total displacement over a wider area, (Needham et al., 1996), which makes it possible for displacement along the principal fault to be accommodated by folding rather than by faulting, as for example in trishear fault propagation fold (Erslev 1991). The principal fault may continue straight in the region of fault splays or on the contrary, a splay may have a different orientation from the principal fault. Splay faults are bound in all directions by branch lines and tip lines (Huggins et al. 1995). The leading edge of a thrust fault splay is the tip line while the trailing edge is the branch line (Elliott and Johnson 1980) which are often kinematically linked (Needham et al., 1996).

### 1.4.4 Cross-Cutting Faults

Cross-cutting mainly occurs when faults, mainly of different origin or age transect one another (Watters and Maxwell 1983; Eaddy *et al.* 2008) (Figure 1.4 f). The faults can change in dip and/or strike at the zone of intersection. The line of intersection where one fault offsets the other is known as cut-off line (Groshong 2006), which is different from branch line (Boyer and Elliott 1982) although, Needham et al (1996), Higgins (2007), used the term branch line for this kind of fault relationship.

Cross-cutting faults can be differentiated into contemporaneous and polyphase faults (Needham et al., 1996, Groshong, 2006). Contemporaneous faults develop synchronously while polyphase faults occur sequentially. Contemporaneous faults commonly show an abrupt change across the cutoff line which contrasts with polyphase faults which show no abnormal change along the cutoff line as demonstrated by Needham et al (1996).

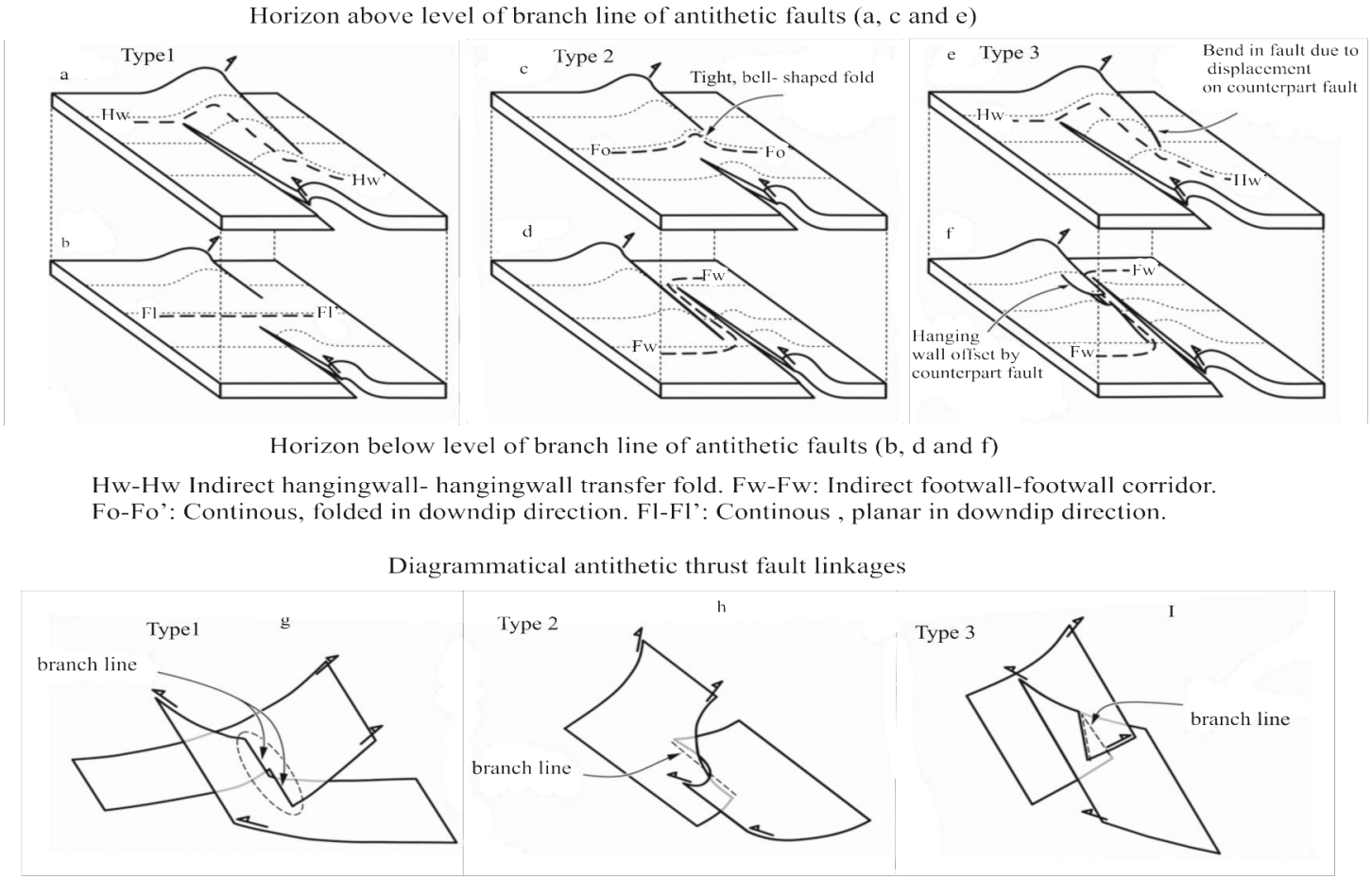


Figure 1.6: Diagrammatic representations of antithetic thrust fault relay zones at two different depths, demonstrating the deformation above a branch line (a, c and e) and below (b, d and f). Simplified fault geometries are given to demonstrate the position of branch lines. Adapted from (Higgins et al. 2007).

One of the aims of this research is to determine where the thrust related folds in the study area are crosscut by strike slip faults using a combination of several kinematic techniques which include structural style, sedimentary packages and displacement distribution analysis.

## 1.5 MECHANICS AND KINEMATICS OF THRUST FAULTS

Fault motion analysis is an important aspect in this thesis because it is used to differentiate isolated faults from segmented ones where clear and systematic changes in fault displacement can be attributed to the primary control of fault segmentation. One of the traditional techniques for analyzing fault motion history is the expansion index, which was introduced by Thorsen (1963). The expansion index of a given fault is obtained by dividing the thickness of a specific unit in the footwall by the thickness of the unit in the associated footwall block. The concept of expansion index is most useful in defining the period of most significant fault growth (McCulloh 1988), but because it is a ratio, it does not quantify any absolute slip or slip rate as demonstrated by Cartwright et al.(1998). An alternative method is either the displacement length plot (d-x) or the throw- depth plot (T-z). Both techniques have been found useful in determining the absolute magnitude of slip as documented in many studies (Mansfield and Cartwright 1996; Briggs et al. 2006; Baudon and Cartwright 2008b).

### 1.5.1 Displacement Distance Relationship

Fault displacement can be measured systematically at specified length along strike of a single horizon and/or at each several stratigraphic layer up dip. The former is termed lateral displacement distribution (Larsen 1988; Manighetti *et al.* 2001a), while the latter is termed vertical displacement distribution (Williams and Chapman 1983; Ellis and Dunlap 1988). If displacement dies out in all directions, the fault is surrounded with a tip line similar to that predicted in the general blind fault model of Barnet et al (1987). Displacement generally dies out up-dip and along strike or transfers displacement to another medium such as faults and folds (Dahlstrom 1970; Suppe 1985b). The transfer of displacement or interference with other structures may influence the overall geometry of the fault. However, a fault may propagate to free surface or may sole into a detachment layer without

losing displacement (Briggs et al. 2006; Baudon and Cartwright 2008a; Baudon and Cartwright 2008b). The variation in both vertical and horizontal displacement distribution depends on structural style and interaction with other structures (Muraoka and Kamata 1983; Ellis and Dunlap 1988; Nicol *et al.* 1995).

Vertical and horizontal displacement variation can be represented using the displacement versus height plot (Figure 1.5 a), and displacement versus width plot (Figure 1.5 b), respectively. Displacement values can also be represented in contoured fault plane projection plots to give a more dimensional view (Figure 1.5 c), especially when the study involves both updip and along strike fault analysis (Baudon and Cartwright 2008b; Higgins et al. 2009).

The standard types of displacement distribution geometries were mainly derived from studies of normal faults. However, similar type of profile geometries have been observed in thrust faults. In theory, an isolated blind fault along any direction (up dip or along strike) would show the C type d-x profile (Muraoka and Kamata 1983) which means maximum displacement is at the centre (Barnett et al. 1987), or close to the centre (Briggs et al. 2006) of the fault length or width (Figure 1.5 a and b). In summary, contours of equal value of displacements for isolated faults would normally produce a concentric ellipse of maximum value at the centre to zero at the tip line loop (Rippon, 1985, Walsh and Watterson, 1989 Figure 1.5 c). The zone of maximum displacement is often assumed to be indicative of the point of initiation (Barnett et al. 1987) . Any deviation from the standard C type profile, or concentric elliptical contour pattern would normally indicate linkage or lithological effects. But these views have been challenged, as other forms of barrier to fault propagation have been identified (Nicol et al. 1995), such overlapping faults, cross cutting faults etc.

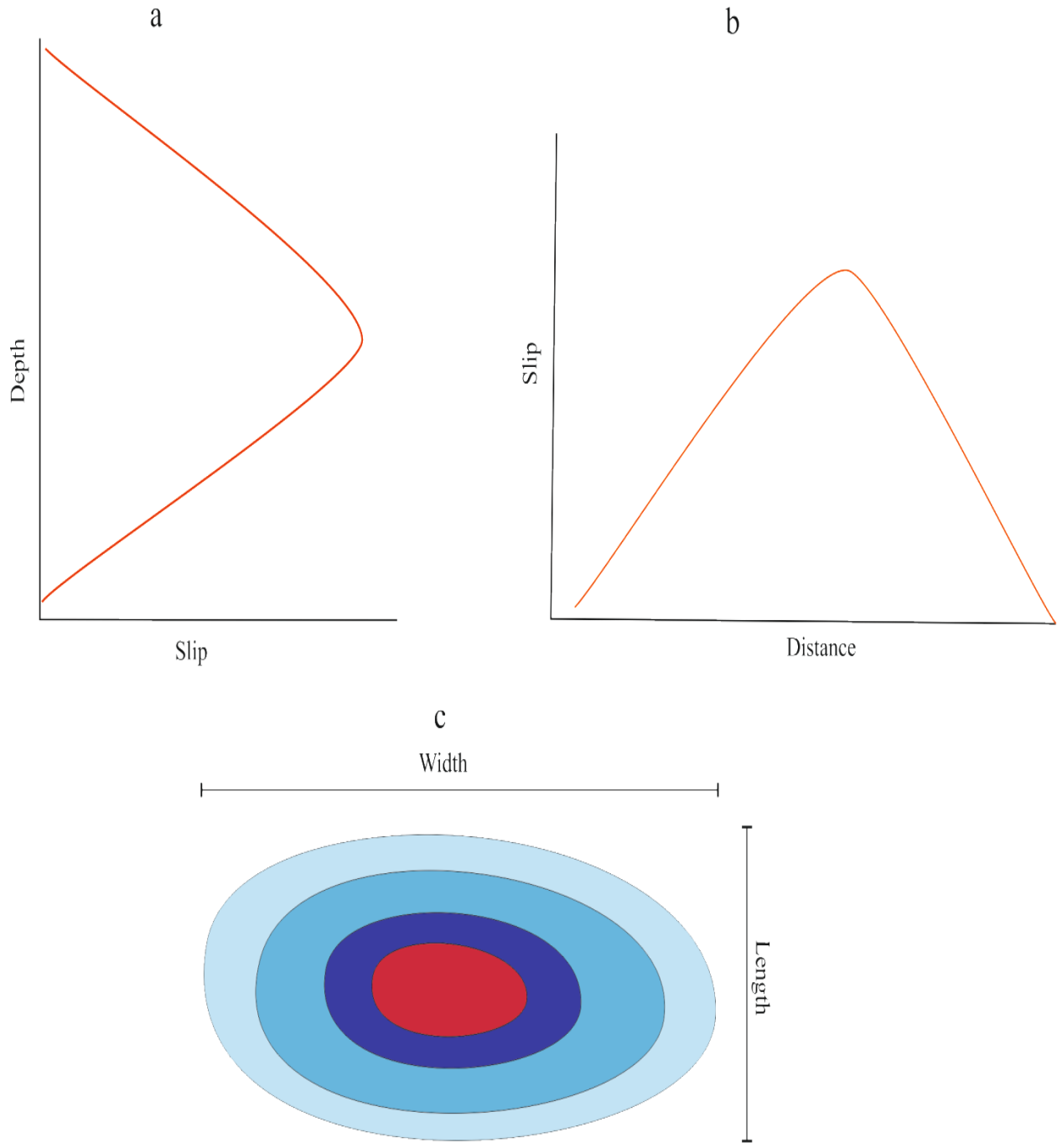


Figure 1.7: Displacement distribution geometry of an isolated blind fault. (a) Relationship between depth and displacement. (b) Relationship between width and slip (c) Contoured displacement distribution.

The different types of displacement geometries which do not conform to the standard blind displacement profile are shown in Figure 1.6. The flat top geometry or the M type profile (Figure 1.6 b) as commonly called signifies that the fault's propagation has been influenced by change in lithology (Muraoka and Kamata 1983; Baudon and Cartwright 2008b; Malik *et al.* 2010). Fault displacement tends to systematically increase at high competent zones and decreases at the incompetent zone but remains almost constant at zones where the lithology shows insignificant variation in character.

Faults which show the asymmetric type geometry (Figure 1.6 c, e and f) have been interpreted as lateral tip restricted faults (Nicol et al. 1995) such as relay faults (Larsen 1988) or those that have been bound by cross cutting faults oblique to the principal faults (Needham et al., 1996) (Figure 1.6 c). These kinds of faults have their maximum displacement or high displacement gradient close to where they have been restricted and they are characterized to have smaller dmax/L ratio than an isolated fault (Kim and Sanderson 2005). This kind of profile type may vary in geometry based on the number of zones or tips restricted. For instance a single tip restricted fault would show the profile asymmetry shown in Figure 1.6 c, which may be termed strongly asymmetric (Manighetti et al. 2001a). Faults which are double restricted tend to be either symmetric having both restricted tips steeply dipping (Figure 1.6 d) or asymmetric characterized by a flat central zone with maximum displacement close to the restricted tip ( Figure 1.5 e).

Another type of profile geometry which has maximum displacement close to one end is the elliptical with taper type (Manighetti et al., 2001, Figure 1.6 f). Profiles of this form are indicative of faults which have propagated past a restricted zone. Some of the fault displacement is transferred to the barrier causing restriction to propagation

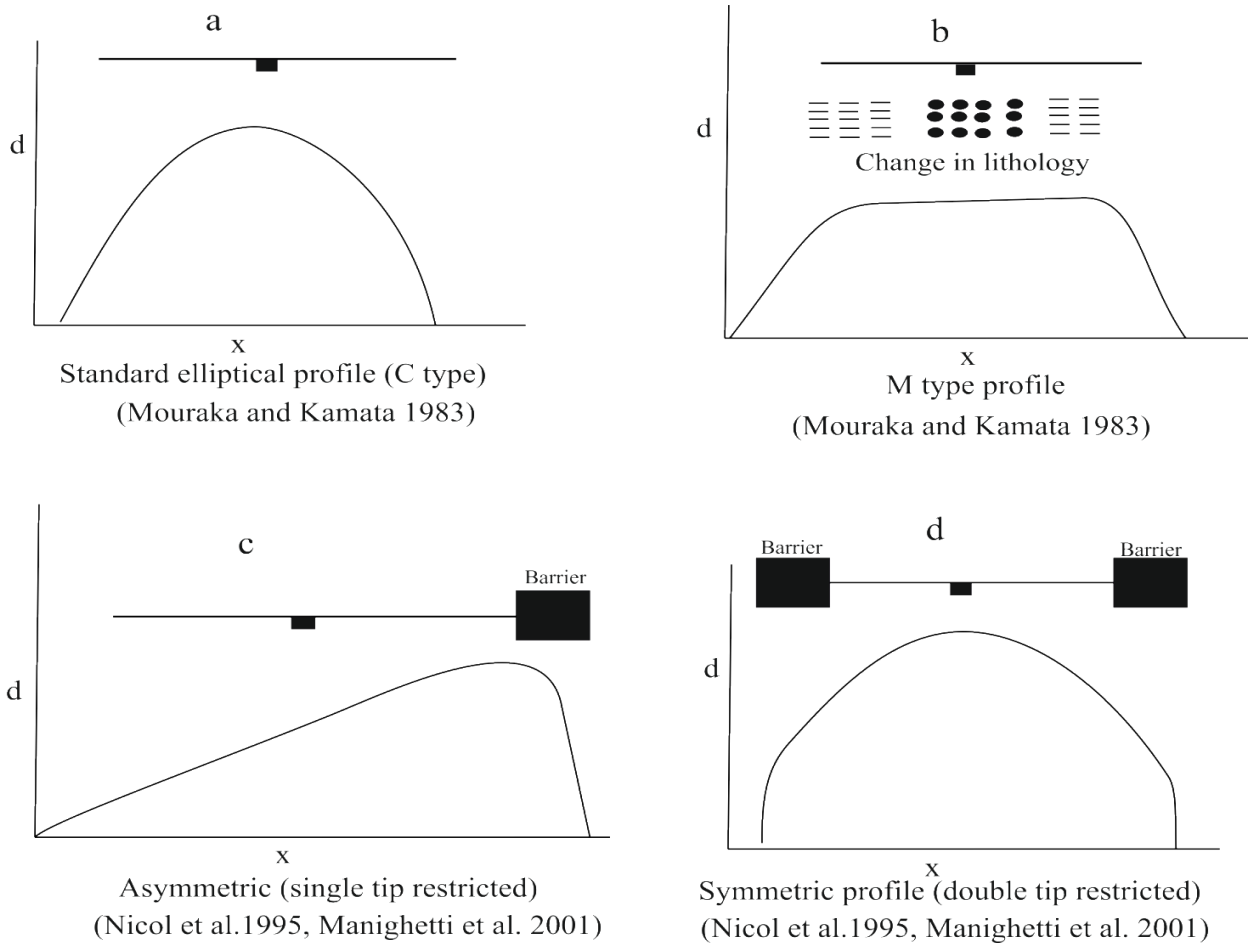


Figure 1.8: Displacement distribution geometries of normal faults which do not conform to the standard C type profiles.

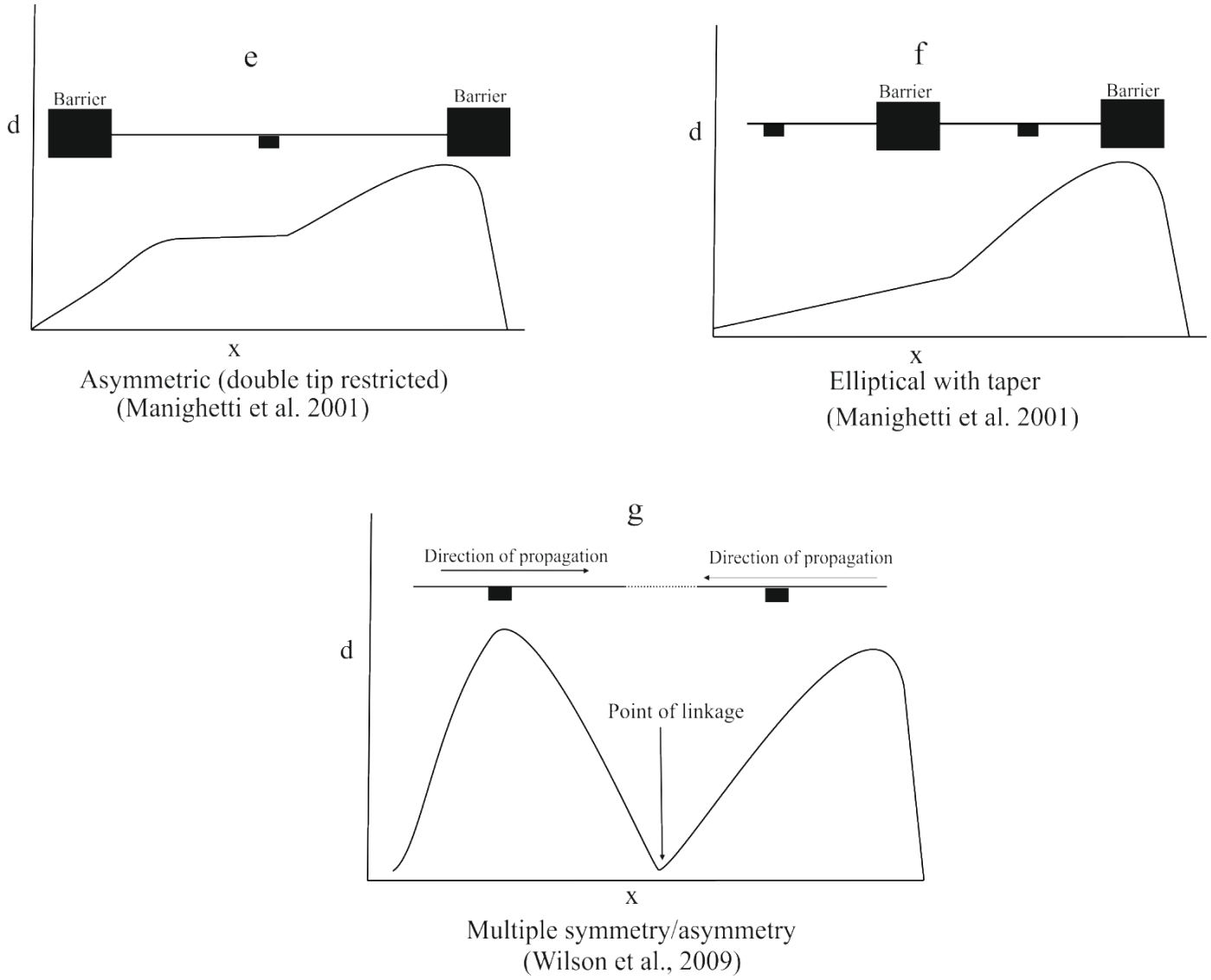


Figure 1.9: Displacement distribution geometries of normal faults which do not conform to the standard C type profiles.

Faults with profiles characterized by multiple maxima separated by a minimum (Figure 1.6 g), have largely been interpreted as a fault formed by the process of linkage and this has been incorporated by many fault growth models (Higgins et al. 2007; Schlagenhauf *et al.* 2008). This model has widely been accepted in the evolution of faults. It states that faults propagate initially as arrays of isolated faults which intersect and link to form a through going fault (Cartwright et al. 1995; Higgins et al. 2007). The zone of minimum displacement is indicative of where the independent faults merge to form a through growing segment (Williams and Chapman 1983; Higgins et al. 2007) . The linkage theory has been used to explain why many faults do not conform to the widely accepted mathematical expression of fault growth model ($d=cl^2$) or a linear relationship (Walsh and Watterson 1988), but rather shows a considerable scattered relationship on dmax-L plot (Cartwright et al. 1995)

## 1.6 THESIS LAYOUT

The thesis is divided into eight (8) chapters, three (3) of which are the main result chapters (Chapters 4, 5 and 6). These represent a logical series of argument relating to the propagation and interactions of thrust related folds.

**Chapter 2** reviews the methods used for this research. This includes the utilization of 3D seismic data and how it is interpreted. There is also a summary of the various types of strain components and how they were measured on seismic sections.

**Chapter 3** reviews the geological setting of the study area. The 3D seismic survey used for this thesis was also introduced, and a description of the main stratigraphic units that are of importance to this study.

**Chapter 4** describes in detail the main structural elements (thrust related folds, and strike slip faults) in the study area, and the factors influencing deformation in the area. It also introduces the possible interactions between the structural elements.

**Chapter 5** investigates the influence of strike slip faults on thrust fault propagation, an observation made in Chapter 4. A combination of kinematic analysis which includes a description of the syn-kinematic sediments, dip slip and shortening distribution along examples of thrust related folds intersected by strike slip faults. The results allow conclusions to be drawn on the timing interactions between thrust faults and strike slip faults.

**Chapter 6** examines an isolated fold internally segmented by thrust faults of similar and opposing dips and strike slip faults. The vertical and horizontal distributions of throw for each of the thrust faults are presented. There is also a presentation of shortening, and summed throw of the faults along strike. The quantification of the strain along the fold allows conclusions on the kinematic interactions between the constituent thrust faults, and the lateral and vertical development of the fold as a whole.

**Chapter 7** draws together the conclusions of Chapter 4, 5 and 6. Displacement and shortening distributions of some thrust faults described in Chapter 4 are presented. The interrelationship between thrust faults and folds, and the main factors influence the propagation of thrust related folds based on fault interactions are discussed. More also, the main factors controlling deformation in the study area are proposed, following observations made in Chapter 4. Finally, the implications, and limitation of the research are discussed and proposals for future work concluded the chapter.

**Chapter 8** lists the main conclusions of the thesis.

# CHAPTER TWO

# 2 METHODS

## 2.1 INTRODUCTION

This study mainly relies on the interpretation of two dimensional (2D) and three dimensional (3D) seismic reflection data Figure 2.1. The aim of this chapter is to give a general overview of the methods used for this thesis. We begin by giving a basic introduction of 3D seismic interpretation, followed by the description of how the results presented in this study were obtained.

## 2.2 THREE DIMENSIONAL SEISMIC DATA

The concept of 3D seismic data commenced in late commenced 60's (Walton 1972) and was introduced in the academic research in the 1990s ( Hart, 1999). 3D seismic data was developed due to the improvement on 2D seismic survey in order to enhance the study of subsurface geology. Generally, 3D seismic interpretation has a higher resolution than 2D survey and their grid lines are extremely dense. This results in greater subsurface sampling which enhances the possibility of developing a more accurate subsurface interpretation (Morozov *et al.* 2009). The ability to map in three dimensions has significantly improved the analysis of subsurface features. For example 3D seismic interpretation techniques have proven useful in describing and analyzing thrust - related folds in deepwater fold and thrust belts (Corredor et al. 2005; Higgins et al. 2009). This has provided a unique insight into the nature of such inherently inaccessible regions and enormously increased the success rate of oil and gas exploration (Davies *et al.* 2004).

3D seismic data are acquired by generating an acoustic pulse at or near the surface, which for marine survey is air gun arrays (Hart 1999). Some of the waves are reflected or refracted from the subsurface interfaces that represent a change in acoustic impedance due to variation in rock properties. This reflected energy is detected by hydrophones and geophones for marine and land surveys respectively (Figure 2.2). The time it takes a seismic wave to travel from the source to the

receiver is measured in seconds or milliseconds two way travel time (TWT). The raw data is processed to increase the quality and resolution by spatially distributing reflection points correctly and eliminating unwanted events commonly known as noise (Yilmaz 2001).

Acoustic impedance which has the symbol "Z" is the product of the velocity (v) and density (ρ) of a rock layer (Philip and Brooks 1991). It determines the acoustic transmission and reflection at the boundaries between two layers having different properties such as fluid content, texture, porosity and composition. The changes in acoustic impedance across an interface are recorded as wavelets on a vertical trace, with waveform amplitude propagating towards the direction of propagation (Philip and Brooks 1991).

The polarity of seismic data is described as SEG normal or SEG reverse (Bacon *et al.* 2003). This refers to the conventions promulgated by the Society of Exploration Geophysicists (SEG). SEG normal corresponds to increase in impedance downwards being represented as peak and is mainly used in the USA (Bacon et al. 2003). The reverse polarity would imply negative amplitude (trough) as the increase in impedance and is commonly employed in Europe (Simm and White, 2002, Figure 2.3). The 3D seismic data used in this study is displayed as the SEG normal standard America polarity convention (Figure 2.3 c and d), where the seabed is a positive reflection (an increase in impedance) (Figure 2.3 a and b).

Another major factor to consider in seismic interpretation is the phase of the wavelet because it aids in understanding polarity (Brown 1999). It is most convenient to work with data that has been deconvolved to zero phase, which means the maximum amplitude occurs at the center of the waveform. The main importance of zero phase data is (1) it almost coincides to time horizon which makes resolution better than other wavelets with same frequency, (2) the shape of the wavelet decreases ambiguity in the associated waveform with subsurface boundaries, and (3) the majority of

the energy is concentrated at the central lobe due to the symmetry of the wavelet (Brown 1999). The data used in this study is processed to near zero phase (Figure 2.3 a and b).

The main purpose of 3D seismic interpretation in this study is to define and visualize subsurface stratigraphy, structure and physical properties of rock. The simplest and most common method of surface mapping in 3 dimensions is by tracking the horizon of interest on a series of lines orthogonal to one another. These lines are termed inlines and crosslines. Horizontal sections, or time slices can also be viewed.

Vertical seismic profiles are made up of numerous reflections. Depending on the dataset, in most cases these horizons vary from high to very low amplitude reflections. The main criteria in choosing a reflection to map depend on the continuity and strength of the event. The most recognizable and continuous event is most convenient to trace through a data grid. In some cases, sequence boundaries are most laterally continuous events on seismic sections such as the Horizon M reflection in the Levant Basin (Bertoni and Cartwright 2006), which is one of the main horizons in the study area.

An attribute is a derivative of a seismic measurement, such as time, amplitude, frequency and azimuth. Attribute maps provide useful geological information that is not so obvious on other platforms for interpretation (Brown 1999). The type of attributes used in 3D seismic interpretation varies depending on the software package used. In this study, Schlumberger IESX Geoframe 4.04 was used for both horizon and fault mapping. The main attributes used for this study include dip, azimuth and RMS amplitude. These attributes were collectively used to reveal and detect small scale changes corresponding to folds, and faults which aided in the production of the structural maps used in this thesis (Chapters 4-7).

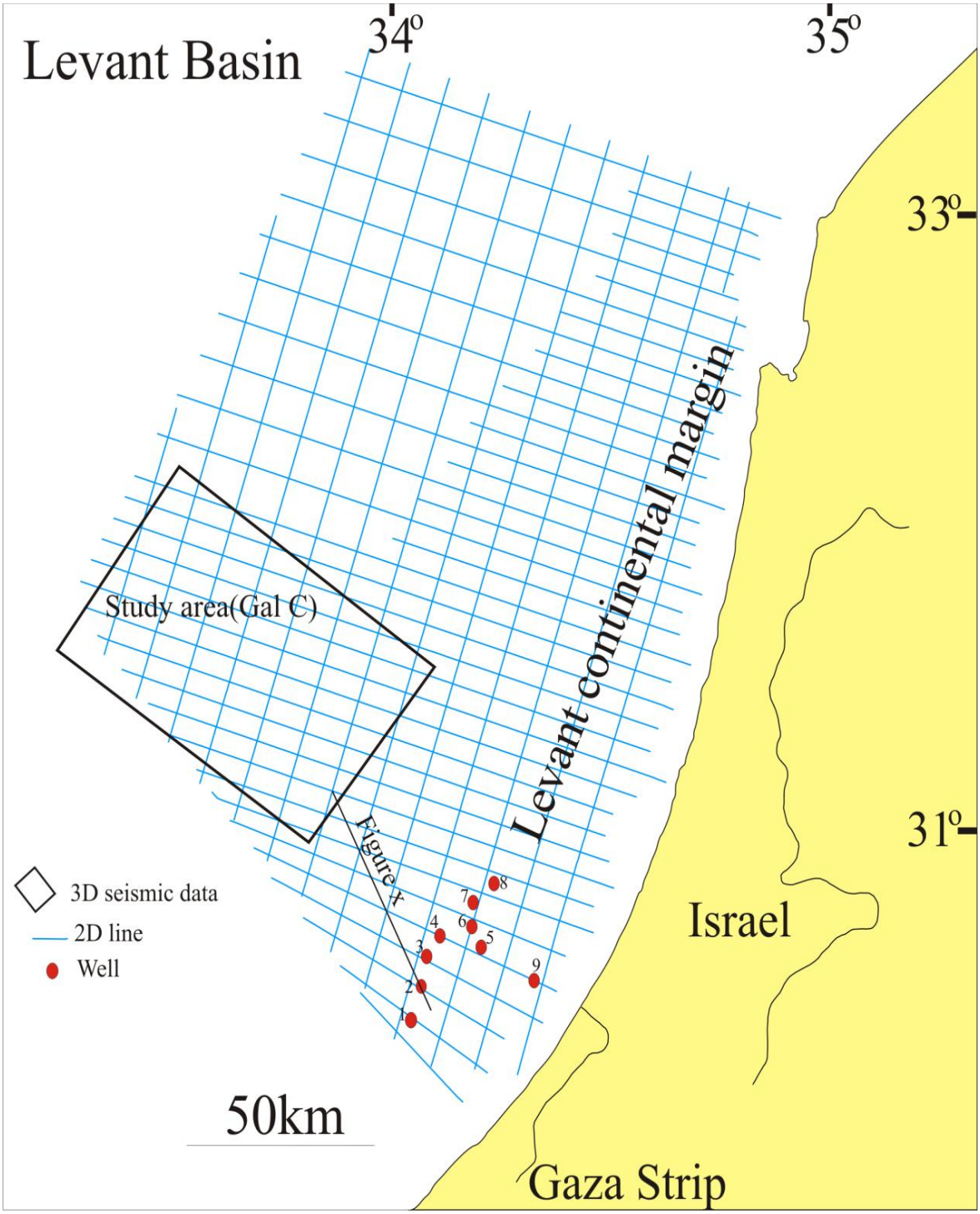


Figure 2.1: Location map of the study area showing the 2D and 3D seismic surveys, and position of the exploration wells used for this study. Nomenclature for the exploration well is 1=Gaza Marine-1, 2=Gaza Marine-2, 3=Noa-1 South, 4=Noa-1, 5=Or South-1, 6=Or-1, 7=Yam West-2, 8=Yam West-1, 9=Nir-1.

### 2.2.1 Resolution

Stratigraphic seismic resolution has been defined by Sheriff (1991) as the ability to separate two features that are very close together; the minimum separation of two bodies before their individual identities are lost. One of the main problems in seismic interpretation is to be able to determine how and where to distinguish geological elements that are resolved and unresolved. Events which are unresolvable or undetectable on seismic sections such as faults with very small displacement are termed sub-seismic faults (Pickering *et al.* 1996) and are one of the many factors capable of modifying displacement geometries in fault mapping (Baudon and Cartwright 2008b). The limit of detectable events in seismic interpretation depends on the vertical and horizontal resolution of the dataset. The resolving power of seismic data is always measured with respect to the seismic wavelength, which is given by the quotient of velocity and frequency (Widess 1973; Brown 1999). Generally, seismic velocity increases with depth because the rocks are older and more compacted. The predominant frequency decreases with depth because the higher frequencies in the seismic signal are more quickly attenuated. This results to a decrease in wavelength with depth making resolution poorer.

Vertical resolution has two limits**,** these include the limits separability and visibility. Both limits result from the interaction of the wavelets from adjacent reflecting interfaces (Brown, 1999). The limit of separability is defined as the one quarter wavelength, which is equivalent to the bed thickness associated with the closest separation of two wavelengths of a given bandwidth (Brown 1999). For a layer thinner than one quarter wavelength, reflection amplitude can be improved due to constructive interference from the wavelet associated with the top and base of the bed. This phenomenon is known as the tuning thickness (Brown 1999). The limit of visibility is reached when a thinned bed (less than one-quarter) is progressively attenuated and the reflection signal becomes obscured due to background noise (Brown 1999). Limit of visibility ranges from $\lambda/8$ to $\lambda/30$ and any structure below this resolution limit may be regarded as sub-seismic structure. The limit of visibility

is influenced by the acoustic impedance of the geological layer of interest, noise in the data set, and the phase of the data set (Brown 1999).

The limit of separability of a given stratigraphic unit can be directly estimated by determining the wavelength, if the formation velocity and dominant frequency are known. For example the vertical resolution of the data set used for this study has been estimated to be 10m and 50 m for the Plio-Quaternary unit and its underlying Messinian unit respectively (see chapter 3 for detailed stratigraphy of the area. The Pliocene unit has a dominant formation velocity of 2000m/s while that of the Messinian unit is 4000 ± 500m/s (see Chapter 3, Figure 3.6 for stratigraphy). These velocity values were determined from a check shot of nearby exploration well (Frey Martinez *et al.* 2005).

Fresnel zone (Figure 2.2), is defined as the part of a reflector covered by the seismic signal at a certain depth (Sheriff 1997). Reflecting interfaces are normally made up of an infinite number of scattered points, each of which contributes backscattered reflections to the receivers (Figure 2.2 a). The area that produces the reflection is known as the first Fresnel zone, this buried reflecting zone insonified by the first quarter of a wavelength (Kearney *et al.* 2002 ). Any feature with lateral extent larger than the Fresnel zone will be visible.

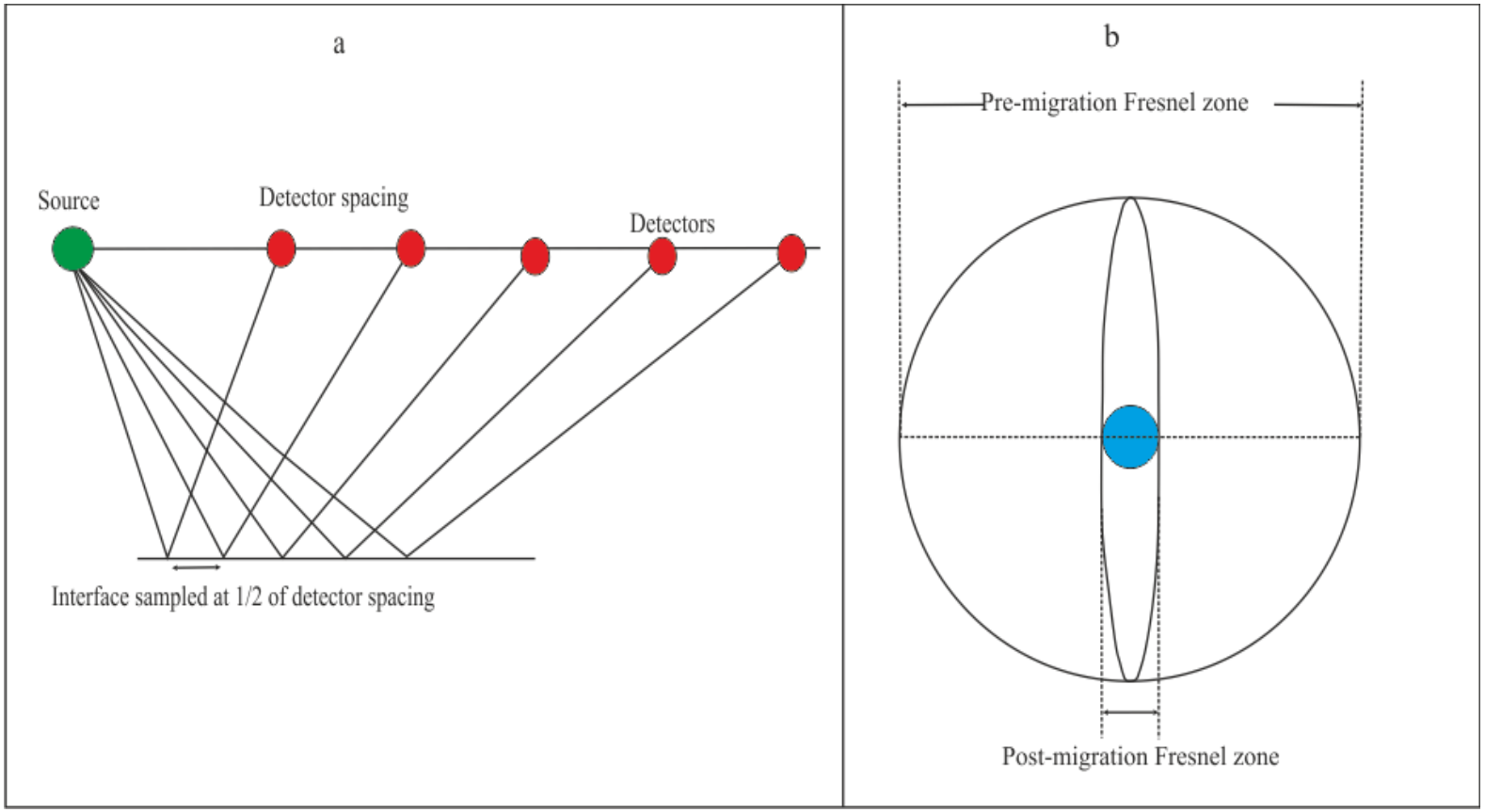


Figure 2.2: Horizon resolution and definition of the Fresnel zone. Horizontal resolution in seismic surveys is determined in part by detector spacing which affects the sampling interval (a). The width of the Fresnel zone (b) also controls the resolution, and 3D migration reduces the size of the Fresnel zone to a small sphere. Adapted from (Brown 1999).

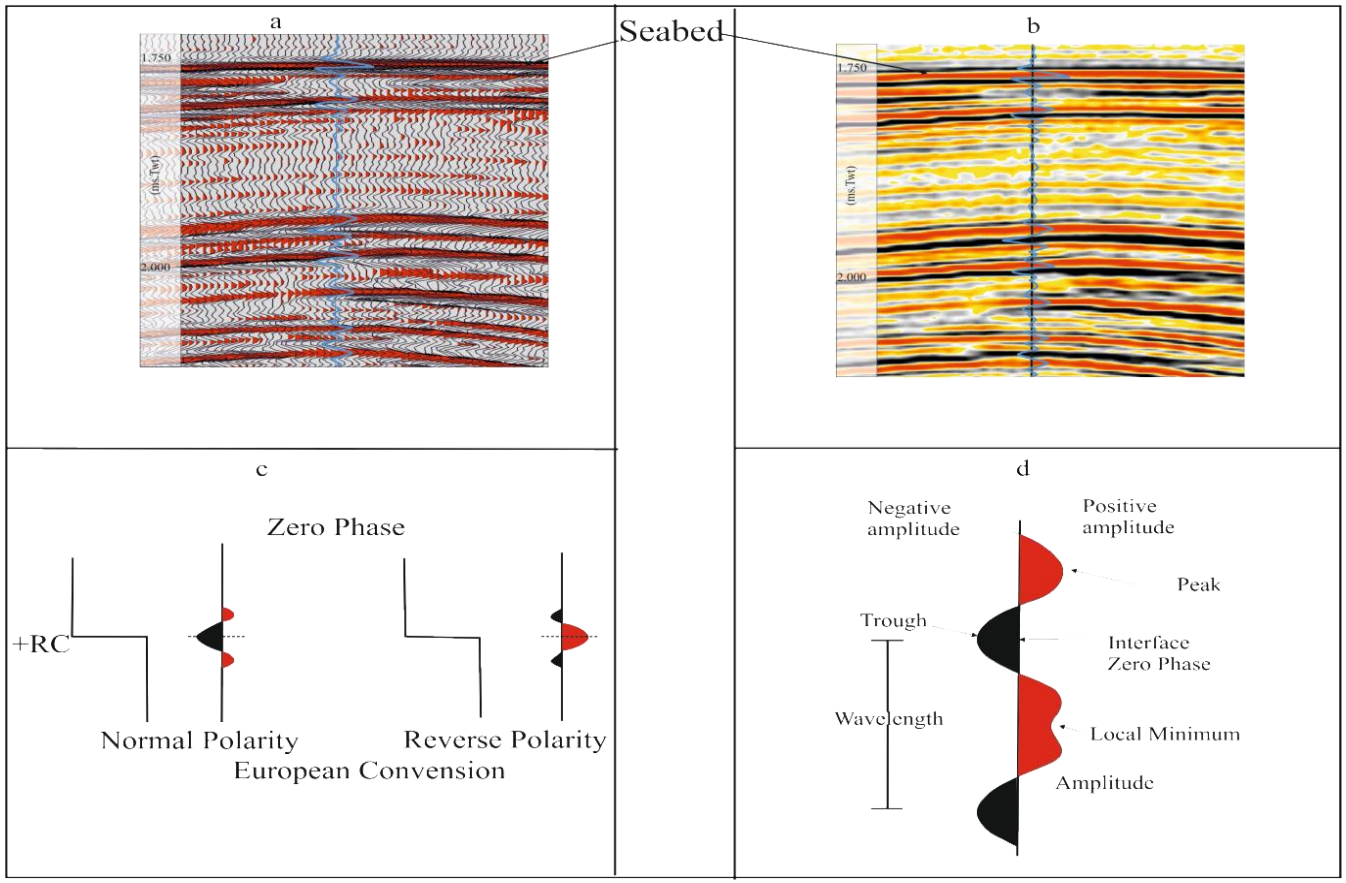


Figure 2.3: Seismic phase and polarity. (a) Seismic time section from a survey in the Levant to show the characteristics of the seabed reflection (displayed as variable area). Note that the seabed produces a positive wavelet (peak). (b) Same section as a variable intensity display. (c) Explanation of the European polarity convension using a zero phase wavelet. Taken from Simm and White (2002). +Rc indicates an increase in acoustic impedance downwards. (d) Nomenclature of the seismic waveform. Positive amplitudes are displayed in red, negative amplitudes in black, as in the seismic section in (b). Taken from Heinio (2007).

Migration is a principal technique which focuses energy spread over a Fresnel zone and removes reflection patterns from points and edges (Brown, 1999 Figure 2.2 b). Thus, improving the horizontal resolution to about one quarter wavelength.

### 2.2.2 Limitations and Pit falls

The main pitfalls in seismic interpretation include misidentification of pull-up and push-down, and multiple reverberations. Pull-ups and push-downs are seismic artifacts due to anomalous seismic velocity structure. A unit with high velocity encased in a velocity unit tend to produces a pull-up while those within the lower velocity environment will produce a push-downs (Eigen 1960). Both pull-ups and push-downs can be eliminated by converting from time to depth if well data is available (Bacon et al. 2003). In the absence of well data, pull-ups and push- downs are always considered especially when analyzing faults and folds. However, fault displacement mapping in this study is based within the Plio-Quaternary overburden, where lateral variation in internal velocity is not significant (Martinez et al., 2005),except across larger displacement thrust faults, or close to the top of the Messinian salt (see Figure 3.6 in Chapter 3). The large velocity contrast between the salt and overburden result in numerous imaging artifacts (poor migration) and velocity anomalies (push-down and pull-up).

## 2.3 DATA AND INTERPRETATION

The results presented in this study rely on the interpretation of two dimensional (2D) and three dimensional (3D) seismic reflection data, and a set of exploration wells located within the Levant Basin. The locations of the seismic and well data are shown in Figure 2.1. Several 2D lines runs though the study area, some of which extends from the marginal area of the Levant to the distal domains of the area.

### 2.3.1 Three Dimensional Dataset

The 3D seismic survey set used for this study is located in the southern area of the contractional domain of the Levant Basin (Gradmann *et al.* 2005) Figure 2.1. The survey set is referred to as Gal C and it has area of about 1450m$^2$. Gal C was acquired in 1990 and processed to near zero phase using SEG normal standard polarity, which equals a positive acoustic impedance on the seismic section. The data was migrated using a single pass 3D post stack time migration, which was used to generate a 12.6m by 12.6m grid at sampling interval of 1ms.

The 3D data set was interpreted using Schlumberger Geoframe 4.04 software on a UNIX workstation. Several key horizons were mapped regionally throughout the survey. The criteria for selecting mappable horizons were mainly dependent on the amplitude strength and continuity of the reflections through the survey. The main horizon reflections mapped in this study is labeled based on the stratigraphic subdivision of the Plio-Quaternary succession and upper Messinian unit (M, M6, IPM1, BPM2, IPM2, and BPM3, see Figure 3.6 in Chapter 3). Additionally, some reflections which are not continuous all through the survey but provided valuable local control on structural geometry were also mapped.

Seismic attribute maps were used as tools for proper detection of the structures and to produce structural maps. Horizon slices cut from the coherency volume were also used in producing structural maps, particularly, along areas where resolution is poor on seismic sections. Coherence slices were useful in detecting kinematic indicators (minor fractures, and sedimentary features), for strike slip fault displacement and their sense of shear.

Vertical fault interpretation was preferentially oriented to strike of the faults. Fault planes were typically interpreted based on the following criteria: (1) stratal reflection discontinuity reflection in a systematic alignment, (2) Juxtaposition across a fault surface of non-correctable units and (3) loss in

amplitude below fault plane possibly as a result of the juxtaposition of higher velocity units in the footwall laterally against slower velocity units in the hanging wall (Figure 2.4 a).

One major limitation in fault interpretation is the uncertainty in the positioning of fault planes, due to the considerable decrease in amplitude reflection close to cut-offs, tips and intersection points. Horizon correlation from footwall to hangingwall was accomplished by use of the combination of in-lines, and cross-line, such that direct correlation around zones of poor resolution was possible.

Another possible limitation of fault interpretation is the mis-representation of upper tip points, as sub-seismic faults could occur in apparent continuous folds on the seismic data without detection (Baudon and Cartwright 2008b). According these authors, the interpretation of fault tip is restricted to structures where visible systematic refection offset is absent across a zone of at least three traces in width (75m). Fault offset invariably passes systematic upward into region where reflections are deflected, but not offset (Baudon and Cartwright 2008b). In this thesis, the upper tips of faults were defined at points where stratal deflection was no longer detectable.

### 2.3.2 Fault Displacement and Shortening Measurement

The apparent displacement (separation) and shortening of the thrust faults interpreted in this study is shown in Figure 2.4. These techniques are similar to those documented by previous studies (Williams and Chapman 1983; Barnett et al. 1987; Baudon and Cartwright 2008b). However, throw and dip slip separation were the main displacement components used for this research (Figure 2.4). The criteria for which component to measure, is mainly dependent on the relative parameter to be compared with or plotted against, for instance it is expected to use throw if plotted against depth since both units are the same (TWT. ms).

#### *2.3.2.1 Throw*

A detailed throw analysis was carried out in place of dip separation and heave (Mansfield and Cartwright 1996; Bertoni and Cartwright 2005) in Chapter 6, because it is representative, easier and faster, and it limits error as described below.

Throw values were measured as the difference in vertical distance between the apparent inflection points of the hangingwall and footwall cut-offs (Figure 2.4 a). The depth of the hangingwall cut-off at a specific horizon was recoded as the depth (z) in TWT of the stratigraphic horizon from which throw was measured. Throw was measured at different stratigraphic depth along strike. In Chapter 6, throw values were measured on thrust faults using seismic profiles orthogonal to fault strike and displayed as throw versus depth plots (T-z plots, Cartwright and Mansfield, 1998), lateral profiles (T-x) and as contoured fault plane projections, following standard techniques outlined by Barnett et al (1987), Baudon and Cartwright (2008b).

One possible error which may arise from this technique is the unavailability of well data in the study area for depth conversion. To simplify the analysis, T-z plots were displayed in values of two-way travel-time (TWT). In order to verify whether TWT time would introduce significant distortion to the throw profile geometry, Baudon and Cartwright (2008b), depth converted faults closest to a control well using check shot velocity data. Depth converted T-z plots display a strikingly similar overall pattern to depth in TWT (Figure 2.5). Furthermore, the Plio-Quaternary units are characterized by minimal velocity variation (Frey Martinez et al. 2005), implying error due to the absence of well data is minimal.

The only quantifiable error from the throw measurement arises from the sample interval and the accuracy of measuring the amplitude peak of the horizon at the specified cutoff position on the fault surface. These errors amount to ± 2ms. Consistency in taking measurements at inflection points minimizes error due to fold drag (Walsh and Watterson 1987) i.e. folds without visible displacements

were measured as zero. Measurements were not taken where horizon resolution was too poor and fault tips were located at points where stratal reflections were not detectable. Areas characterized by poor data quality were also interpolated based on the profile geometry which may amount to an additional error that is difficult to quantify. However, interpolations were based on the profile geometry of the fault.

#### *2.3.2.2 Dip- slip displacement*

The dip slip displacements of the thrust-related folds (Chapters 5 - 7) were measured using a similar technique to that described by Williams and Chapman (1983), and Tearpock and Bischke (1991). Dip-slip values were measured as the difference in sub-vertical distance between the apparent inflection points of the hangingwall and footwall cut-offs (Figure 2.4 a). This was done at specific intervals (125m or 250m) depending on the length of the structure and were plotted against the horizontal distance of the thrust folds (Chapter 5 and 7). The plotting convention allows direct comparison between bulk shortening and summed displacement.

A major limitation of this dip-slip method, however, is that the displacement distribution geometry may not be directly compared to other slip parameters such as throw and heave which have been used in other studies (Baudon and Cartwright 2008a; Higgins et al. 2009). This restriction will be true if faults planes vary in dip in cross-sectional profiles, as horizontal displacement will be seen to decrease at steeper fault dips. This geometry may produce an apparent increase or decrease in displacement gradient. This issue of variable fault dip has limited impact however, because the thrust faults in this study have an almost constant dip along strike and down dip. For comparison purposes, all 3 parameters (dip-slip, heave and throw) of a thrust fault in the study area (Fault T24, see Chapter 4, Figure 4.4), are shown on the same plot for comparison (Figure 2.4b). The plots display almost similar pattern. Additionally, the dip-slip technique is most widely used in fault slip analysis

(Muraoka and Kamata 1983; Williams and Chapman 1983; Ellis and Dunlap 1988), this implies, the data can easily be compared to other published results.

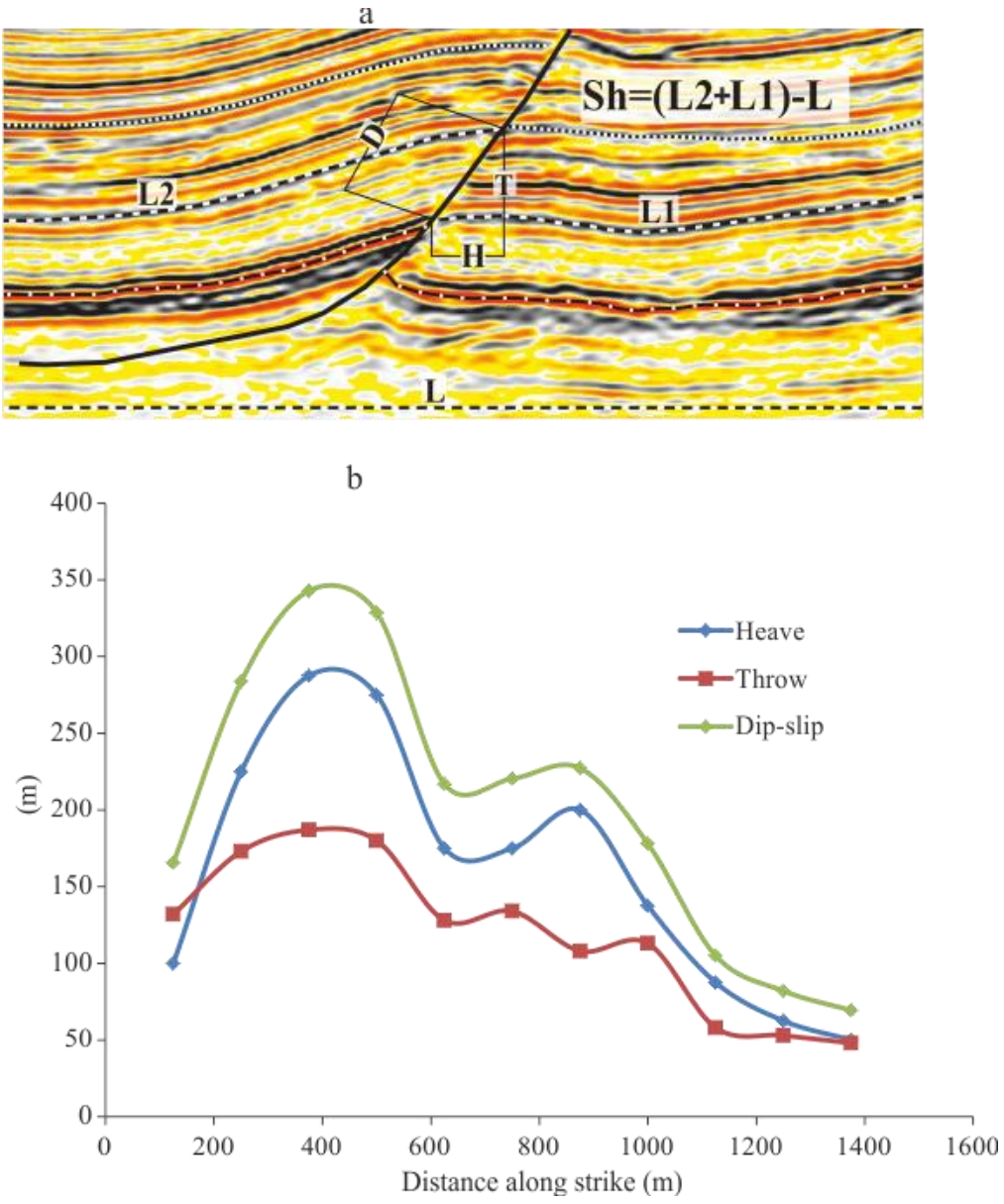


Figure 2.4: Methodology for calculating slip and shortening. (a) Diagram illustrating the methods used in measuring displacement and shortening. Values of shortening were calculated by line length analysis: Sh= (L2+L1)-L, where L2 and L1 represent the length of hangingwall and footwall respectively while L is length of the selected horizon. D- dip slip, T- throw and H- Heave, here, dipslip was used in place of heave and throw similar to the line length technique used by Briggs et al (2006), Baudon and Cartwright (2008b) and (Higgins et al (2009). (b) Shows a plot of the 3 displacement parameters (dip slip, throw and heave) along a thrust fault (T24) in Gal C for comparison purposes. D represents Dip slip, T- Throw and H- Heave.

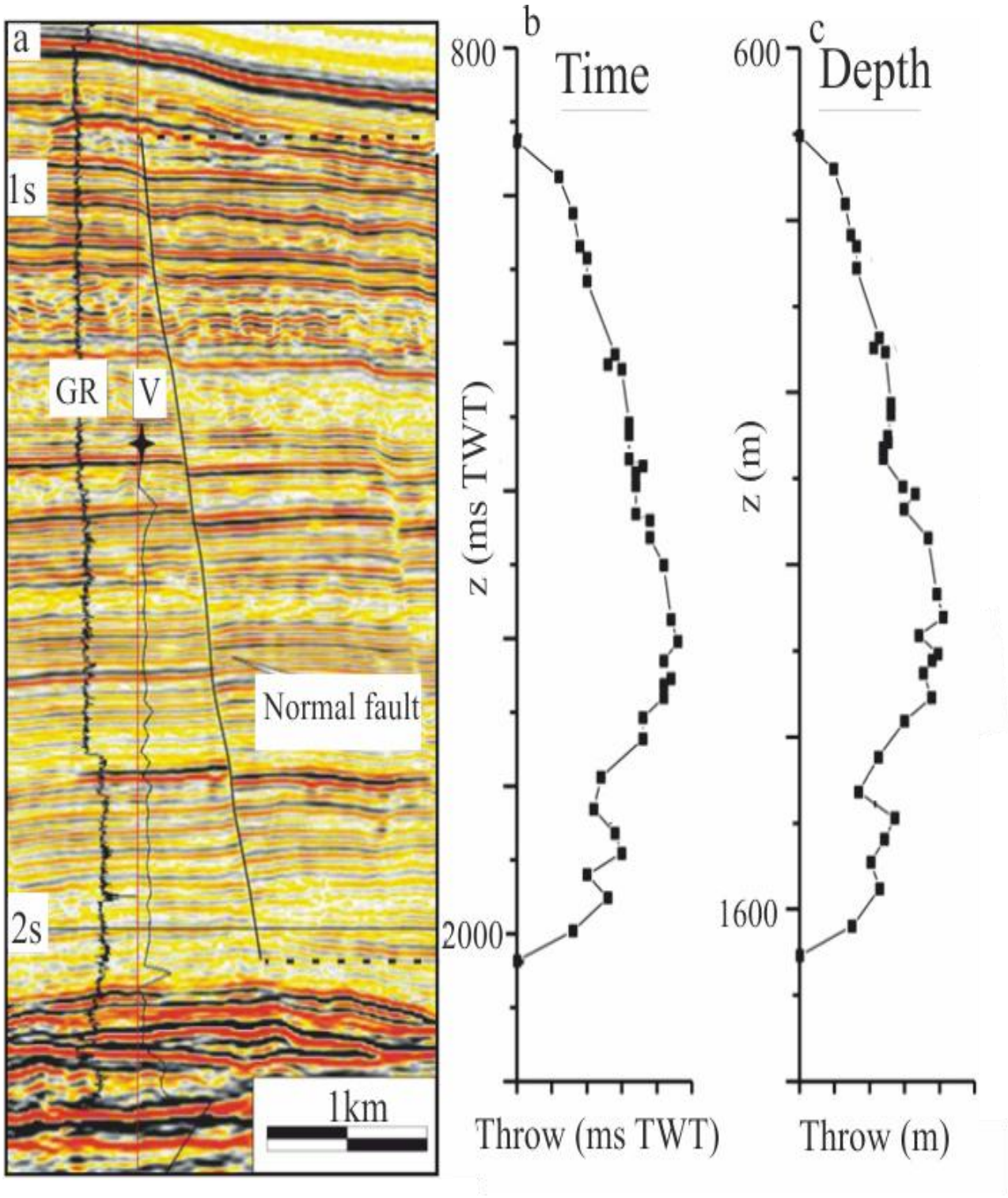


Figure 2.5: Throw plot at different stratigraphic interval of an extensional faults in the marginal area of the Levant. (a) Sesimic section showing gamma ray (GR) and Velocity (V) profiles from a well in the marginal area of the Levant. (b) T-z plot in two-wat-travel-time (TWT), (c) T-z plot in meters. Modified from Baudon and Cartwright (2008b).

Potential errors for dip-slip measurements arise from the sample interval, vertical compaction, accuracy to take measurement from the amplitude peak intersecting the interpreted fault displacement and inaccurate velocity value used in depth conversion, particularly in throw value conversion from two way travel time (ms) to one way travel time (m). These errors amount to ±10 percent. Consistency in the position of inflection points minimizes error due to fold drag (Walsh and Watterson 1987) i.e. folds without visible displacements were measured as zero. Measurements were not taken, where resolution was poor particularly in areas where tips are restricted. Such areas were interpolated based on assumed displacement geometry.

#### *2.3.2.3 Shortening Measurement*

Shortening values were measured and calculated by simple line length balancing technique (Dahlstrom 1969; Higgins et al. 2009). The values were measured on the same seismic horizon where displacement values were obtained to allow direct comparison between both parameters on some of the fold and fault pair examples (Chapter 5-7).

The sections were pinned away from the fold structure at a point of un-deformed layer- cake stratigraphy. The width of the section is assumed to be the pre-deformed length which was subtracted from the summed length of hanging wall and footwall sections, such that shortening (sh) = (L2+L1)-L (Figure 2.4 a). This method is important in allowing time efficient calculation and it is representative for facilitating high definition plot of shortening distribution.

Additionally, the method has the advantage to be less prone to error induced by algorithms and assumptions (Higgins et al. 2009). Similar to the dip-slip measurement, the main possible error occurs from the sampling interval, and imprecision in measuring amplitude peak. Total errors are ±10 percent and are limited due to consistency in the measurement technique.

### 2.3.3 Well Data.

A total of 9 exploratory wells were made available within the extensional domain (Figure 2.1) and these wells have previously been used for stratigraphic studies (Bertoni and Cartwright 2005, 2006; Baudon and Cartwright 2008b). However, only the gamma ray log within well 2 gives a full coverage of the Plio-Quatenary succession which is the main focus of this study. For the purpose of well calibration we tied information from well 2 to the Gal C survey at a distance of c. 100 km (Figure 2.1,). The displayed well data is shown in Figure 2.6.

Well 2 is characterized by regular variability in gamma radiation, with distinctive peaks, some of which do not coincide with high amplitude reflections (Figure 2.6). Those anomalies which do not coincides with high reflection (for instance at 1.7s and 1.9s, TWT) may be attributed to shift in well bore (Cartwright in press). Beyond this abnormal characteristic in the log signature, the well displays insignificant changes from the sea bed to about 1.35s (TWT) where it abruptly increases in radiation due to increase in clay content. At depth (2-2.3s, TWT) the GR values exhibit a gradual decrease in radiation followed by an abrupt increase, corresponding to the Yafo Sand Member (Frey Martinez et al. 2005).

# CHAPTER THREE

# 3 GEOLOGY OF THE LEVANT BASIN

## 3.1 INTRODUCTION

The aim of this chapter is to review the regional geology of the Levant Basin. We begin by giving a summary of the formation of the Basin, followed by the structural setting of the area. We concluded by reviewing the seismic stratigraphy of the dataset as established by previous authors (Bertoni and Cartwright 2006; Clark and Cartwright 2009) and the main horizons mapped in this study.

## 3.2 REGIONAL GEOLOGY

The Levant Basin is located in the easternmost part of the Mediterranean Sea (Figure 3.1 a and b). It is bounded to the east by the passive continental margins of Israel, Lebanon, and Syria, to the south by the north-eastern lobe of the Nile Deep Sea Fan; to the north west by Eratosthenes Seamount and to the north by the subduction zone and transform fault of the Cyprian Arc (Ben-Avraham et al., 1988, 1995; Vidal et al., 2000a).

The Levant Basin is overlain by over 14km thick sediment mainly deposited by tectonic forces caused by both several compressional and extensional tectonics (Figure 3.1). The regional stratigraphy and structural domains of the Levant Basin is shown in Figure 3.2. Formation of the Levant Basin is associated with the opening of the Neo-Tethys Ocean following the break-up of the Pangaea in the Early Mesozoic (Garfunkel 1998; Netzeband *et al.* 2006a). The Basin began to close during the Middle- Late Cretaceous, during which they were several phases of compression and uplift. The northern margins were intensely deformed and subsequently subducted particularly at the present day region of Cyprus and southern Turkey (Figure 3.1b and 3.3) (Garfunkel 1998). The southern margins, at the Israel-

Sinai margin, remained stable near the coastline between Israel and Sinai (Peacock *et al.* 2000).

Associated with rifting of the Tethys, the Dead Sea system formed as transform fault (Vidal *et al.* 2000), as it accommodates the differential motion between the African and Arabian plates by left- lateral slip (Girdler 1990). The Dead Sea fault slips at a rate of 4mm/yr and it extends about 1000km from the Red Sea Rift to the collision zone in the eastern Turkey (Klinger *et al.* 2000). Rifting subsequently resulted in the detachment of the Eratosthenes as a single block as it drifted away from the African-Arabian plate (Badawy and Horváth 1999).

The end of rifting was followed by cooling and subsidence of newly formed crust or modification of the Levant Basin (Garfunkel 1998). The composition of the crust in the Levant Basin is still disputed. It is either oceanic lithosphere formed when early rifting evolved into full scale seafloor spreading (Makris *et al.* 1983; Ben-Avraham and Ginzburg 1990) or thinned continental crust formed during inter-plate rifting (Hirsch 1984; Cohen *et al.* 1988). Recent studies suggest it is composed of highly stretched, thinned continental crust with an estimated β factor (The ratio between the crustal thickness before and after stretching) of 2.3-30 (Gardosh and Druckman 2006; Netzeband et al. 2006a).

During the Middle Jurassic, a paleo-depositional hinge belt which parallels the Levant and Sinai coast was formed at the eastern margin of the Basin (Ginzburg and Gvirtzman 1979). The belt separated a vast shallow marine platform in the east from a deep setting basin to the west (Ginzburg and Gvirtzman 1979). It has been interpreted as a zone in which a transition from a continental to an oceanic crust occurs and in which there is a rapid change in the thickness and deposition of sedimentary cover (Ginzburg and Gvirtzman 1979).

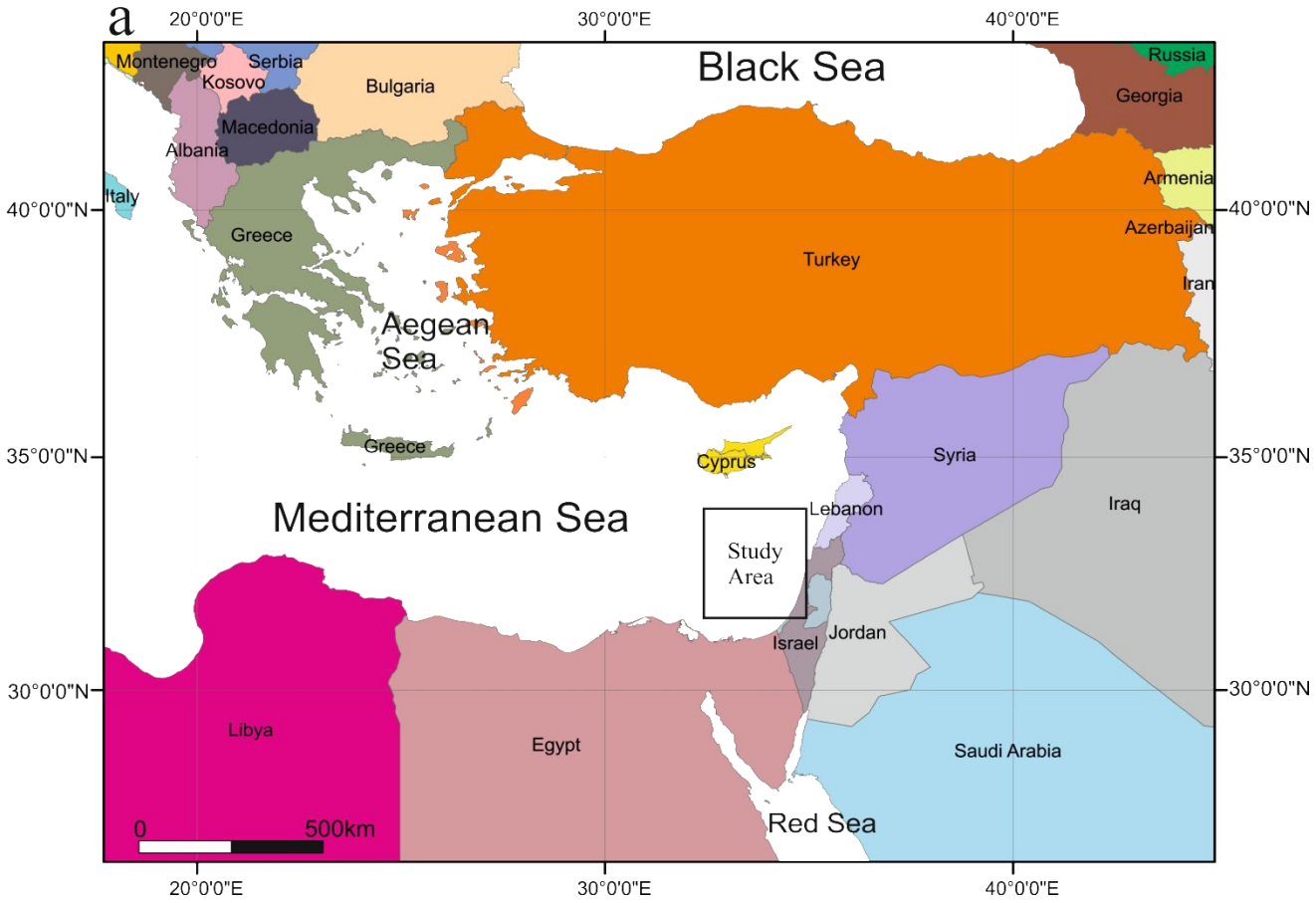


Figure 3.1: Location maps of the study area. (a) Showing countries that border the eastern Mediterranean Sea. (b) The tectonic setting of the Eastern Mediterranean Sea. Arrows indicate the sense of plate motion; half arrows indicate transform/strike-slip faults. DSF- Dead Sea fault system, Es-Eratosthenes Seamount. Adapted from Gardosh et al (2006). (c) Showing the structural domains and features along the Levant Margin. The updip edge of the Messinian salt (red dashes) correlates closely with the updip limit of extension (blue areas). The frontal scarp (hachured) also tracks these features in the north but deviates in the south. P marks the Palmahim submarine landslide. Adapted from Cartwright et al (2008).

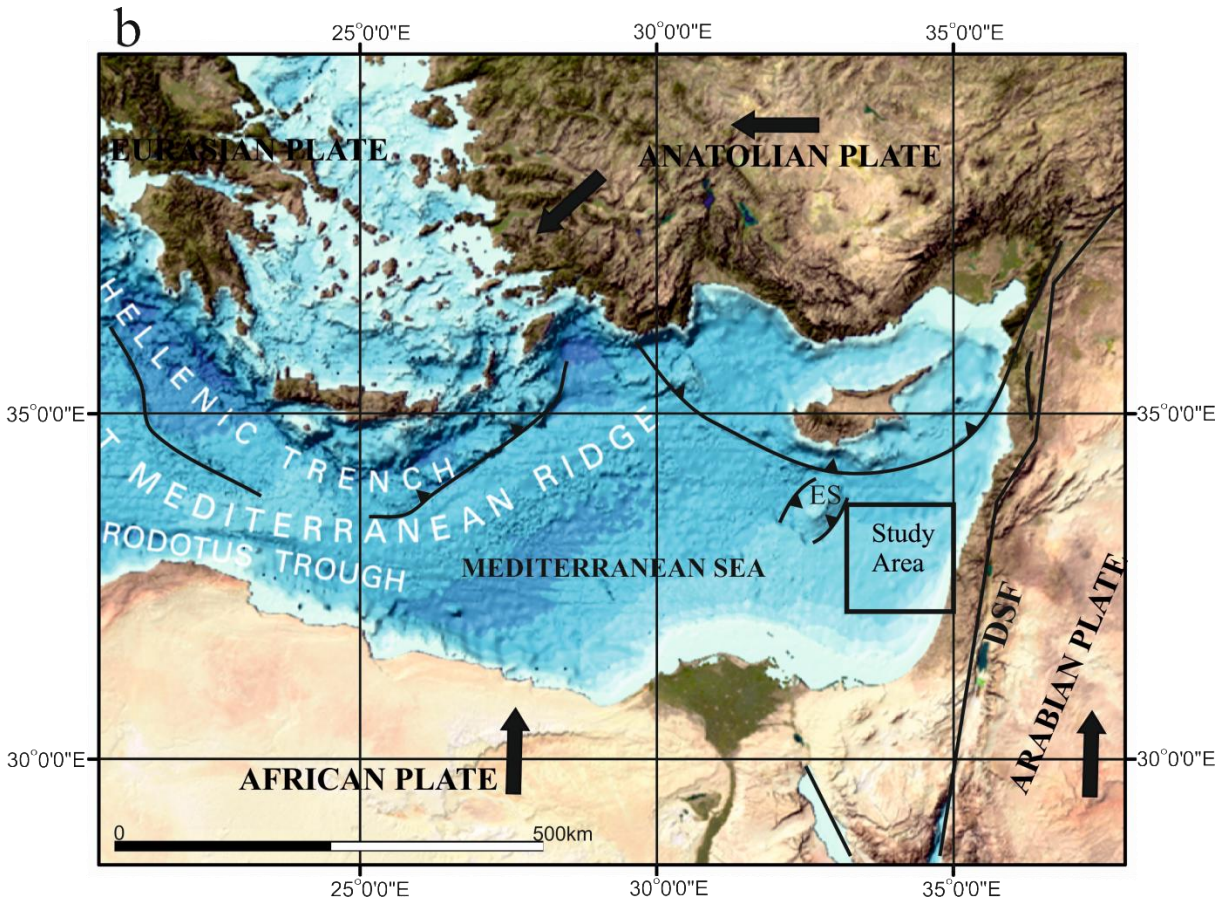


Figure 3.1: Location maps of the study area. (a) Showing countries that border the eastern Mediterranean Sea. (b) The tectonic setting of the Eastern Mediterranean Sea. Arrows indicate the sense of plate motion; half arrows indicate transform/strike-slip faults. DSF- Dead Sea fault system, Es-Eratosthenes Seamount. Adapted from Gardosh et al (2006). (c) Showing the structural domains and features along the Levant Margin. The updip edge of the Messinian salt (red dashes) correlates closely with the updip limit of extension (blue areas). The frontal scarp (hachured) also tracks these features in the north but deviates in the south. P marks the Palmahim submarine landslide. Adapted from Cartwright et al (2008).

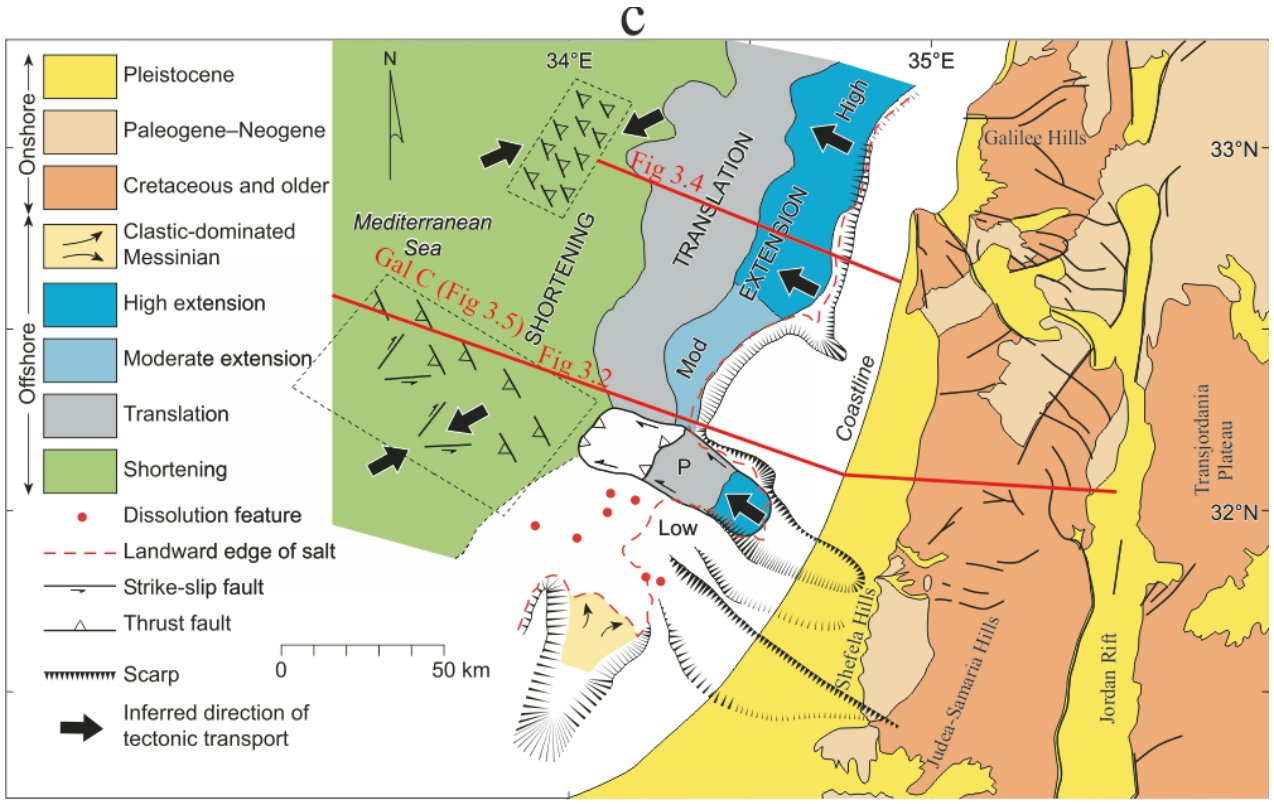


Figure 3.1: Location maps of the study area. (a) Showing countries that border the eastern Mediterranean Sea. (b) The tectonic setting of the Eastern Mediterranean Sea. Arrows indicate the sense of plate motion; half arrows indicate transform/strike-slip faults. DSF- Dead Sea fault system, Es-Eratosthenes Seamount. Adapted from Gardosh et al (2006). (c) Showing the structural domains and features along the Levant Margin. The updip edge of the Messinian salt (red dashes) correlates closely with the updip limit of extension (blue areas). The frontal scarp (hachured) also tracks these features in the north but deviates in the south. P marks the Palmahim submarine landslide. Adapted from Cartwright et al (2008).

The Late Cretaceous to Early Tertiary stratigraphy is composed of hemi-pelagic to pelagic sediments which marks the termination of the extensive shallow marine carbonate deposition in the Levant Basin (Gardosh *et al.* 2008). This change in lithology indicates a major drowning event and ecological transition associated with plate re-arrangement and the beginning of the closure of the Neo-Tethys Ocean (Sass and Bein 1982). The collision of the Anatolian plate and the Afro-Arabian plate in the Senonian (Late Cretaceous) initiated a northward dipping subduction zone at the southern Neo-Tethys Ocean in the present day areas of Cyprus and Southern Turkey (Figure 3.1b and 3.3) (Gardosh et al. 2008). The convergence of the plates (Eurasia plate and Afro-Arabian plate) is the main cause of the formation of a series of NE and NNE striking folds and faults commonly known as the Syrian Arc or Levantine Fold and Thrust Belt (Livnat and Kronfeld 1985; Gardosh *et al.* 1990; Garfunkel 1998) (Figure 3.2). The Syrian Arc forms an S shape, extending from western Egypt, through the Sinai and the Levant into central Syria (El-Motaal and Kusky 2003).

Deformation of the Syrian Arc has been interpreted to have evolved as an extensional rift in the Late Palaeocene times followed by contractional tectonics that began to inverse the rift basin in the Late Cretaceous (El-Motaal and Kusky 2003)**.** At the time of the formation of the Syrian Arc, there was uplift in the eastern part of the Levant Coast and updoming of the Arabian shield south of the Levant. This activity is represented by a regional unconformity surface that is identified in the upper section of the Eocene unit, which demarcates the older carbonate section from the overlying Oligo-Miocene siliciclastics of the Saqyie Group (Ball and Ball 1953; Tibor and Ben-Avraham 1992). Deposition of the Oligocene-Miocene unit is associated with the widespread erosion and basinward transport of sediments through an extensively modified submarine drainage system by the Afiq Canyon on the Levant margin (Druckman *et al.* 1995) .

Towards the middle of the Miocene, Seafloor spreading in the Red sea which is mainly caused by the breakup of the Arabian Craton initiated the Dead Sea Transform Fault (Gradmann et al. 2005). In this context, there was shifting of motion from the Gulf of Suez to the Dead Sea system, and the creation of the postulated Sinai sub plate (Badawy and Horváth 1999). At the same time, the motion was associated with a strike slip stress pattern, with minimum principal stress trending towards NE and maximum stress NW, which resulted to the lateral motion between the Arabian plate and Sinai sub-plate (Badawy and Horváth 1999). The formation of this plate boundary is the main cause of the tectonic movement of the Miocene-Pliocene Levant Basin (Buchbinder and Zilberman 1997).

In the late Miocene, the collision of the African plate and the Eurasian Plates caused isolation of the Mediterranean Sea from the Atlantic Ocean. This caused sea level fall that resulted in the so called Messinian Salinity Crisis (Hsü et al. 1973, 1978), which led to the deposition of upto 2km thick evaporite (Müller and Mueller 1991; Bertoni and Cartwright 2006). The Messinian evaporites represent an influential part of the eastern Mediterranean stratigraphy, and they are likely madeup of gypsum, anhydrite, halite and some shaly layers. The evaporites are part of the Mavqiim formation which were deposited in both the marginal and basinal domains of the Levant Basin (Garfunkel *et al.* 1979). The marginal domain covers the coastal plain and the offshore area which extends to the present continental slope where the Messinian salt pinches out (Figure 3.2). The marginal domain was greatly dissected by erosion, and the relief is covered only in part by thin evaporite less than 150m thick (Tibor and Ben-Avraham 1992). The Messinian thickens towards the basinal domain where it has a maximum thickness of more than 1.5km (Bertoni and Cartwright 2006). The Messinian salt represents the detachment zone of the thrust related folds and strike slip faults analysed in this thesis (Figure 3.2).

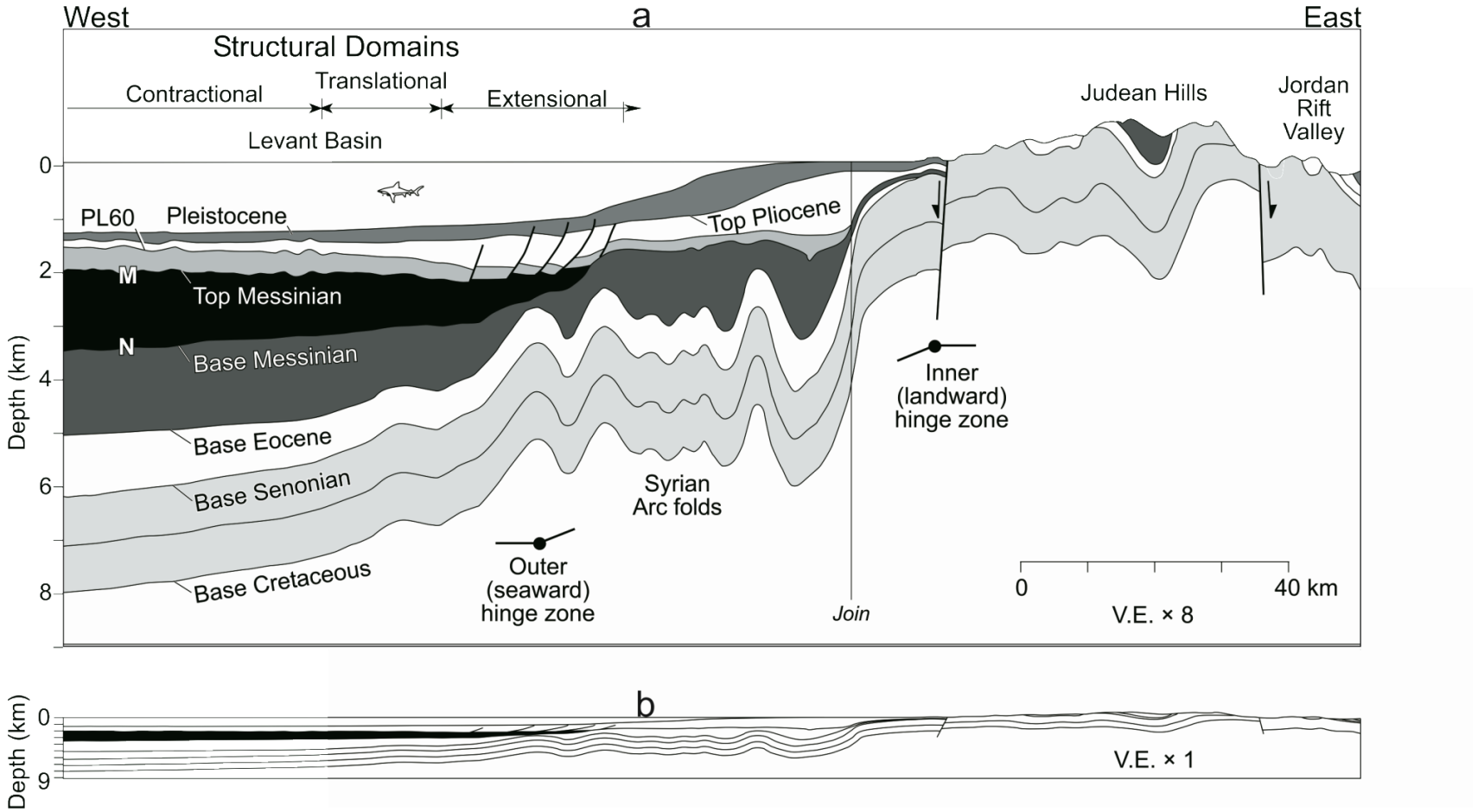


Figure 3.2: Regional section showing the offshore thin-skinned structural domains and inner and outer crustal hinge zones. (a) Vertically exaggerated section (b) unexaggerated section. Large upright folds in the Syrian Arc dominate the pre-Messinian structure. Figure 3.1d shows location of the onshore geological section (based on Survey of Israel, 1960) and offshore section based on a depth- converted seismic line, joined at the bend on the map. Figure adapted from Cartwright et al., (2012).

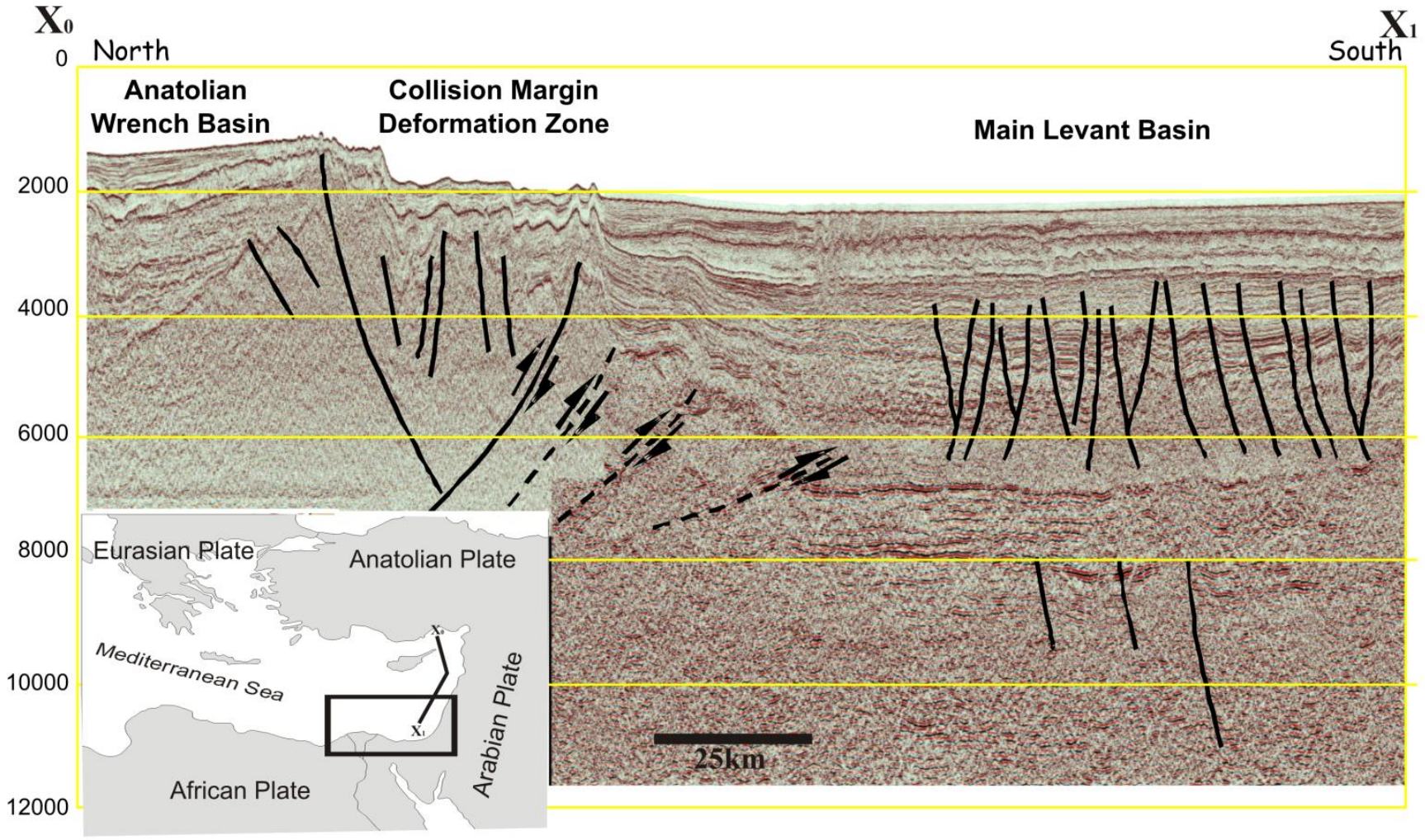


Figure 3.3: Seismic section showing deformation along the Cyprus Arc, close to the boundary between the Anatolian and Arabian plates. Interpretation by Matt Farris & Mark Griffiths, courtesy .Shell U.K. Exploration and Production. Inset is location map showing section location.

The Messinian Salinity Crisis ended in the early Pliocene, due to the restoration of normal marine condition across the Mediterranean (Cita and Ryan 1978; Ryan and Cita 1978). During the early Pliocene, the shelf and slope began to prograde seaward, which led to very high sedimentation and subsidence rates towards the basin margin (Gradmann et al. 2005). Sandy turbidites known as the Yafo Sand Member (Frey Martinez et al. 2005) were deposited above the Oligocene-Miocene canyons (where Messinian evaporites are absent). From the middle of the Pliocene to Recent, clay rich siliciclastic sediments, mainly derived from the Nile Delta, prograded over the Yafo Sand Member and the Messinian salt layer (Cartwright and Jackson 2008). The unconformity surface at the top of the Mavquiim evaporites and the base of the Yafo Formation is termed the M reflection (Ryan 1973), and it is marked on the seismic data by a white marker (Figure 3.6).

The post-Messinian progradation of sediment from the Nile coupled with the Messinian salts likely caused subsidence in the southern part of the Levant Margin, this resulted to increases in sedimentation rate in the region (Tibor *et al.* 1992). According (Cartwright and Jackson 2008), the present day slope is modified by two main active gravity driven deformation systems: (1) local thin-skinned slope failure depicted as slides and slumps (Almagor 1984; Garfunkel and Almagor 1984; Frey Martinez et al. 2005) and (2) regional thin-skinned tectonics involving almost the entire Plio-Quaternary shelf and slope overburden detaching in the Messinian evaporite (Garfunkel and Almagor 1984; Tibor and Ben-Avraham 1992). The 3 main structural domains of gravity spreading are shown in Figure 3.2 and 3.4. Two major crustal hinges underpin these thin-skinned domians of deformation further east : (1) an onshore inner hinge zone towards the hinterland separates the uplifted Judean Hills from the Seaward cascade of the Syrian Arc folds and (2) an outer hinge zone which separates the seaward fold cascade from the more gentle dipping piedmont of the Syrian Arc (Cartwright and Jackson 2008).

## 3.3 GENERAL STRUCTURE

Structurally, the study area is divided into an up dip extensional zone, a translational zone, and down slope compressional zone (Cartwright and Jackson 2008) Figure 3.2 and 3.4. Deformation across these structural domains remains active today, this can be inferred from the highly pronounced folds and faults on the bathymetric map shown in (Figure 3.1 b).

### 3.3.1 Extensional Domain

The extensional domain occupies the present day continental shelf and slope of the Basin, (Figure 3.2 and 3.4). The domain has been extensively studied (Garfunkel and Almagor 1984; Baudon and Cartwright 2008b; Cartwright and Jackson 2008).

The outer shelf and slope of the margin is made-up of thin-skinned extensional structures which includes listric normal growth faults, rotated blocks, grabens, slumps and salt rollers. The listric and growth fault anticlines are the most striking extensional features caused by lateral movement of the Messinian evaporite and its overburden (Figure 3.4). These faults are syn-sedimentary and they are characterized by variable throws up-dip and along strike, and they detached into several locations within the Messinian unit (Gradmann et al. 2005). Detailed study using tight grids of seismic data within a small area in the province show that fault length along strike are within 5-10 km (Garfunkel and Almagor 1984).

The extensional domain is relatively linear along the northern and central sectors and it diminishes in strain (high- low) southward due to variation in structural style (Cartwright and Jackson 2008) (Figure 3.1 c). The up-dip limit of the Messinian salt, almost corresponds with the landwards boundary of the extensional zone along the continental margin (Figure 3.1 c). Both boundaries are shifted landward in a southern region known as the Palmahim Disturbance (Garfunkel et al. 1979) (Figure 3.1 c).According to Cartwright and Jackson (2008), the Palmahim Disturbance represents zone of a major landward migration of

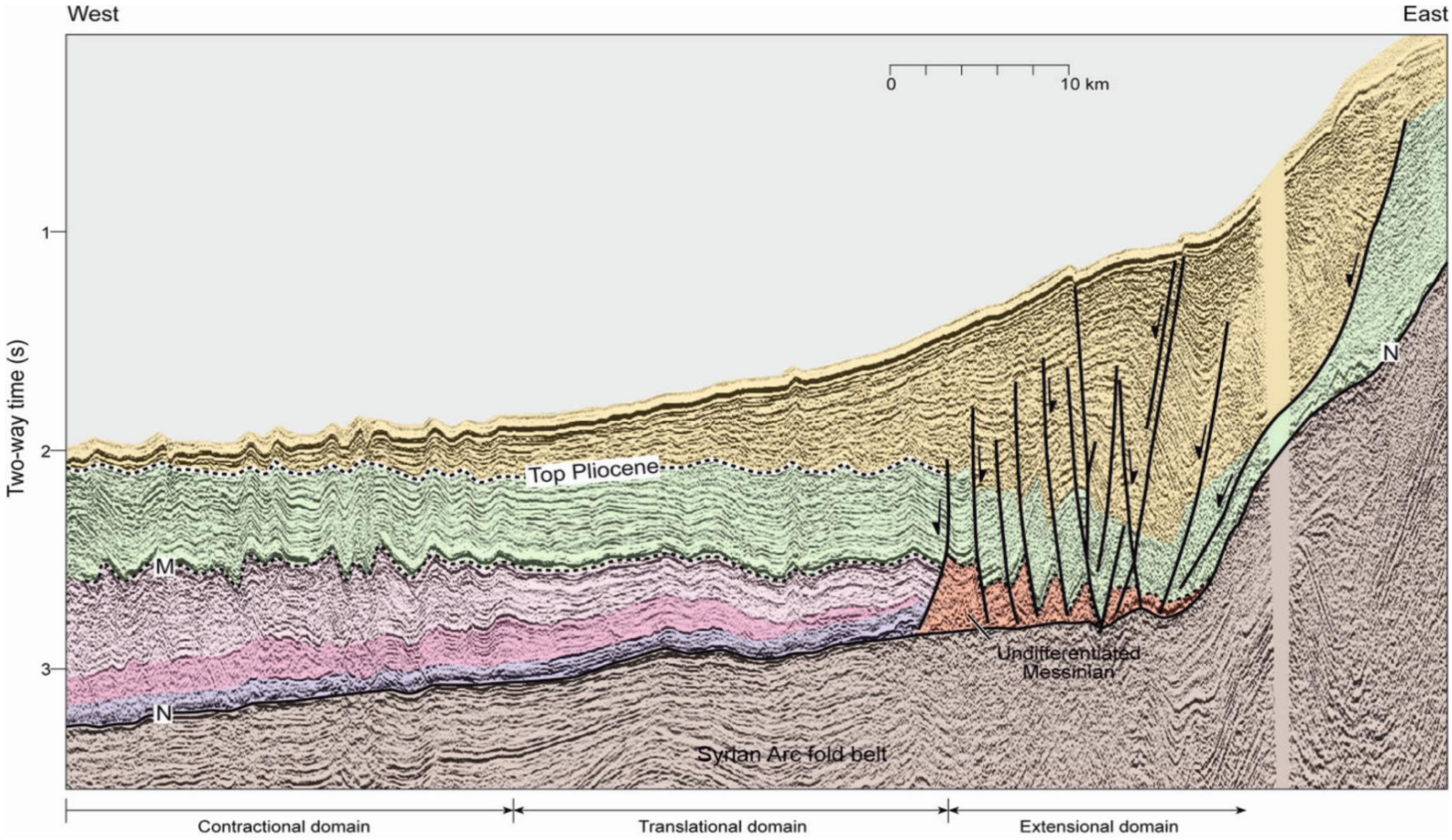


Figure 3.4: Seismic section showing structural style along the structural domains. The evaporite wedge pinches out by structural thinning due to normal faulting. Diverging synkinematic strata records progressive rotation of the extensional fault blocks in the overburden unit. Figure Location in Figure 3.1 c. Adapted from Cartwright et al (2008).

evaporite, this was inferred from the evaporite fill and onlapping of the Ashdod Canyon Cartwright and Jackson (2008).

### 3.3.2 Translational Domain

The Messinian and its associated overburden are relatively undeformed within this zone. However, small extensional and contractional features are locally present and they are likely to be few kilometres or less in length (Gradmann et al. 2005; Cartwright and Jackson 2008).

### 3.3.3 Contractional Domain

This domain is dominated by folds, thrust faults and strike slip faults (Figure 3.1 and 3.5). The folds have a short-wave length (1-4km), upright or gentle inclined folds with amplitude of 50- 200m and overlying thrust faults with variable displacement along strike length (Cartwright and Jackson 2008; Cartwright et al. 2012). These faults detach at different levels within the Messinian interval and ramp up through the overburden layer (Cartwright et al. 2012).

The thrust faults within the evaporite and its overburden have been defined as northward verging structures (Netzeband *et al.* 2006b), and they strike northwest (Figure 3.1 c). The limited variation in orientation of the folds and thrust faults have been interpreted as northward squeezing of the evaporites by the gravitational collapse of the Nile Delta (Netzeband et al. 2006b). Other boundary effects have also been stipulated by Cartwright and Jackson, (2008) to affect the structural expression of the contractional domain such as the underlying Sinai microplate kinematics, and buttressing effect of the Eratosthenes Seamount and the Cyprus trench. These interfering boundaries make deformation in the compressional domain of the Levant Basin complex relative to other gravity driven systems in the world e.g the Niger Delta (Damuth 1994), Bight Basin (MacDonald *et al.*), NW Borneo (Hesse *et al.* 2009).

Deformation of the salt layer does not entirely correspond to that of the post- Messinian unit (Bertoni and Cartwright 2006; Netzeband et al. 2006b). This discordant relationship has been interpreted to represent multiple phases of deformation (Bertoni and Cartwright 2006; Netzeband et al. 2006b). Conversely, the most recent study in the area supports a one phase system which began in the earliest Pleistocene (Cartwright et al. 2012). One of the aims of this thesis is to describe the styles of deformation in details between the top Messinian unit and the Post-Messinian overburden (see Chapter 4, Figure 4.2).

## 3.4 SEISMIC STRATIGRAPHY

The stratigraphical interval of interest to this thesis, are sediments deposited from Miocene to Recent (Figure 3.2, 3.3 and 3.6). The reflection series is up to 2.8s (TWT) thick, comprises the Messinian layer separated from the Plio-Quaternary overburden by the regional unconformity known as Horizon M (Ryan 1973) (Figure 3.4 and 3.6).

At least a total of 8 seismic packages have been identified from the base of the Messinian interval to the seabed by previous workers (Bertoni and Cartwright 2006). The packages are distinct seismic units that are bounded by notable regional markers recognized through truncation, onlapping and downlapping reflections.

The Messinian evaporite is a member of the Mavqiim Formation (middle Saqiye Group) identified throughout the Mediterranean region (Tibor and Ben-Avraham 1992). It thickens towards the contractional domain of the Levant Basin, reaching a maximum thickness of 0.8s (TWT) and it is bounded at its base and top by the N and M Horizons respectively (Ryan 1973).

The origin of the internal layering of the Messinian unit is not clear due to the absence of well data. Garfunkel (1984), and Garfunkel and Almagor (1984), postulated over pressured shales

interbeded within impermeable evaporite. Netzeband et al (2006), suggested halite-rich and sulphate rich evaporite sequence. This explains the deformation of the uppermost evaporates, as already described by Gradmann et al (2005), owing to the presence of anhydrite or gypsium at the top of each sequence. A recent study in the area interpreted the internal layering as alternating pure and impure evaporite (Cartwright et al. 2012), accounting for the brittle behaviour at the top sequence (Figure 3.6).

The precise lithology of the Messinian is not certain; therefore Horizon N is defined on basis of a strong negative amplitude seismic reflection at the top of the pre-Messinian unit (Figure 3.6). The horizon is relatively undeformed, although it appears to be locally irregular, having up warped or down sagged geometries. These irregular geometries have been attributed to seismic pull up or push down effects resulting from seismic velocity contrast (Bertoni and Cartwright 2006). Horizon M is defined by a high amplitude positive seismic reflection and it represents the top of the Messinian evaporite. This horizon is regionally continuous and locally deformed by a series of short-wavelength structures (Gradmann et al. 2005). Immediately above Horizon M, are Plio-Quaternary clinoformal sediments which onlaps Horizon M in the marginal areas and downlaps or tangentially converges with the horizon in distal areas.

Horizons M and N converge towards the continental margin, such that the evaporite unit thins and pinches out in a wedge like manner (Figure 3.4). The Messinian evaporites is characterized by several prominent internal seismic reflections that can be traced for a long distance (Ben-Avraham 1978). These prominent reflections have been interpreted as pure and impure salt in the absence of well data (Cartwright et al. 2012).

The Messinian packages are labelled T1-T7 (Figure 3.6). The packages can be divided into layered seismic facies, and transparent seismic facies following the classification established by Bertoni and Cartwright (2006). T6, T4 and T3 are layered seismic facies, bounded

respectively by Horizons M6-M5, M4-M3, and M3-M2 (Figure 3.6). The package T6 has an average thickness of 0.25s (TWT), it is internally composed of medium to high amplitude positive reflections. The dominant frequency in this layer package (T6) is 50Hz. The layered package T4 and T3 are relatively thin compared to T6, they have thickness ranging between 0.005s and 0.15s (TWT). Both packages (T4 and T3) where defined as a single package (L2) by Bertoni and Cartwright (2006). They are composed of medium to low amplitude positive reflection with a dominant frequency of 30Hz.

T7, T5, T2 and T1 are defined as transparent seismic packages (Bertoni and Cartwright 2006). The packages T7, T2 and T1 are bounded by horizon M-M6, M5-M4, M2-M1, and M1-N, respectively (Figure 3.6). All 3 transparent packages show almost equal maximum thickness: an average of 0.23s (TWT). T7 is the most deformed sub-unit amongst all the evaporites and the majority of faults described here, detach into this unit (Figure 3.6). Although horizon M6 has a partial patchy distribution, but this is not common where the faults in the Messinian detached.

The Plio-Quaternary layers along with the upper units of the Messinian evaporite are the main focus of this study. The majority of the faults described in later chapters, ramp up from the Messinian layer and cut through the post-Messinian sediment. The overburden sediment attains its maximal thickness of 1.6km (TWT) along the eastern Margin (Gardosh and Druckman 2006) and thins towards the distal part of the Levant Basin (Figure 3.4). Within the Gal C survey, it has maximum thickness of 1.1s (TWT) and it thins towards the north-eastern part of the data set (Figure 3.6). In the eastern margin of the Levant, where the Messinian evaporite pinches out (merging of the M and N Horizons), the composite horizon surface corresponds with the base of the Messinian unconformity.

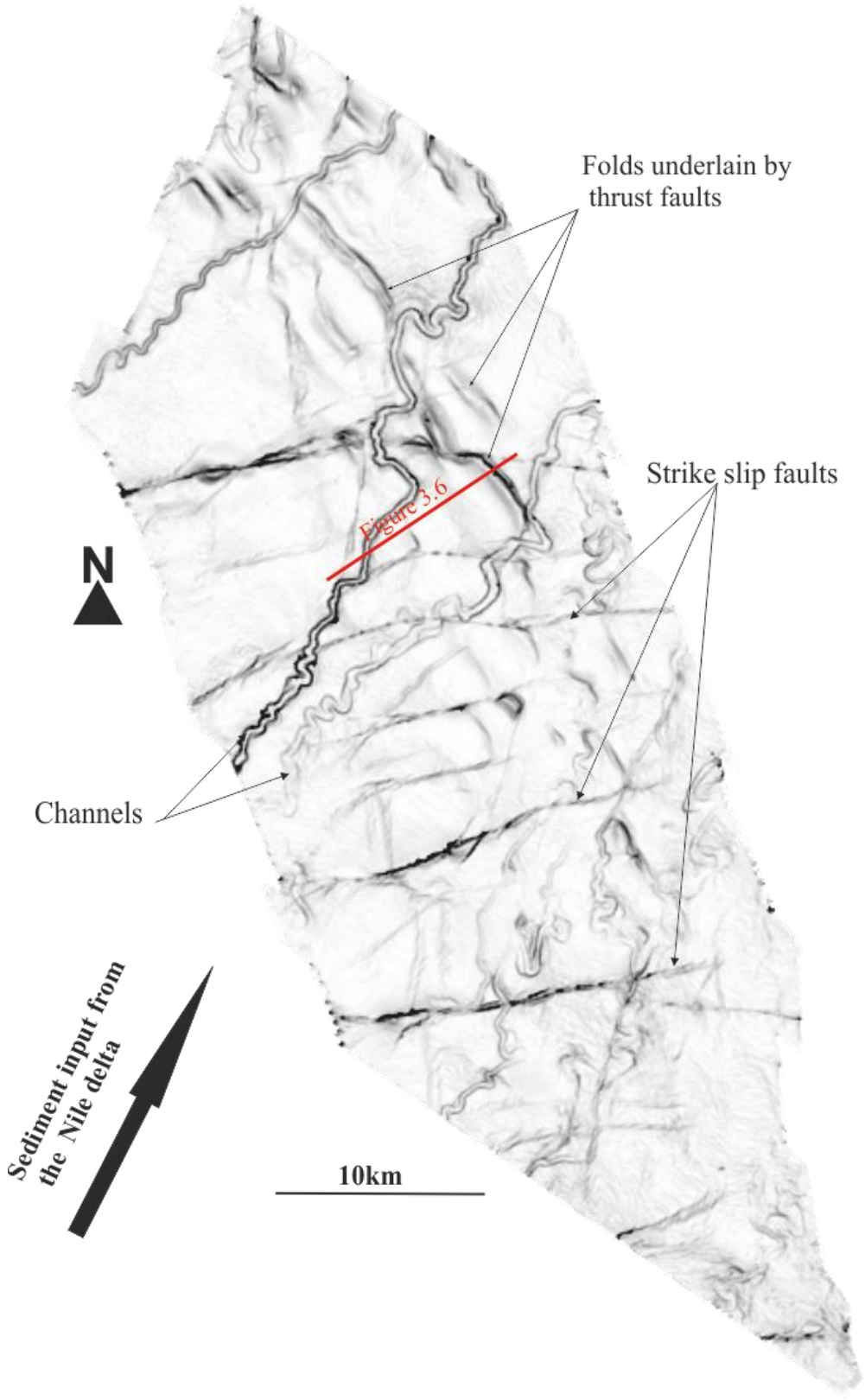


Figure 3.5: Time dip seabed map of the 3D dataset used for this study, showing the main structural features within the study area.

Well data (see Figure 2.6) show that the Plio-Quaternary sediment is mud dominated, it consists mostly of marine silty clays known as the Yafo Formation (Garfunkel and Almagor 1984). Isolated, coarser grained sand bodies interceded with thin clays and marls have also been found within the margins of the Levant. These sand bodies are termed Yafo Sand members (Baudon and Cartwright, 2008) and are rich in biogenic gas (Gardosh and Druckman 2006). On seismic sections, most of the Plio-Quaternary series are well bedded all through the Levant Basin; it is characterized by continuous, thin, and medium to high amplitude reflections (Figure 3.6).

Clark and Cartwright (2009) subdivided the post-Messinian overburden into 3 main sub units (PM1-PM3), based on their seismic stratigraphic character and channel distribution. This study uses the same stratigraphic scheme established by Clark and Cartwright (2009) (Figure 3.6).

### 3.4.1 Unit PM1

Unit PM1 immediately overlies the M Reflection and is composed of weak to high amplitude reflections (Clark and Cartwright 2009). The continuity of the majority of the high amplitude reflections is poor and the base of unit is characterized by an acoustically transparent reflection (Figure 3.6 and 3.7a). However, some of the high amplitude reflections are considerably continuous such as horizon IPM1, which was mapped all through the dataset. The majority of the faults described in the Gal C survey, show a maximum displacement close to IPM1, therefore it is used as one of the key horizons for this thesis (chapter 4, 5 and 6).

Unit PM1 displays no evidence of syn-kinematic deformation. Local thickness variations observed within the unit are related to deposition from channel levee (Clark and Cartwright 2009). The majority of these channels are over 450m wide and they predate deformation within the unit.

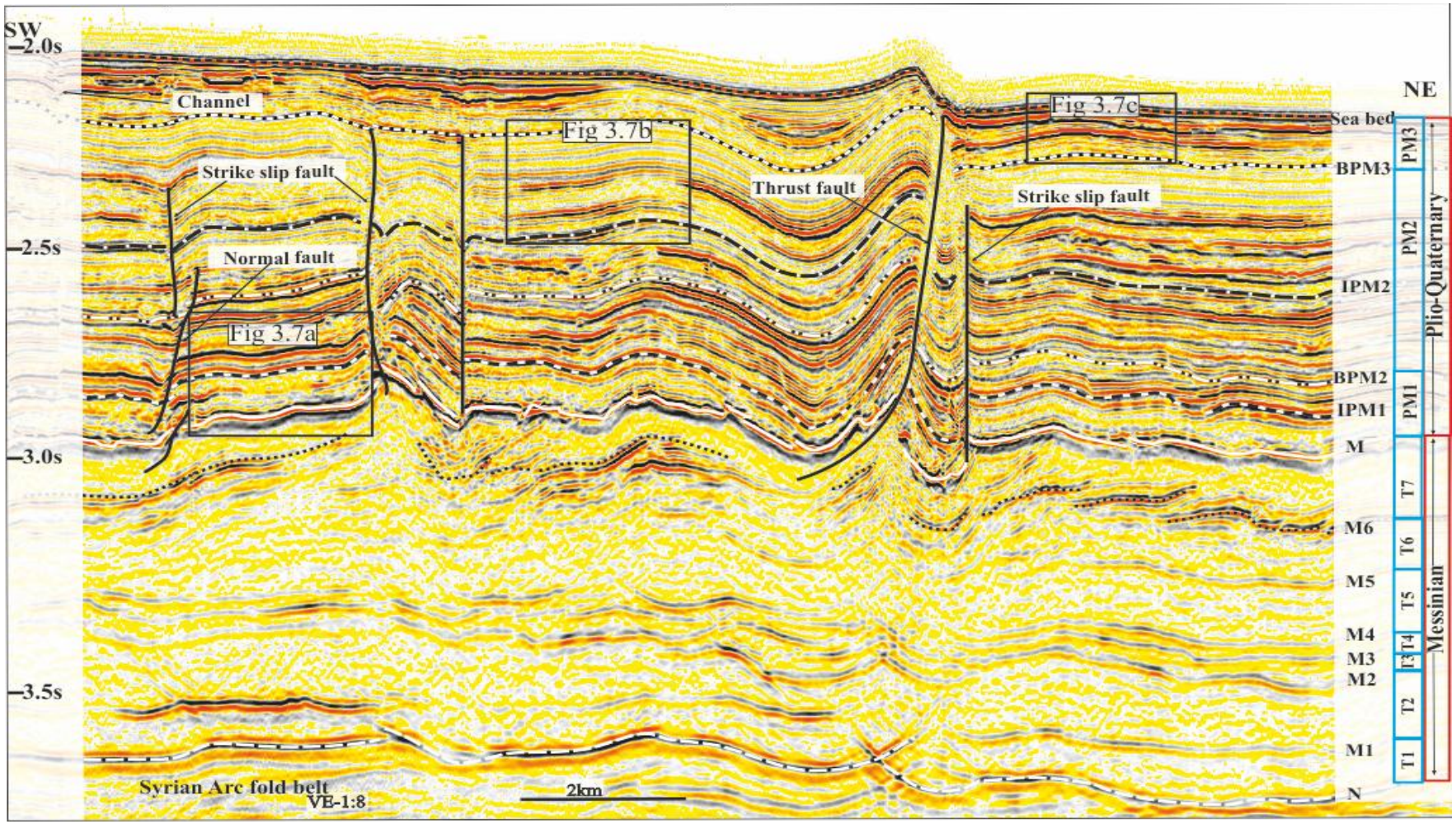


Figure 3.6: Seismic profile showing the main stratigraphy and structural within the study area. Figure Location in Figure 3.5. The data stratigraphy uses the same nomenclature established by Clark and Cartwright (2009) for post-Messinian interval while that of the Messinian was from Cartwright et al., (2012).M and PM denotes Messinian and post Messinian units.

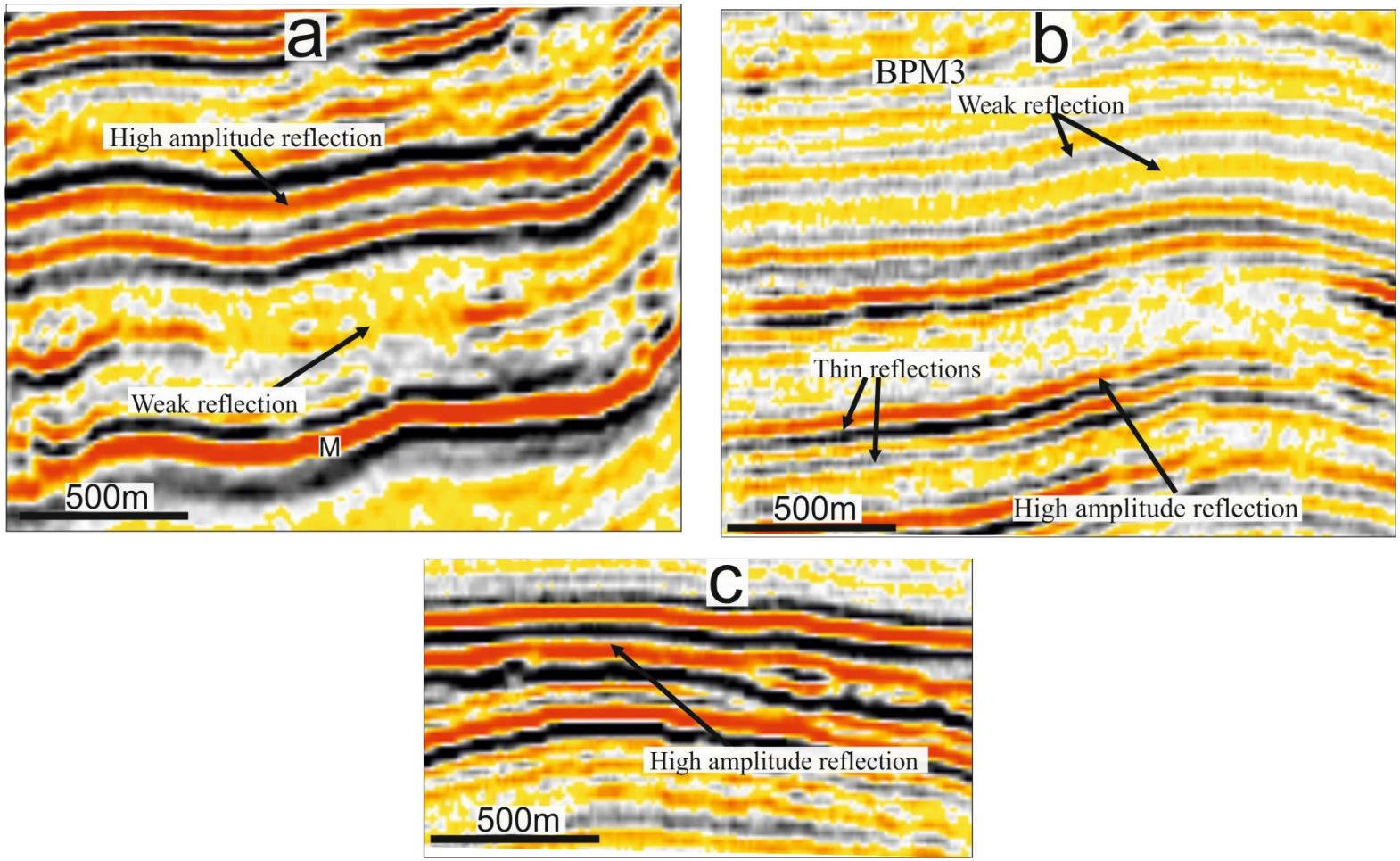


Figure 3.7: Magnified sections from Figure 3.6 showing horizon reflection characteristics within the post-Messinian overburden. (a) Unit PM1 (b) Unit PM2 (c) Unit PM3.

### 3.4.2 Unit PM2

This unit has an average thickness of 0.6s (TWT) and is predominantly made up of low to medium amplitude reflections (Figure 3.6 and 3.7b). These reflections are mainly continuous all through the data set and are generally thinner than those in unit PM1 (Figure 3.7b). The base of the unit shows higher amplitude reflections compared to the top of the unit (Figure 3.6). Unit PM2 is also a pre-kinematic unit, however, it shows internal variation in thickness associated to channel levee systems that appear as onlap onto some fold crests (Clark and Cartwright 2009). In the absence of these irregular thinning effects, true synkinematic sediments are limited within unit PM2.

### 3.4.3 Unit PM3

This unit is composed of medium to high amplitude reflections (Figure 3.7c). It is associated with the development of channel levee systems as clearly visible on time dip seabed map (Figure 3.5). Unit PM3 reaches a thickness of 0.3s (TWT) in areas where deformation is limited, however, notable thickness occurs due to post- Messinian deformation (Gradmann et al. 2005). Internal packages within unit PM3 thin towards the folds in the Gal C survey showing onlaps and offlaps against these fold limbs. This is a characteristic of syn-kinematic sediments associated with growth folds (Poblet *et al.* 1997; Storti and Poblet 1997a). The amount of onlapping sediments in unit PM3, coupled with the expression of fold crest on the time dip bathymetric map suggest that the rate of deformation exceeds sedimentation in the area.

# CHAPTER FOUR

## 4 THE STRUCTURES IN GAL C

### 4.1 INTRODUCTION

This study is based on the general description of the structural elements and their possible relationships in the Gal C survey, located in contractional domain of the Levant Basin. The contractional domain of the Levant Basin is one of the least studied belts in the Eastern Mediterranean Sea, yet it remains one of the World's most suitable areas for studying thin-skin deformation (Hsü et al. 1973; Garfunkel and Almagor 1984; Bertoni and Cartwright 2006; Netzeband et al. 2006c; Clark and Cartwright 2009; Cartwright et al. 2012).

The Levant Basin is not as simple offshore as most thin-skin deformation systems where upslope extension is accommodated by downslope compression (Damuth 1994; Fort *et al.* 2004; Rowan et al. 2004). The contractional domain of the Levant Basin is located in an area of complex tectonic interactions which involves the combination of lateral compression resulting from the: (1) gravity collapse and subsequent basinward spreading of the Nile cone in the south (2) tilting induced collapse of the eastern Levant Margin (3) buttressing effect of the Erathoshnes seamount from the west, and (4) Subduction along the Cyprus Arc in the north (Figures 4.1). All these interfering boundary conditions led to the formation of networks of thrust faults and strike slip faults in the study area (Figure 4.2-4.4). The description of these structures, their possible interactions and how they relate to shortening in the Levant Basin are the main focus of this chapter.

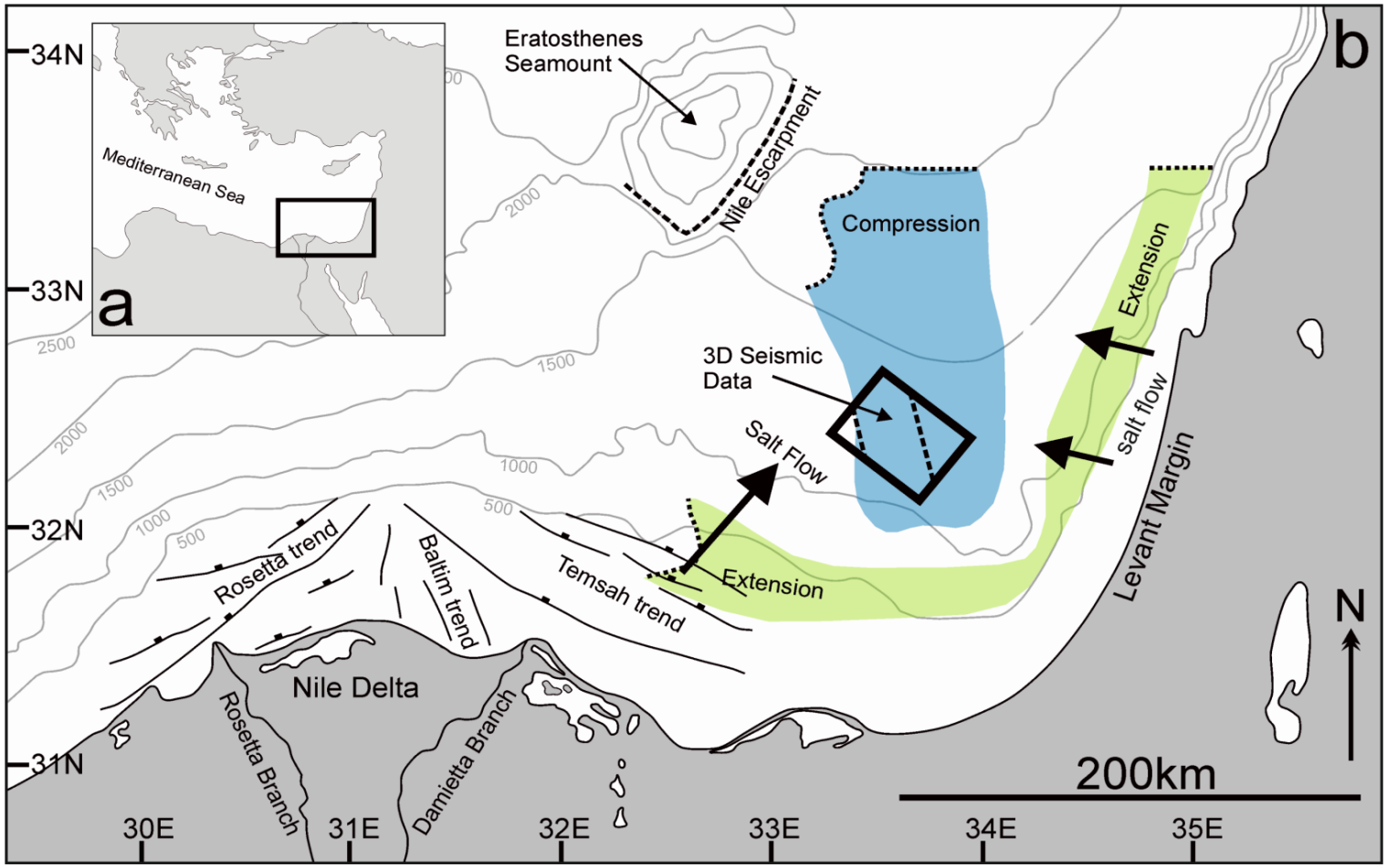


4.1: Location of the survey area within the context of the Nile Delta. (a) (Inset) shows the area of interest in the Eastern Mediterranean sea. (b) Shows the setting of the Nile Delta and the location of the seismic survey used in this study. The area covers a portion of the eastern Nile deep sea fan which is currently undergoing thin-skinned compression. The zone of compression within the Levant basin is driven by the gravitational collapse of both the Nile Delta and the Levant Margin. Figure adapted from (Gradmann et al. 2005; Netzeband et al. 2006b; Clark and Cartwright 2009).

The main structural elements in the study area have been presented on maps and sections in previous studies (Clark and Cartwright 2009; Cartwright et al. 2012). These studies show that the interaction of thrust related folds and strike slip faults play an important role in deformation, but did not describe the structures in details. The scope of this chapter does not cover the entire fold and thrust belt in the Levant, but the 3D dataset (Gal C) used for this thesis. It is important to note that this chapter does not give the kinematic analysis of the structural elements but instead highlights on the various probable relationships between the thrust faults, folds and strike slip faults.

This study begins by a result section which gives an overview of the study area, and the description of the main structural elements. This is followed by the structural interpretation and discussion of notable observations. In the interpretation and discussion section, the stress orientation and deformation in the study area is addressed based on information from previous studies and the description of the structural elements. The possible development of the thrust related folds, and probable fault interactions which will further be investigated and analysed in preceding chapters.

## 4.2 RESULTS

### 4.2.1 General Overview

Gal C, the 3 dimensional dataset used for this study, covers an area of c. 1,450km$^2$ in the southern area of the contractional domain of the Levant Basin (Garfunkel 1998; Ben-Gai *et al.* 2005; Gradmann et al. 2005; Cartwright and Jackson 2008) (Figure 4.4). The average bathymetric gradient of the survey is c. 0.45$^0$ towards N-NE, and water depth ranges between 1000m to 1400m.

The stratigraphic units and nomenclature of the horizons mapped for this study are shown and described in chapter 3 (Figure 3.6). The main thin-skin structures are most distinct between

the top Messinian unit (Horizons M5- M) and Plio-Quaternary overburden. Horizon maps of key horizons and seismic sections clearly show the main features within the Gal C Survey Figure 4.2 and 4.3. The Messinian and its overburden is deformed by thrust faults and folds bounded or compartmentalized by strike slip faults, and other minor structures associated with local transpression and transtension. The overburden unit is in some places deformed concordantly with the structural deformation exhibited by the top Messinian layers (Figure 4.3 a). Conversely, in other parts of the study area, the top Messinian is relatively unstructured in comparison with post-Messinian unit (Figure 4.3 b).

The Upper Messinian units are characterized by distinctive sets of structures which have been interpreted by Bertoni and Cartwright (2006) as thrust related folds. These structures partly define the structural style of the Messinian unit. In order to simplify the description of the structural elements in Gal C, the structures that occur within the Plio-Quaternary overburden are termed (1) Post Messinian structures, while those that do not ramp through the M reflection (2) Messinian structures.

### 4.2.2 Post Messinian Structures

The structures within the post-Messinian structures are evident on the time dip map and time dip structural map of IPM1, which is used as a reference horizon (Figure 4.2 c, 4.4). Horizon IPM1 is used as a reference because the majority of the faults in Gal C attain their maximum displacement closest to it, and it captures the distribution of the structural elements within the study area. The main structures within the post Messinian overburden includes thrust faults and their overlying folds and conjugate sets of strike slip faults (Figure 4.2 - 4.4).

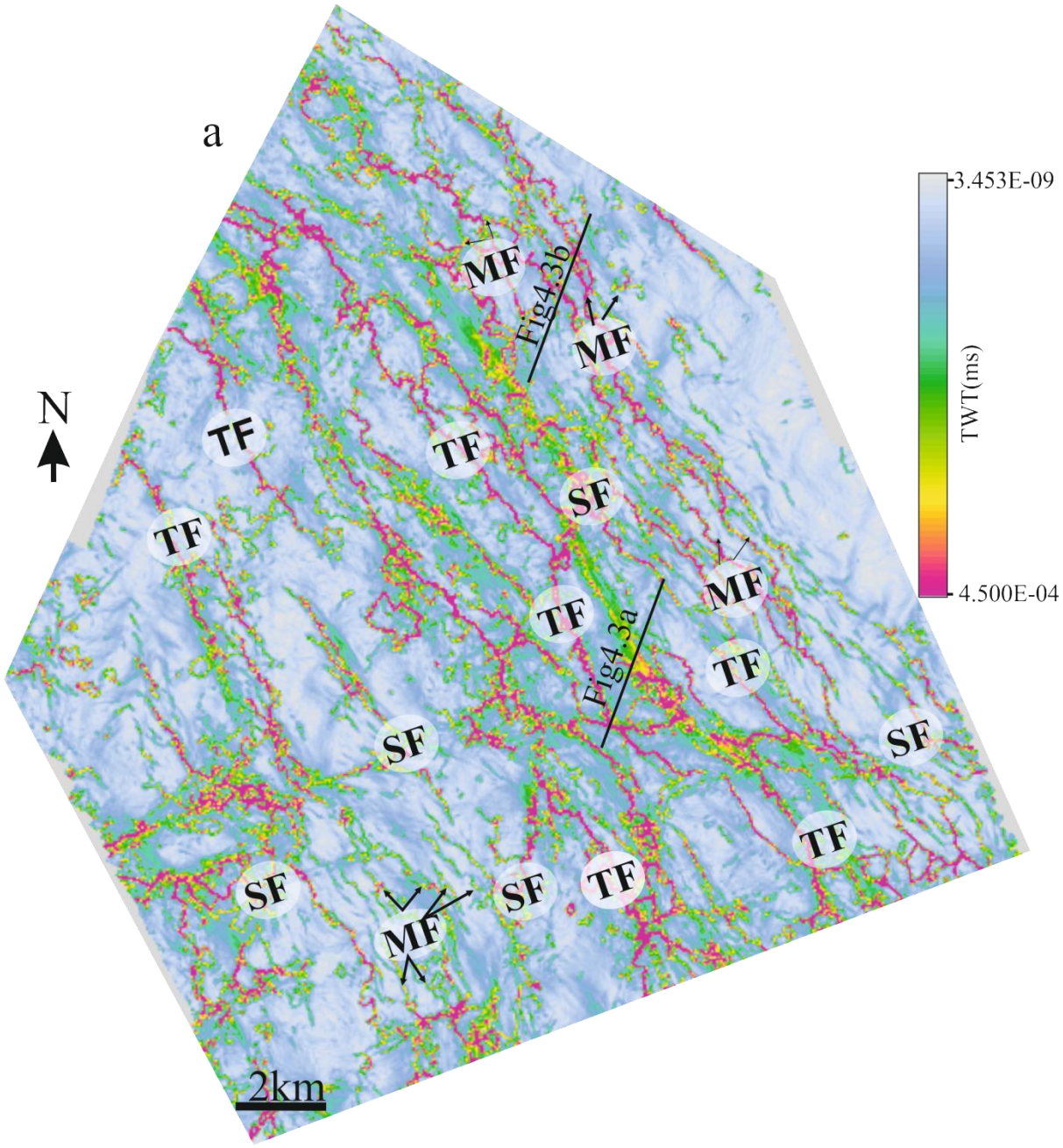


Figure 4.2: Time dip attribute maps of the northern half of the Gal C survey showing the main structural elements in the study area. The structural trend between structures in the Messinian and its overlying layers: the all point towards the same direction. (a) M6 reflection , (b) M reflection, (c) Intra PM1 reflection (IPM1), (d) Seabed reflection. F-Fold, TF- Thrust Fault, SF-Strike slip fault, MF-Messinian Thrust faults, , RL- Releasing step over, RS- Restraining step over, C- Channel.

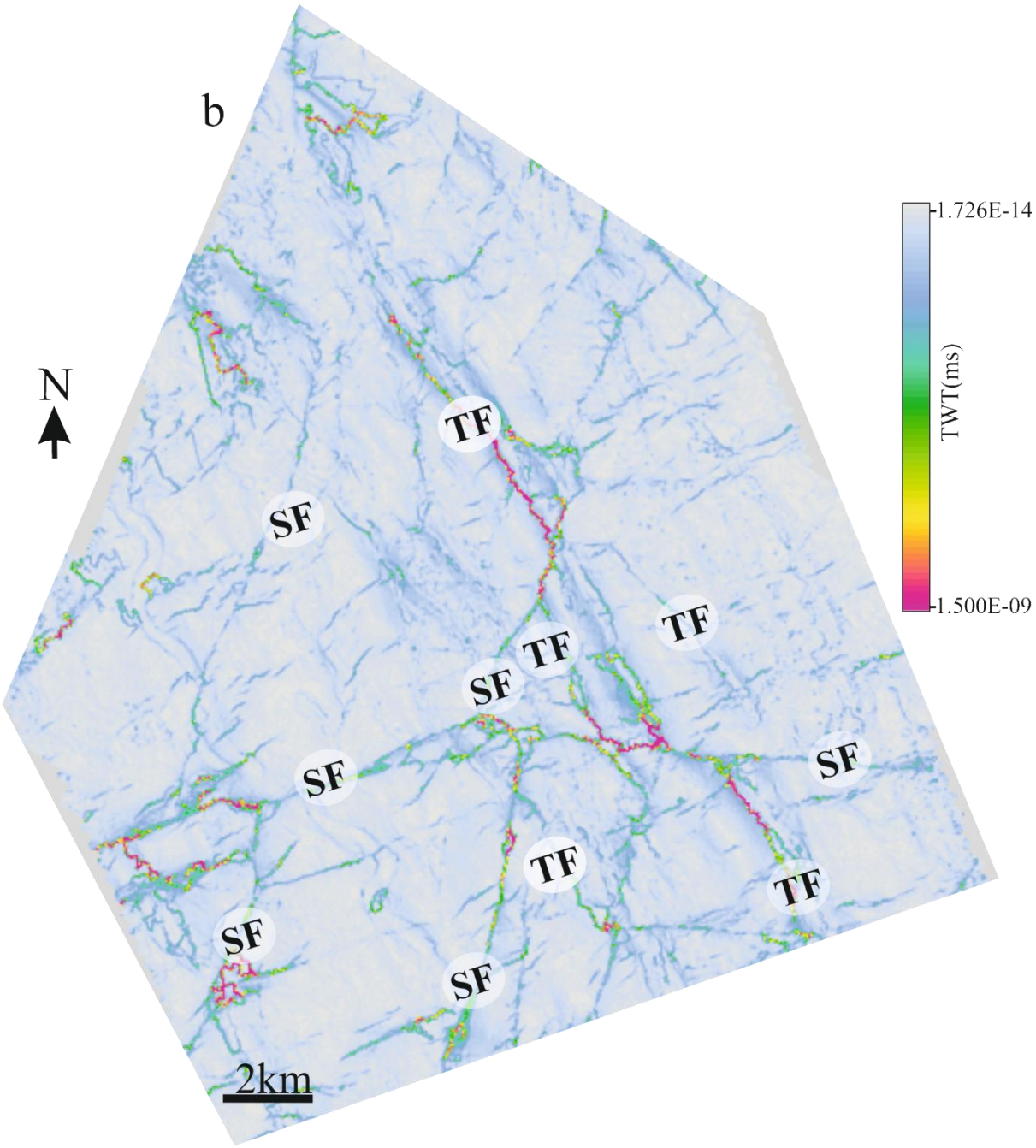


Figure 4.2: Time dip attribute maps of the northern half of the Gal C survey showing the main structural elements in the study area. The structural trend between structures in the Messinian and its overlying layers: the all point towards the same direction. (a) M6 reflection , (b) M reflection, (c) Intra PM1 reflection (IPM1), (d) Seabed reflection. F-Fold, TF- Thrust Fault, SF-Strike slip fault, MF-Messinian Thrust faults, , RL- Releasing step over, RS- Restraining step over, C- Channel.

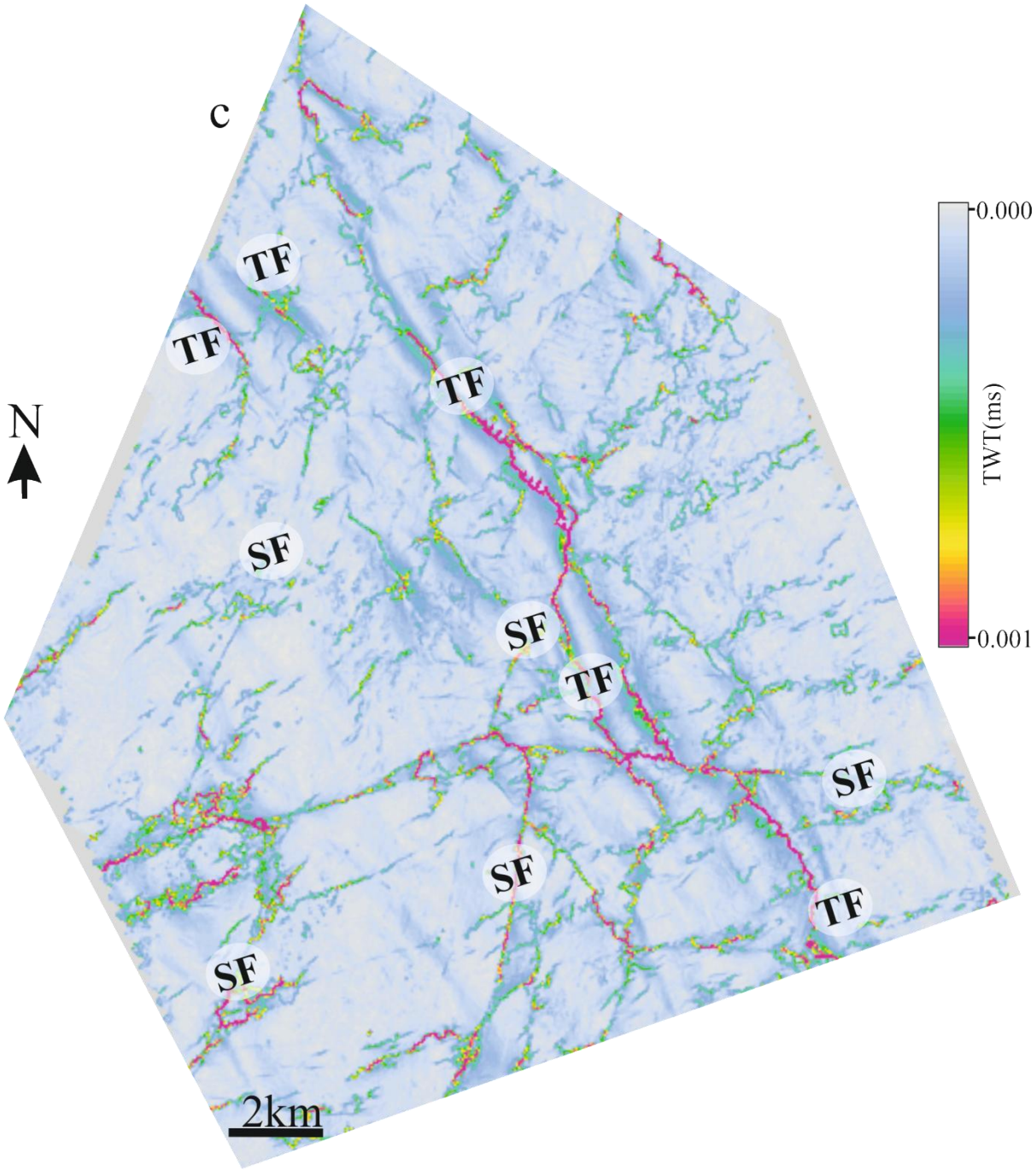


Figure 4.2: Time dip attribute maps of the northern half of the Gal C survey showing the main structural elements in the study area. The structural trend between structures in the Messinian and its overlying layers: the all point towards the same direction. (a) M6 reflection , (b) M reflection, (c) Intra PM1 reflection (IPM1), (d) Seabed reflection. F-Fold, TF- Thrust Fault, SF-Strike slip fault, MF-Messinian Thrust faults, , RL- Releasing step over, RS- Restraining step over, C- Channel.

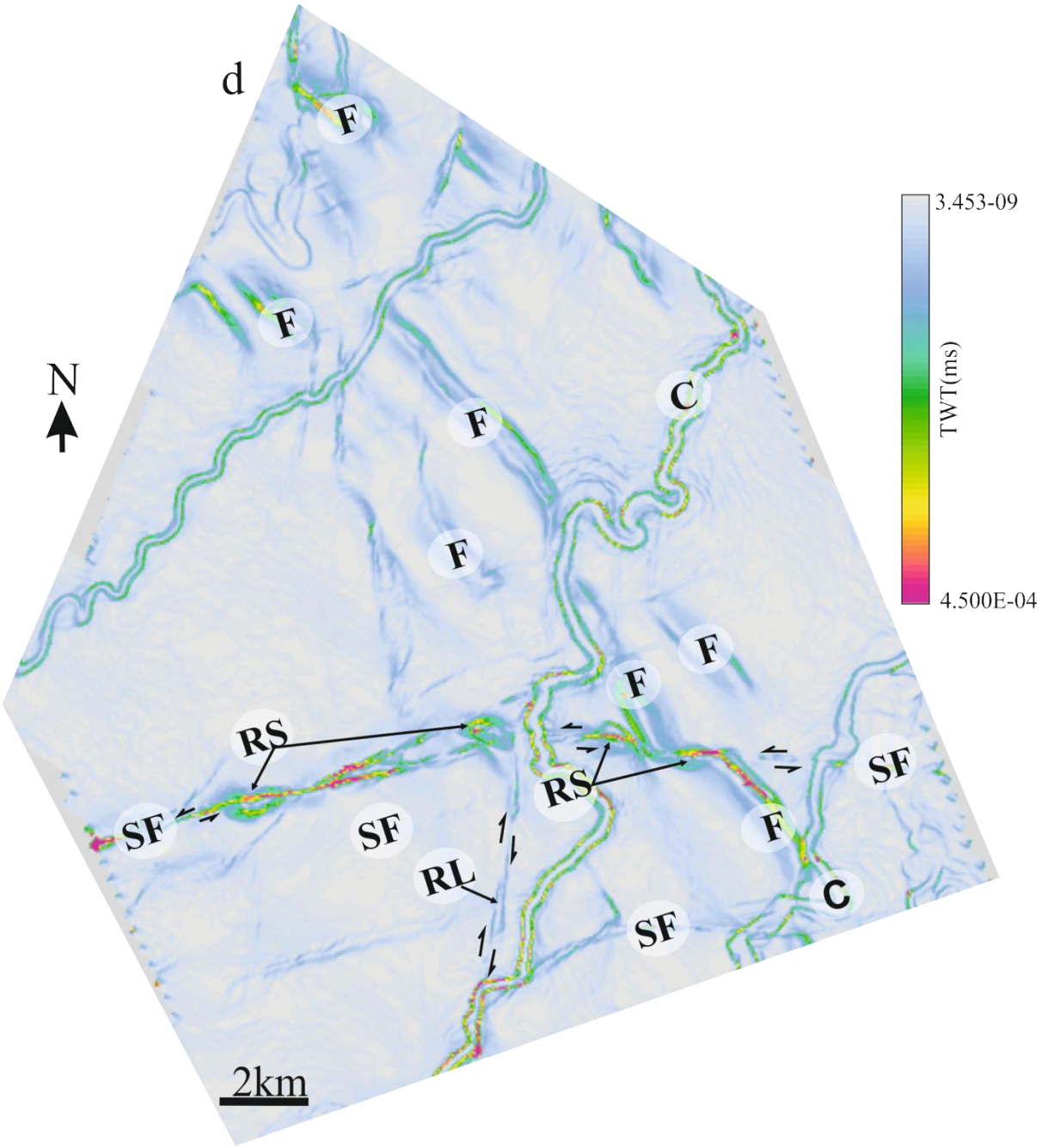


Figure 4.2: Time dip attribute maps of the northern half of the Gal C survey showing the main structural elements in the study area. The structural trend between structures in the Messinian and its overlying layers: the all point towards the same direction. (a) M6 reflection , (b) M reflection, (c) Intra PM1 reflection (IPM1), (d) Seabed reflection. F-Fold, TF- Thrust Fault, SF-Strike slip fault, MF-Messinian Thrust faults, , RL- Releasing step over, RS- Restraining step over, C- Channel.

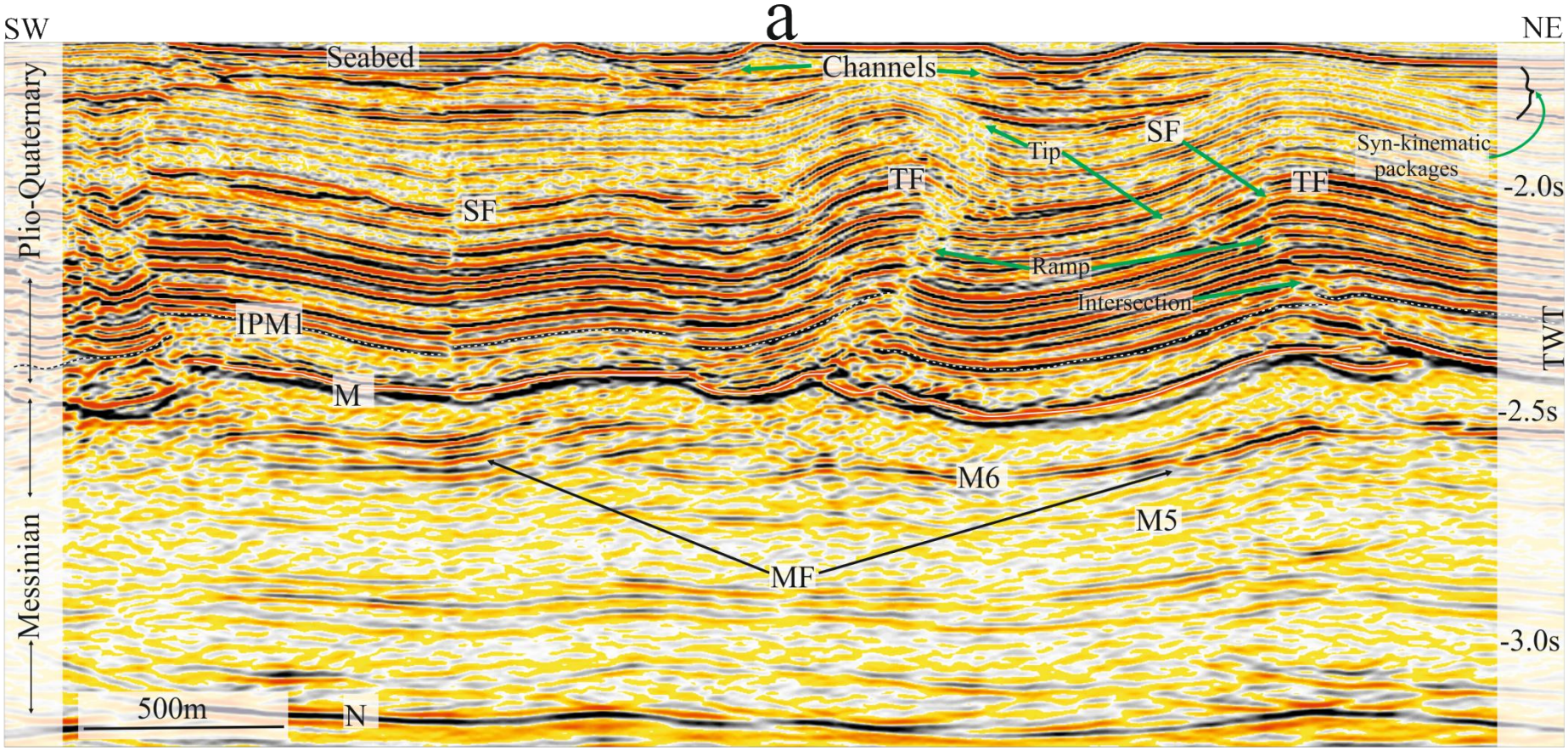


Figure 4.3**:** Seismic profile showing the relationship between deformation in upper Messinian (M5 and M6) unit and lower post-Messinian units (M and IPM1). (A) Concordant (B) Discordant. SF- Strike-slip fault, TF-Thrust fault in the post-Messinian, MF-Thrust fault in the Messinian. For location see Figure 4.2 a.

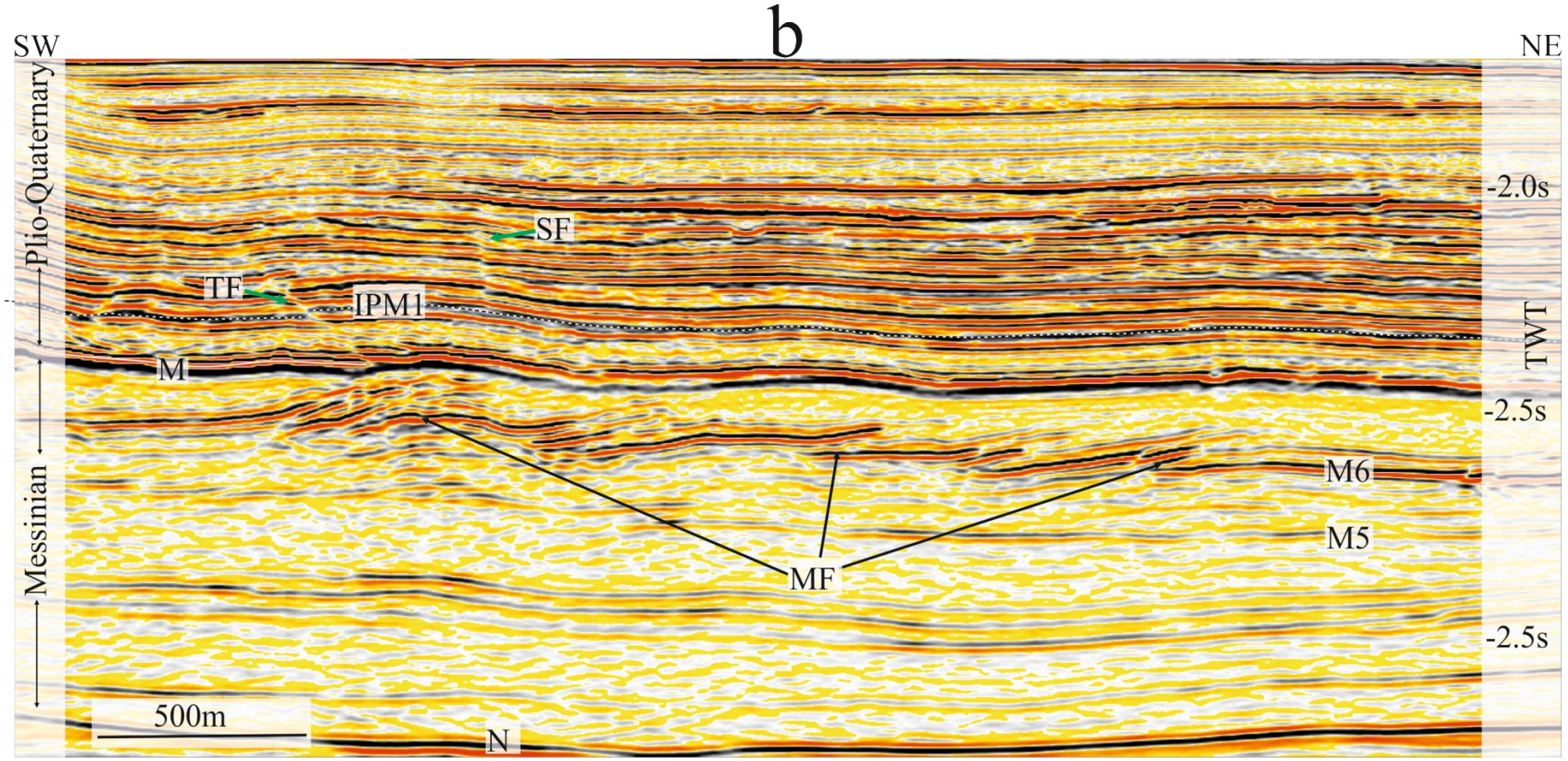


Figure 4.3**:** Seismic profile showing the relationship between deformation in upper Messinian (M5 and M6) unit and lower post-Messinian units (M and IPM1). (A) Concordant (B) Discordant. SF- Strike-slip fault, TF-Thrust fault in the post-Messinian, MF-Thrust fault in the Messinian. For location see Figure 4.2 a.

### 4.2.3 Thrust Faults and Thrust Related Folds

The thrust faults and their overlying folds commonly strike 135$^{o}$-170$^{o}$. Generally, the thrust folds are curvi-linear, with only a few that are almost linear in map view and they extend laterally from a few meters to thousands of meters (Figure 4.4). The thrust faults commonly overlap each other with overlapping distances ranging between 1000 m and 5000 m.

The majority of the thrust faults and their associated overlying folds are observed to be intersected or bounded by strike slip faults (Figure 4.4). These strike-slip faults intersect at an angle whose bisectrix is almost orthogonal to the bounded thrust related folds. Zones where thrusted structures intersect strike-slip faults are generally poorly resolved in seismic sections which make it difficult to establish their actual intersection zones. However, the distance from the mappable fault segment to intersection zones falls within the range of 20 – 200 m. These poorly constrained horizon reflections at intersection zones are probably due to steeply dipping surfaces (Tucker 1982).

Thrust fault ramps are typically defined on vertical seismic sections by prominent strata discontinuities with a systematic alignment (Figure 4.3 a) and they extend in height from tens to hundreds of meters. Their upper tips are well defined by the shallowest of resolvable offsets of seismic markers, although loss of signal coherence in shallow reflections around the upper tips sometimes obscures their precise location (Figure 4.3 a).

Fault planes are planar to curvi-planar, dipping between 29$^{o}$-40$^{o}$, with steeper dips occurring locally at intersection zones. They generally tend to be listric (concave upward) downward towards Horizon M, where the dip decreases (Figure 4.3 a). The listricity of these thrust faults and their generally asymptotic relationship as well the regional stratigraphy at their base (below Horizon M) is strongly indicative of the presence of a detachment zone (McNeill *et al.* 1997; Briggs et al. 2006). Fault detachment levels are defined in this study by tracing the

discordance between reflections in footwall and hangingwall to a position where there is no visible discordance (Figure 4.3 a). Their main site of the detachment is at the top Messinian, where they generally decrease in dip (Briggs et al. 2006).

The thrust faults in Gal C are generally blind: upper tips do not extend beyond the seabed. Larger fault segments are characterized by their tips terminating beyond the base of unit PM3 (Figure 4.3). Maximum displacement varies from 10-800m recorded close to the lower units of the post-Messinian overburden (see Chapter 6, Figure 6.6-6.8). The majority of the fault plane have their hanging wall verging north-east with only a small number verging in the opposite direction.

Folds without ramp such as those of detachment folds (Jamison 1987), are not common in the data set and the majority of the thrust faults do not have upper detachment layers such as that of the fault bend fold (Rich 1934; Suppe 1983). They appear to have the characteristics of a fault propagation fold (Suppe 1985b), or fault detachment fold (Mitra 2002) .This is inferred from the presence of ramps and the absence of upper detachments (Jamison 1987).

The folds are mainly symmetric to sub-asymmetric, kink band geometries are not common within the dataset, but fold hinges and crest are almost round or curved. Inter-limb angle varies between $60^{o}$-$80^{o}$ with folds wavelengths of up to 200m. The folds show a wide range in amplitude values, with some showing amplitudes up to 0.4s (TWT), while others show amplitude less than 0.07s TWT. For detailed description, thrust related folds with maximum amplitudes less than 0.07s along Horizon IPM1 are termed Type A, while those with larger maximum amplitudes are termed Type B.

#### *4.2.3.1 Type A thrust related fold*

These are faults with limited folding associated with footwall and hangingwall, recognised within the south-eastern segment of the dataset (Figure 4.4 and 4.5). They are readily

distinguished from classical examples of thrust related folds because both their hanging wall and footwall are characterized by low amplitude. Generally, their maximum amplitude is less than (0.07s TWT).

Two representative examples of the Type A thrust related folds (T46 and T49) are presented in this study. These case study examples are described using two key horizon maps and seismic sections along strike (Figure 4.6-4.9).

**Fault T46**

T46 is located towards the south-eastern part of the survey area (Figure 4.4 and 4.5). The thrust fault strikes c. 140$^{o}$ and it is delimited at its NW end by a sinistral fault (S53) trending c. 110$^{o}$ with a dextral fault S72 striking c. 050$^{o}$ which also has its lateral tip terminating onto the S53 (Figure 4.6). Map view shows that T46 has an along strike distance of c. 1400 m at Horizon IPM1 (Figure 4.6 b) and less than 1,000 m at IPM2a (Figure 4.6 a) indicating that the thrust fault decreases in length upward.

Seismic Sections along T46 close to and away from strike-slip faults are shown in Figure 4.7. The thrust related fold is symmetric with maximum amplitude less than 0.04s (~40m), an average wavelength of c. 2200m and it dips 40$^{o}$. No notable change in amplitude and dip was observed along strike (Figure 4.5). However maximum displacement was measured to be c. 162m close to the intersection zone at line a0 along Horizon IPM1 which makes Dmax/L= 0.12 (L=1800m). The thrust fault is planar. Its basal tip terminates close to Horizon M. No significant change in dip is observed at down tip as that of a detachment fault (Briggs et al. 2006; Higgins et al. 2007).

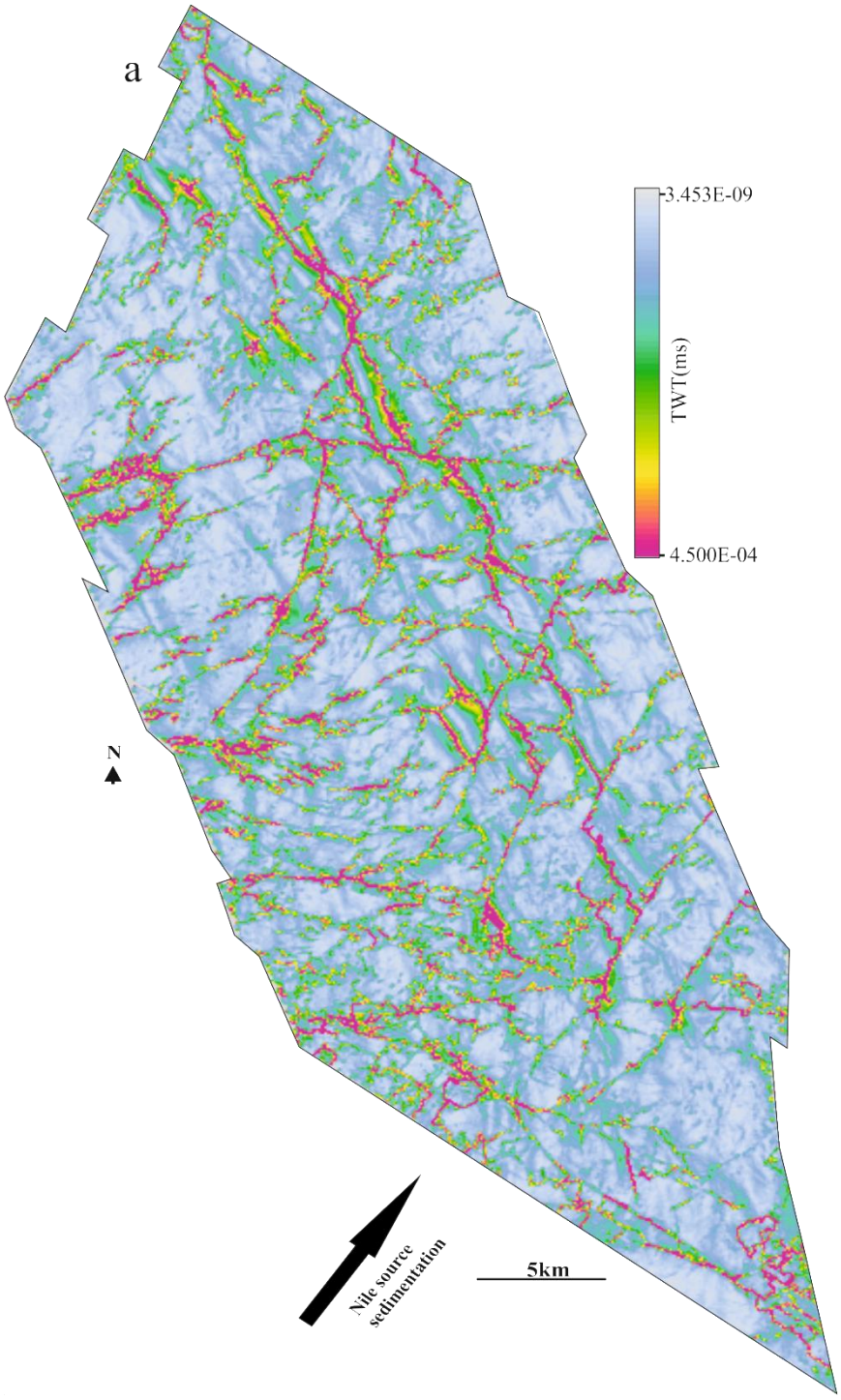


Figure 4.4: Maps showing the distribution of the main structural elements of IPM1. (a) Time dip map. (b) Time dip structural map. The thrust faults are numbered T1-T50 while the strike slip faults are number S1-S71. Displacement values for the strike slip faults are recorded in Figure 5.1b, blue circles represent offset values from channel offsets while green squares represent fold and thrust fault offset values. The rose diagram shows the main structural trends of the thrust faults and strike slip faults.
The rose diagram shows the main structural trends of the thrust faults and strike slip faults.

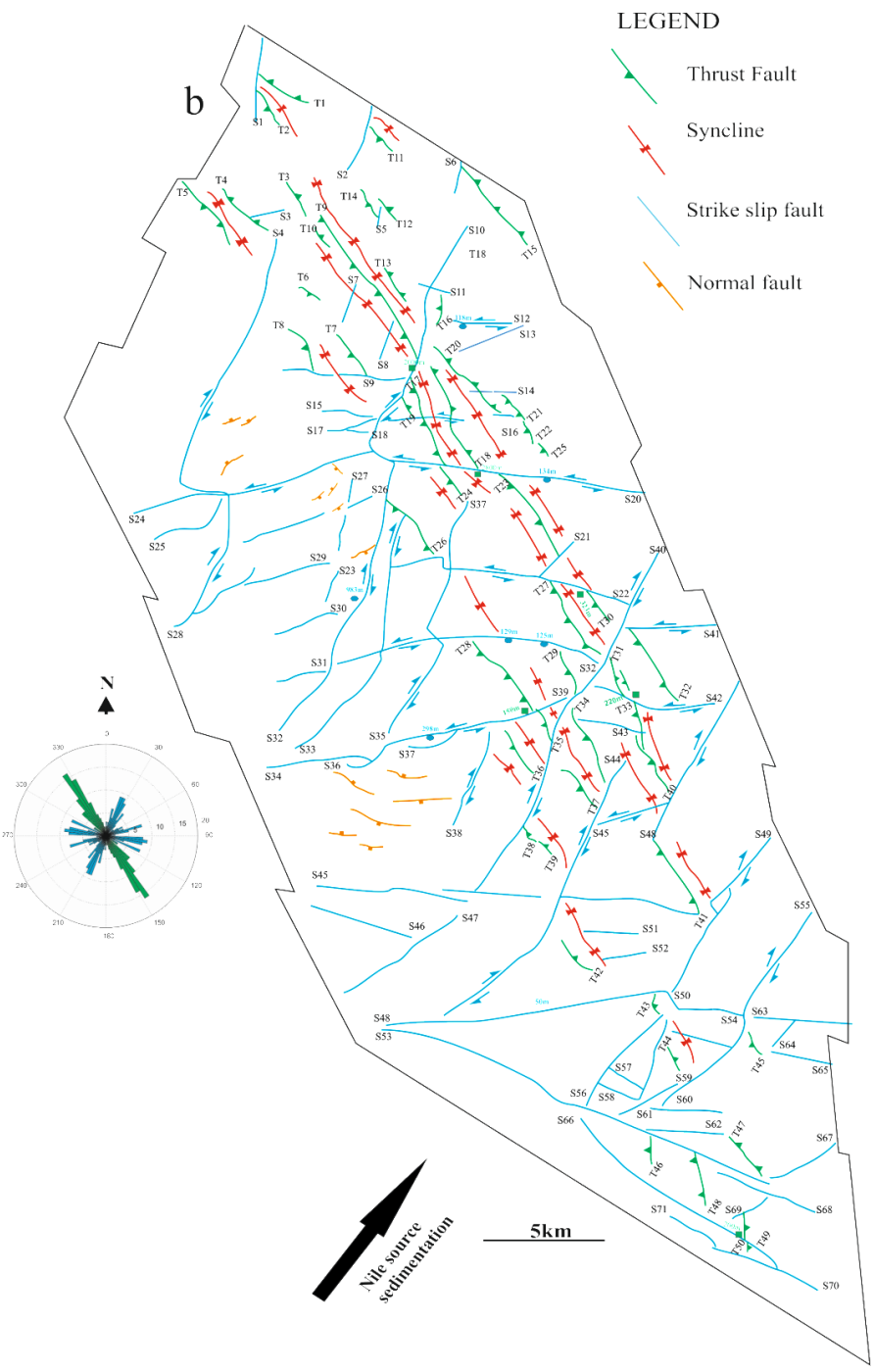


Figure 4.4: Maps showing the distribution of the main structural elements of IPM1. (a) Time dip map. (b) Time dip structural map. The thrust faults are numbered T1-T50 while the strike slip faults are number S1-S71. Displacement values for the strike slip faults are recorded in Figure 5.1b, blue circles represent offset values from channel offsets while green squares represent fold and thrust fault offset values. The rose diagram shows the main structural trends of the thrust faults and strike slip faults. The rose diagram shows the main structural trends of the thrust faults and strike slip faults.

**Fault T49**

Thrust fault T49 is a low amplitude thrust related fold located towards the south eastern region of the survey set (Figure 4.4 and 4.5). The thrust fault strikes c. 160$^{o}$ and has a maximum lateral distance of c. 2,650 m along Horizon IPM1 which decreases upward (Figure 4.8).

Thrust fault T49 is segmented by strike slip faults of different sense of shear (Figure 4.8). T49 is delimited close to its north-western lateral tip by a dextral fault (S69), and intersected towards its south eastern end by a sinistral fault (S66) at 4300m along Horizon IPM1 Figure 4.8 a. Along Horizon IPM2a, T49 is free at its north-western tip end and intersects S69 towards its south eastern end at 2100m (Figure 4.8a), this indicates that the fault dies upward towards S69.

Seismic sections along strike of thrust fold T49 shows that it is symmetric in form having maximum amplitude less than 0.02s TWT (~20m) measured at Horizon IPM1. No notable change in amplitude and displacement is observed close to intersection relative to the isolated segment of the thrust fault (Figure 4.9).

T49 is planar, dipping 47$^{o}$ NE, with no significant change in dip, towards the detachment layer. It has its lower vertical tip terminating at the M reflection or slightly below it (Figure 4.9). At the south eastern intersection zone, T49 is observed to cross-cut S66 into 2 sub vertical segments with a slight change in dip at intersection zone (Figure 4.9 c). Displacement reaches a maximum of c. 150 m close to the cross-cutting zone, this makes Dmax/L= 0.06.

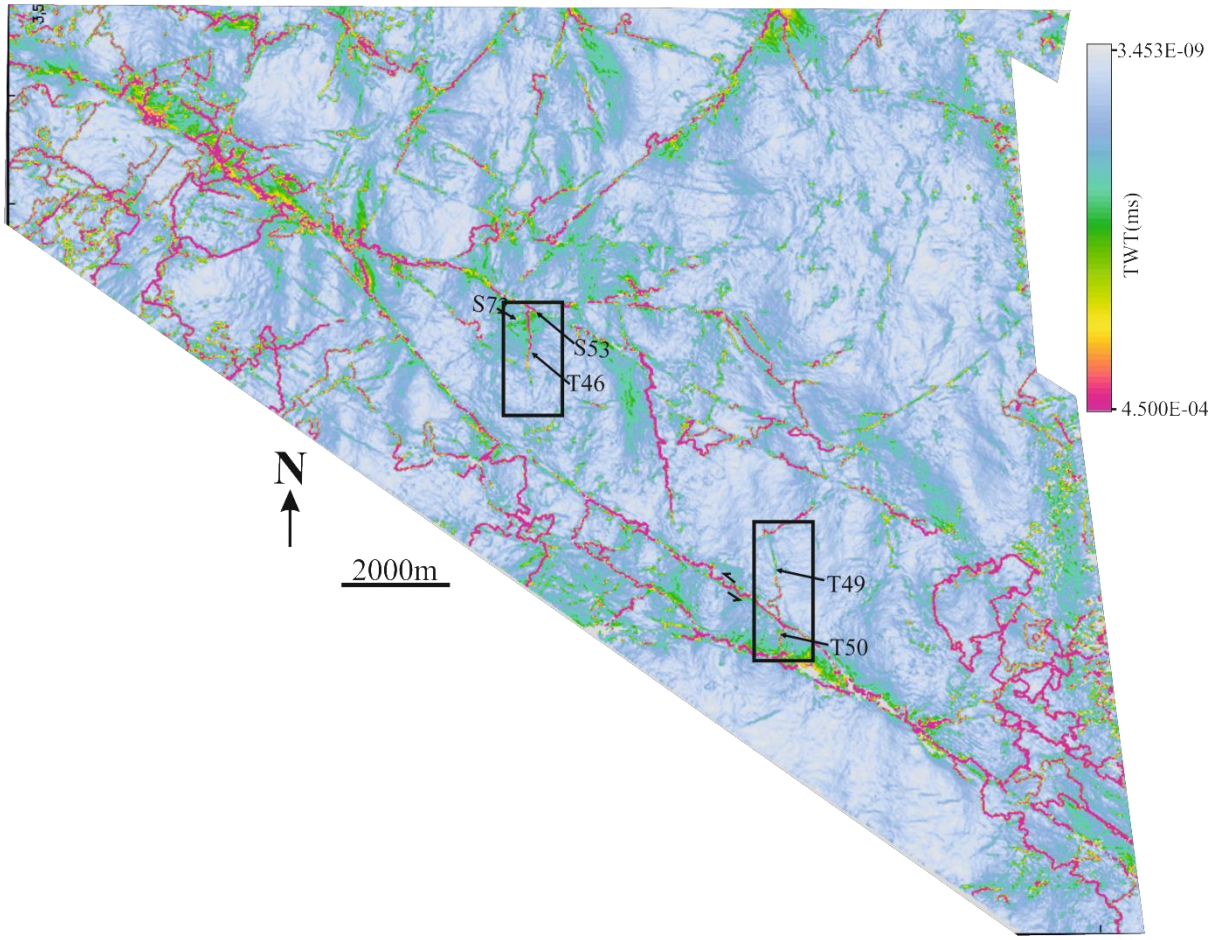


Figure 4.5: Time dip horizon (IPM1) map of the southern segment of the Gal C survey showing the Type A case study faults described in this study. T represents thrust fault, and S strike slip fault.

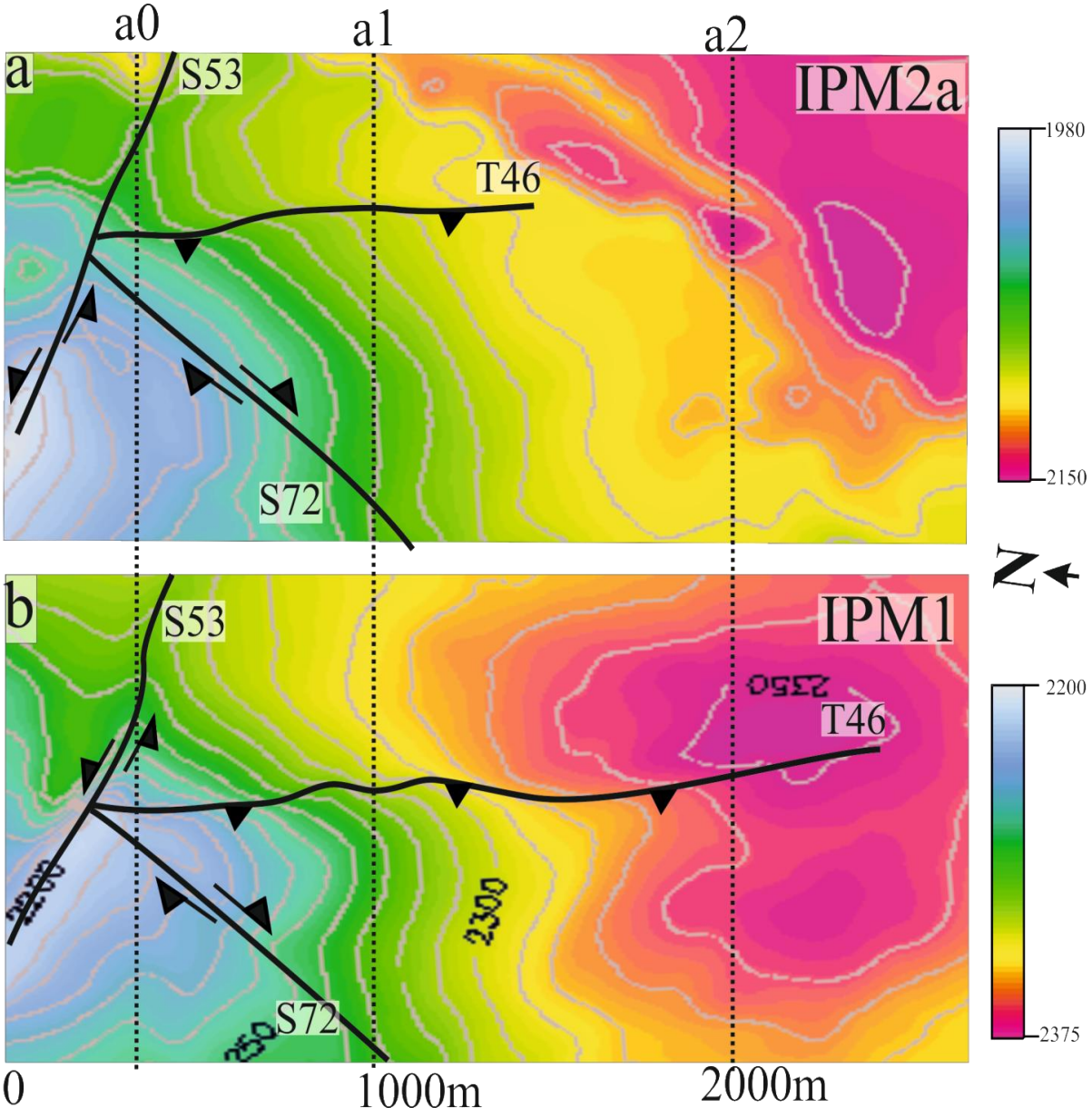


Figure 4.6: Maps of horizon elevation in two-way –time (ms).Location shown in Figure 4.5. (a) Horizon 1PM2a (b) Horizon IPM1. Traces of a major thrust fault T46 intersected at one end by strike slip faults (S53 and S72). Thrust fault trace is denoted by black triangles in the hangingwalls. Lines a0- a2 show locations of the 3 sections in Figure 4.7. Blue/green colours represent structural high. Red/orange colour represents structural low. Contour interval: 10ms.

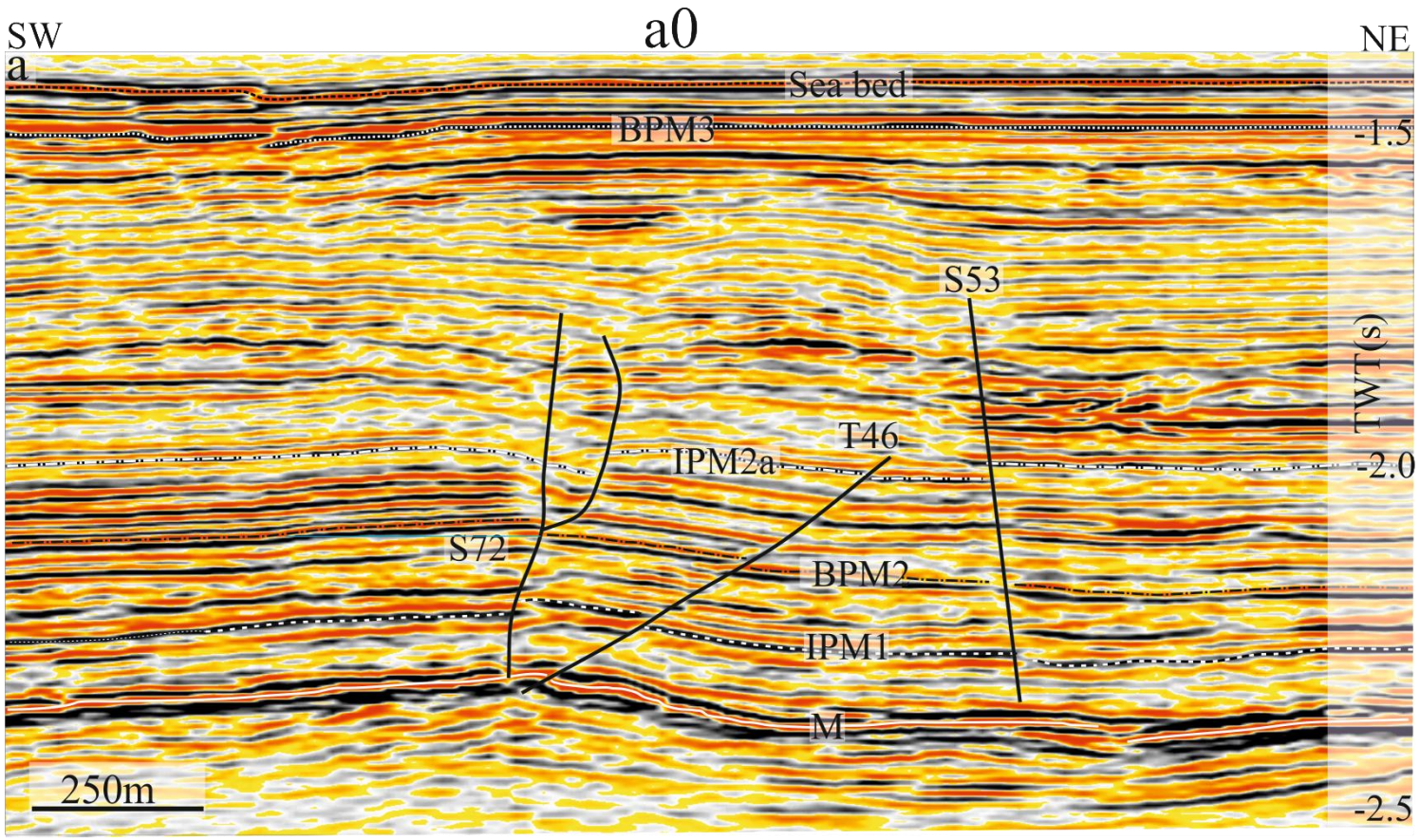


Figure 4.7: Selected seismic sections perpendicular to T46 illustrating along strike changes in fold and fault shape, and magnitude. Locations of seismic lines (a0-a2) in Figure 4.6. Sections have an approximate vertical exaggeration of 1.5. Horizons M, IPM1, BPM2, IPM2a and BPM3 are regional stratigraphic horizons.

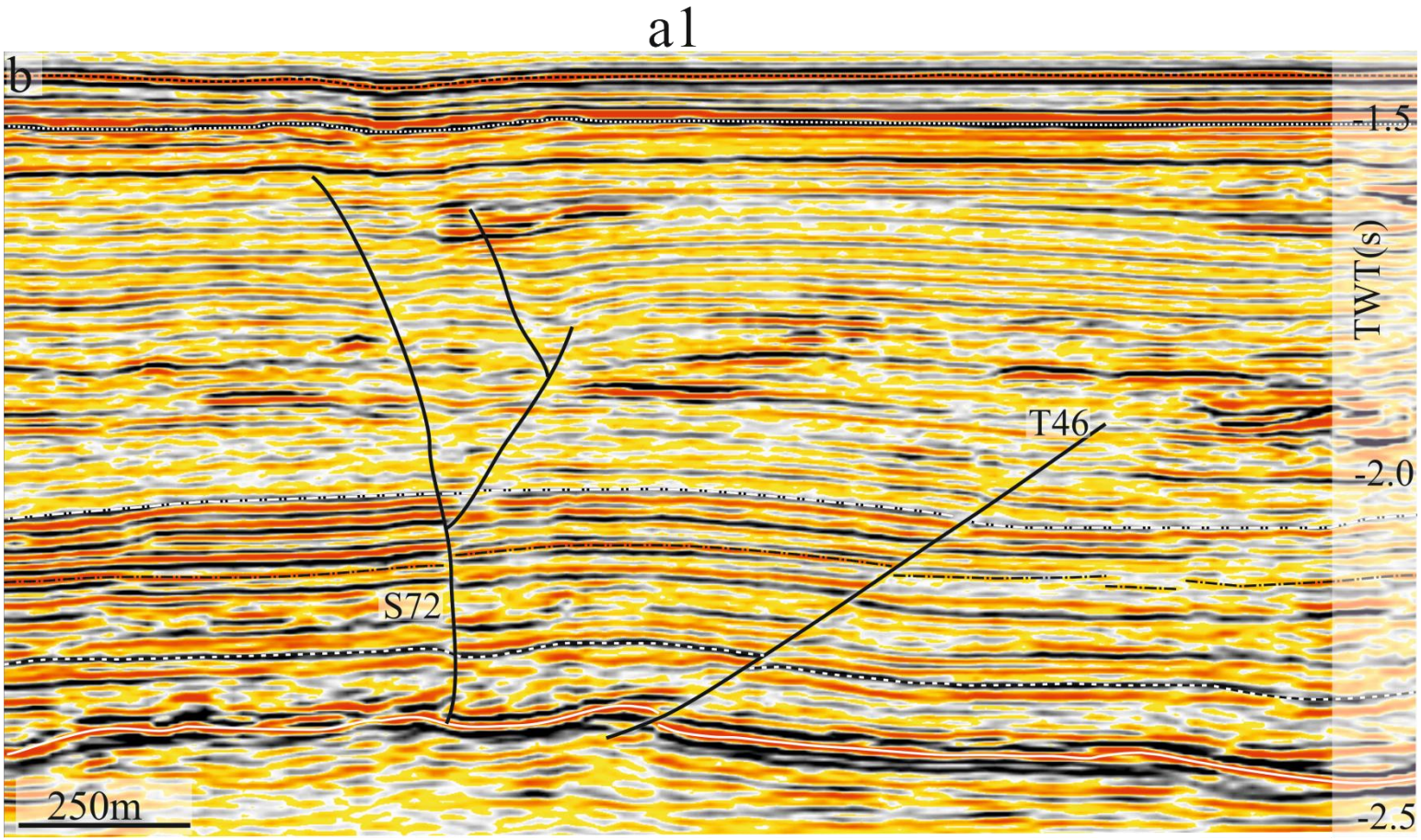


Figure 4.7: Selected seismic sections perpendicular to T46 illustrating along strike changes in fold and fault shape, and magnitude. Locations of seismic lines (a0-a2) in Figure 4.6. Sections have an approximate vertical exaggeration of 1.5. Horizons M, IPM1, BPM2, IPM2a and BPM3 are regional stratigraphic horizons.

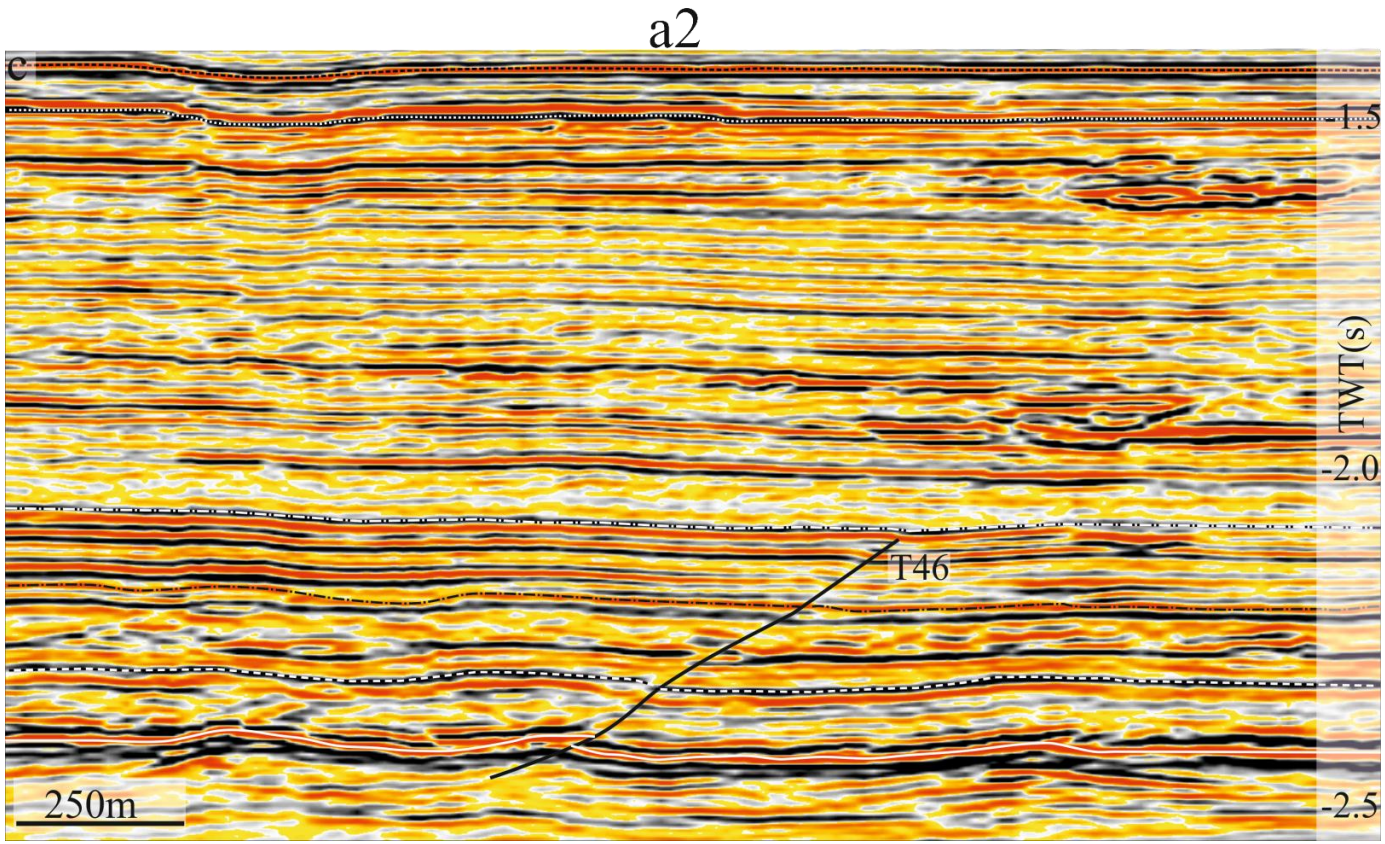


Figure 4.7: Selected seismic sections perpendicular to T46 illustrating along strike changes in fold and fault shape, and magnitude. Locations of seismic lines (a0-a2) in Figure 4.6. Sections have an approximate vertical exaggeration of 1.5. Horizons M, IPM1, BPM2, IPM2a and BPM3 are regional stratigraphic horizons.

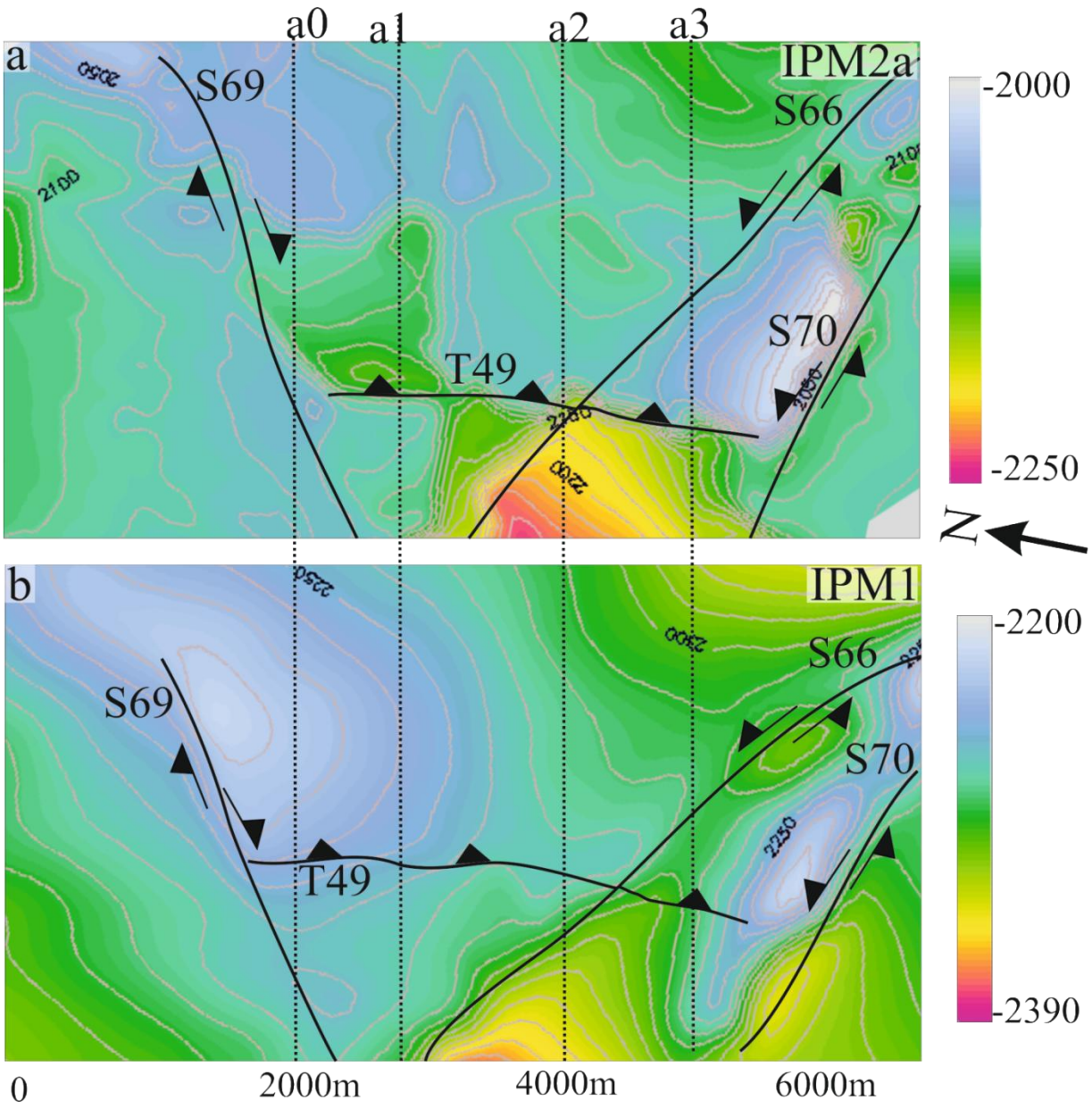


Figure 4.8 :Maps of horizon elevation in two-way –time (ms). Locations shown in Figure 4.5. (a)Horizons IPM2a (b) Horizon IPM1. Traces of a major thrust fault T49 and T50 intersected at their lateral tips by strike slip faults (S69, S66 and S70). Thrust fault trace is denoted by black triangles in the hangingwalls, red broken lines represents zone where resolution is too poor to map. Lines a0- a4 show locations of the 5 seismic sections in Figure 4.9. Blue/green colours represent structural high. Red/orange colour represents structural low. Contour interval: 10ms

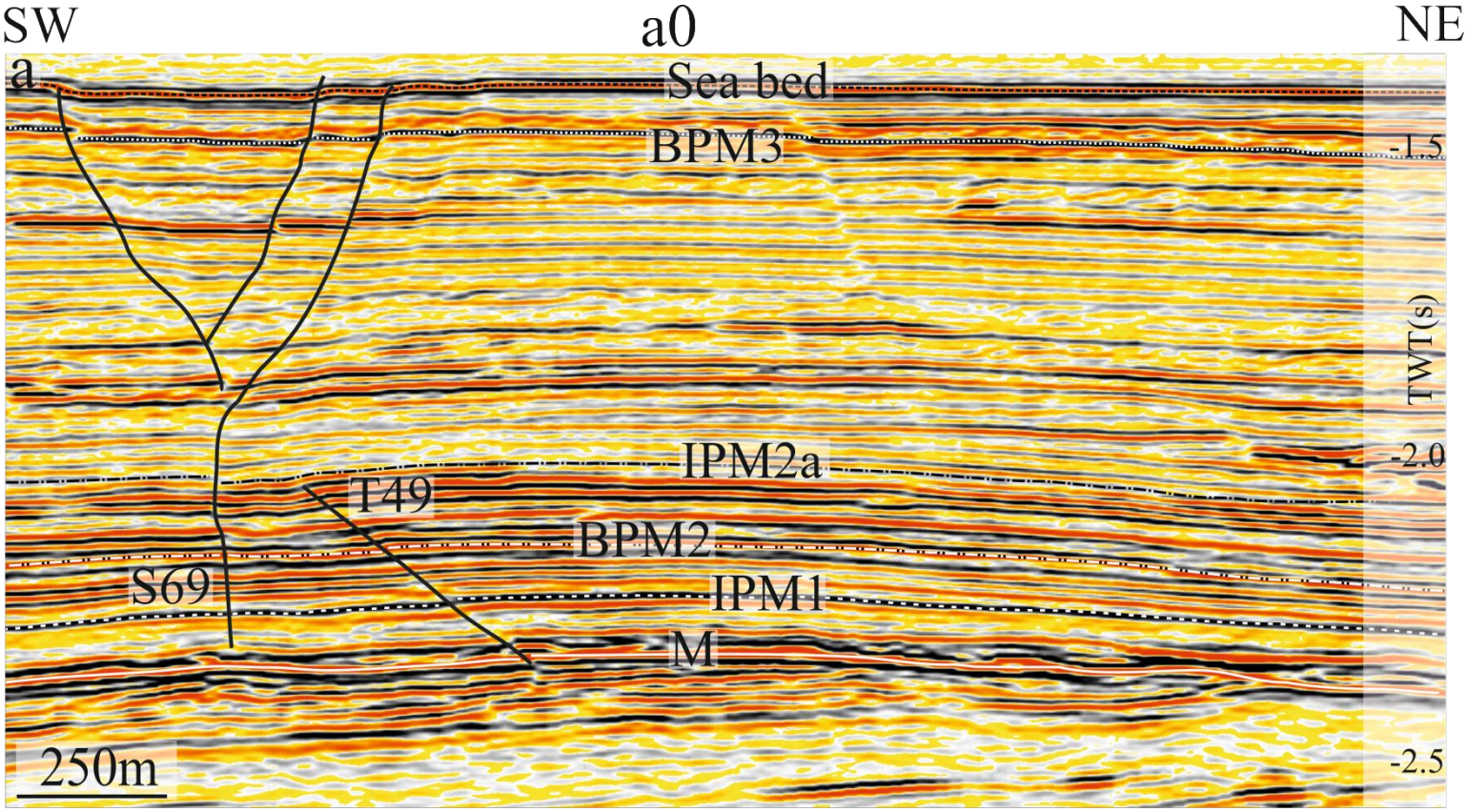


Figure 4.9: Selected seismic sections perpendicular to T49 illustrating along strike changes in fold and fault shape, and magnitude. Locations of seismic lines (a-d) in Figure 4.8. Sections have an approximate vertical exaggeration of 1.5. Horizons M, IPM1, BPM2, IPM2a and BPM3 are regional stratigraphic horizons.

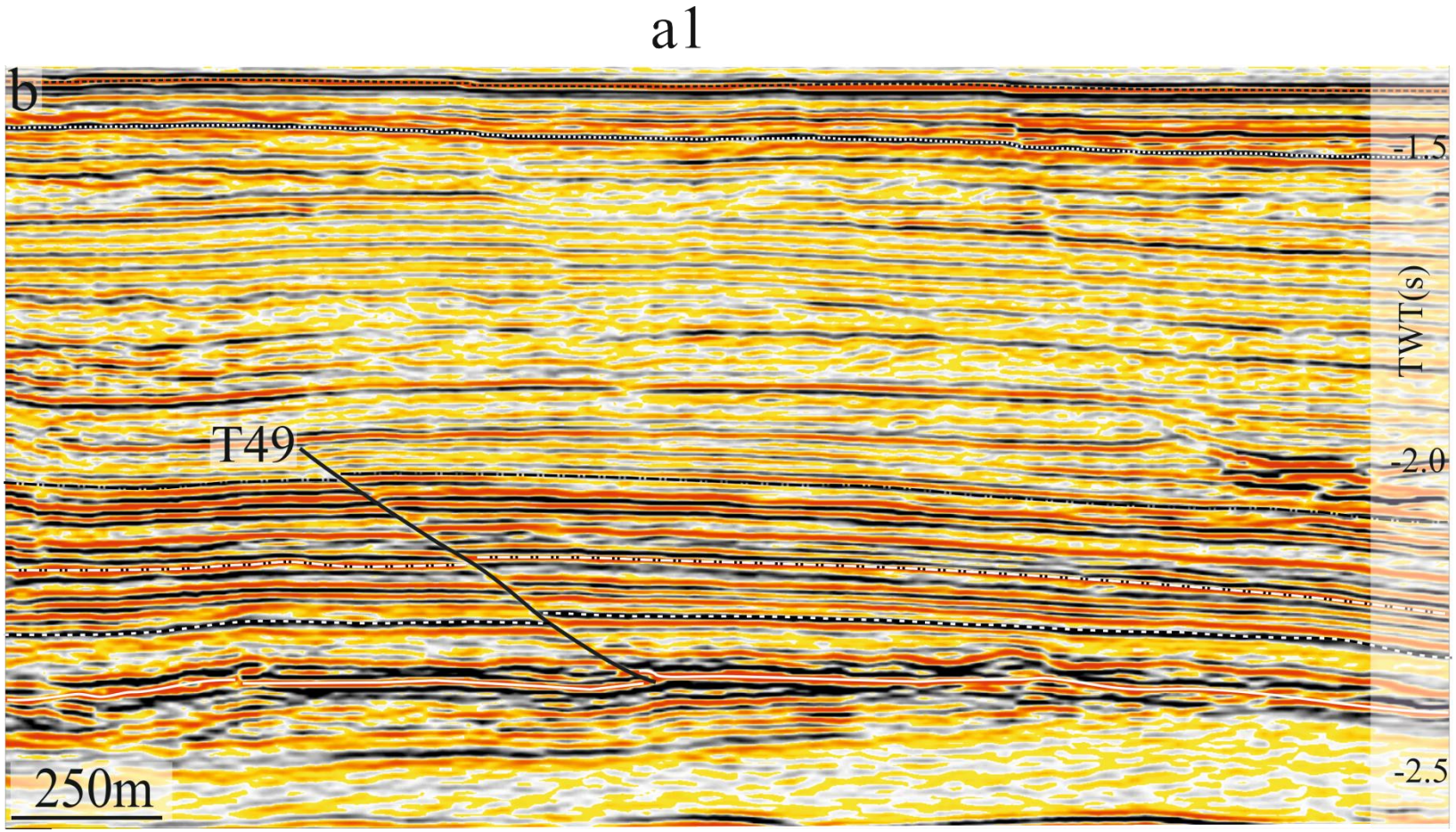


Figure 4.9: Selected seismic sections perpendicular to T49 illustrating along strike changes in fold and fault shape, and magnitude. Locations of seismic lines (a-d) in Figure 4.8. Sections have an approximate vertical exaggeration of 1.5. Horizons M, IPM1, BPM2, IPM2a and BPM3 are regional stratigraphic horizons.

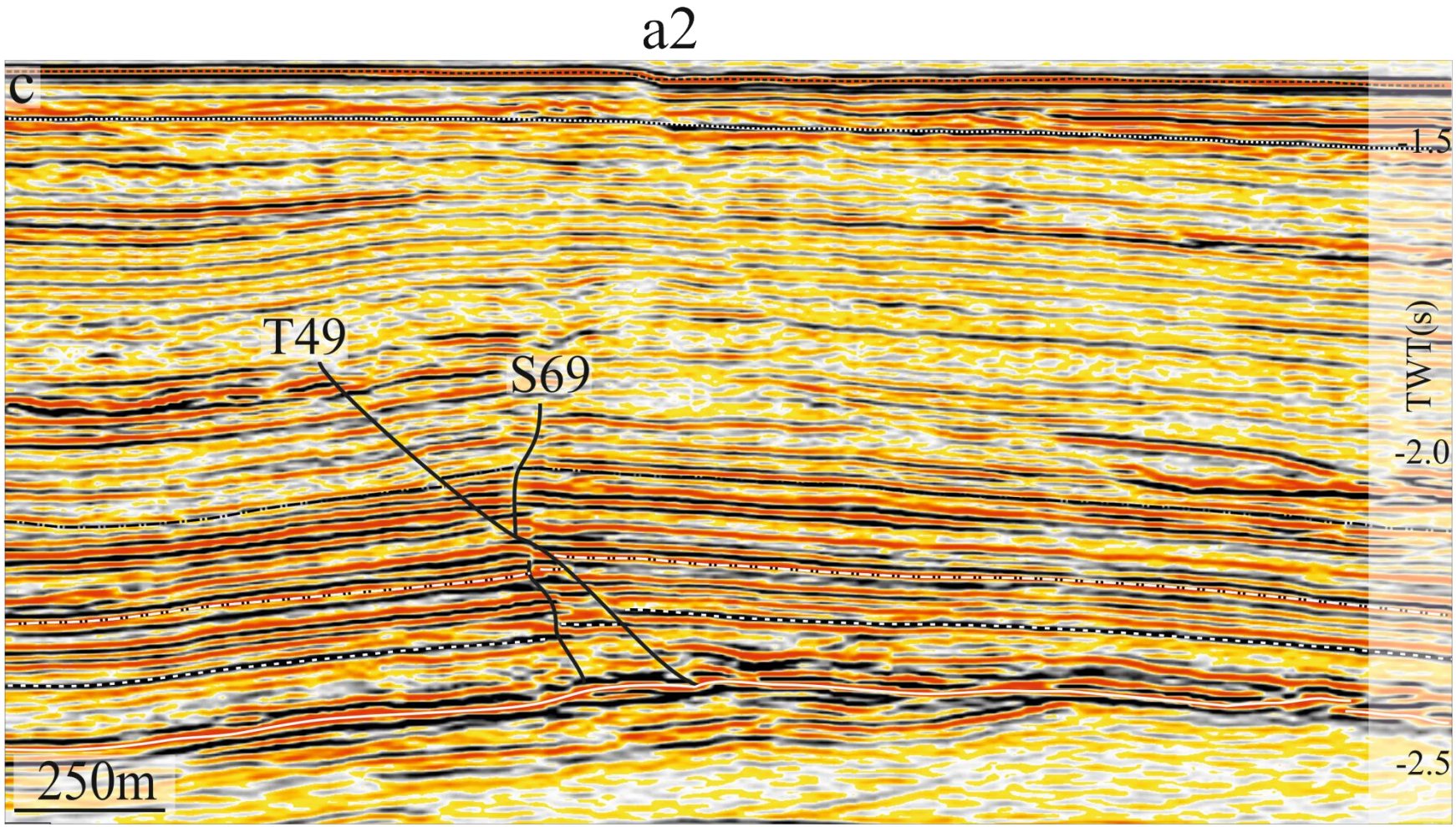


Figure 4.9: Selected seismic sections perpendicular to T49 illustrating along strike changes in fold and fault shape, and magnitude. Locations of seismic lines (a-d) in Figure 4.8. Sections have an approximate vertical exaggeration of 1.5. Horizons M, IPM1, BPM2, IPM2a and BPM3 are regional stratigraphic horizons.

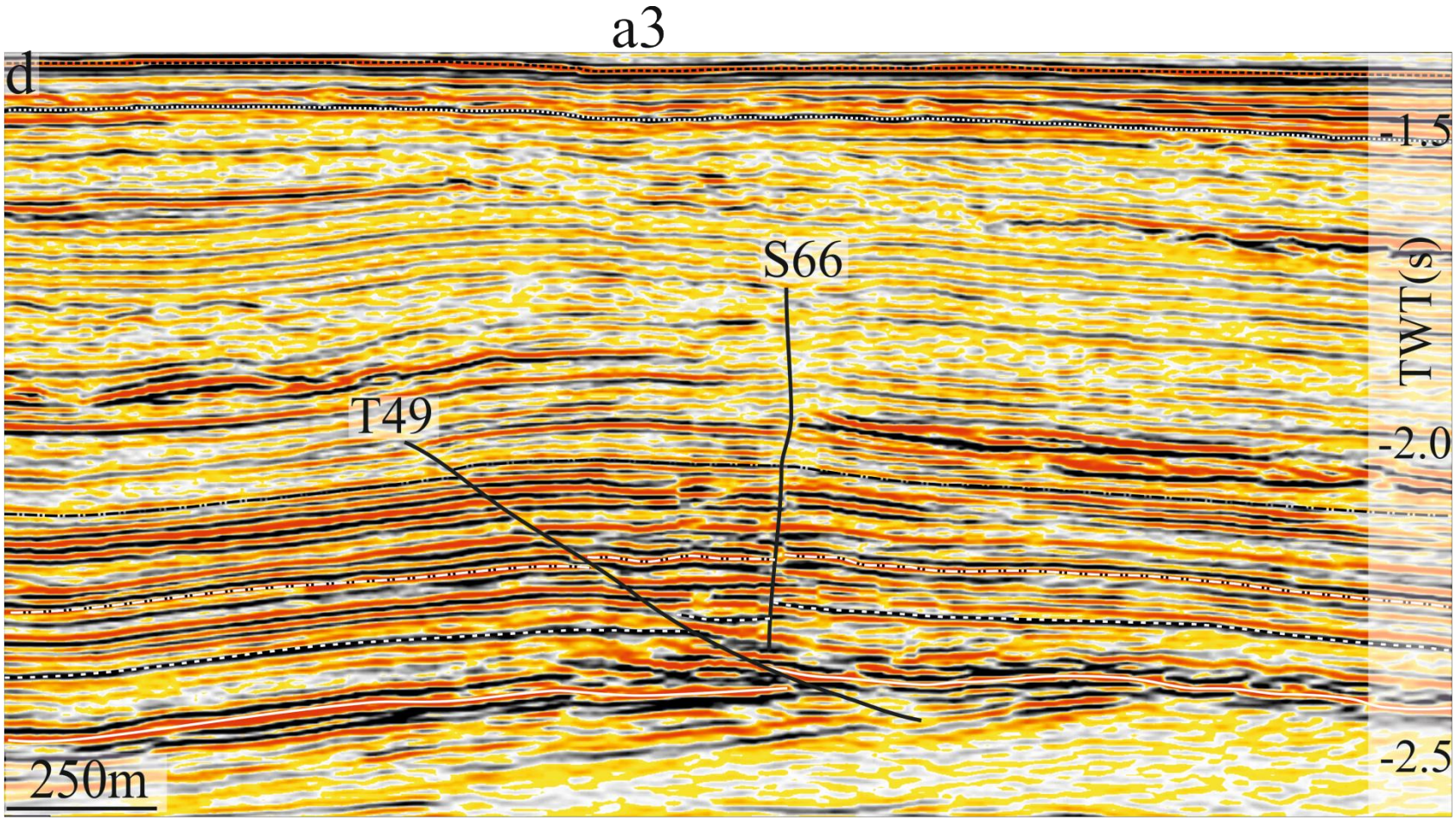


Figure 4.9: Selected seismic sections perpendicular to T49 illustrating along strike changes in fold and fault shape, and magnitude. Locations of seismic lines (a-d) in Figure 4.8. Sections have an approximate vertical exaggeration of 1.5. Horizons M, IPM1, BPM2, IPM2a and BPM3 are regional stratigraphic horizons.

#### *4.2.3.2 Type B thrust related fold*

Type B thrust related folds are similar to the classical examples (Suppe 1983; Jamison 1987; McClay 2004; Corredor et al. 2005). Type B thrusts are more common within the study area compared to the Type A thrust faults. They are randomly spaced with an average spacing distance of 1500m. Individual thrust faults of these types extend laterally from 400m to tens of thousands of metres. They are mainly linear but tend to be abnormally curved when breached by strike slip faults (Figure 4.4).

Generally, the Type B are more complex than the Type A thrust faults. Fold amplitude vary from 0.1s to 0.5s (TWT) and they are mainly asymmetric with most of the structures verging north-east, with a small number verging the opposite direction (Figure 4.4,). The folds are generally characterized by back limbs that dip less than the forelimbs (Figure 4.3a). They are overlain by growth strata which generally shallow in dip upward. The presence of growth packages indicates that deformation is contemporaneous with sedimentation (Suppe and Medwedeff 1990; Higgins et al. 2009).

Thrust fault ramps, underlying the folds, do not vertically propagate to surface, but some penetrate the base of unit PM3. Positive bathymetric relief develop above the vertical tips of most these faults which are well expressed on the time dip map of the seabed (Figure 4.2d). This indicates that the deformation rate exceeds deposition (Storti and Poblet 1997c; Corredor et al. 2005). Their main site of detachment is within the upper Messinian interval (Figure 4.3a).

Maximum displacement varies from 100-800m, this decreases upward towards the vertical tips (see Chapter 6 for details). Generally fault ramps of Type B dip much less than the Type A thrust faults. Type B faults dip between $33^{o}$-$38^{o}$, although some are steeper at intersection zones.

For a regional structural study, over 30 Type B thrust related folds were mapped in this data set (Figure 4.4). In this section, 3 (T9, T17 and T18) of these structures are described in detail as represented examples. These structures are associated with minor other thrusts faults (T10, T13 and T19). For simplicity purposes, this study labelled T9 and its associated minor trust faults (T10 and T13) as structure A, while T17, T18 and T19 as structure B (Figure 4.10). The structures were described using 3 key horizon reflections (IPM1, BPM2 and IPM2) and seismic lines (Figure 4.11- 4.14).

**Structure A**

Structure A is made up of thrust fault T9, T10 and T13 located in the NNE region of the dataset (Figure 4.4, 4.10, 4.11). T9 is a good example of a Type B thrust fault and fold pair. It is associated with minor fore thrust (T10) and back thrust (T13) which dip towards and away from the principal thrust fault (T9) respectively, forming various antithetic type relationships along strike (Morley et al. 1990; Higgins et al. 2007) (Figure 4.11 and 4.12).

Seismic sections across T9 shows that its hanging wall anticline and footwall syncline increases in amplitude from northwest to south east (Figure 4.11 and 4.12a-d). It attains maximum amplitude of c.380 m measured at C. 6100 m along the fold length (Figure 4.12c). The fold is mainly symmetric but slightly asymmetric towards the central zone (Figure 4.12 a-d).

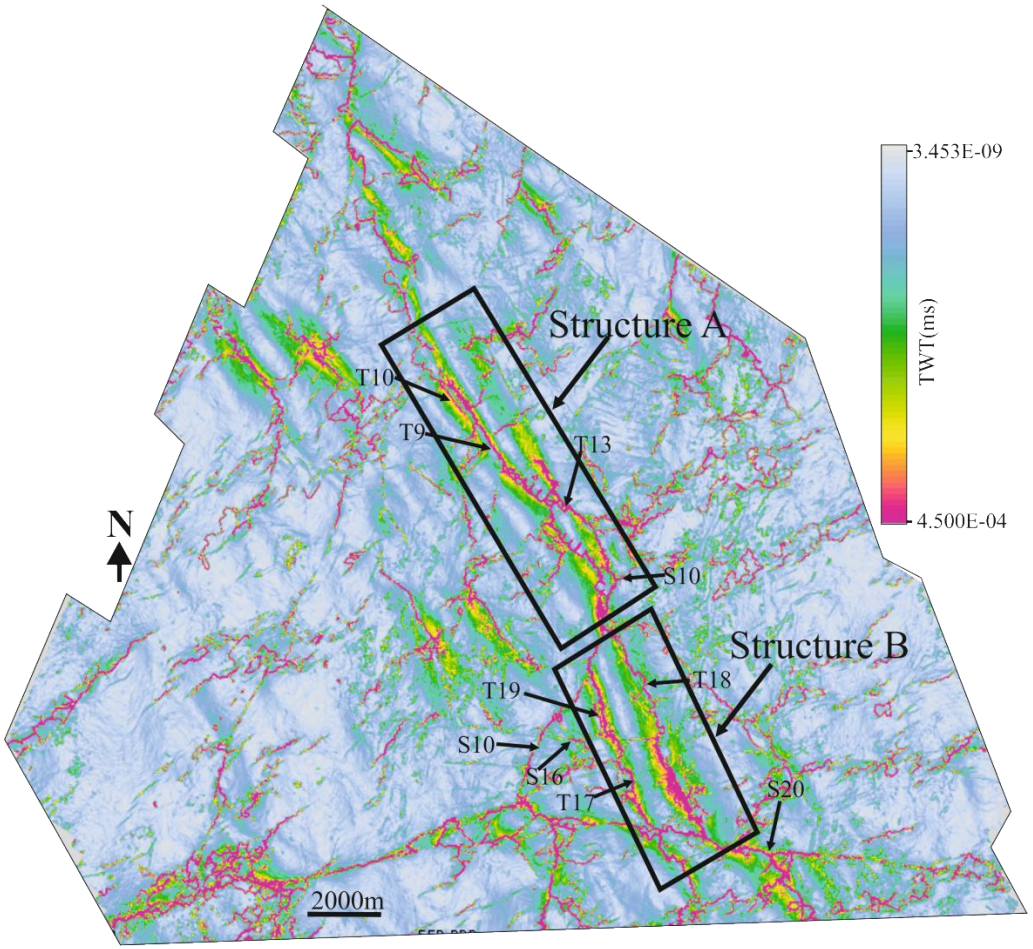


Figure 4.10: Time dip horizon (IPM1) map of the northern segment of the Gal C survey showing the Type A case study structures (A and B). T represent thrust fault, while is S is strike slip fault.

Fault T9 has a strike length of c. 7,400 m along Horizon IPM1, measured between its NW end, and SE tip close to where it intersects a dextral fault (S10) striking c. 010$^{o}$ (Figure 4.11 and 4.12 c). T9 decreases in length upward and it appears to tip freely at Horizon IPM2 (Figure 4.11 a). It mainly strikes c. 145$^{o}$ and it is the only thrust fault plane which cuts through the base of unit PM3 (BPM3) within structure A (Figure 4.12 b and c). T9 reaches a height of c. 0.82s (TWT), at c. 6,700m close to intersection zone and decreases from this zone of maximum culmination to both lateral ends (Figure 4.12).

T9 is almost planar, dipping 38$^{o}$SW. It shallows in dip asymptotically downwards to the top Messinian unit (between M reflection and MX), where the fault plane becomes parallel to the stratal reflection (Figure 4.12 c and e). This zone is defined as the zone of detachment for T9 and it is observed that this zone of detachment thins towards the faults surface, in this case it decreases in thickness from T0 (c. 0.55s, TWT) to T2 (c. 0.85s, TWT) (Figure 4.12 e).

Maps of key horizons show that the zone of intersection between T9 and S10 (at c 7000m along the structure) is characterized by closely spaced contours indicating a region of steep gradient associated with deformation (Figure 4.11). Seismic profile close to this zone of intersection (Figure 4.12 d), shows that T9 is cross cut by S10 into 2 segments of different dipping angle: down segment dipping c. 33$^{o}$ and up segment dipping c. 50$^{o}$. Fold amplitude and fault displacement appear to be relatively higher close to intersection zone (Figure 4.12 c and d). It reached a maximum displacement of c. 760m at c. 6,700 m, this decreases towards the north-western end (see Chapter 5, Figure 5.10). The minimum and maximum displacement close to the north-western and south eastern ends of T9 implies that deformation increases towards the intersection zone.

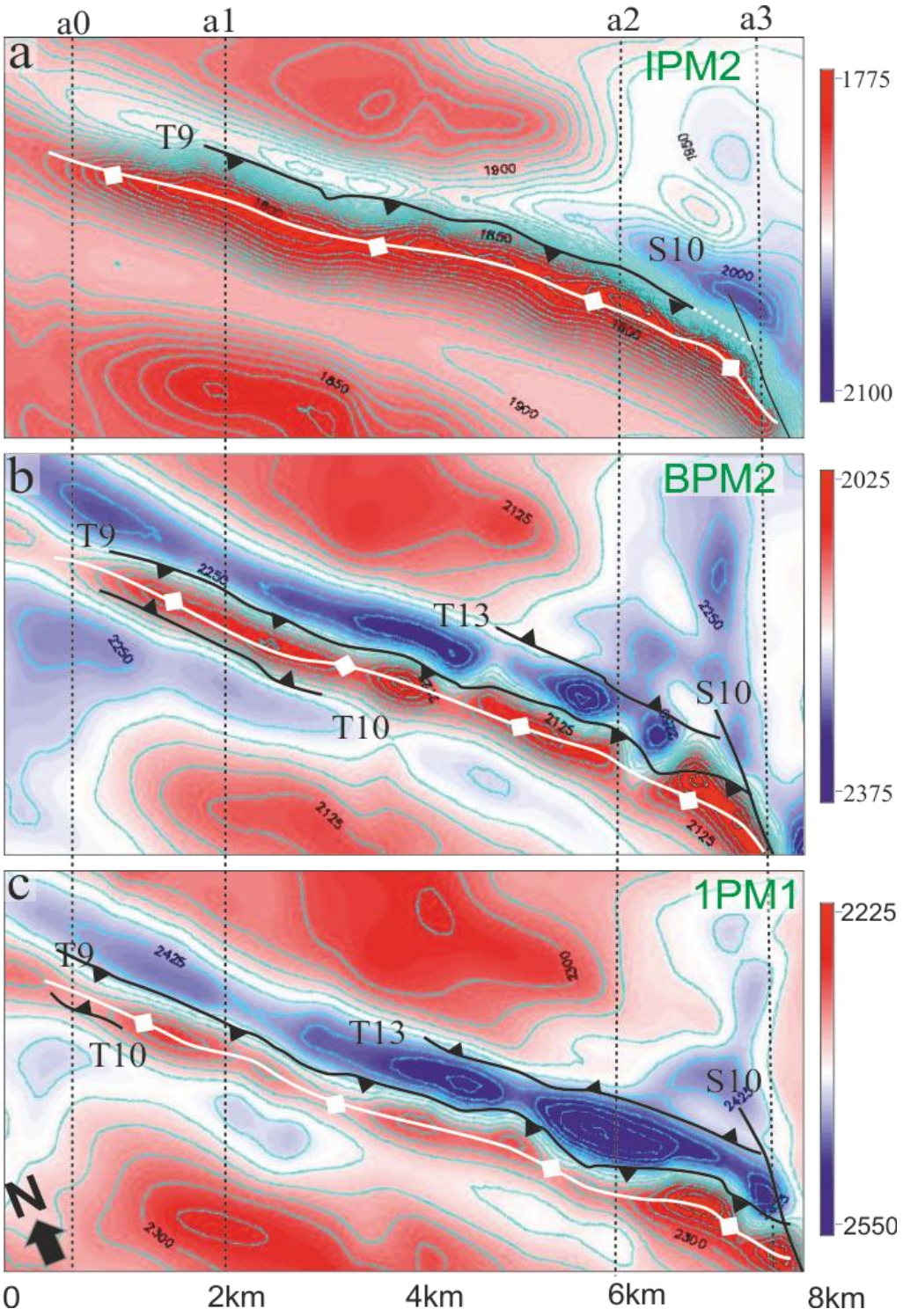


Figure 4.11: Maps of horizon elevation in TWT (ms). (A) Horizon IPM2 (B) Horizon BPM2 (C) Horizon IPM1. Traces of faults in structure A: thrust faults T9, T10, and T13 and strike slip fault S10. Thrust fault trace is denoted by black triangles in the hangingwalls, with white broken lines represents zone where resolution is too poor to map. Lines a0- a3 show locations of the 4 sections in Figure 4.12. Red colour represents structural high. Blue colour represents structural low. Contour interval: 25ms.

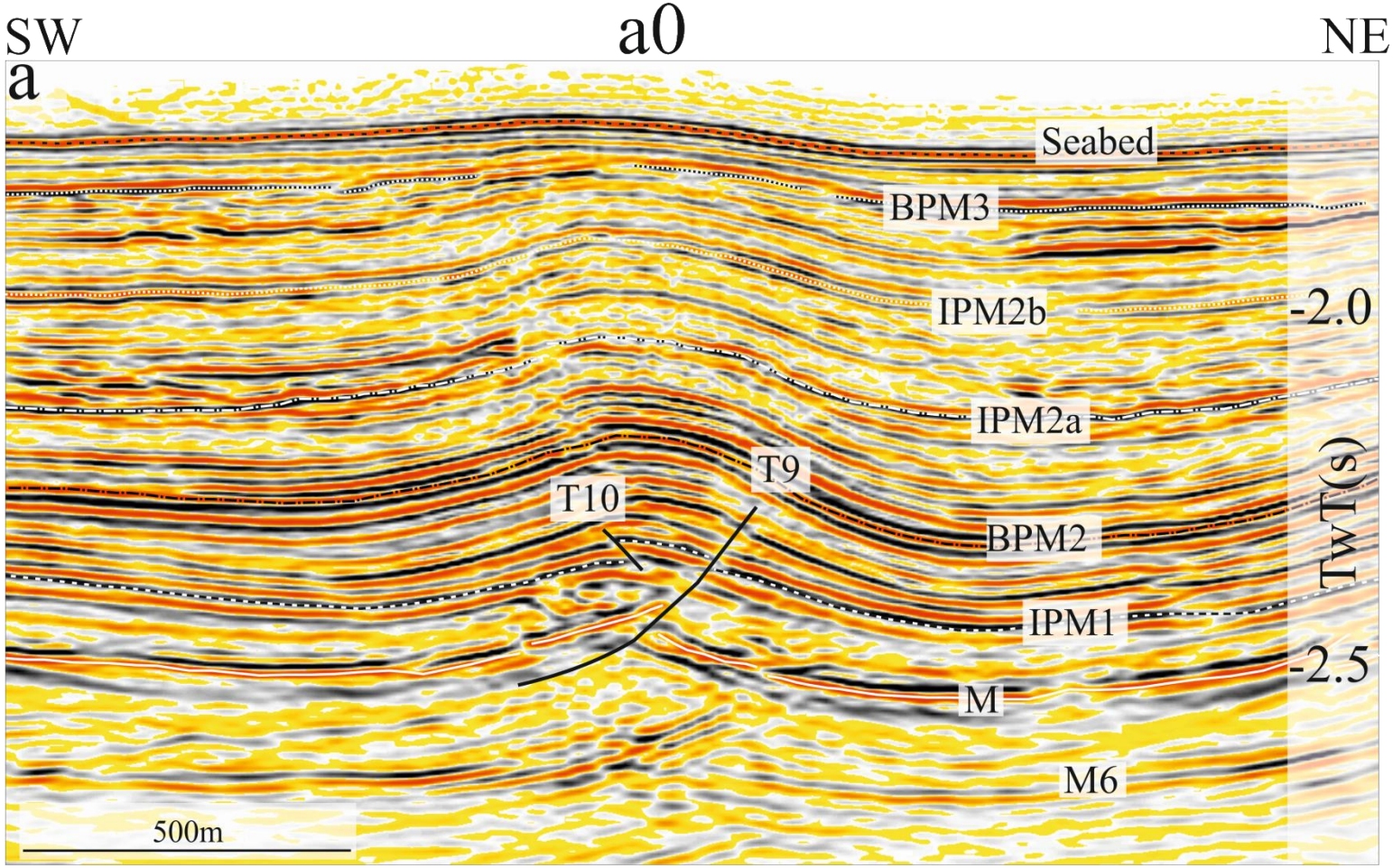


Figure 4.12: ( a-d). Selected seismic sections perpendicular to structure A illustrating along strike changes in fold and fault shape, and magnitude. Locations of seismic lines (a-d) in Figure 4.11. (e) is the zoomed version of the detachment zone from Figure 4.12 c, T0 (0.5s), T1 (0.8s) and T2 (0.14s) represent thickness of detachment zone (M50-Mx) in two way travel time. Sections have an approximate vertical exaggeration of 1:1.5. Horizons M6, M, IPM1, IPM2a, IPM2, and BPM3 are regional stratigraphic horizons.

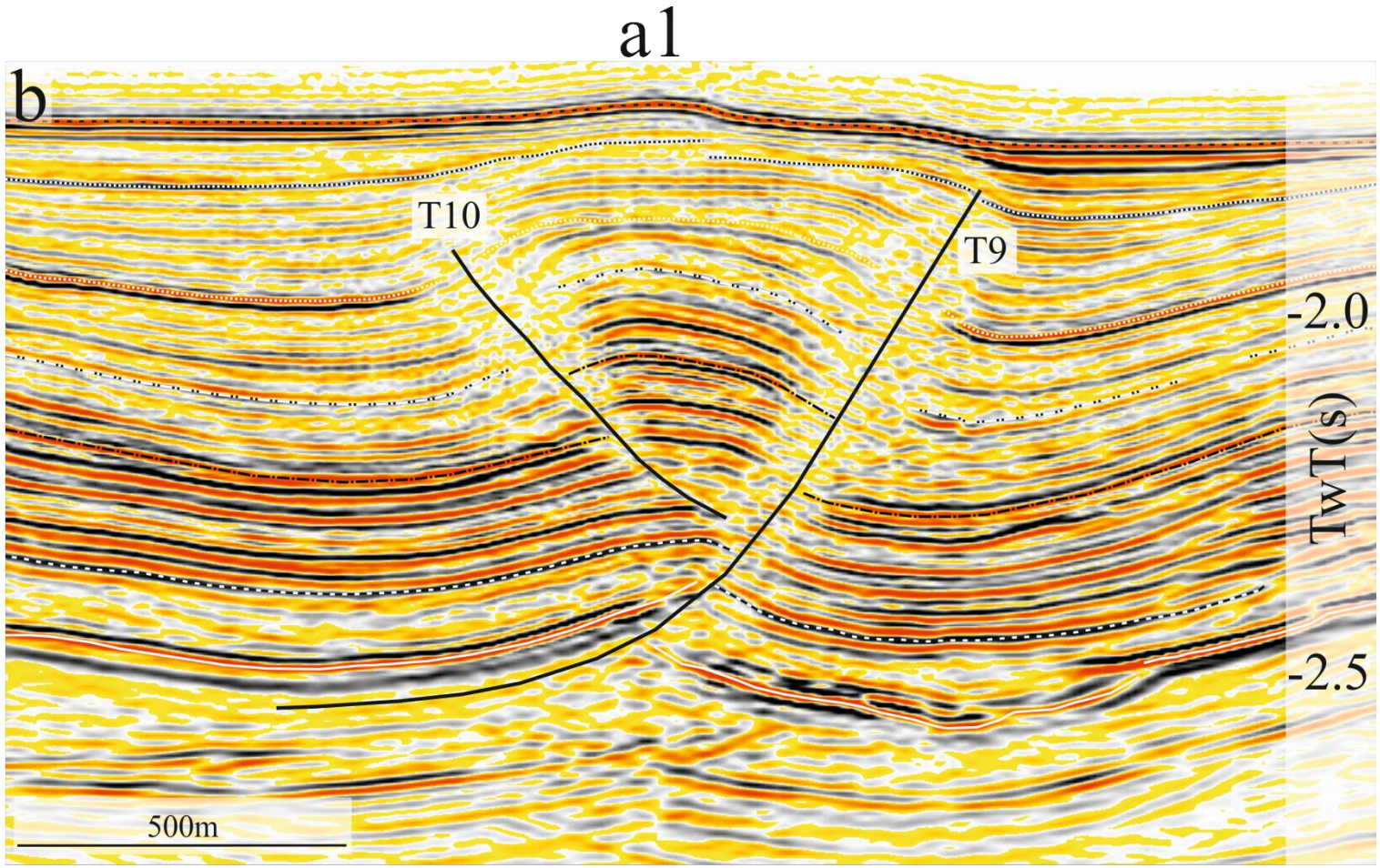


Figure 4.12: ( a-d). Selected seismic sections perpendicular to structure A illustrating along strike changes in fold and fault shape, and magnitude. Locations of seismic lines (a-d) in Figure 4.11. (e) is the zoomed version of the detachment zone from Figure 4.12 c, T0 (0.5s), T1 (0.8s) and T2 (0.14s) represent thickness of detachment zone (M50-Mx) in two way travel time. Sections have an approximate vertical exaggeration of 1:1.5. Horizons M6, M, IPM1, IPM2a, IPM2, and BPM3 are regional stratigraphic horizons.

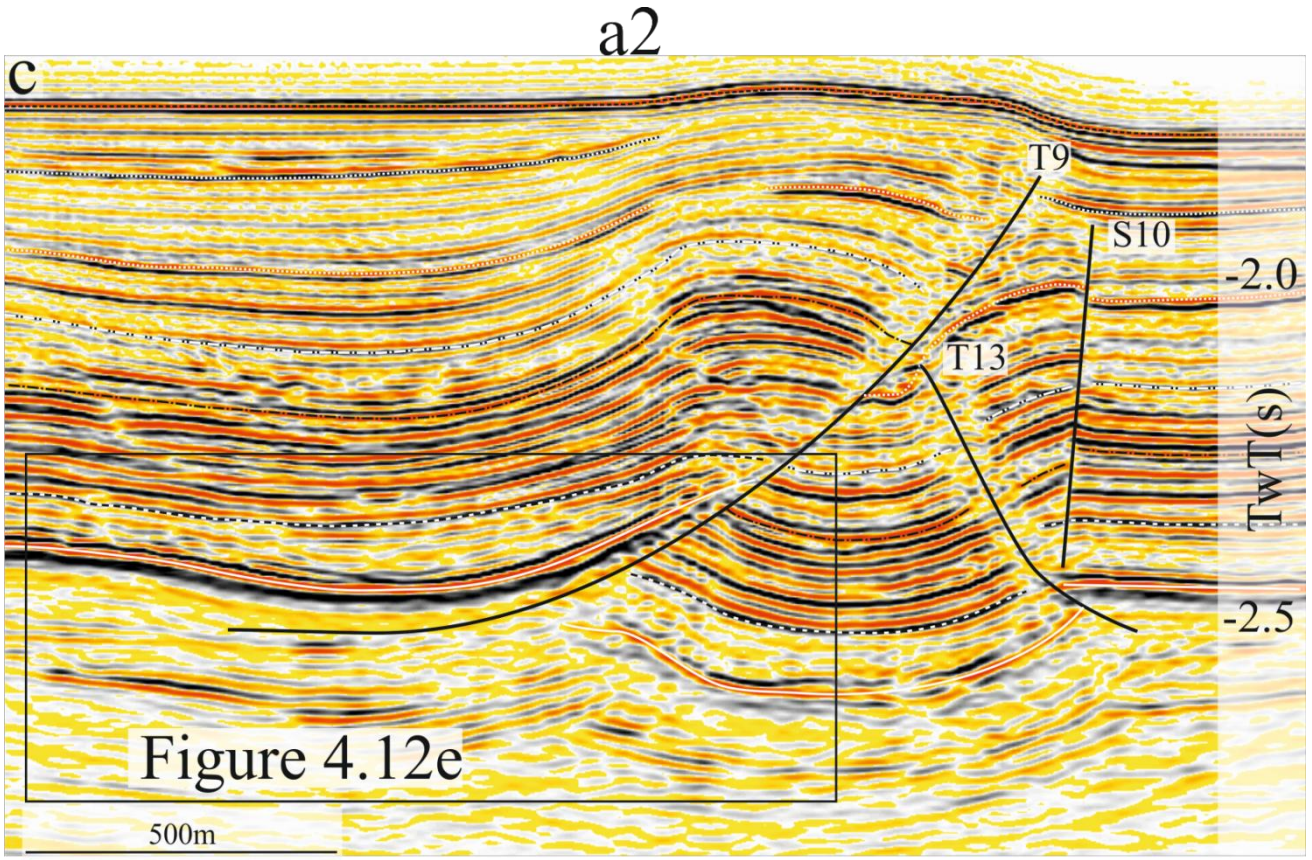


Figure 4.12: ( a-d). Selected seismic sections perpendicular to structure A, illustrating along strike changes in fold and fault shape, and magnitude. Locations of seismic lines (a-d) in Figure 4.11. (e) is the zoomed version of the detachment zone from Figure 4.12 c, T0 (0.5s), T1 (0.8s) and T2 (0.14s) represent thickness of detachment zone (M50-Mx) in two way travel time. Sections have an approximate vertical exaggeration of 1:1.5. Horizons M6, M, IPM1, IPM2a, IPM2, and BPM3 are regional stratigraphic horizons.

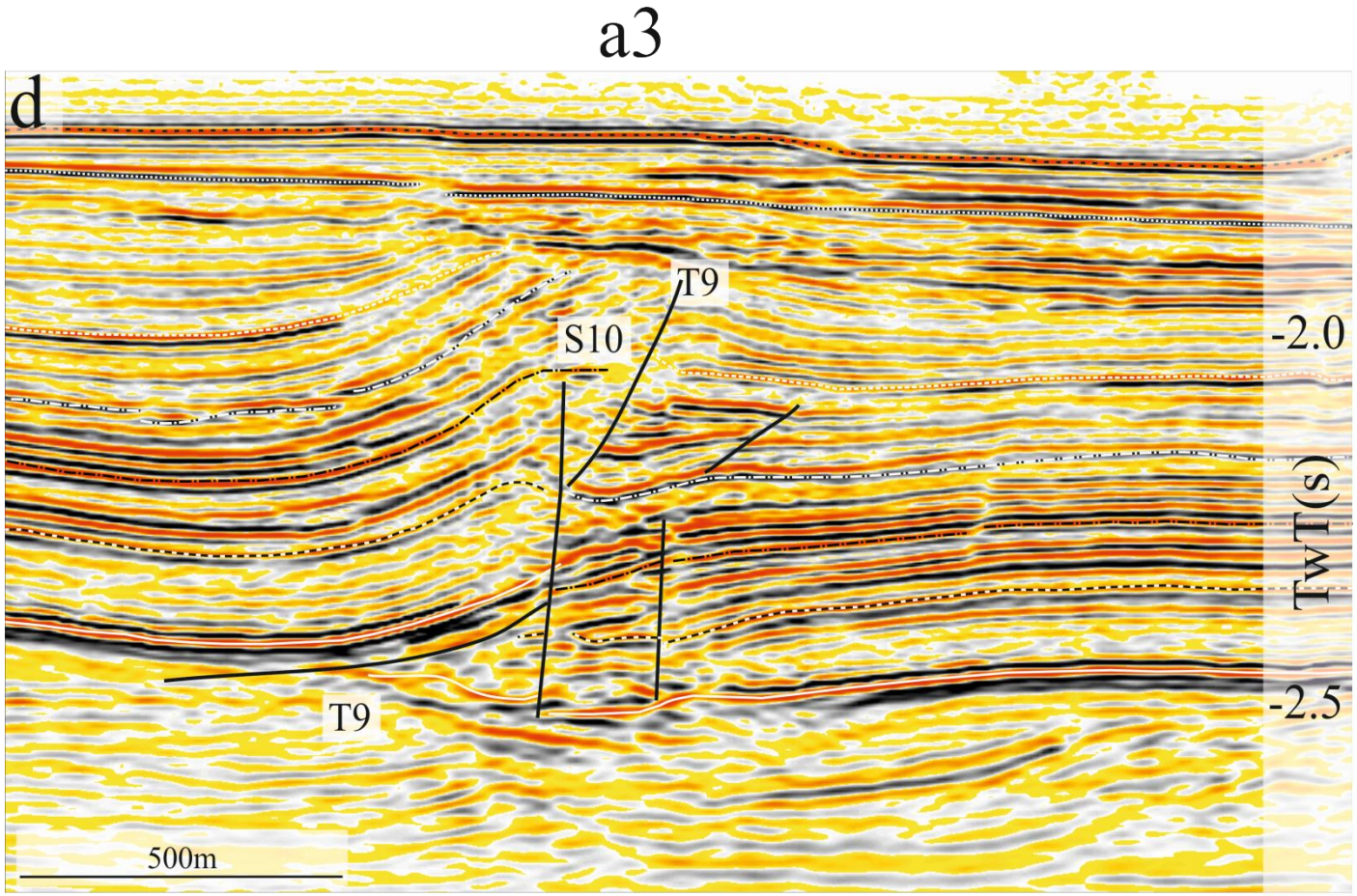


Figure 4.121: ( a-d). Selected seismic sections perpendicular to structure A, illustrating along strike changes in fold and fault shape, and magnitude. Locations of seismic lines (a-d) in Figure 4.11. (e) is the zoomed version of the detachment zone from Figure 4.12 c, T0 (0.5s), T1 (0.8s) and T2 (0.14s) represent thickness of detachment zone (M50-Mx) in two way travel time. Sections have an approximate vertical exaggeration of 1:1.5. Horizons M6, M, IPM1, IPM2a, IPM2, and BPM3 are regional stratigraphic horizons.

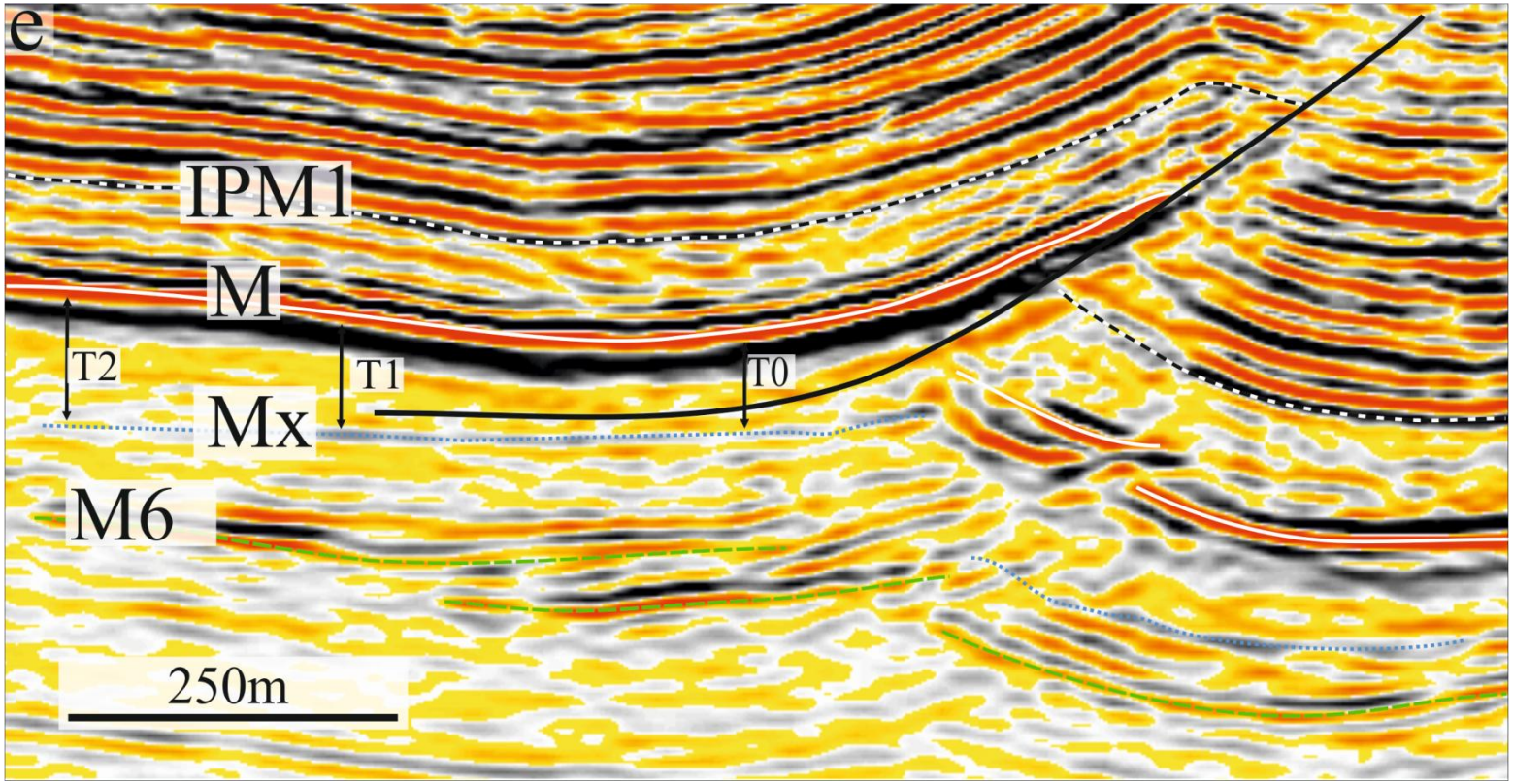


Figure 4.12: ( a-d). Selected seismic sections perpendicular to Structure A, illustrating along the strike changes in fold and fault shape, and magnitude. Locations of seismic lines (a-d) in Figure 4.11. (e) is the zoomed version of the detachment zone from Figure 4.12 c, T0 (0.5s), T1 (0.8s) and T2 (0.14s) represent thickness of detachment zone (M50-Mx) in two way travel time. Sections have an approximate vertical exaggeration of 1:1.5. Horizons M6, M, IPM1, IPM2a, IPM2, and BPM3 are regional stratigraphic horizons.

Fault T10 is one of the few faults which is neither bounded nor intersected by strike-slip faults in the study area (Figure 4.4, and 4.10). It overlaps the principal fault (T9) and dips c. $35^{o}$ towards it, forming a convergent zone (Morley et al. 1990). This convergent zone extends from 400 m to 2,200 m along the fold lateral length (Figure 4.11). T10 is arcuate in map view, mainly striking c. $133^{o}$ and has a maximum length of c. 2100 m it decreases both upward and downward (Figure 4.11).

Fault T13 is another fault within the fold which intersects S10 at its south eastern end (Figure 4.11). It does exhibit maximum displacement towards the intersection zone comparable to that of T9 (see Figure 5.12 in Chapter 5). It has a maximum displacement of c. 65 m at its central zone which decreases at both sides. Its along strike length is c. 3,000 m at Horizon IPM1 which makes D.max/L= 0.02. It strikes c. $130^{o}$ and dips c. $39^{o}$NE away from T9, defining an antithetic divergence zone (Morley et al. 1990) (Figure 4.12 c). The divergent zone is mainly symmetric and it extends from 4,000 to 8,000 m, where the zone intersects S10. T13 is listric and it detaches within the top of the Messinian evaporate, where it decreases asymptotically. Its zone of detachment shows no significant variation in thickness as that of T9 (Figure 4.12d).

**Structure B**

This structure is also made up of good examples of Type B thrust fault and fold pairs (Figure 4.13 and 4.14). T17 and T18 are oppositely dipping thrust fault anticlines, with maximum amplitudes of c. 240 m and c. 260 m respectively, measured along Horizon IPM1. These anticlines are separated by a syncline which broadens down dip. T19 is a minor thrust fault dipping oppositely towards T17 forming a local convergent zone in the north-western region of the structure B (4.13b, c and 4.14 b). These folds individually have maximum amplitudes ranging from 200 m to 250 m along Horizon IPM1.

Map view shows that they are linear to arcuate in geometry and are bounded and intersected by strike-slip faults with different senses of shear. Maps show that the traces of the intersection zones are characterized by closely spaced contour lines which indicate a very steep gradient caused by intense deformation (Figure 4.13).

T17 is intersected at its north-western and south eastern ends by a dextral fault (S10) striking c. 010$^{o}$ and a sinistral fault (S20) striking c. 078$^{o}$,respectively (Figure 4.13 a). These obliquely trending strike-slip faults (S10 and S20) define the lateral extent of T17, which was measured to be c. 5,000 m along Horizon IPM1. T17 is also intersected by another sinistral fault (S16) striking c. 080$^{o}$ at c. 4,400 m. At this zone of intersection with S16, T17 has its upper tip below Horizon IPM2, but it cuts through Horizon IPM2 at both lateral ends close to where it intersects S10 and S20, in such a way that it appears as two separate fault segments along IPM2. T17 strikes 148$^{o}$ towards both lateral ends but changes to c. 178$^{o}$ at c. 4,000 m, close to where it intersects S16 (Figure 4.13 b and c).

Seismic sections perpendicular to the structure shows that the hangingwall of T17 is mainly symmetric, but tends to be asymmetric with a westward vergence between 2,500 m and 3,800 m of the structure length (Figure 4.13 and 4.14 b). Fault T17 cross-cuts S10 at the north western intersection zone without any notable change in dip. Whereas, where it intersects S20, it is characterized by considerable loss in seismic amplitude (Figure 4.14 e). At this zone of intersection (c. 6,700 m), only Horizon IPM1 was mapped with confidence. Although, traces of mapable stratal discontinuities were observed at c. 6,100 m. T17 is curvi-planar dipping c. 38$^{o}$ at the central zone, which becomes steeper (reaching a dip angle of c. 50$^{o}$) at the north-western intersection zone. It is clear that the Upper Messinian unit is the point where it becomes layer parallel (i.e the zone where it detaches). The zone of detachment does not show any significant thickness variation as that of T9 (Figure 4.14 b).

Displacement increases from the central zone (c. 4,000 m) of minimum displacement towards both lateral ends where it intersects strike slip faults. It has a maximum displacement of c. 512 m measured at c. 2,500 m along Horizon IPM1, this makes D.max/L=0.1.

Fault T18 dips oppositely away from T17 and it forms intersection zones at its central zone and southern tip with S16 and S20, respectively, but free from strike-slip fault at its northern end (Figure 4.13). It extends c. 4,700 m along Horizon IPM1 and striking c. $150^{o}$ towards both lateral ends and changes in orientation to c. $178^{o}$ at 4.6km close to the central intersection zone (Figure 4.13 b and c). Similar to T17, it cuts through Horizon IPM2a towards both lateral ends where it intersects S10 and S20, but decreases in height below IPM2a as it approaches S16 between 3,200 m and 4,800 m respectively (Figure 4.13 and 4.14).

Sections along T18 (Figure 4.13), shows that it is curvi-plannar with variable dip along strike. It has a maximum apparent dip of c. $54^{o}$ close to S20, which decreases to c. $35^{o}$ towards mid-zone and increases towards its north-western end. It has a displacement less than c. 10 m close to the S16 intersection zone which increases towards both lateral ends (see Chapter 5). Its maximum displacement is c. 300 m, recorded close to the south-eastern lateral tip. This makes D.max/L= 0.06.

T18 becomes layer parallel with stratal reflections (detachment zone) at 2 main subunits along strike which includes the unit between Horizons M and IPM1 (Figure 4.14 a), and M and Mx (Figure 4.14 d and f). The upper detachment zone (M and IPM1) does not show significant change in thickness towards the fault surface (Figure 4.14). The lower detachment zone which is at the upper Messinian unit (M and Mx), displays an increase in thickness towards the detachment zone (Figure 4.14 f), as opposed to that of T9.

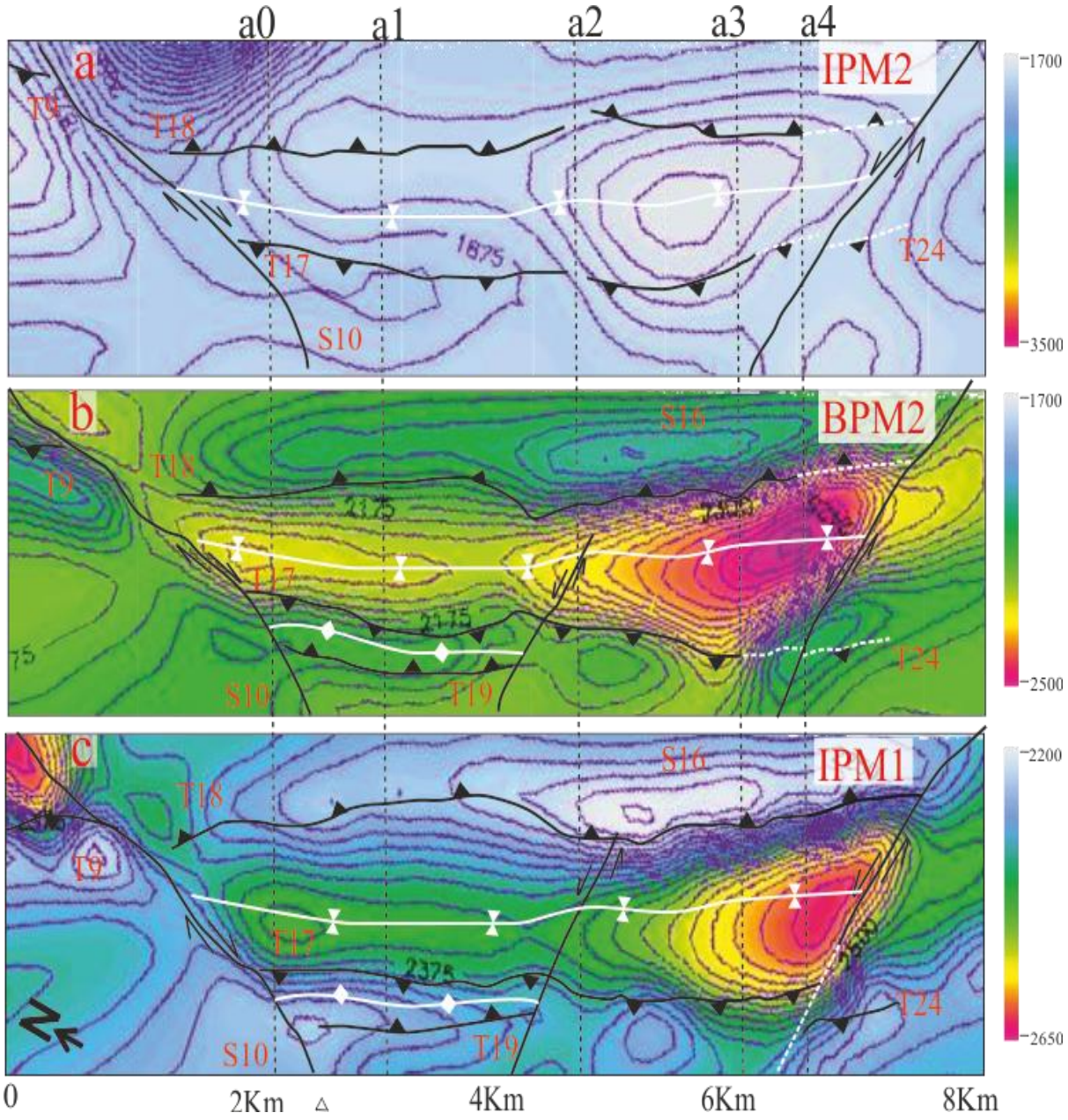


Figure 4.13: Maps of horizon elevation in TWT (ms). (A) Horizon IPM2 (B) Horizon BPM2 (C) Horizon IPM1. Traces of the faults in Structure B: thrust faults T17, T18, and T19, and strike slip fault S10, S16 and S20. White broken lines represent fault segments not mappable due to poor resolution. Lines a0- a4 show locations of the 4 seismic sections in Figure 4.11. Red/yellow colour represents structural low. Blue/green colour represents structural high. Contour interval: 25ms.

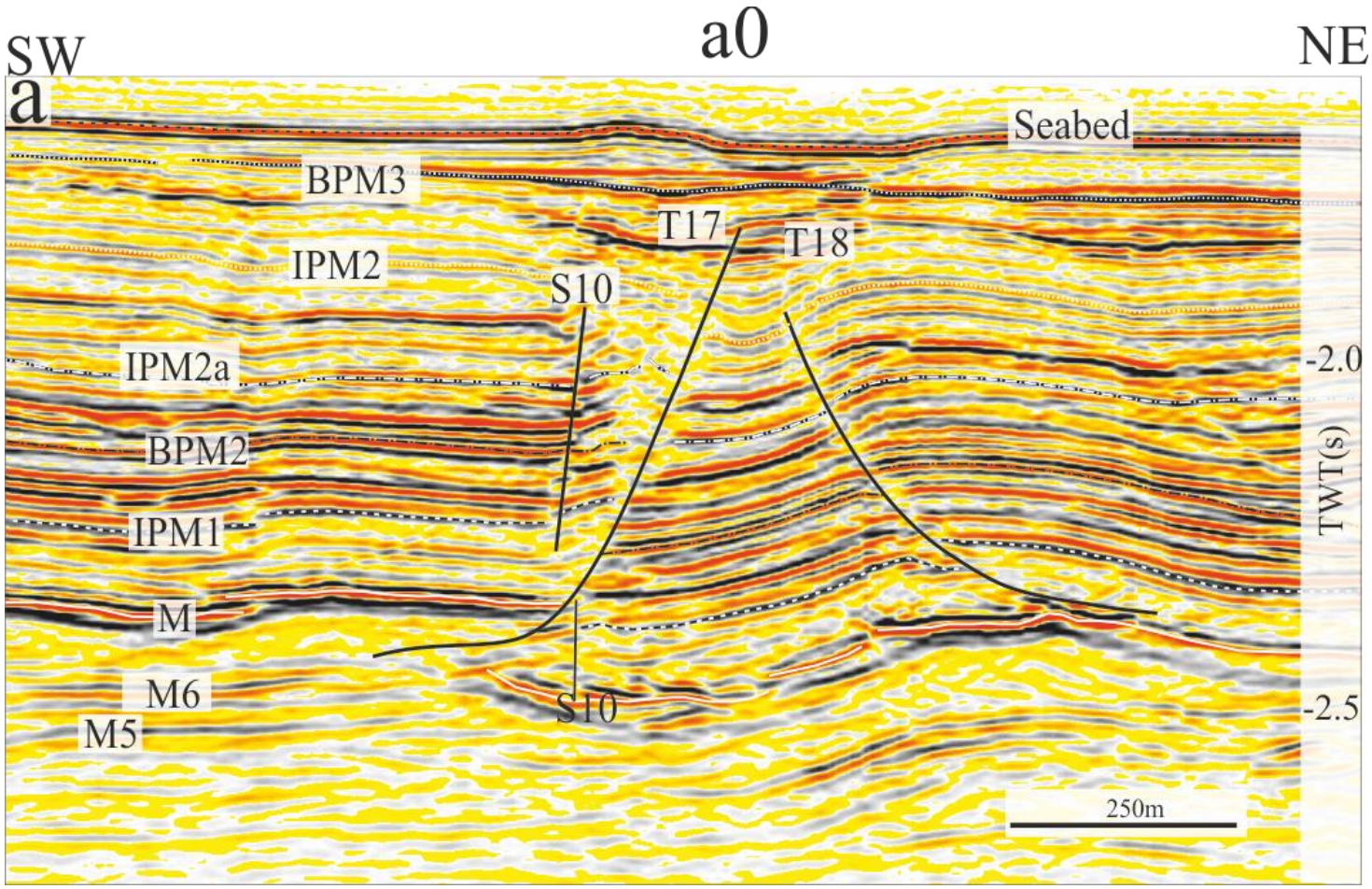


Figure 4.14: (a-e). Selected seismic sections perpendicular to Structure B, illustrating the along strike changes in fold and fault shape, and magnitude. Locations of seismic lines (a-e) in Figure 4.13, (f) is the zoomed version of the detachment zone from Figure 4.14 d, T0 (0.5s), T1 (0.8s) and T2 (0.14s) represent thickness of detachment zone (M - Mx) in two way travel time. Sections have an approximate vertical exaggeration of 1:1.5. Horizons M6, M, IPM1, IPM2a, IPM2, BPM3 are regional stratigraphic horizons.

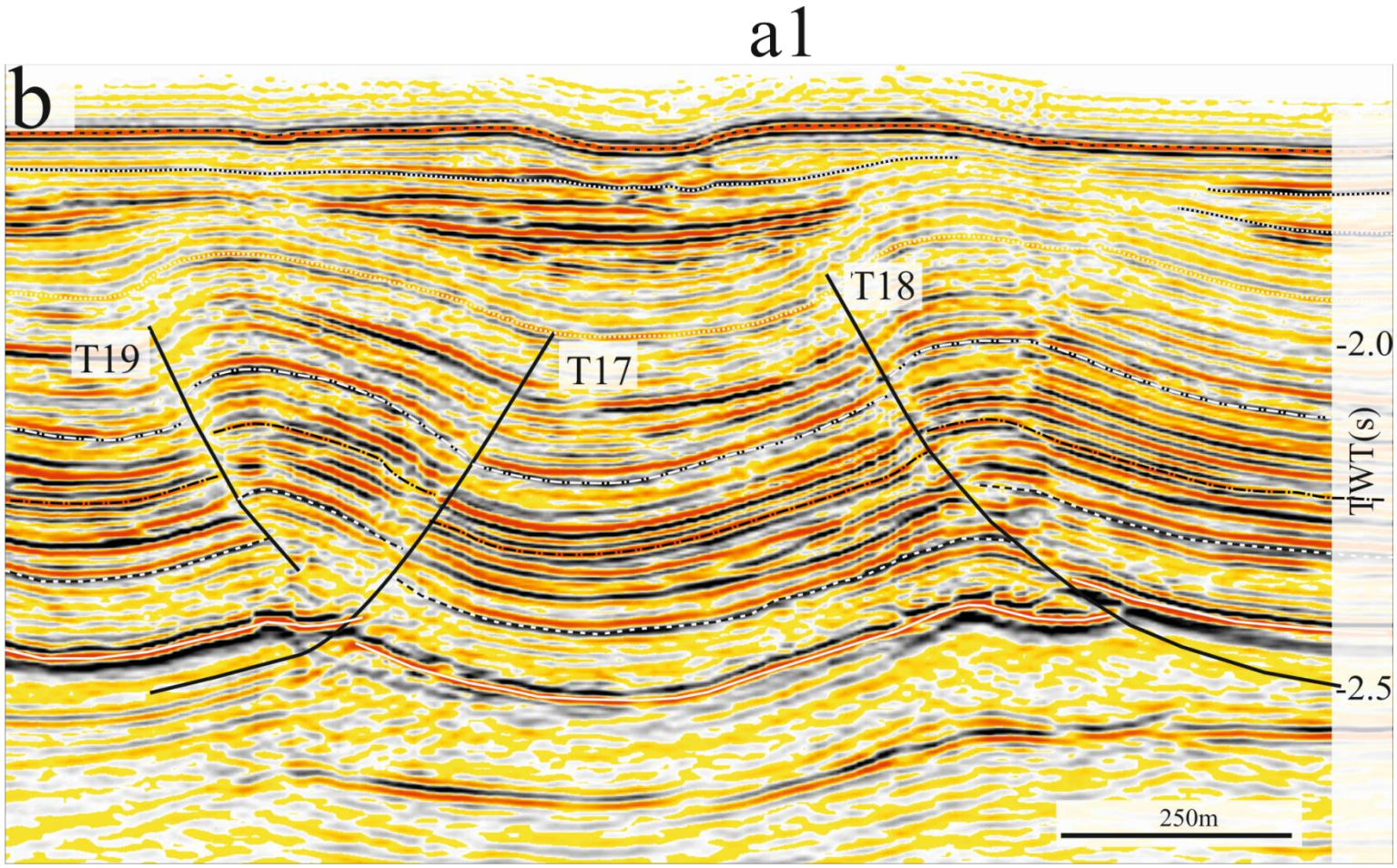


Figure 4.14: (a-e). Selected seismic sections perpendicular to Structure B, illustrating the along strike changes in fold and fault shape, and magnitude. Locations of seismic lines (a-e) in Figure 4.13, (f) is the zoomed version of the detachment zone from Figure 4.14 d, T0 (0.5s), T1 (0.8s) and T2 (0.14s) represent thickness of detachment zone (M - Mx) in two way travel time. Sections have an approximate vertical exaggeration of 1:1.5. Horizons M6, M, IPM1, IPM2a, IPM2, BPM3 are regional stratigraphic horizons.

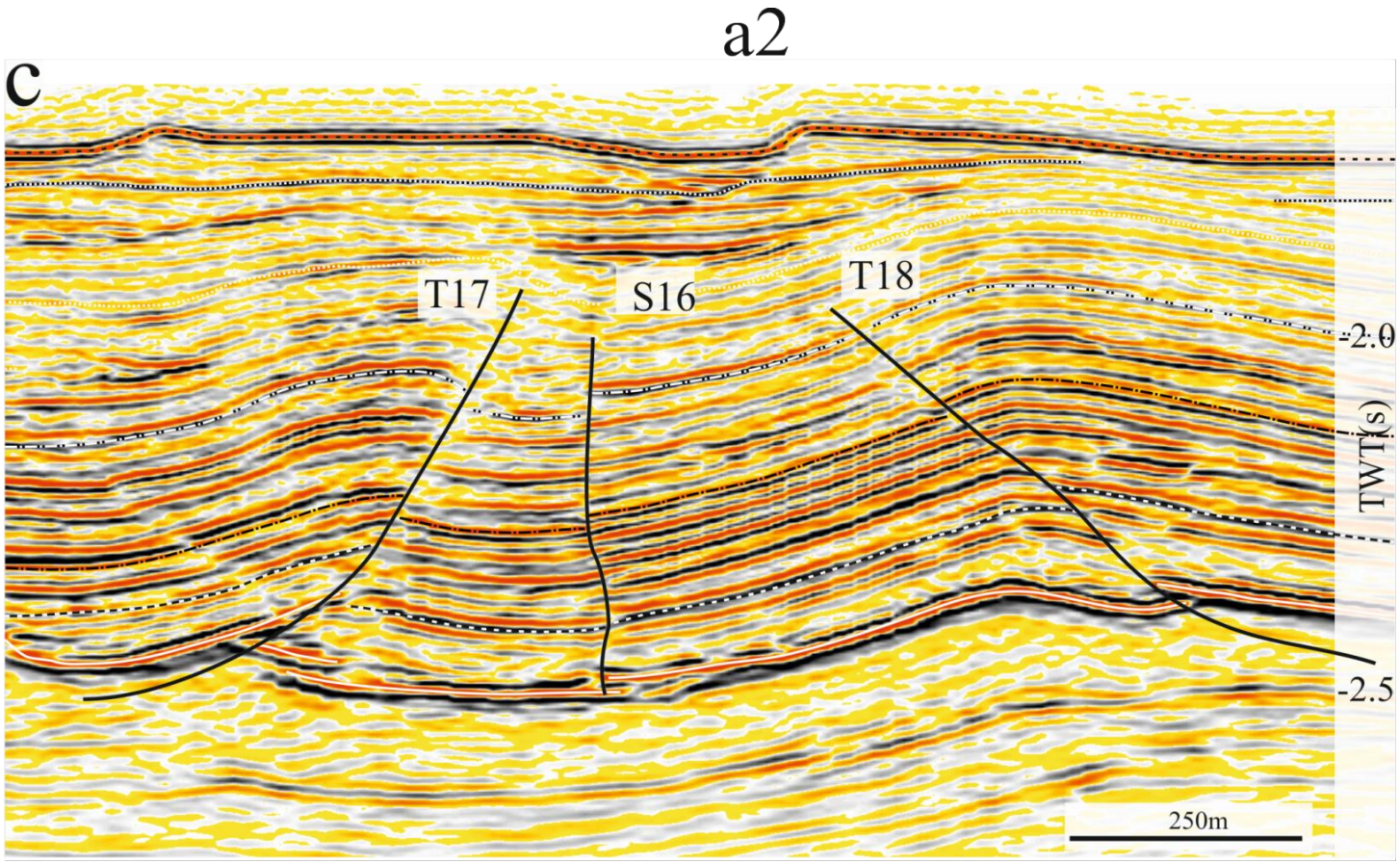


Figure 4.14: (a-e). Selected seismic sections perpendicular to Structure B, illustrating the along strike changes in fold and fault shape, and magnitude. Locations of seismic lines (a-e) in Figure 4.13, (f) is the zoomed version of the detachment zone from Figure 4.14 d, T0 (0.5s), T1 (0.8s) and T2 (0.14s) represent thickness of detachment zone (M - Mx) in two way travel time. Sections have an approximate vertical exaggeration of 1:1.5. Horizons M6, M, IPM1, IPM2a, IPM2, BPM3 are regional stratigraphic horizons.

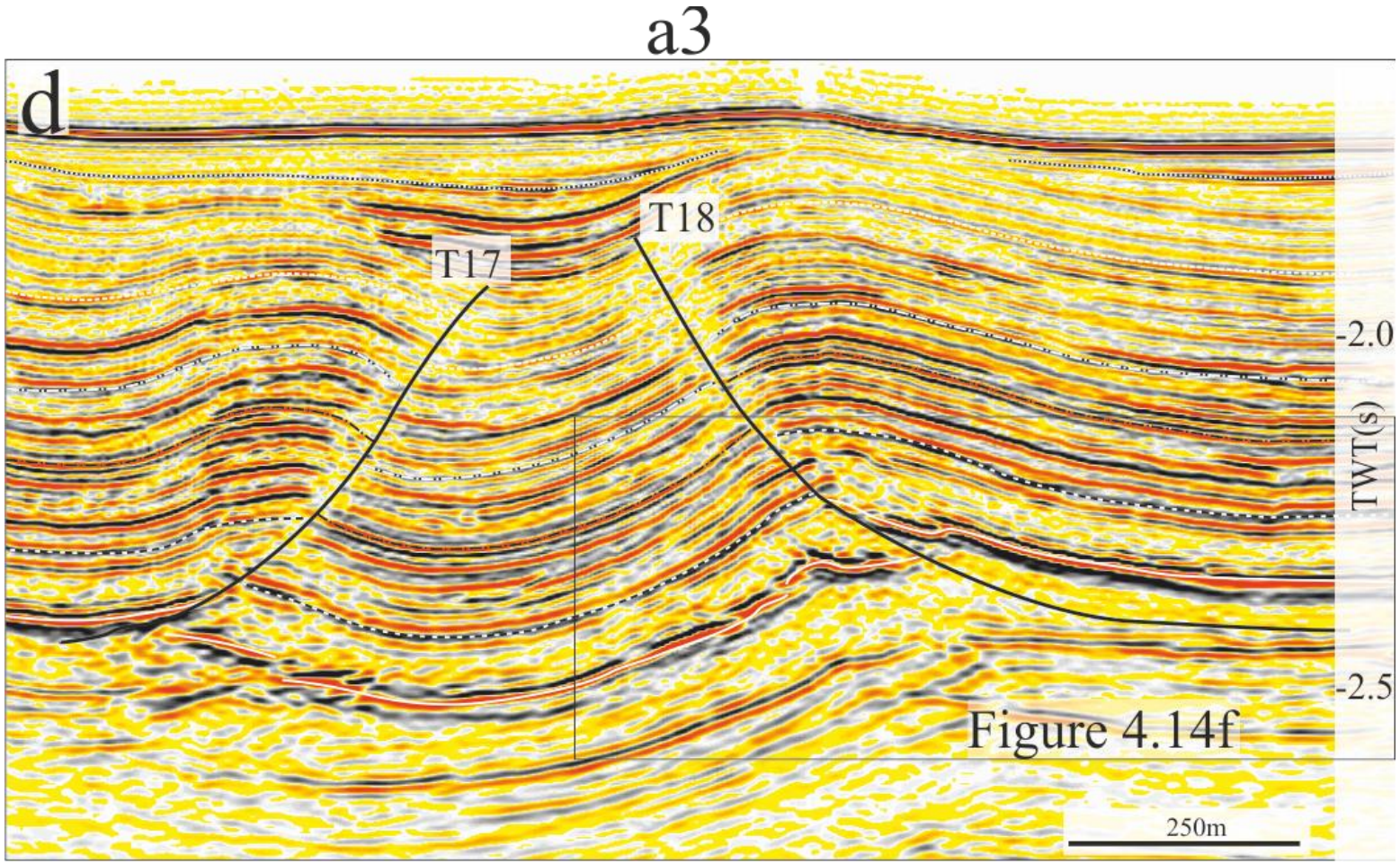


Figure 4.14: (a-e). Selected seismic sections perpendicular to Structure B, illustrating the along strike changes in fold and fault shape, and magnitude. Locations of seismic lines (a-e) in Figure 4.13, (f) is the zoomed version of the detachment zone from Figure 4.14 d, T0 (0.5s), T1 (0.8s) and T2 (0.14s) represent thickness of detachment zone (M - Mx) in two way travel time. Sections have an approximate vertical exaggeration of 1:1.5. Horizons M6, M, IPM1, IPM2a, IPM2, BPM3 are regional stratigraphic horizons.

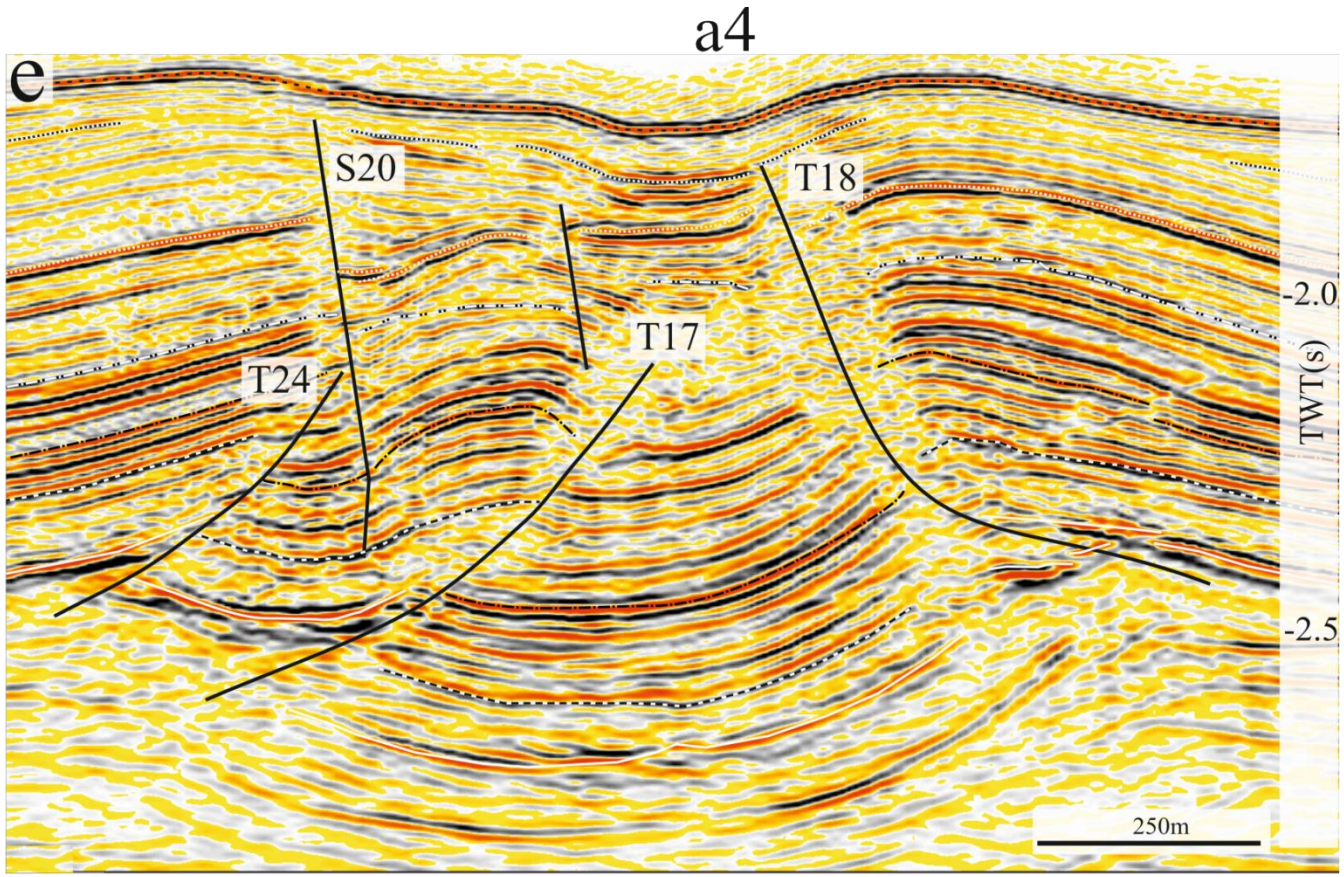


Figure 4.14: (a-e). Selected seismic sections perpendicular to Structure B, illustrating the along strike changes in fold and fault shape, and magnitude. Locations of seismic lines (a-e) in Figure 4.13, (f) is the zoomed version of the detachment zone from Figure 4.14 d, T0 (0.5s), T1 (0.8s) and T2 (0.14s) represent thickness of detachment zone (M - Mx) in two way travel time. Sections have an approximate vertical exaggeration of 1:1.5. Horizons M6, M, IPM1, IPM2a, IPM2, BPM3 are regional stratigraphic horizons.

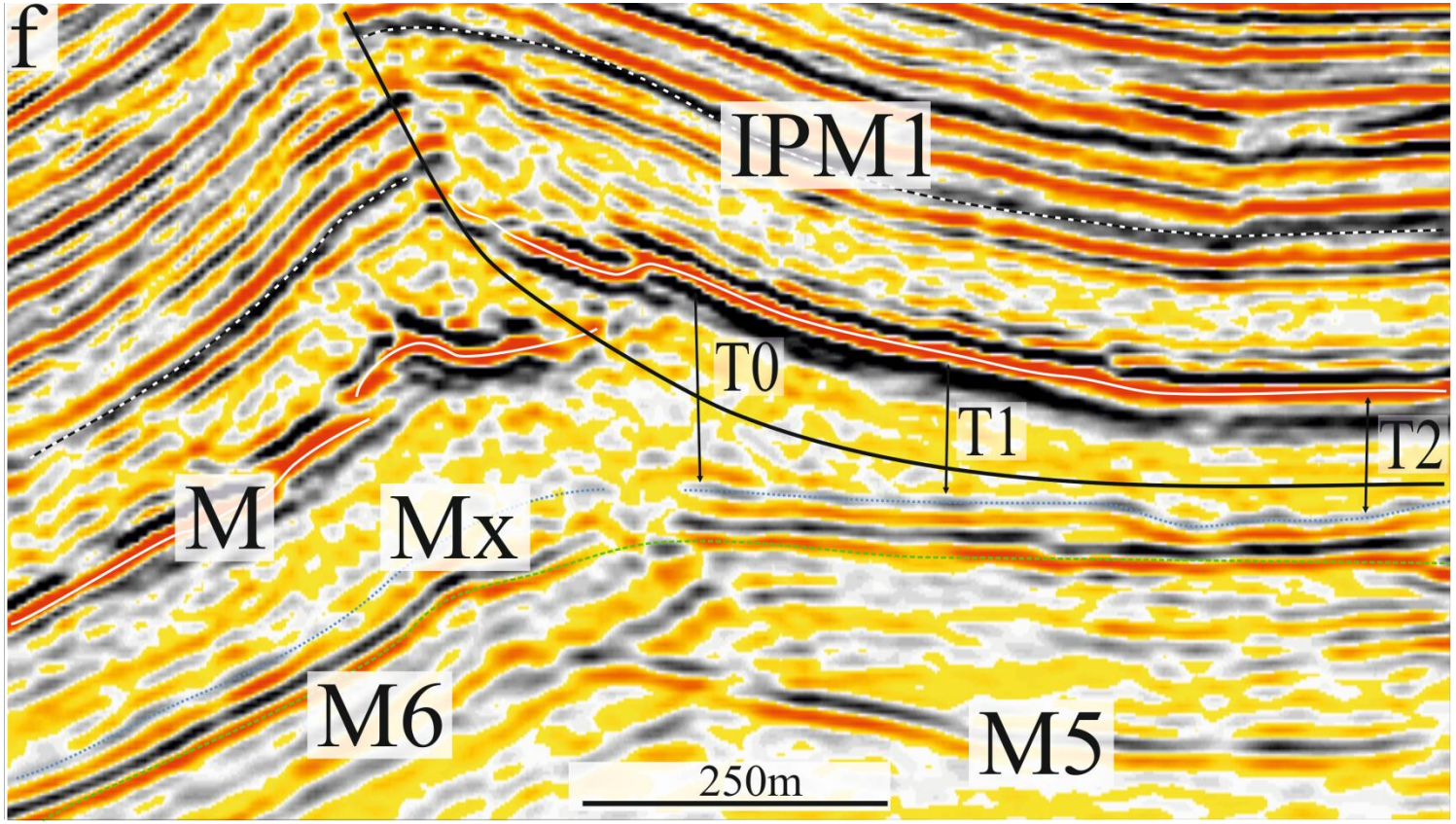


Figure 4.14: (a-e). Selected seismic sections perpendicular to Structure B, illustrating the along strike changes in fold and fault shape, and magnitude. Locations of seismic lines (a-e) in Figure 4.13, (f) is the zoomed version of the detachment zone from Figure 4.14 d, T0 (0.5s), T1 (0.8s) and T2 (0.14s) represent thickness of detachment zone (M - Mx) in two way travel time. Sections have an approximate vertical exaggeration of 1:1.5. Horizons M6, M, IPM1, IPM2a, IPM2, BPM3 are regional stratigraphic horizons.

Fault T19 is a minor thrust fault at the hanging wall of T17, dipping ($40^{o}$NE) oppositely towards it, forming a local asymmetric anticline (T17, Figure 4.13 and 4.14 b). It mainly detaches at the unit between Horizon M and IPM1 (Figure 4.14 b). It is arcuate in map view, striking $155^{o}$ and $125^{o}$ towards its north-western and south-eastern end respectively. The south-eastern end is intersected by S16 while the north-western end is intersected by S10 along Horizon IPM2a (Figure 4.13). This south eastern lateral tip of T19, appears to be isolated from strike slip fault along IPM1, indicating decreases along strike down dip. T19 has a length of c. 1,900 m measured from where it intersects S10 and S16 along Horizon IPM2a and maximum displacement of c.180 m (in IPM2a), which makes D.max/L=0.09.

The syncline separating T17 and T18 increases in wavelength downward towards where the divergent thrust faults (T17 and T18) detaches, and it has maximum amplitude of 200 m measured close to the SE intersection zone along Horizon IPM1. The syncline is mainly symmetric but tends have a north-eastern vergence close to the south-eastern end of the thrust faults.

The syncline appears to be highly deformed by small faults close to where it intersects S20 between 6,300 -7,500 m (Figure 4.14 e). At this zone of intersection, the synclinal structure appears to be steeply pushed down into the salt sequence by more intensely fractured stratigraphic sequence (Figure 4.14 e). This zone is characterized by poor seismic resolution which impairs reflection continuity and makes it difficult to correlate across faults.

### 4.2.4 Strike Slip Faults

Strike-slip faults in the study area show a wide variation in length from tens to thousands of metres (Figure 4.2, 4.4 and 4.15). Mapping and coherent attributes reveal that the smaller strike slip faults are almost linear while the larger ones vary from linear to arcuate to sinusoidal in geometry.

The strike slip faults in the study area strike in two dominant orientations, 030$^{o}$ and 110$^{o}$ (Figure 4.4 and 4.15). Kinematic indicators shows that majority of those striking 030$^{o}$ are dextral faults while those striking 110$^{o}$ are sinistral faults; both of which can show considerable change in orientation along their width (Figure 4.15). The majority of these strike-slip faults are in conjugate sets, because they commonly intersect at an angle whose bisectrix (060$^{o}$) is almost orthogonal to the thrust folds (Figure 4.4 and 4.15).

The sense of shear and displacement of the strike slip faults are determined by segments of channels whose course may have been influenced by the topography of the area (Folkman and Mart 2008; Clark and Cartwright 2009) and segments of fold and thrust separation oblique to the strike-slip faults (Figure 4.15a). However, lateral displacements of the strike-slip faults fall within the range of 100-300m, measured from channel offset, and if fold separation is taken it ranges between 150 and 1800m (Figure 4.4b). The wide difference from both kinematic markers (channel and fold) leaves a question on the timing relationship and hence interaction between the folds and strike slip faults (see Chapter 5). Other kinematic marker such as restraining and releasing bends where also used to determine their sense of shear (Figure 4.15 a).

Large strike slip faults (lengthier than 6km) in the area are almost regularly distributed, while the small ones occur randomly within the dataset (Figure 4.15). Some of the strike slip faults laterally extend from highly deformed areas to zones less dominated by thrust faults and folds. The majority of the strike-slip faults located near the area where thrust faults persist are characterized by poor seismic section (Figure 4.15).

On seismic section, strike slip faults are interpreted as steeply dipping stratal reflection discontinuities, systematically aligned and characterized by low throw values (not more than 0.07s TWT, approximately 70m) (Figure 4.16). Strike-slip fault do not show a decrease in

dip close to detachment layers like thrust faults or normal faults (McClay and Ellis 1987; Briggs et al. 2006). In this study, the strike-slip fault's basal and upper tips are interpreted at regions where stratal reflections decrease to zero. Their basal tip mostly extends down to the upper units of the Messinian salt, but a few have their basal tip within unit PM1. Strike slip faults in Gal C range in height from 100 to 1500 m. Most of the faults have their upper tips just below the seabed, but some extend to the seafloor (Figure 4.16).

Isolated segments of the strike slip faults in the dataset are well imaged on seismic sections but the resolution tends to be limited in areas where they intersect other strike slip faults and thrust faults or where local step-overs or bends occur. Some of the strike slip faults are characterized by small scale contractional and extensional structures, which may have developed at zones of local transpression and transtension, respectively (Woodcock and Fischer 1986; Dooley and McClay 1997).

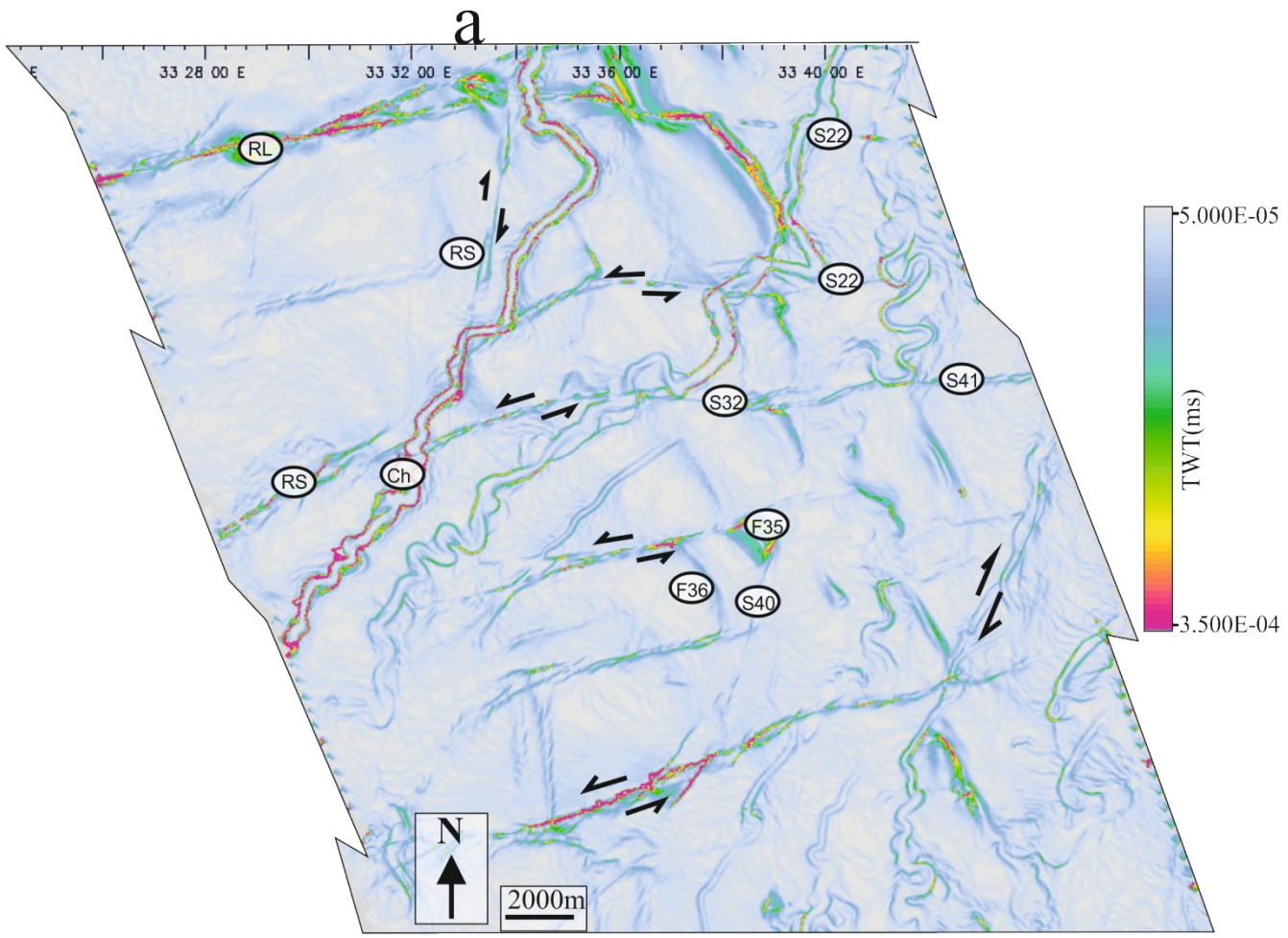


Figure 4.15: Time dips attribute maps of the central region of the Gal C survey. (a) Sea bed horizon showing kinematic indicators (releasing and restraining bends) on strike slip fault (b) Horizon BP3, (c) Horizon IPM1 showing case study representative example of strike slip fault (S40) and neighbouring faults. The faults are labelled as numbered in Figure 4.4b. RS- restraining bend, RL- Releasing bend, S- strike slip fault, T- thrust fault, F- fold.

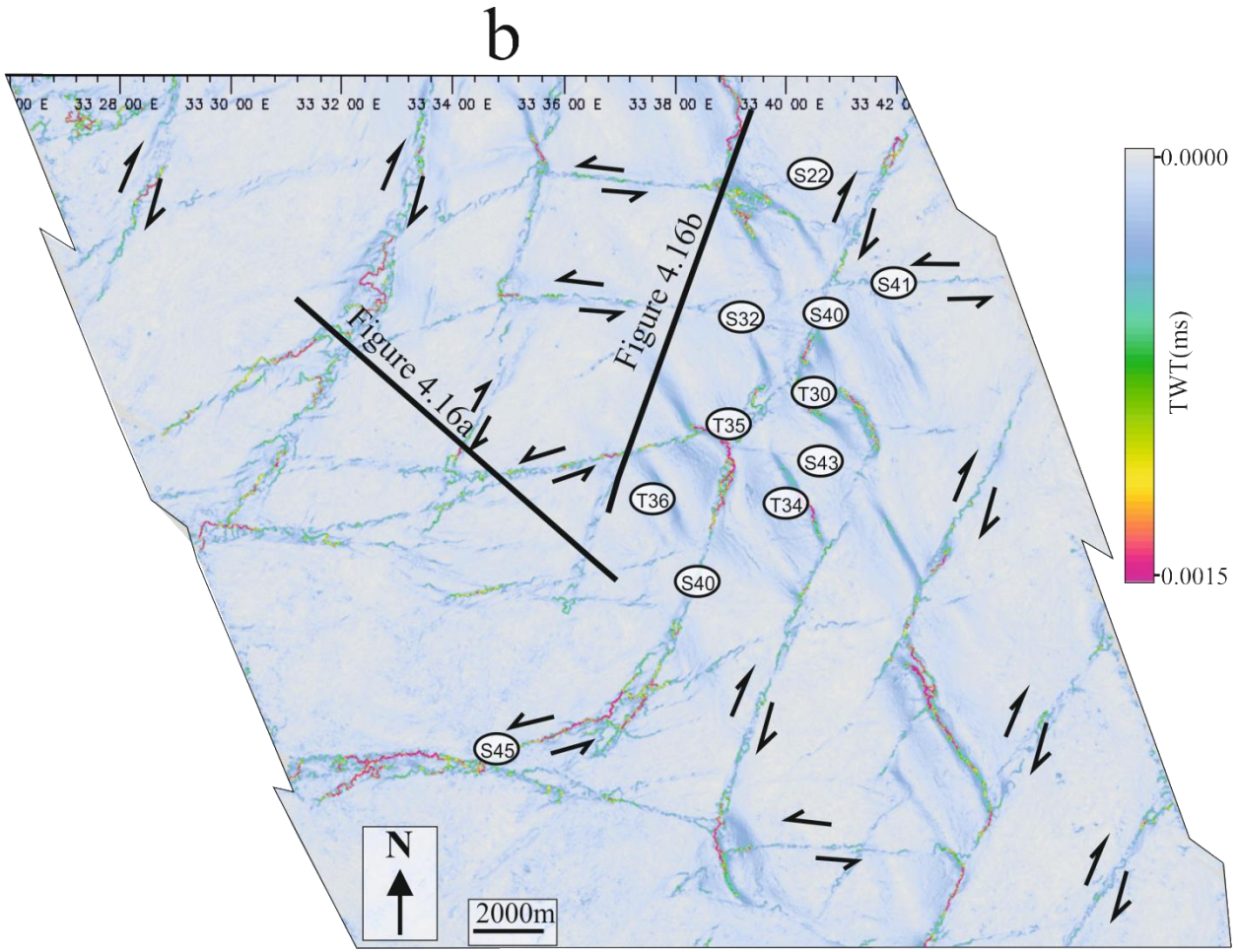


Figure 4.15: Time dips attribute maps of the central region of the Gal C survey. (a) Sea bed horizon showing kinematic indicators (releasing and restraining bends) on strike slip fault (b) Horizon BP3, (c) Horizon IPM1 showing case study representative example of strike slip fault (S40) and neighbouring faults. The faults are labelled as numbered in Figure 4.4b. RS- restraining bend, RL- Releasing bend, S- strike slip fault, T- thrust fault, F- fold.

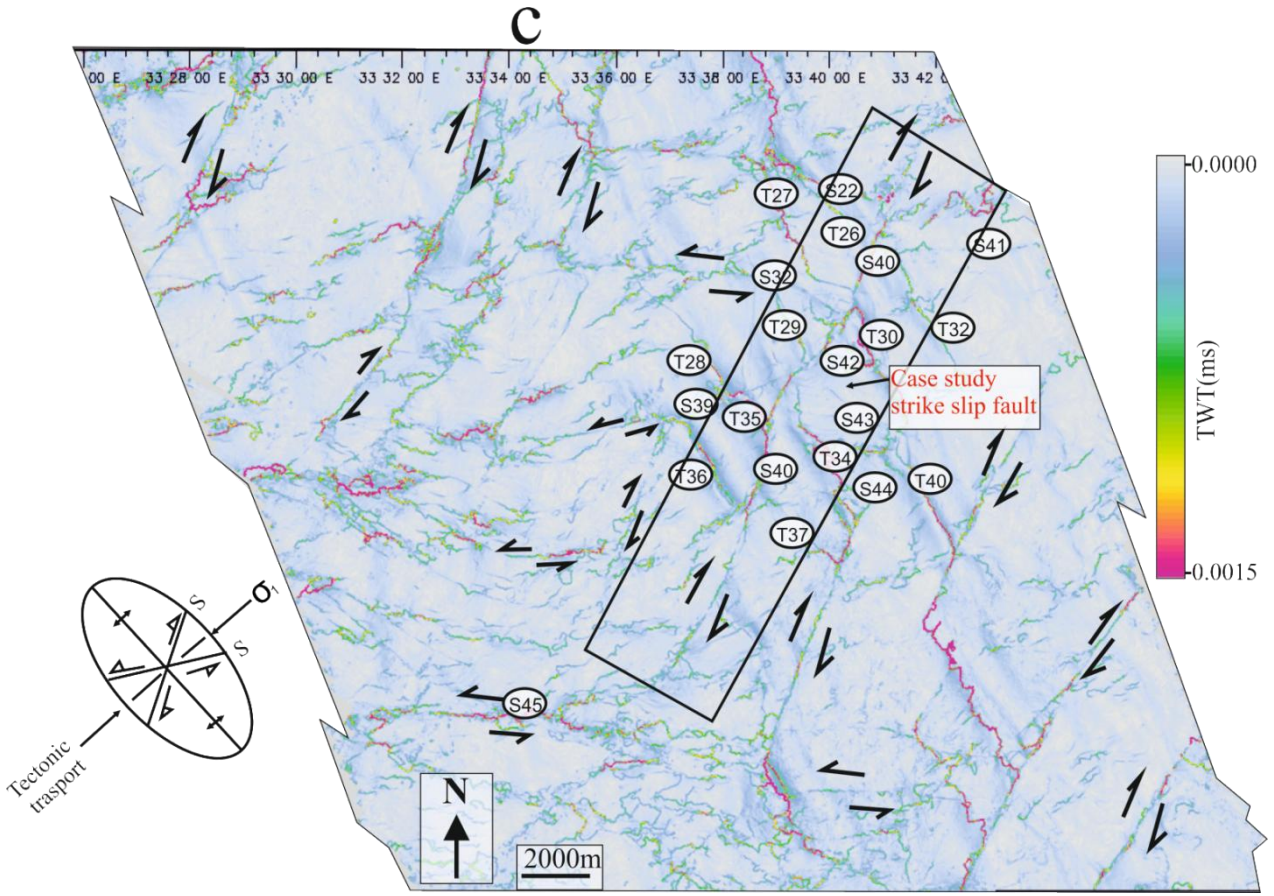


Figure 4.15: Time dips attribute maps of the central region of the Gal C survey. (a) Sea bed horizon showing kinematic indicators (releasing and restraining bends) on strike slip fault (b) Horizon BP3, (c) Horizon IPM1 showing case study representative example of strike slip fault (S40) and neighbouring faults. The faults are labelled as numbered in Figure 4.4b. RS- restraining bend, RL- Releasing bend, S- strike slip fault, T- thrust fault, F- fold.

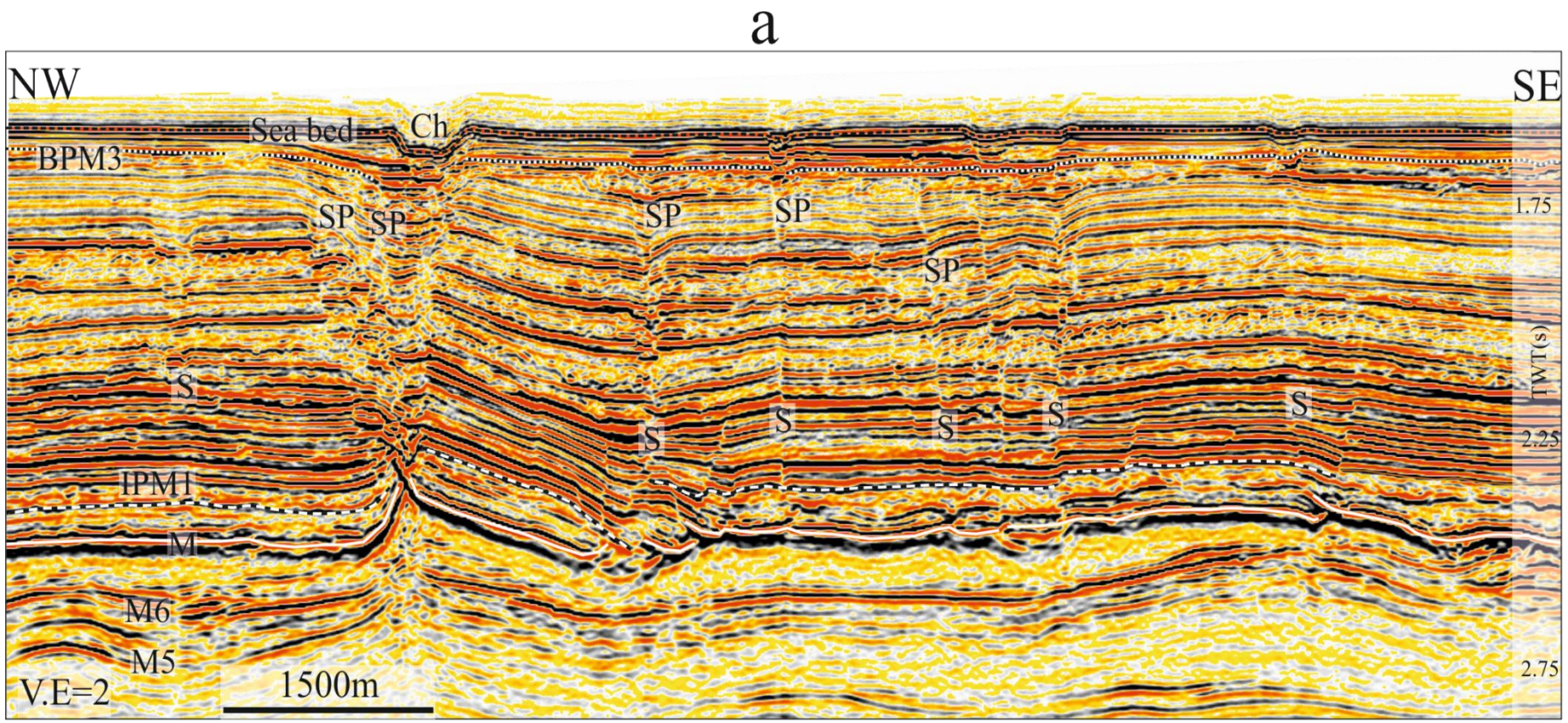


Figure 4.16: Seismic sections showing the common geometries of strike slip faults in Gal C. Locations of seismic lines (a and b) in Figure 4.15 b. Horizons M6, M, IPM1, BPM3 are regional stratigraphic horizons. S - Strike slip fault, SP-Splay, TF –thrust related fold, ch –channel.

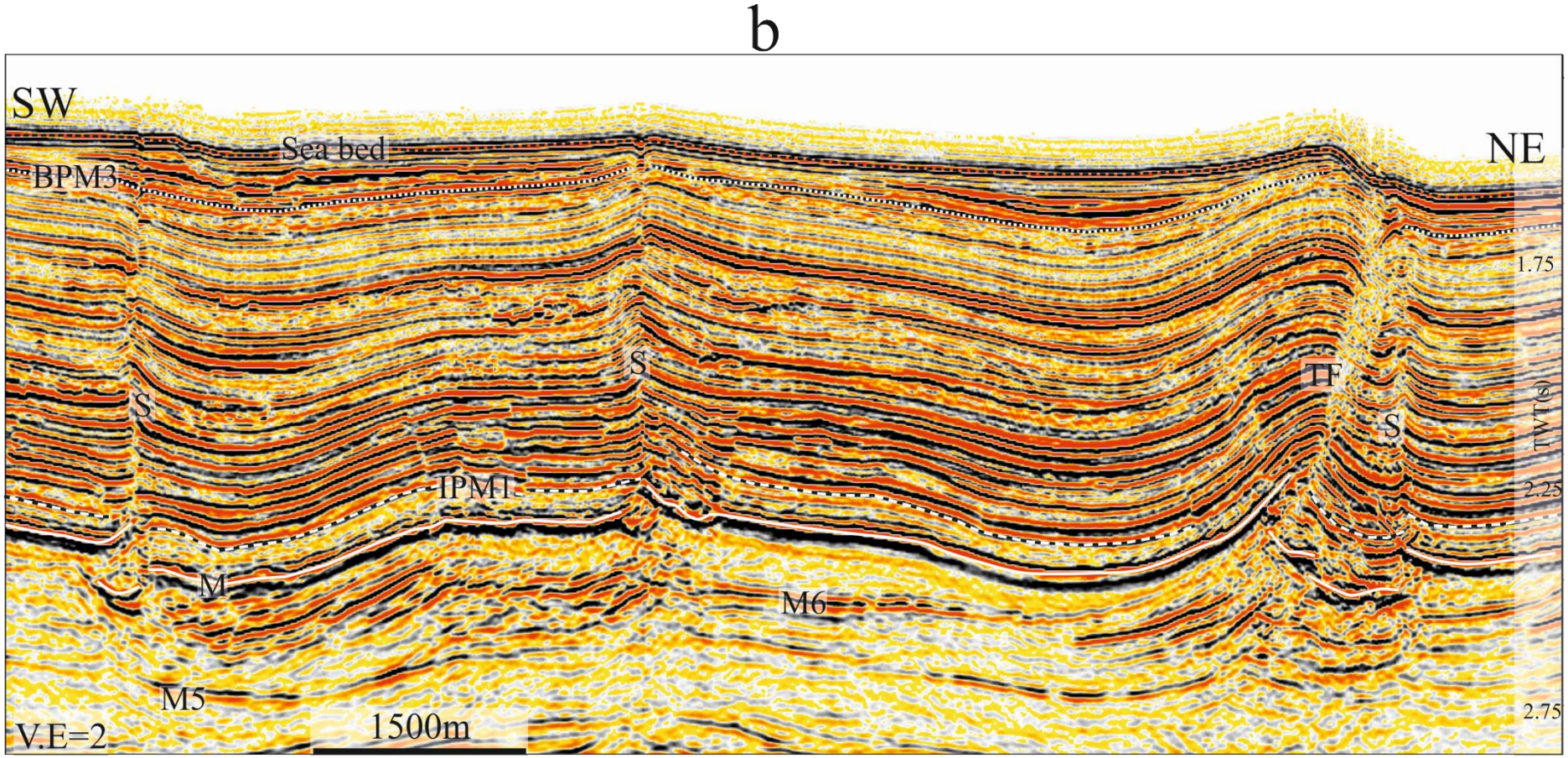


Figure 4.16: Seismic sections showing the common geometries of strike slip faults in Gal C. Locations of seismic lines (a and b) in Figure 4.15 b. Horizons M6, M, IPM1, BPM3 are regional stratigraphic horizons. S - Strike slip fault, SP-Splay, TF –thrust related fold, ch –channel.

The strike slip faults in Gal C are characterized by several types of cross-sectional geometries from those which are steeply dipping ($60^{o}$-$90^{o}$), to those which abruptly or gently change in dip up section to those that splay upwards to several converging or diverging fault strands (Figure 4.16). These several converging and diverging fault strands intersect with their principal counterparts down dip forming either positive or negative flowing structures (Woodcock and Fischer 1986; McClay and Bonora 2001). Some of the splay faults converge so that both tips intersect with the principal through going faults, forming ellipsoidal and lozenge geometries (Figure 4.16 a). The positive and negative flower structures observed in the study area mainly occur at local restraining or releasing bends (Figure 4.15).

In order to describe the strike slip faults in greater detail, this study presents a single strike slip fault (S40) as a representative example from over 71 faults mapped in the study area (Figure 4.4 and 4.15 c). This fault is used as a representative example because it runs through an area almost isolated from folds and thrust faults to a more deformed zone where it notably shows along strike changes in geometry which characterizes the strike slip faults in the study area (Figure 4.15 c). 3 main stratigraphic horizons (IPM1, IPM2 and BPM3) and 6 seismic sections (a0-a4) reveal the internal geometry of S40 and its associated intersecting faults (Figure, 4.17 and 4.18). Only the intersecting or neighbouring faults interpreted on the seismic sections were labelled on the maps (Figure, 4.15 and 4.17). Intersecting faults which do not cut through Horizon IPM1 are labelled e1-e5.

**Fault S40**

Strike slip fault S40 is located within the central region of the survey set (Figure 4.4 and 4.15 c). It extends from the south-western to north-eastern edge of the data set, having an along strike length of more than 16km (Figure 4.17). Structure maps of Horizons IPM1, IPM2 and

BPM3 and seismic sections show that S40 changes in geometry, elevation, magnitude and intersect other faults along strike and up dip (Figure 4.17 and 4.18).

Fault S40 is linear to arcuate in geometry striking ($040^o$) 0-3km, ($025^o$), 3-7.3km, ($020^o$) 7.3-8km, ($047^o$) 8-10.5km, ($033^o$) 10-16km along its width (Figure 4.17). It is probably a dextral fault; this is inferred from the kinematic observations on the majority of the strike slip faults trending between $025^o$ to $050^o$ in the dataset. There is no notable channel or fold offset along S40 to justify a right sense of shear.

Fault S40 extends vertically from its basal tip region close to the top detachment level (Horizons M and M6) to the seabed where it tips out with only a small seabed scrap. Sections close to the south eastern end of S40 shows that it dips almost $90^o$ close to basal tip and splays upward into normal faults e1 and e2 forming a local depression as that of a negative flower structure (McClay et al. 1998) (Figure 4.18 a). At 5.8 km along strike length, sectional view shows that S40 cross-cuts thrust fault T36 into two segments close to their zone of intersection (Figure 4.18 b). Whereas at 8km, S40 is cross cut by T35 (Figure 4.18 c). This opposing crosscutting relationship between the strike slip fault (S40) and thrust faults (T35 and T36) may aid in defining the timing interaction between both types of faults. A higher structural relief is observed within IPM1 and IPM2 close to the cross-cutting zone compared to other areas through which S40 transects. This zone extends laterally from 6km to 12km along strike (Figure 4.17). Within this local zone of high structural relief (at c. 7km), S40 is intersected by S39. Both of these strike slip faults bound T35 at both lateral ends. Similar to S40, S39 has its basal tip close to the upper Messinian unit and it dips almost $85^o$, but has an elliptical lens at the centre (Figure 4.18 c).

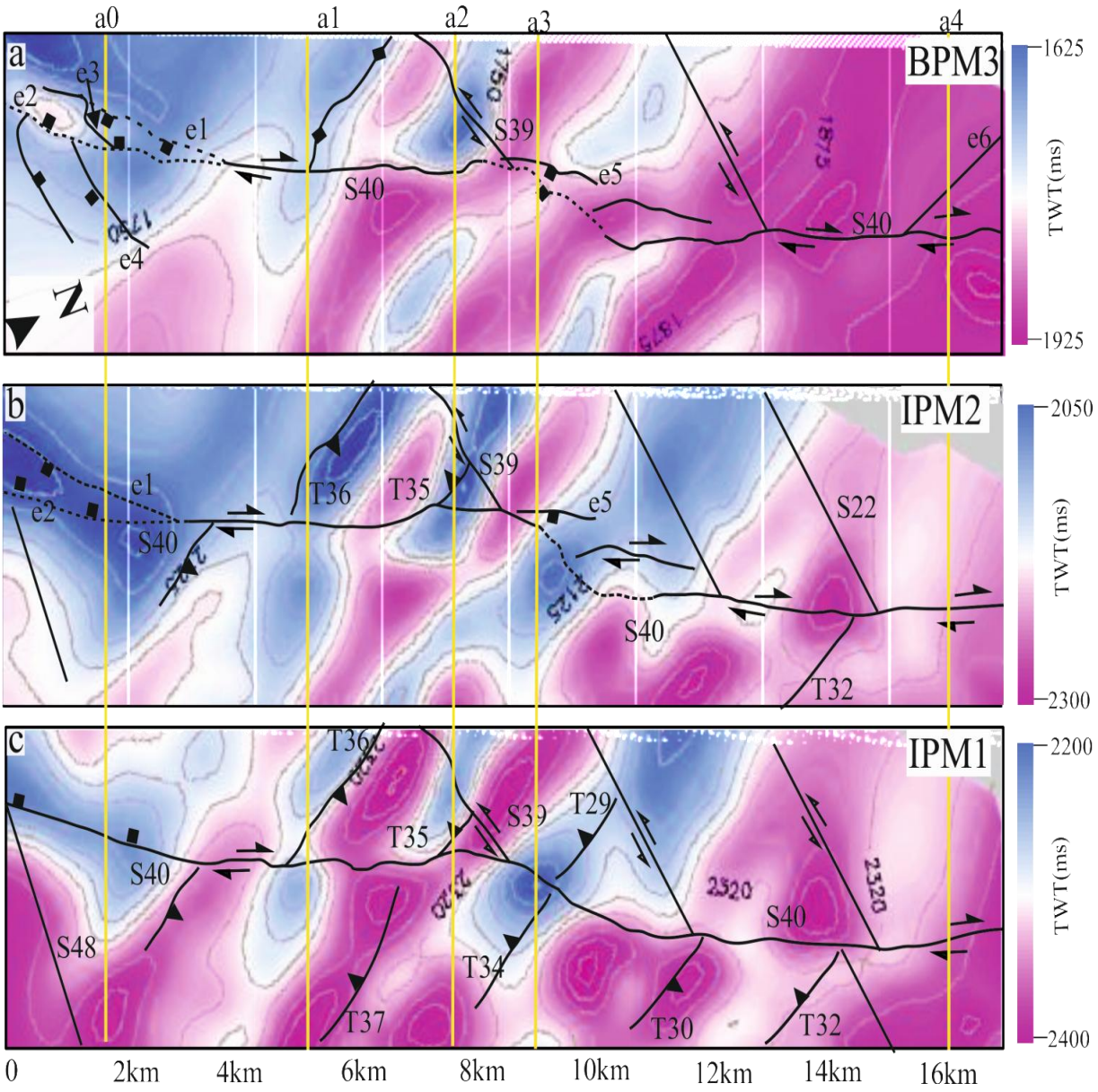


Figure 4.17: Maps of horizon elevation in TWT (ms). Locations shown in Figure 4.15 c. (A) Horizon BPM3 (B) Horizon IPM2 (C) Horizon IPM1. Trace of S40 intersected by traces of strike-slip faults and thrust faults. e1- e6 are splays associated with S40. Broken lines represent fault segments not correlatable due to poor resolution. Lines a0-a4 show locations of the 4 sections in Figure 4.18. Purple colour represents structural low. Blue colour represents structural high. Contour interval: 25ms.

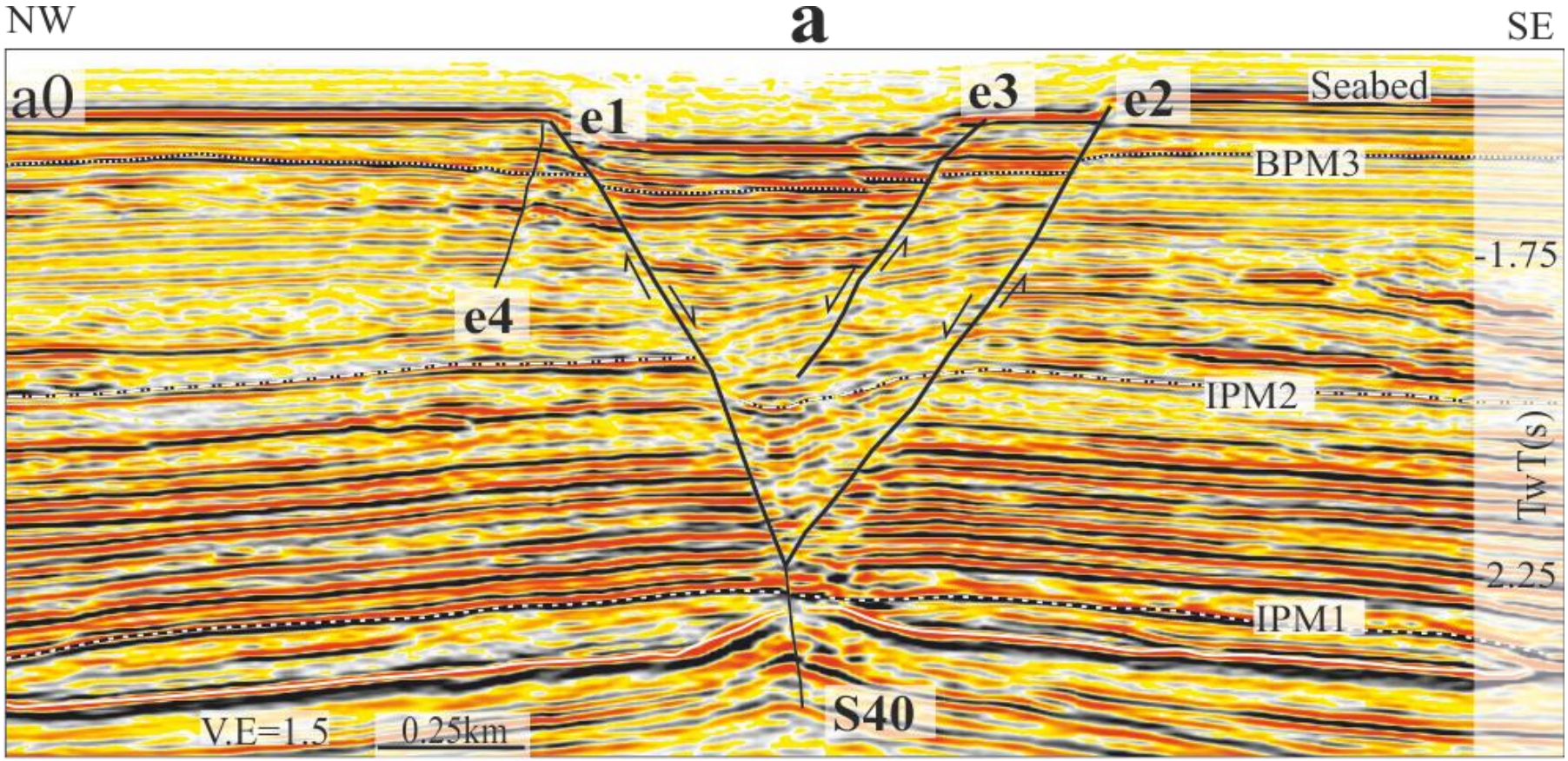


Figure 4.18: Selected seismic sections perpendicular to a selected strike slip fault (S40) illustrating change in shape and scale. Locations of seismic lines a0-a4 (a-e) in Fig. 4.17. Sections have an approximate vertical exaggeration of 1:1.5. Horizons M, IPM1, IPM2, and BPM3 are regional stratigraphic horizons.

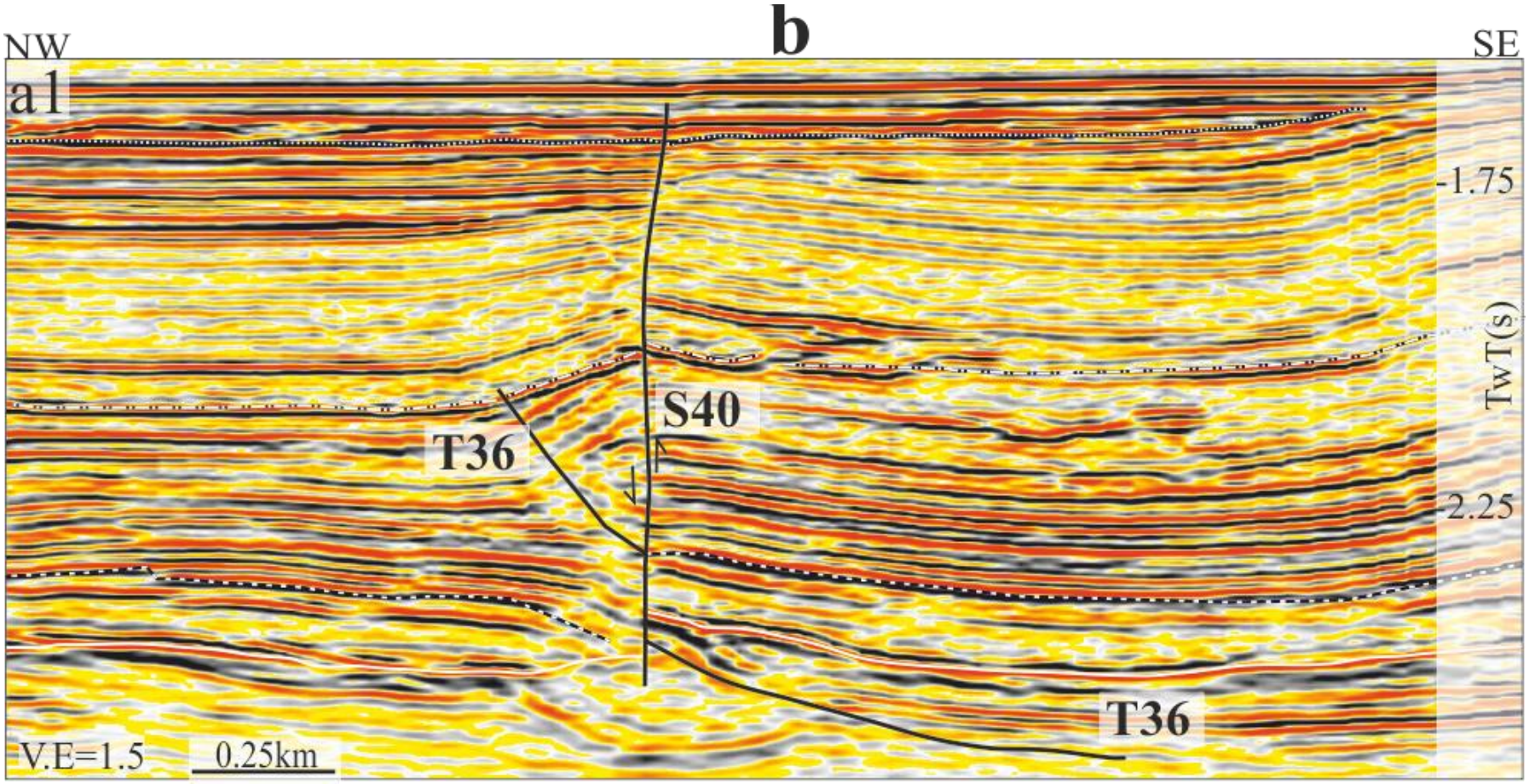


Figure 4.18: Selected seismic sections perpendicular to a selected strike slip fault (S40) illustrating change in shape and scale. Locations of seismic lines a0-a4 (a-e) in Fig. 4.17. Sections have an approximate vertical exaggeration of 1:1.5. Horizons M, IPM1, IPM2, and BPM3 are regional stratigraphic horizons.

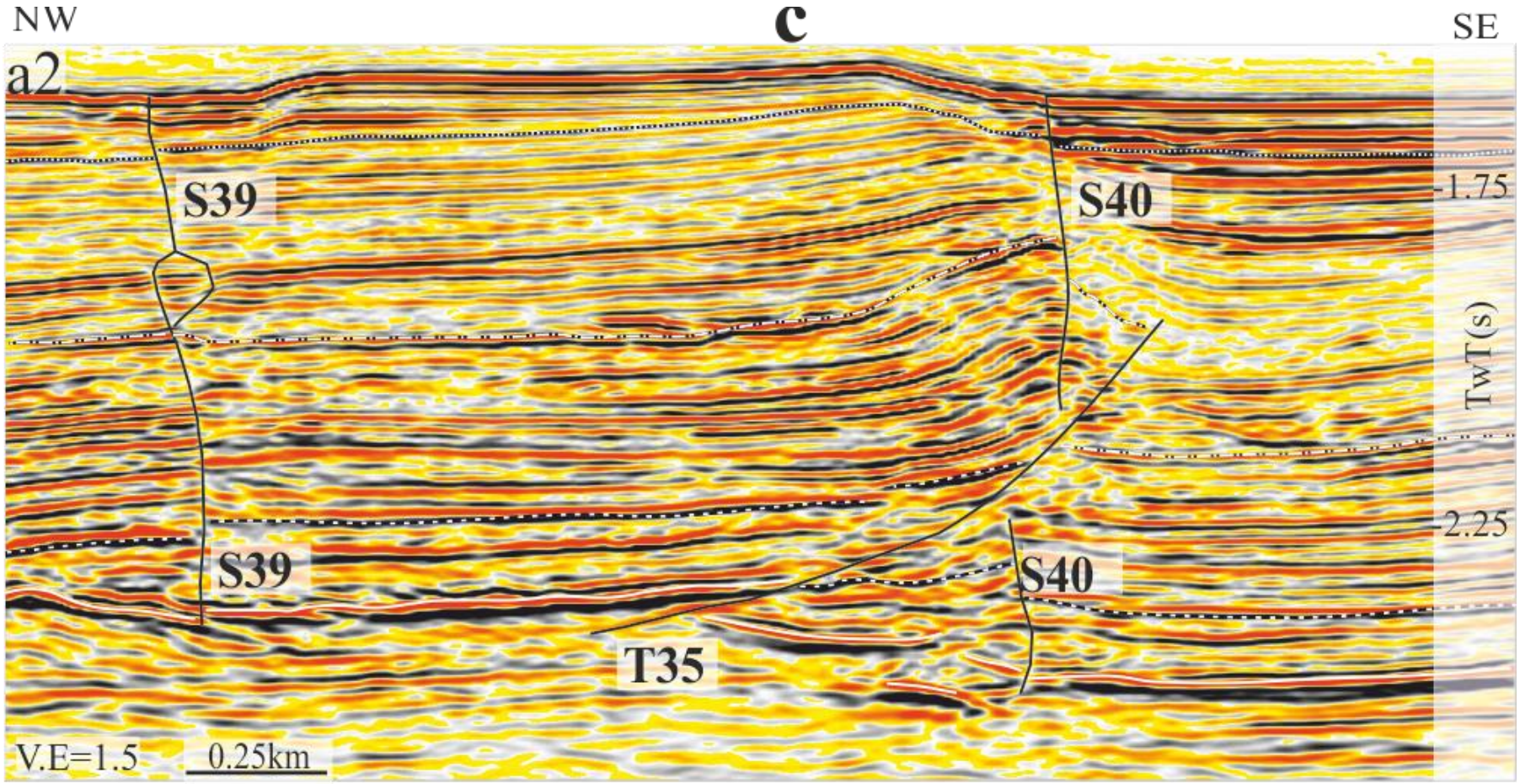


Figure 4.18: Selected seismic sections perpendicular to a selected strike slip fault (S40) illustrating change in shape and scale. Locations of seismic lines a0-a4 (a-e) in Fig. 4.17. Sections have an approximate vertical exaggeration of 1:1.5. Horizons M, IPM1, IPM2, and BPM3 are regional stratigraphic horizons.

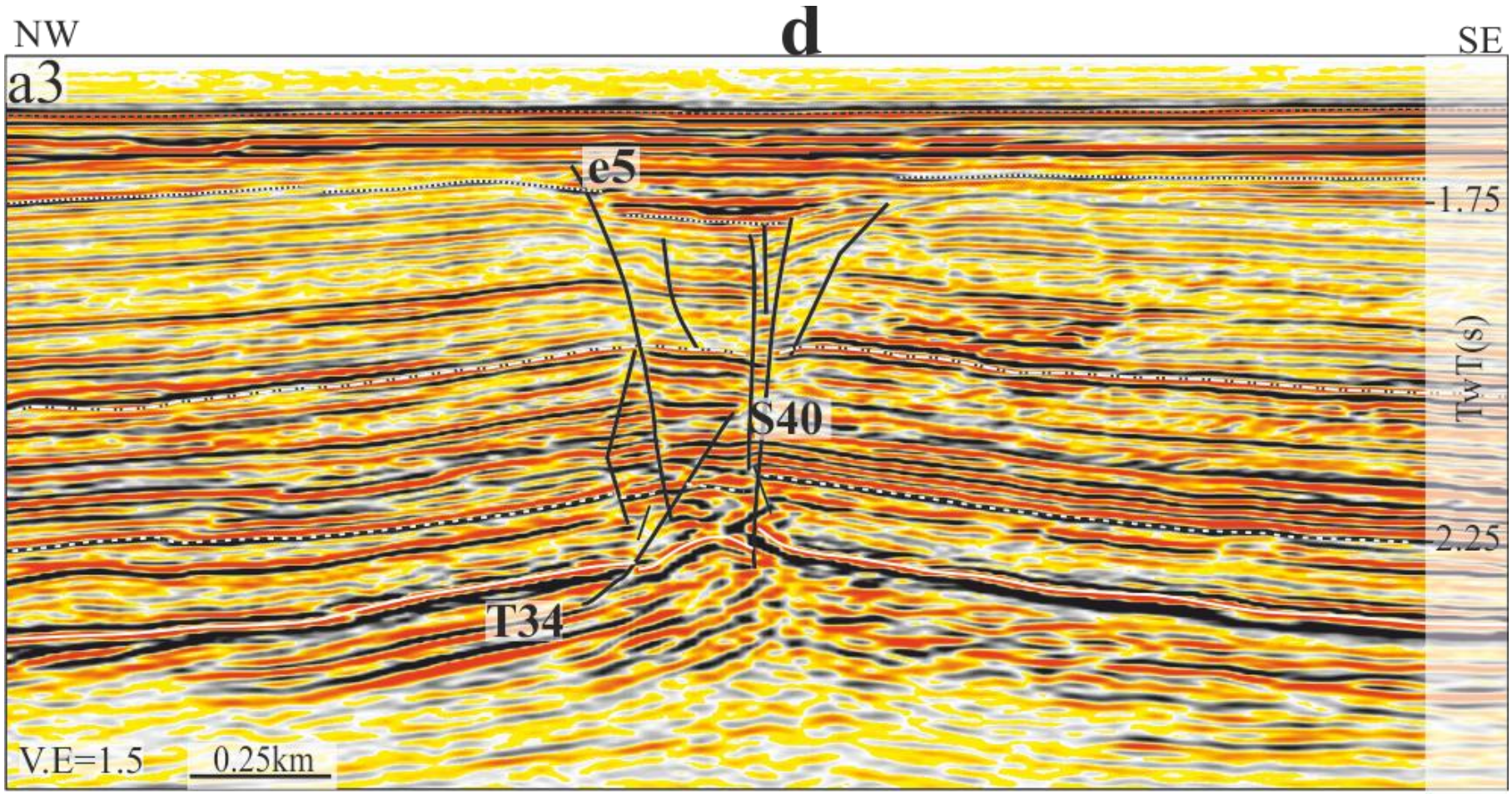


Figure 4.18: Selected seismic sections perpendicular to a selected strike slip fault (S40) illustrating change in shape and scale. Locations of seismic lines a0-a4 (a-e) in Fig. 4.17. Sections have an approximate vertical exaggeration of 1:1.5. Horizons M, IPM1, IPM2, and BPM3 are regional stratigraphic horizons.

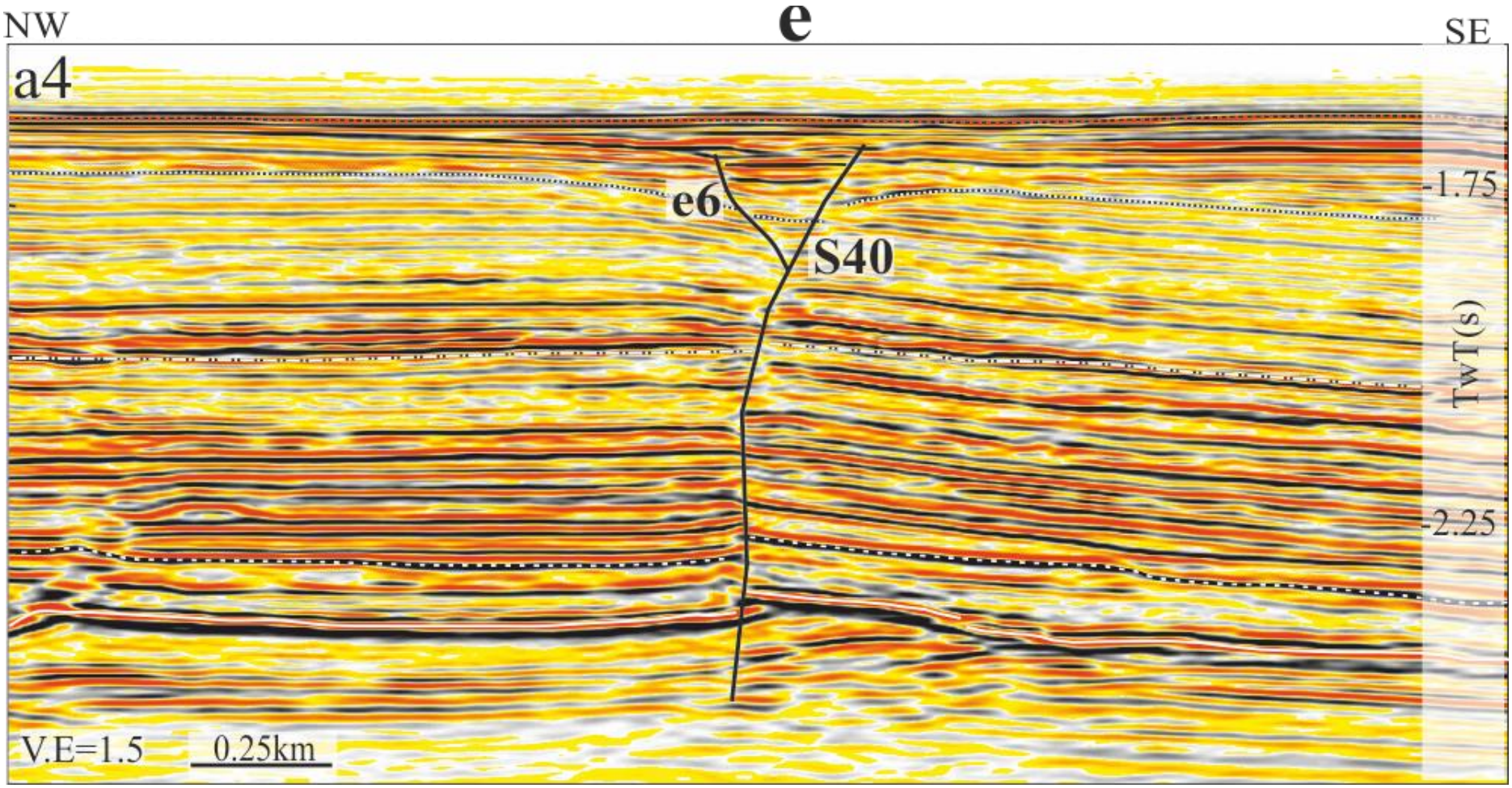


Figure 4.18: Selected seismic sections perpendicular to a selected strike slip fault (S40) illustrating change in shape and scale. Locations of seismic lines a0-a4 (a-e) in Fig. 4.17. Sections have an approximate vertical exaggeration of 1:1.5. Horizons M, IPM1, IPM2, and BPM3 are regional stratigraphic horizons.

The strike-slip fault (S40) makes a bend between 8-12.5 km of its length (Figure 4.17), this zone is characterized by a poor seismic reflection. However, horizon reflections can be correlated close to this zone at c. 9km (Figure 4.18 d). This zone is characterized by an extensional depression, possibly a pull-apart structure (Dooley and McClay 1997). This extensional depression is most obvious within the unit PM2 between e5 and S40 (Figure 4.18 d). This local depression overlies a thrust faults (T34), which transects Horizon IPM. Fault S40, towards the north-eastern edge of the data set, forms a splay (e6) upward. At this zone it dips almost $80^{o}$ and decreases upward to c. $70^{o}$ (Figure 4.18 e).

### 4.2.5 Messinian Structures.

The Messinian unit is characterized by distinctive sets of structures, identified as low amplitude, weakly asymmetric folds and thrust faults (Figure 4.2a and 4.3), following the interpretation of Bertoni and Cartwright (2006). These structures are most prominent within the upper units of the Messinian (M6 - M3) and they define deformation in the Messinian evaporite which does not wholly conform to that of the Plio-Quaternary overburden (Gradmann et al., 2005, Bertoni and Cartwright, 2006, Netzeband et al., 2006b).

These sets of Messinian thrust related structures are characterized by an imbricate geometry arrangement. They strike at similar orientation to the post-Messinian thrust faults and folds ($140^{o}$-$170^{o}$ Figure 4.2a). They do not occur uniformly throughout the study area, but are extensively developed within the northern region of the data set.

This study uses a single horizon reflection (M6) and 3 selected vertical seismic sections to describe examples of thrust faults in the upper Messinian intervals located within the northern region of the Gal C survey (Figure 4.19). These case study structures are collectively referred to as Structure M and are representative of the structural style of the Messinian thrust faults

because they are almost isolated from the region where the post-Messinian detached (Figure 4.2).

Structure M consists of several thrust faults number F1-F15. These faults are curvi-linear in map view, with a change in separation distance along their widths and having the same strike orientation to the post-Messinian ramping faults (NW-SE), with only a few minor faults striking NNW-SSE. Individual thrust faults within the echelon system have an along strike length ranging from 0.5km to 9km and they tend to soft-link or transfer shortening to each other along strike, common for imbricate faults located in a compressional setting (Dahlstrom 1970; Morley et al. 1990).

Seismic sections along Structure M show that the faults are characterized by hanging wall anticlines, and footwalls which are synclinal (Figure 4.21). The hanging walls vary from symmetric to asymmetric generally verging northeast. This vergence direction is opposite to the regional compression expected from downslope gravity gliding of the Levant margin (Figure 4.1). The faults dip between $07^{o}$ to $15^{o}$SW, and they ramp through M45 and M50, with variable detachment above and below Horizon M45 (Figure 4.20). Individual thrust faults within the imbricate array have throws ranging from a few ms to 100 ms (TWT) as maximum values. The hangingwalls and footwalls of some of the thrust faults are observed to terminate onto Horizon M as described by Bertoni and Cartwright (2006), while others have their upper tip terminating onto the hangingwall of other faults in succession. Some appear to have their hangingwalls almost horizontally transposed above the footwall, similar to fault bend folds (Rich 1934), while others show absence of roof detachment, and resembling fault propagation folds (Suppe, 1983, 1985).

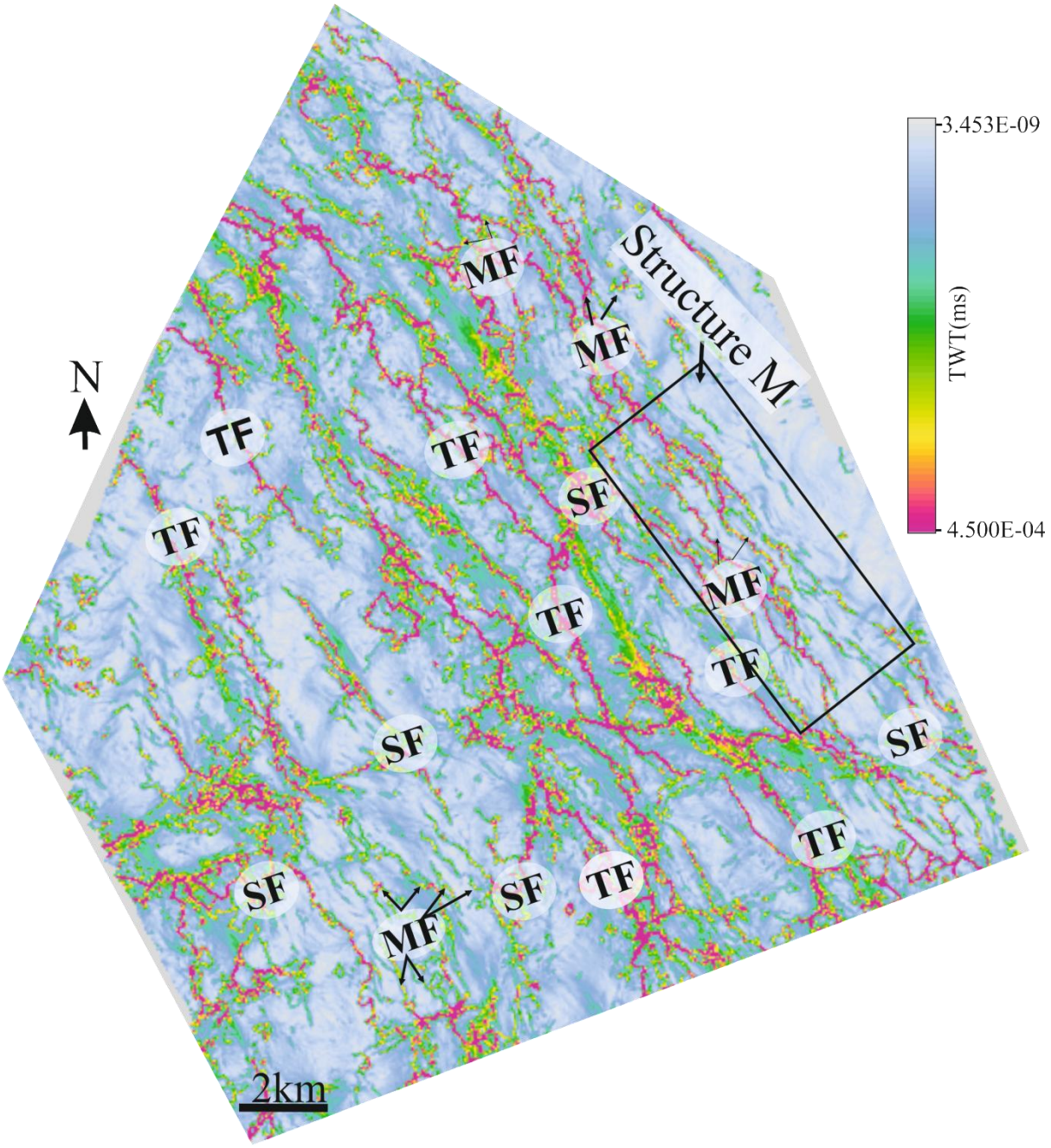


Figure 4.19: Time dip horizon (M6) map of the northern segment of the Gal C survey showing the case study thrust faults (Structure M). SF represents Strike-slip fault, TF-Thrust fault in the post-Messinian, MF-Thrust fault in the Messinian.

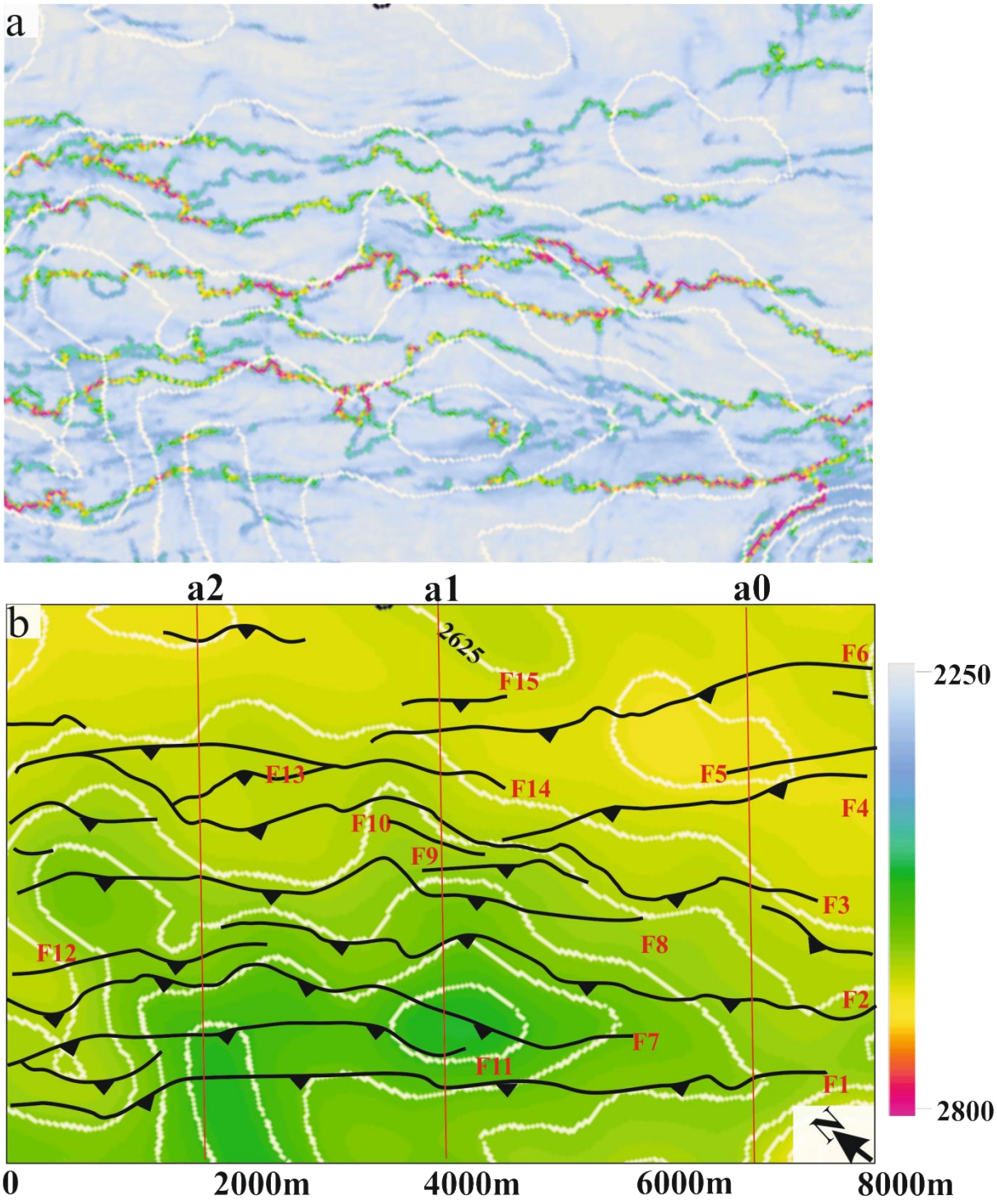


Figure 4.20: Map of Horizon M5 in TWT (ms). (a) Time dip map (b) Time dip structural map. Traces of Messinian thrust faults (F1-F15) in echelon arrangement. Map location is shown in Figure 4.19.. Line a0- a2 show locations of the 3 sections in Figure 4.21. Blue and green colours represent structural high. Red and yellow colours structural low. Contour interval: 25ms.

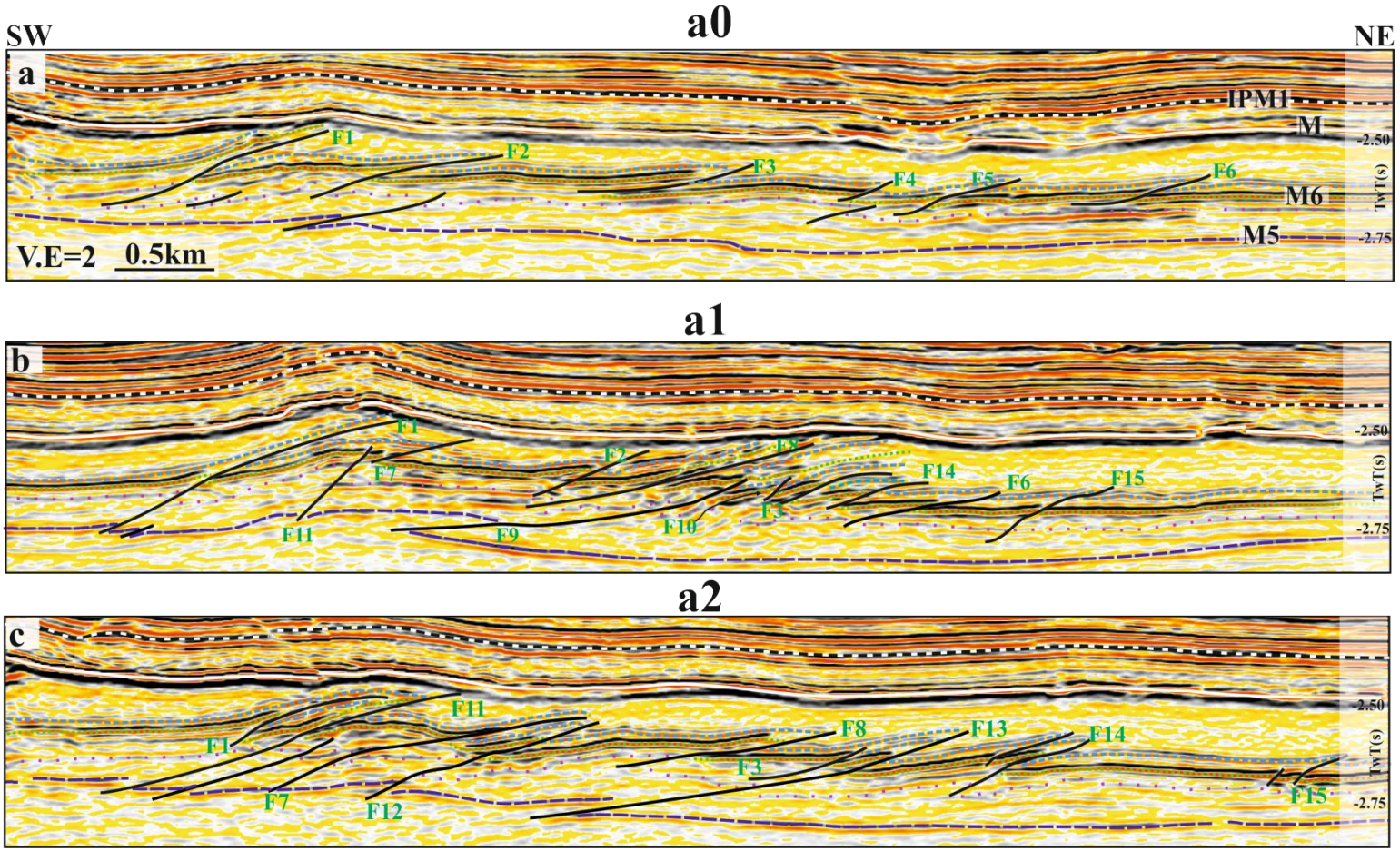


Figure 4.21: Selected seismic sections perpendicular to structure B illustrating along strike changes in structural arrangement along strike. Locations of seismic lines a0-a2 (a-c) in Figure 4.20. Sections have an approximate vertical exaggeration of 2. Horizons M5, M6 and IPM1 are regional stratigraphic horizons.

The thrust faults within Structure M, show changes in structural style and arrangement from independent ramp anticlines to overlapping hybrid duplexes (Mitra 1986), along strike (Figure 4.20 and 4.21). The simplest form is observed towards the north western end of Structure M (Figure 4.20 and 4.21a). In this zone, the thrust faults (F1 to F6) along Horizon M6, tend to have almost equal spacing distance, ranging between 800 -1000 m with exception of F4 and F5 which have a spacing distance less than 400 m (Figure 4.21 a). The apparent dip slip displacement of each of the thrust faults (F1-F6) at the north-western zone is between c. 100 m and c. 250 m (Figure 4.21 a). F1 to F6 in pairs closely resemble those of the independent ramp anticlines (Mitra 1986), because their relative spacing distances are greater than their displacements. Most of the faults (F1-F6) at this zone are observed to detach above Horizon M5 and they tend to overlie other minor faults similar to the duplex structures described by Dahlstrom (1970) (Figure 4.21 a).

The mid to south eastern region of Structure M shows a more complex fault imbrication compared to the north western end (Figure 4.21 b and c). The relative spacing distances between the faults (F1-F3, F7-F15) in these zones are generally lower than those in Figure 4.21 a. The relationship between F2, F8-F10 in the mid zone (Figure 4.22 b), and F1, F7,F11-F12 close to the south eastern end of Structure M (Figure 4.22 c), closely approaches the partial overlap to complete overlap duplex type (Mitra 1986). F1 and F11 are characterized to have their upper tip terminate onto Horizon M at the central zone (Figure 4.21 b), this may indicate Horizon M is an erosional surface as suggested by (Bertoni and Cartwright 2006). The profile in the south eastern end of Structure M (Figure 4.21 c), shows that F1 and F7 tend to decrease in dip towards their upper tips such as they appear to have an upper detachment zone. F11 at this zone, has its upper tip unto Horizon M and it's partially overlapped by F1. F12 on the other hand has its tip within the unit between Horizon M and M6 and it is

overlapped by F11. Majority of the faults are observed to detach below M5, with only a few that detach above 1t (Figure 4.21 c)**.**

## 4.3 INTERPRETATION AND DISCUSSION

The interpretation and study of 2D and 3D seismic survey close to the study area have been shown to have almost similar structural style to the Gal C survey (Netzeband et al. 2006c; Cartwright et al. 2012). Therefore, by interpolation, the structural style of the Gal C survey applies to the entire contractional domain of the Levant Basin (Figure 4.1).

### 4.3.1 Structural Deformation of Contractional Domain

Deformation of the contractional domain of the Levant Basin has previously been interpreted as a product of the post Messinian gravitational system induced by differential sediment loading and regional tilting of the Levant Margin (Cartwright and Jackson 2008). Deformation driven solely by the thin skin response of the Levant margin would imply a maximum principal stress direction ranging between $100^{o}$ and $120^{o}$. This stress direction range is not compatible with the study of the structures described in this study. The vergence direction of folds, the strike trends of thrust related folds and conjugate strike slip faults suggest that the salt and its overburden may have undergone a single phase of deformation whose maximum principal stress direction is between $060^{o} – 070^{o}$.

Shortening in the ENE direction indicates that there are other boundary conditions influencing deformation in the area (Figure 4.1), (Cartwright et al. 2012) . These boundary conditions include: (1) the thinskin response of the Nile cone to the south (Loncke *et al.* 2006), (2) the westwards buttressing effects of the Eratosthenes Seamount (Mascle et al. 2001), and (3) the Cyprus Subduction Trench (Netzeband et al., 2006b). The orientation of the principal stress direction determined in this study indicates Nile Cone spreading is the main cause of deformation and tectonic trasport in the contractional domain of the Levant

Basin (Figure 4.1). This inference is also supported by the northwards bathymetric dip of the Nile cone and present-day dip of the top salt ( Netzeband et al., 2006, Figure 12 and 14).

In contrast to a single phase of shortening in the contractional domain, the difference in structural style of the post-Messinian thrust related folds and those in the Messinian may suggests multiple phases of deformation (Bertoni and Cartwright 2005; Netzeband et al. 2006c). All the kinematic indicators in both the salt and its overburden points towards thesame direction which supports a single phase of deformation. However, single phase deformation does not explain the up dip reflection terminations against Horizon M (Figure 4.21). The updip terminations indicates that Horizon M is either a non-depositional unconformity, or an erosional unconformity (Mitchum and Van Wagoner 1991). Recent studies suggest an erosional unconformity (Bertoni and Cartwright 2006), based on the geometry of the termination of the intra-evaporite.

The up dip reflection terminations against the unconformity surface, indicates there was an earlier phase of deformation which predates the completion of the unconformity surface expressed as Horizon M (Bertoni and Cartwright 2006). This phase probably occurred towards the end of the Messinian crisis which led to the deposition of over 2km thick evaporite (Netzeband et al., 2006).

### 4.3.2 Relationship between Structural Elements.

There are three main types of relationships and hence interactions between the structural elements in Gal C. These are fault-fold relationship, thrust fault and thrust faults, and thrust and strike-slip interactions. These interactions are easily described using examples of the post-Messinian structures. This study reiterates that the detailed kinematic analysis such as shortening and displacement distribution of some of the structures in Gal C are described in

further chapters. Here, relationship of these elements is based on notable observations from maps and sections.

#### *4.3.2.1 Relationship between thrust faults and folds.*

The different examples of the thrust and folds presented here are interpreted as pure fault propagation fold, instead of fault detachment fold (Jamison 1987). Models of detachment folds, above a salt layer, overlain by an overburden cover, suggests fold growth would be accompanied by redistribution of salt into the fold core (Wiltschko and Chapple 1977). It is further inferred that if there were insufficient salt available to fill the core, the fold growth will be inhibited and deformation would have to be accommodated by the formation of a thrust fault. Thrust faults which show such transition from a detachment fold, to a progressive fault propagation fold, are termed fault detachment folds (Mitra 2002) or translated detachment folds (Nemcok et al., 2005). Such structure should have very small displacements relative to their fold amplitudes (Mitra et al., 2006), since faulting is secondary to folding. In the study area, the thrust faults have much larger displacements than their associated fold amplitudes, similar to fault propagation folds.

Thrust faults characterized by minimal folding have been termed shear thrust faults (Willis 1893). This class of thrust faults are similar to the Type A thrust related folds. The presence of the Type A thrust related folds, and the scarcity of folds without ramps, implies a progression from shear thrust fault (Willis 1893), to fault propagation fold. Whether both types of structure (Folds and thrust faults) were formed simultaneously or thrust faulting predates folding, can only be determined by comparing the shortening and total displacement distribution along a thrust related fold (see Chapter 5 and 6, Figure 5.17 and 6.10). It is considered here that the Type A thrust related fold structures reflect the very early development stage of the Type B structure. At this early stage, Type A shears with little or no

folding, similar to the shear thrust fault described by Willis (1893). Continued compression results in anticlines with relatively equal dip limbs. The folds initially developed as symmetric folds, with equal limb dips, further fault propagation results to semi-asymmetric folds with front limbs steeper than back limbs (see Chapter 7 for more detailed explanation).

#### *4.3.2.2 Interaction between thrust faults*

Overlapping or relay thrust faults of similar and opposing dips are common within the Gal C (Figure 4.4). Overlapping zones in most cases are regions of fault interaction (Larsen 1988; Morley et al. 1990), where by fault propagation is hindered or displacement is transferred from one fault to another (Needham et al., 1996b). Thrust fault propagation and interaction at zones of overlap is addressed in Chapter 6.

#### *4.3.2.3 Interaction between thrust faults and strike slip faults*

The interaction between thrust faults and strike slips is evident in map view (Figure 4.1, 4.3). Thrust faults and folds are either segmented or bounded by strike slip faults. In most cases, the thrust faults tend to show important displacement variation close to where they intersect strike slip faults. A more detailed analysis of these interactions is presented in subsequent chapters.

The examples of structures presented in this study illustrate 4 main end member thrust faults and strike slip fault interaction (Figure 4.22): (1) Non-intersected type (Class A), (2) Single end type or Class B (Figure 4.22 b) (3) Double end type (Class C or D) (Figure 4.22 c and d) and (4) Cross cutting type (Class E or F) (Figure 4.22 e and f).

Each end member is characterized by a specific pattern of bounding or segmentation, although, more than one end member type may occur within a single structure. In order to aid the recognition and description of similar kinds of end member interaction elsewhere, it is

define below with reference to type examples within the dataset. A bar chart of the ratio of maximum displacement and length (Dmax/L) for the end members is shown in Figure 4.23.

**Non-intersected type (Class A)** – These are thrust faults free from strike slip fault intersection. Such are faults are very few in Gal C. A typical example is Fault T10 (Figure 4.11). They generally have Dmax/L values less than 0.1 with only a few exceeding 0.05 (Figure 4.23).

**Single end type (Class B)** – These are thrust faults that have been intersected or crosscut by a strike slip fault at one end (Figure 4.22 b). Based on displacement distribution curves, they are expected to display a similar pattern of a tip restricted or half restricted profile with their maximum displacement close to the intersection zone similar to those described by Nicol et al (1995). Some of the thrust faults in this class have D.max/L values have greater than 0.2 (Figure 4.11).

**Double end type -** This type of interaction is formed when a thrust fault is branched at both ends by strike slip faults (Figure 4.22d and c). They can further be divided into (1) Class B (Figure 4.22c) and (2) Class C (Figure 4.22 d). The Class C type, are thrust faults bounded by strike slip faults with different senses of shear. An example is Fault T17 (Figure 4.22 c). On the other hand, the Class D type, are thrust faults bounded at both ends by strike-slip faults with the same sense of shear. An example is Fault T32 (Figure 4.4), segments of Fault T17 and T18 bounded by strike slip fault S16 and S20 are examples of this class of interaction (Figure 4.13). Although the zones of strike slip fault S16 intersection are not interpreted as lateral ends or tips of thrust faults (T17 and T18). There is no clear difference in Dmax/L values between the Double end type and the Single end. Both types have their Dmax/L values greater than 0.2.

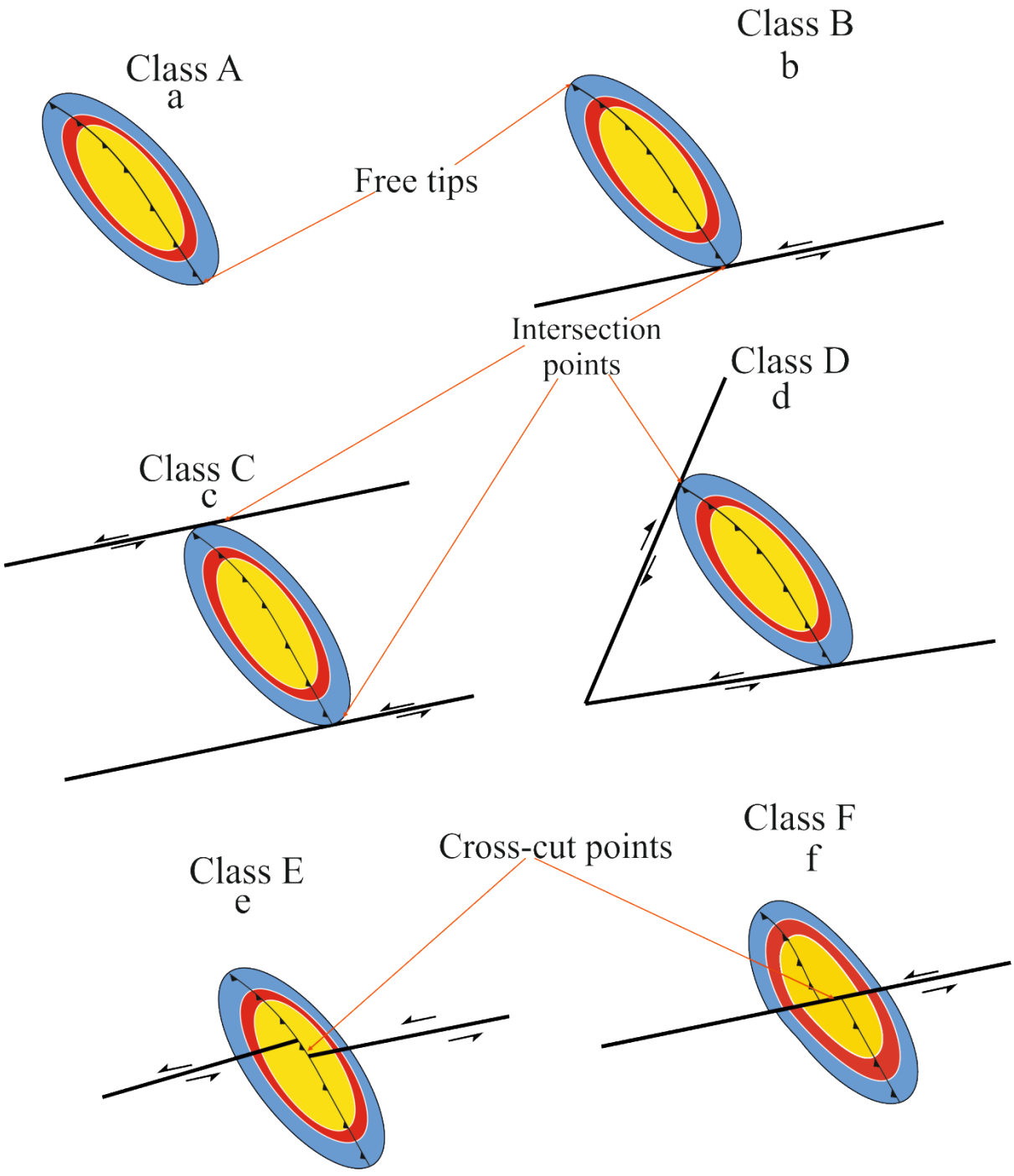


Figure 4.22: Diagram illustrating the different end member thrust related fold-strike slip fault interactions. (a) Class A- free tipping thrust fault. (b) Class B- single bounded type (c) Class C – bounded by strike slip faults of the same direction of shear (d) Class D- bounded by strike slip faults of different sense of shear. (e) Class E- thrust related fold crosscutting strike slip fault (f) Class F- strike slip fault cross cutting thrust related fold fault.

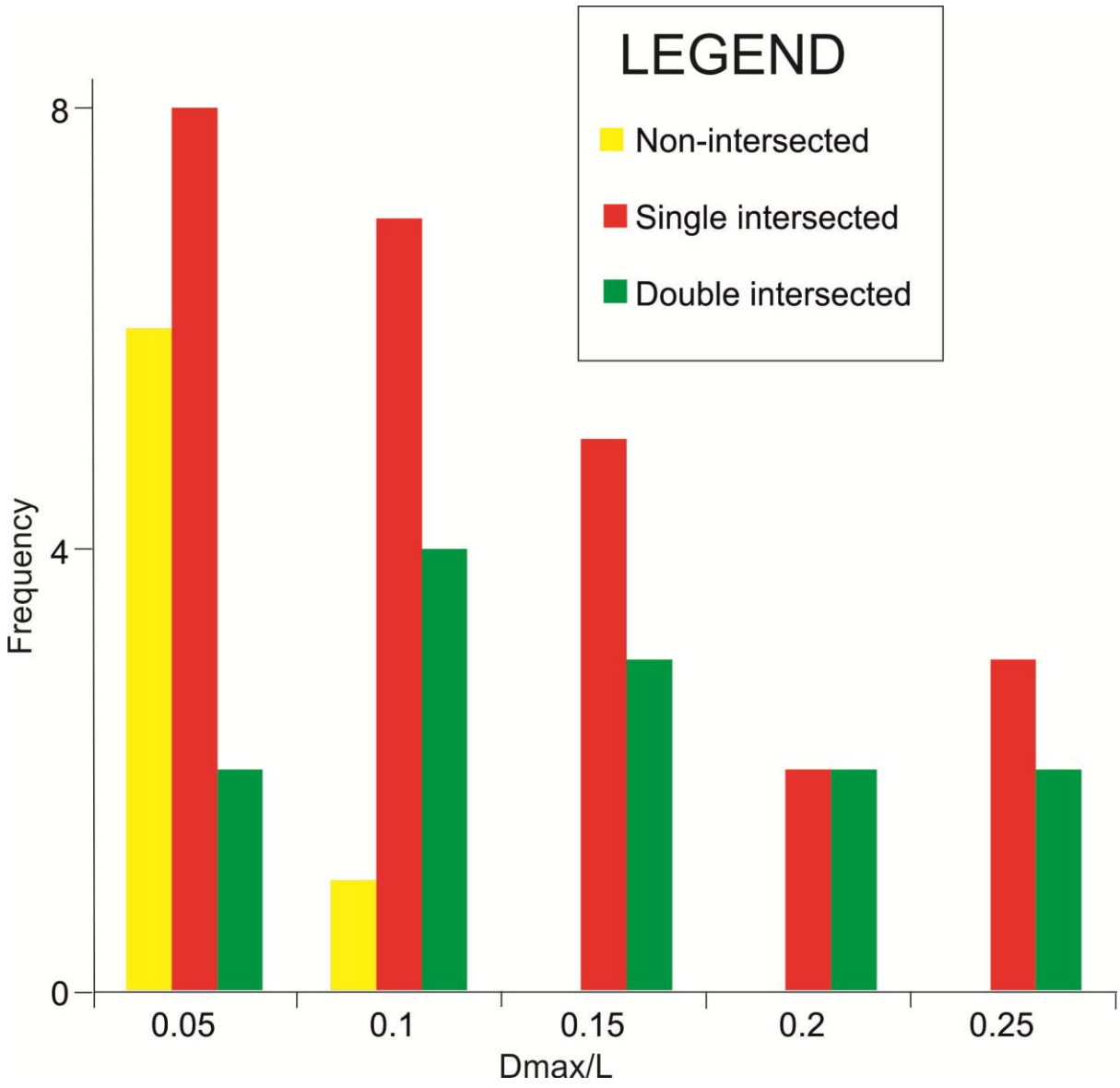


Figure 4.23: Bar chart of D.max/L values for unrestricted, double and single tip restricted thrust related faults.

Cross cutting faults -These are faults that run through or offset pre-existing faults (Watters and Maxwell 1983; Needham *et al.* 1996a). This relationship has been observed in both extensional and compressional domains where converging or diverging faults are observed to shear their principal faults or vice versa (Watters and Maxwell 1983; Tearpock and Bischke 1991; Needham et al. 1996a; Higgins et al. 2007). In this study area, thrust faults either crosscut strike slip faults or are by themselves crosscut by strike slip faults. The former is termed Class D (Figure 4.22e) while the latter is termed Class E (Figure 4.22f). The majority

of the thrust faults in Gal C appear to be crosscut by strike slip faults. For instance Faults T9 and T17 appear to be one and the same thrust fault segment before being crosscut by Fault S10 (Figure 4.13). To determine whether faults crosscut each other or not, a detailed analysis is required (See Chapter 5 for detailed analysis).

## 4.4 CONCLUSION

This study gives an overview of the main structural elements in the Gal C survey. This includes thrust related strike slip faults, and imbricate thrust related fold systems. Deformation in the area is associated with two main phase systems; a Messinian phase which occurred immediately after the deposition of the evaporite layer, and a Plio-Quaternary phase involving the thin skin response of the Levant Margin and the Nile cone, and other boundary effects associated with the Cyprus Arc and Eratosthenes Seamount.

The thrust fault and fold pairs are interpreted to be pure fault propagation folds which evolved from faults with low amplitude folds to fault propagation folds, bounded or segmented by strike slip faults, and/or thrust faults. 4 main end members thrust faults and strike slip fault interaction were defined in the study area. Non intersected type or Class A are thrust faults free from strike slip fault intersection; Single end type or Class B are thrust faults bounded at one end by strike slip fault; Double end (Class C or D) - Thrust faults bounded at both ends by strike slip faults; Crosscutting faults (Class E or F) - Thrust faults sheared by strike slip faults. Thrust faults that shear through strike slip fault.

# CHAPTER FIVE

# 5 THE INTERACTION BETWEEN THRUST FAULTS AND STRIKE SLIP FAULTS

## 5.1 INTRODUCTION

This chapter examines the lateral propagation and interaction of thrust related folds compartmentalized by strike slip faults. In Chapter 4, it was made clear that the thrust related folds in Gal C are either bounded or segmented (compartmentalized) by strike slip faults and several end member thrust fault-strike slip fault interaction were proposed. This begs the question on the timing interaction of the structures: are the thrust faults and folds cross cut by the strike slip faults? or did the thrust faults individually propagate towards pre-existed strike slip faults and got restricted at the intersections?. In order to answer this question, a number of kinematic techniques, which includes displacement and shortening distribution and syn-kinematic packages, were used to investigate the interactions between thrust related folds and strike slip faults.

### 5.1.1 Aim and scope

The aim of this chapter is to analyse the displacement and shortening variations of thrust related folds intersected by strike slip faults. It does not cover other factors which may influence displacement distribution such as linkage, overlapping faults and lithological contrast (Cartwright et al. 1995; Childs et al. 1995; Baudon and Cartwright 2008b). Models were proposed to describe the possible evolution and interaction between thrust faults and strike slip faults. It is also aimed at analysing the relationship between displacements and shortening distributions, with the main focus on how both parameters vary close to intersections.

This chapter starts by giving an overview of the method used in analysing the faults and folds. This is followed by the result section, which starts by the description and characteristics of non-intersected thrust related folds. The result section continues with a summary description of the case study compartmentalized structures on maps and seismic sections, and the description of syn- kinematic sediments above the folds. Next, the fault surface and displacement distribution are described, followed by the description of the summed fault displacement and fold shortening distribution. The results were interpreted by analysing displacement distribution, which are discussed in section 5.3.5 before the conclusion.

## 5.2 METHODOLOGY

The methodology and techniques used in this study has been described in details in Chapter 2 of this thesis. This study uses dip slip displacement in place of throw and heave, because it is most widely used in displacement distribution studies and can be easily compared with other published results (Muraoka and Kamata 1983; Williams and Chapman 1983; Ellis and Dunlap 1988). More also, dip-slip is most preferred because it is considerable the largest displacement parameter than can be measured on seismic section.

Measurement of dip-slip was done on seismic sections perpendicular to fault length at specific intervals (every 125 m) and plotted against the horizontal distance of the thrust folds. This plotting convention, allows direct comparison between shortening and summed displacement.

The along strike displacement distribution was focused on a key horizon (IPM1). This horizon is located close to where the majority of the thrust faults attained their maximum displacement and it captures the main structural elements within the dataset (Figure 5.1 a). Therefore, Horizon IPM1 is used as a reference horizon in producing the structural maps in

this chapter (Figure 5.1 b). More also, the sense of shear, and displacement for the strike slip faults in the area were determined using apparent thrust related fold and channel offsets for comparison purposes. The values are posted on the map of Horizon IPM1 (Figure 5.1 b). Strike-slip offset values were measured on several horizons up-dip from Horizon IPM1, and show no significant changes in offset.

## 5.3 RESULT

This study mapped over 35 thrust related folds intersected by strike slip faults within the dataset (Figure 5.1). Representative examples of these faults and folds have been described in Chapter 4, but were not quantitatively analysed in great detail. Time dip structural maps showing the main structural elements in the study area and case study examples (Structure A, B and C) are shown in (Figure 5.1). The case study structure as a whole comprises of several examples of thrust faults – strike slip faults end member (class A-F) as listed in Chapter 4 (see Figure 4.22). As qualitatively described in Chapter 4, the case study thrust faults show notable changes in displacement close to intersection; therefore they are ideal for this study.

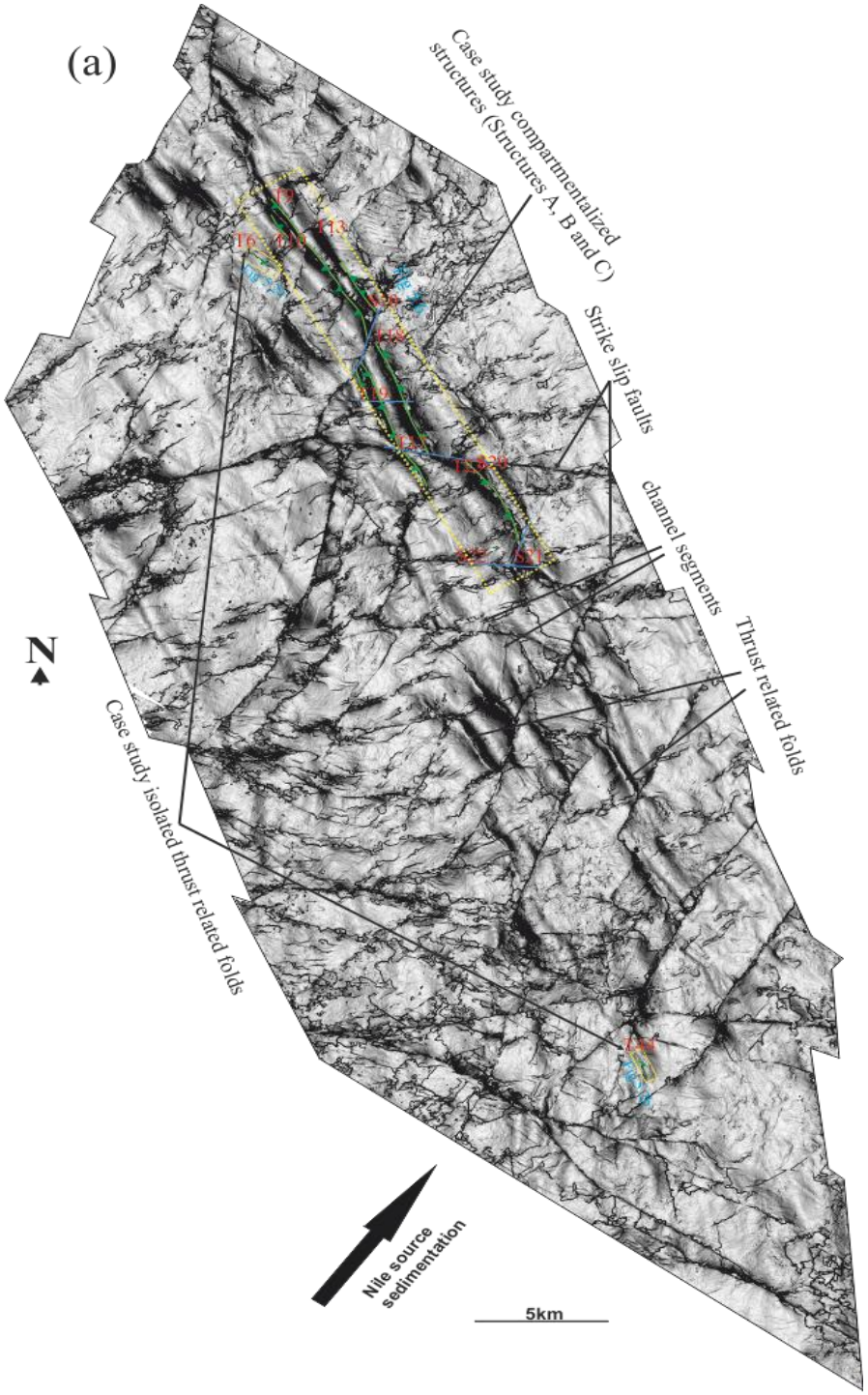


Figure 5.1: Time dip map of a key horizon from the 3D dataset used for this thesis, showing the case study non-intersected and compartmentalized thrust related folds. (a) Uninterpreted (b) interpreted. The isolated faults (T6 and T44) are used as reference standards to establish the characteristic of an uninteracted thrust related fold. Displacement values for the strike slip faults are recorded in Figure 5.1b, blue circles represent offset values from channel offsets while green squares represent fold and thrust fault offset values. The rose diagram shows the main structural trends of the thrust faults and strike slip faults.

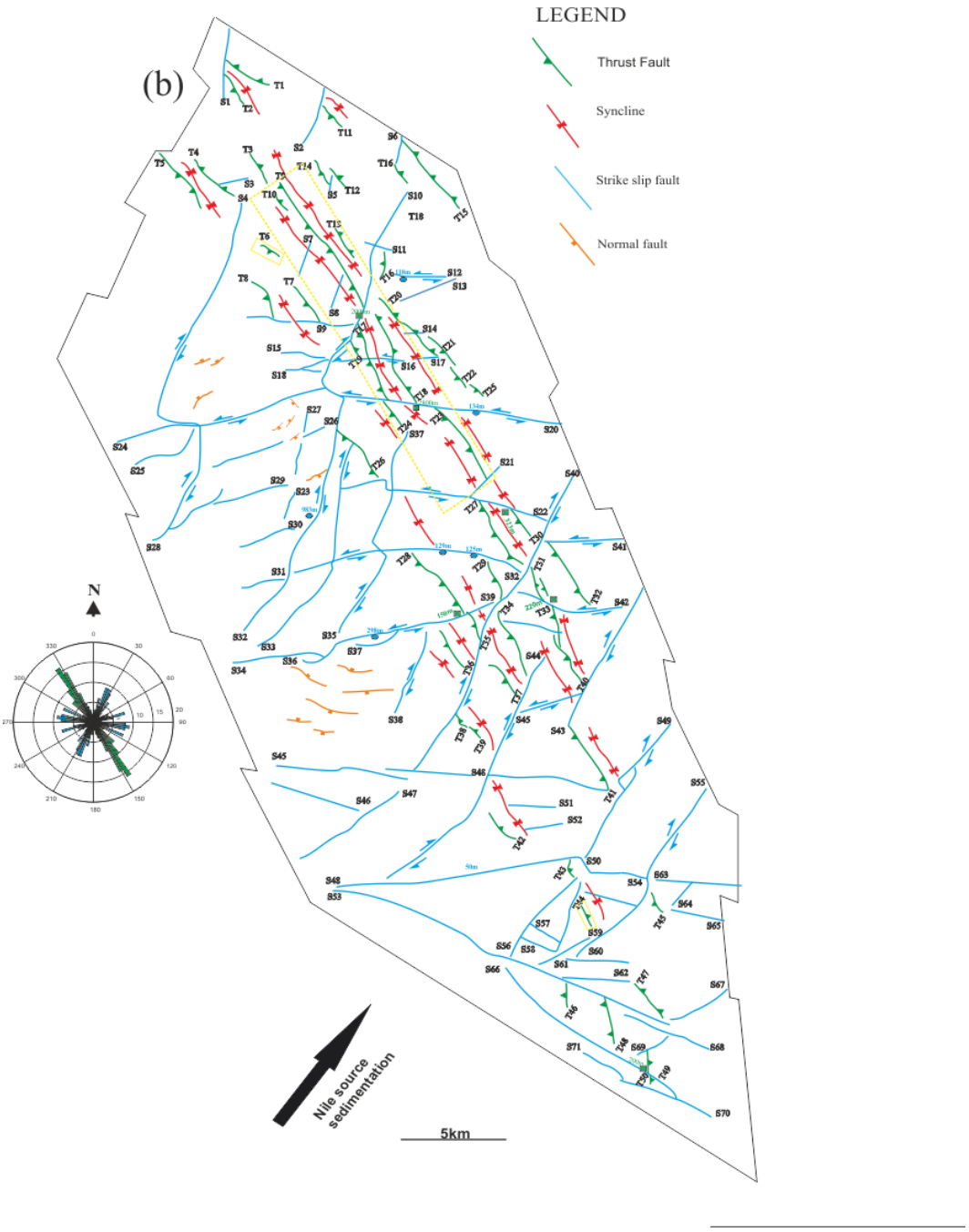


Figure 5.1: Time dip map of a key horizon from the 3D dataset used for this thesis, showing the case study non-intersected and compartmentalized thrust related folds. (a) Uninterpreted (b) interpreted. The isolated faults (T6 and T44) are used as reference standards to establish the characteristic of an uninteracted thrust related fold. Displacement values for the strike slip faults are recorded in Figure 5.1b, blue circles represent offset values from channel offsets while green squares represent fold and thrust fault offset values. The rose diagram shows the main structural trends of the thrust faults and strike slip faults.

### 5.3.1 Geometry and Characteristic of Isolated Thrust Related Fold.

Many studies of fault interaction use a single isolated faults as a reference standard from which to define modification to fault geometry (Barnett et al. 1987; Walsh *et al.* 1991; Manighetti et al. 2001a; Higgins et al. 2007). In the dataset used for this study, very few of the thrust faults and folds can be classified as wholly or partially free from strike slip fault intersection (Figure 4.2 and 5.1). The majority of the thrust related folds are either bounded or segmented by strike slip faults. However, two (2) examples of thrust related folds (T6 and T44) that show little evidence of having been intersected by strike slip faults are described here for reference (Figure 5.2 and 5.3). These faults and their associated folds are fully contained within the dataset, and are used as a representative standard to establish the shape, dip slip and shortening distribution geometries of isolated faults within the dataset (Figure 5.1, 5.2 and 5.3).

Thrust fault T6 has an along strike length of c. 2100 m, striking c.125$^{o}$, while T44 laterally extends a distance of c. 1300 m, with a strike trend of 155$^{o}$ (Figure 5.2). The traces of the thrust faults (T6 and T44) are somewhat linear in map view and show no significant curvature at lateral tips to indicate effect from intervening faults or fractures (Figure 5.2). T6 dips c. 33$^{o}$SW and it detaches below the M reflection (Figure 5.3 a). Conversely, T44 dips c. 31$^{o}$NE, it has its down tip terminating between M reflection and Horizon IPM1: it does not decrease in dip down tip (Figure 5.3 b). The entire perimeter of the T44 tip line can be defined while the bottom of T6 is partially obscured due to a loss in amplitude in the Messinian evaporite layer.

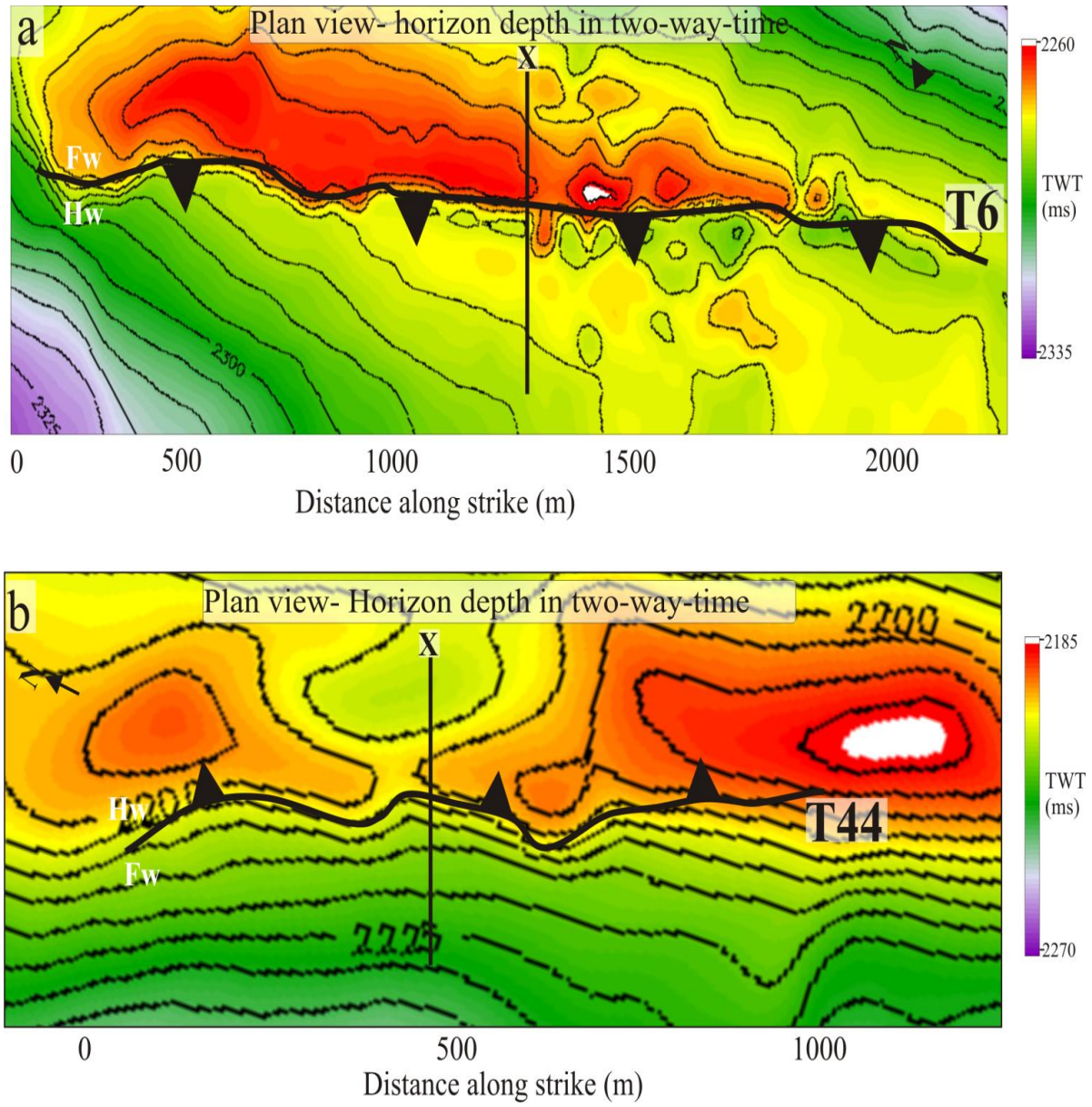


Figure 5.2: Time dip structural maps along Horizon IPM1 showing the case study isolated thrust faults given in two-way-travel time. (a) T6 (b) T44. Line X shows location of the seismic sections in Figure 5.3. White/red represents structural high; purple/green is structural low. FW, footwall; HW, hanging wall.

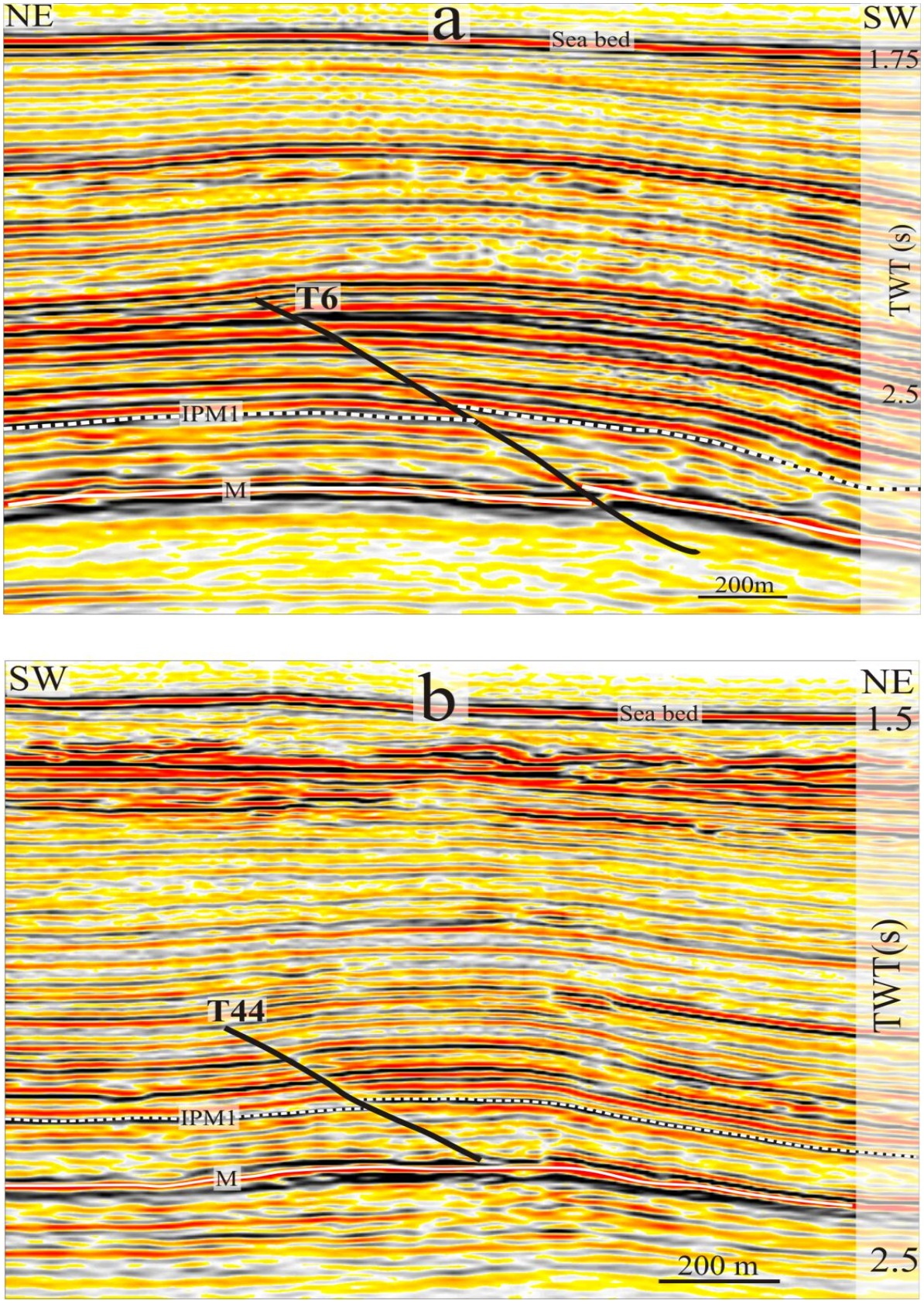


Figure 5.3: Seismic sections along the case study isolated faults (a) T6 (b) T44. Locations of seismic line X in Figure 5.2.

Dip slip and shortening distribution profiles for Faults T6 and T44 along Horizon IPM1 are shown in Figure 5.4. The profiles resemble the C type profile, similar to the isolated faults described in other studies (Muraoka and Kamata 1983; Manighetti et al. 2001a). Profiles for both thrust faults (T6 and T44), decrease towards their lateral tips with no significant gradient change from their centres of maximum value (Figure 5.4). The profile gradient of the faults ranges between 0.03-0.07, and the ratio of maximum displacement and length is 0.02 and 0.04 for T6 and T44 respectively Figure 5.4.

From the dip-slip and shortening plots of Faults T44 and T6, it can be said that that isolated thrust faults within the dataset are symmetric profile in geometry. It is therefore a main focus in this study to see whether compartmentalized thrust faults and folds will display a modification to these geometries.

### 5.3.2 Geometry and Characteristic of Compartmentalized Thrust Related Fold

The case study structures (A and B) have been described in Chapter 4. In this chapter, a new case study is introduced termed Structure C (Figure 5.5), in order to have a better understanding of fault interaction.

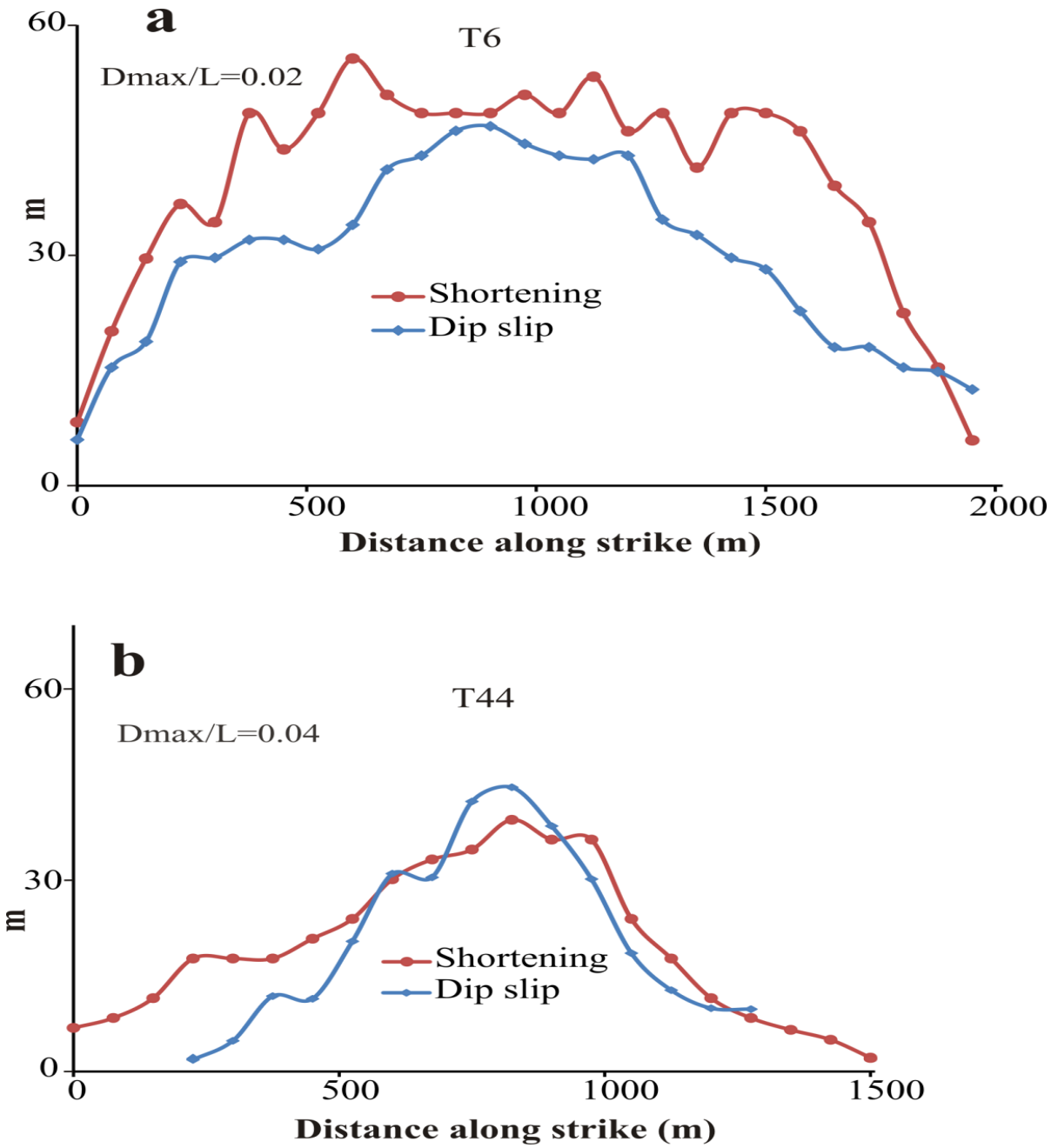


Figure 5.4: Dip slip and shortening distribution along a key horizon (IPM1) for isolated thrust related folds. (a) T6. (b) T44.

The thrust fault and fold pairs in Structure A, B and C include Faults T9, T10, T13, T17, T18, T19, T23 and T24. These thrust folds are either segmented or bounded by strike slip fault S10, S16, S20, and S21 (Figure 5.5). The structures were selected as representative examples to show the full range of interactions between thrust faults and strike slip faults within the dataset. Some of these structures have been described in Chapter 4 (Structure A and B), using structural maps of key horizons and seismic sections along strike. Here, the description of these structures is summarized using a time dip structural map of a single key horizon (IPM1) and seismic profiles, focusing on thrust fault and strike slip fault intersection zones. Sections were taken where seismic resolution is good, as zones of intersection are characterized by considerable loss in seismic amplitude (see Figure 4.14 e). Time dip structural map of Horizon IPM1 and seismic sections showing the internal geometry of the structure are shown in Figure 5.5 and 5.6.

#### *5.3.2.1 Map view*

Structures A, B and C when considered as a simple structure, has an along strike length of c. 24,000 m measured from the north-western end of Thrust fault T10 to the south-eastern lateral tip of Fault T23 (Figure 5.5). The thrust faults are generally linear, but some tend to curve close to their lateral tips where they are either intersected or bounded by strike slip faults.

Thrust fault T9 is intersected at one end by Fault S10, the interaction between both faults (T9 and S10) is a typical example of the Single end thrust fault - strike slip fault Interaction (Class B) described in Chapter 4 (see Figure 4. 22 b). The north-western end of T9 is overlapped by a minor back thrust (T10). This fault dips oppositely towards T9 forming a local antithetic convergent zone. T9 laterally extends c. 7,400 m, and is roughly linear with a strike trend of 145$^{o}$, but slightly curves close to S10 intersection zone. The footwall of T9 is

cut by another thrust fault (T13), which also displays the Class B Interaction with S10. T13 strikes c. 130$^{o}$, with a lateral length of c. 3400 m and it dips oppositely away from T9, displaying an antithetic divergent relationship (Morley et al. 1990; Higgins et al. 2007).

Thrust faults T17 and T18 are divergent antithetic thrust faults (Morley et al. 1990; Higgins et al. 2007), separated by a syncline. They are both intersected by strike slip fault at their central zone and lateral tips. They mainly strike 148$^{o}$ and 150$^{o}$ for T17 and T18, respectively, and show tip curvature close to their lateral ends (Figure 5.5).

The along strike length of T17 is c. 4,800 m measured between both lateral tips bounded by strike slip faults of opposing sense of shear and trend. The south-eastern and north-western tips of T17 are intersected by strike slip fault S10 and S20, respectively. T18 has a strike length of c. 4,700 m, and is bounded at its north-western end by S20, while the south-eastern end is free from strike slip fault intersection. Both thrust faults (T17 and T18) are intersected at their central zone by strike slip fault S16 at c. 1200m. A minor thrust fault (T19) occurs at the hanging wall of T17, forming a local convergent zone within the folded structure. The width of T19 is c. 1800 m, striking c. 155$^{o}$ and it is intersected at its south-eastern end by strike slip fault S16.

Fault T23 is another fault bounded at both tips by strike slip faults of different shear sense: its north western and south eastern end is intersected by S20 and S21, respectively. The strike trend for T23 is 145$^{o}$ and it has a lateral length of c. 4,100 m. Fault T24 is synthetic to fault T23, and it strikes 144$^{o}$ and it has a lateral distance of 1,750m.

The strike slip faults cross-cutting the case study thrust faults extend beyond the selected area of study (Figure 5.5). They are generally sinusoidal: exhibiting the shape of an S along their whole length (Figure 5.5). However, within the selected case region, these strike slip faults are almost straight with slight bends close to where they intersect thrust faults (Figure 5.5).

S10 and S21 are dextral faults, segment of these faults within the case study area strike between 010 and 013. Fault S10 intersect the south-eastern end of T9 and T13, and the north western end of T17, while S21 intersects the south eastern end of T23. In contrast, S16 and S20 are sinistral faults striking 078 and 080 respectively. S20 marks the NW limits of T23 and T24, and the SE limits of T19 and T18.

#### *5.3.2.2 Sectional view*

Seismic sections along the compartmentalized structures are shown in Figure 5.6 a-f. The principal thrust faults underlying anticlines (T9, T17, T18 and T23) are blind: their upper tips lie below Horizon BPM3. They mainly detach within the upper Messinian unit and dip between $35^{o}$ and $40^{o}$ (Figure 5.6 a-f).

The strike slip faults are almost vertical, dipping between $80^{o}$ and $90^{o}$ (Figure 5.6 g-h). They extend from the detachment layer (below Horizon M) to BPM3, with some reaching the seabed horizon. Strike slip faults S10, S16 and S20 generally splay upward forming flower structures (McClay and Bonora 2001).

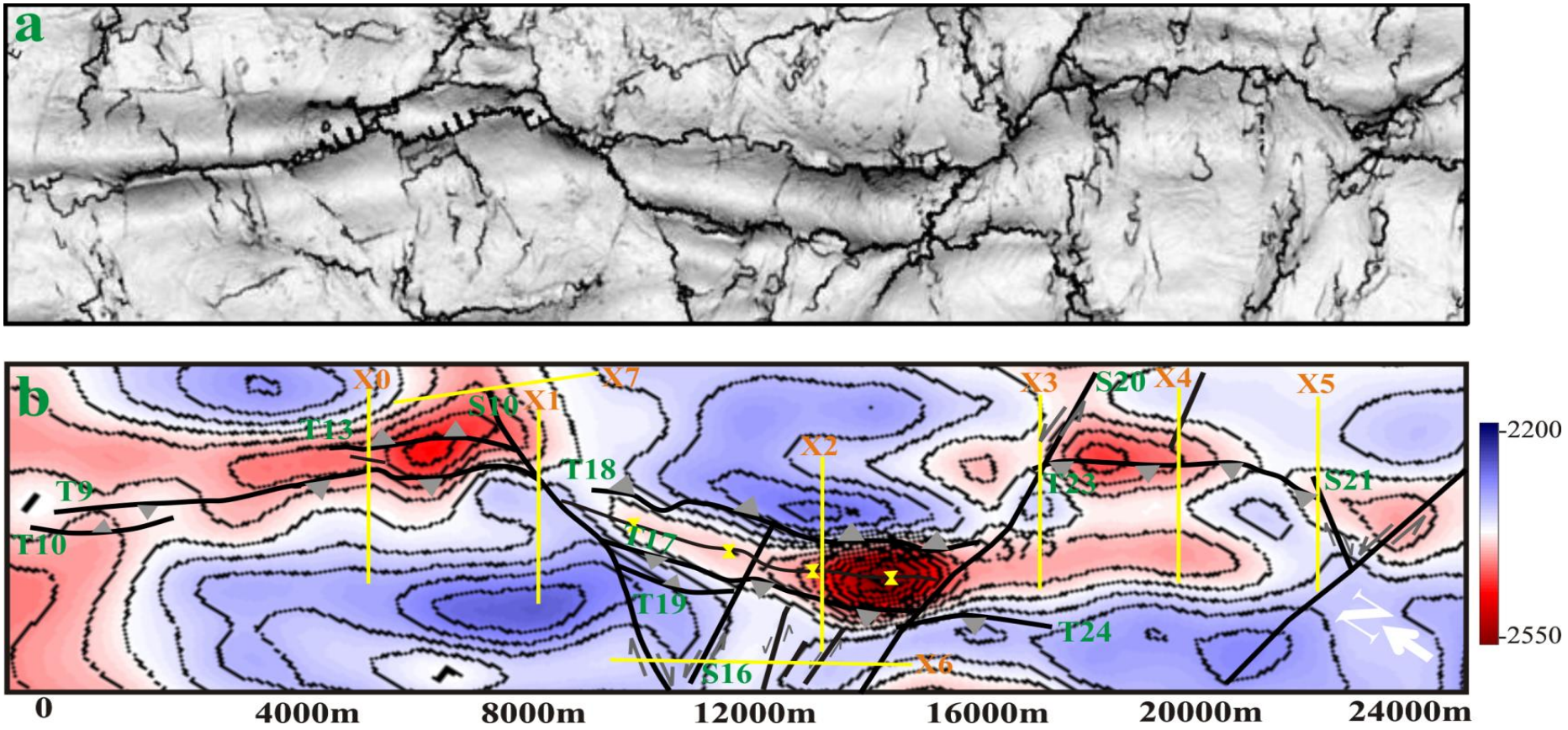


Figure 5.5: Time dip Map of horizon elevation IPM1 in two-way –time (ms) showing traces of thrust faults T10, T9, T13, T17, T18, T19, and T23 segmented or bounded by strike slip fault S10, S16, S20, and S21. (a) Uninterpreted (b) Interpreted. Line x0 - x7 show locations of the seismic sections in Figure 5.6. Red/yellow colour represents structural low. Red represents structural low. Blue colour represents structural high. Contour interval: 25ms.

The zones of intersections between the thrust faults and strike slip faults are characterized by poor seismic resolution as noted in the previous section. However, notable fault cross-cutting relationships can be observed close to some intersection zones (Figure 5.6 b, d and f see Figure 5.5 for location). Thrust fault T9 appears to have been cross-cut at its south eastern tip by S10 into two segments: upper and lower (Figure 5.6 b). Whereas, for T23, its north-western end appears to cross-cut S20 with no notable change in dip at the zone of intersection (Figure 5.6 d). The south-eastern end of T23, however, is cross-cut by S21, at this zone, S21 shows an abnormal, probably due to intense shear (Figure 5.6 f).

### 5.3.3 Kinematic Packages and Fold Dating

Generally, the folds described in this study are overlain by syn-kinematic packages (Figure 5.6). These sediments have been used to examine the kinematic interaction between deformation and channel levee development in the study area (Clark and Cartwright 2009, 2011). Here, kinematic sediments were used to predict the onset and rate of uplift of the principal thrust folds in Structures A, B and C relative to deposition. Generally, the sediments overlying the folds show more consistent reflections at backlimb compared to forelimb. Therefore, for easy description, this study focuses on the backlimb fold sediments.

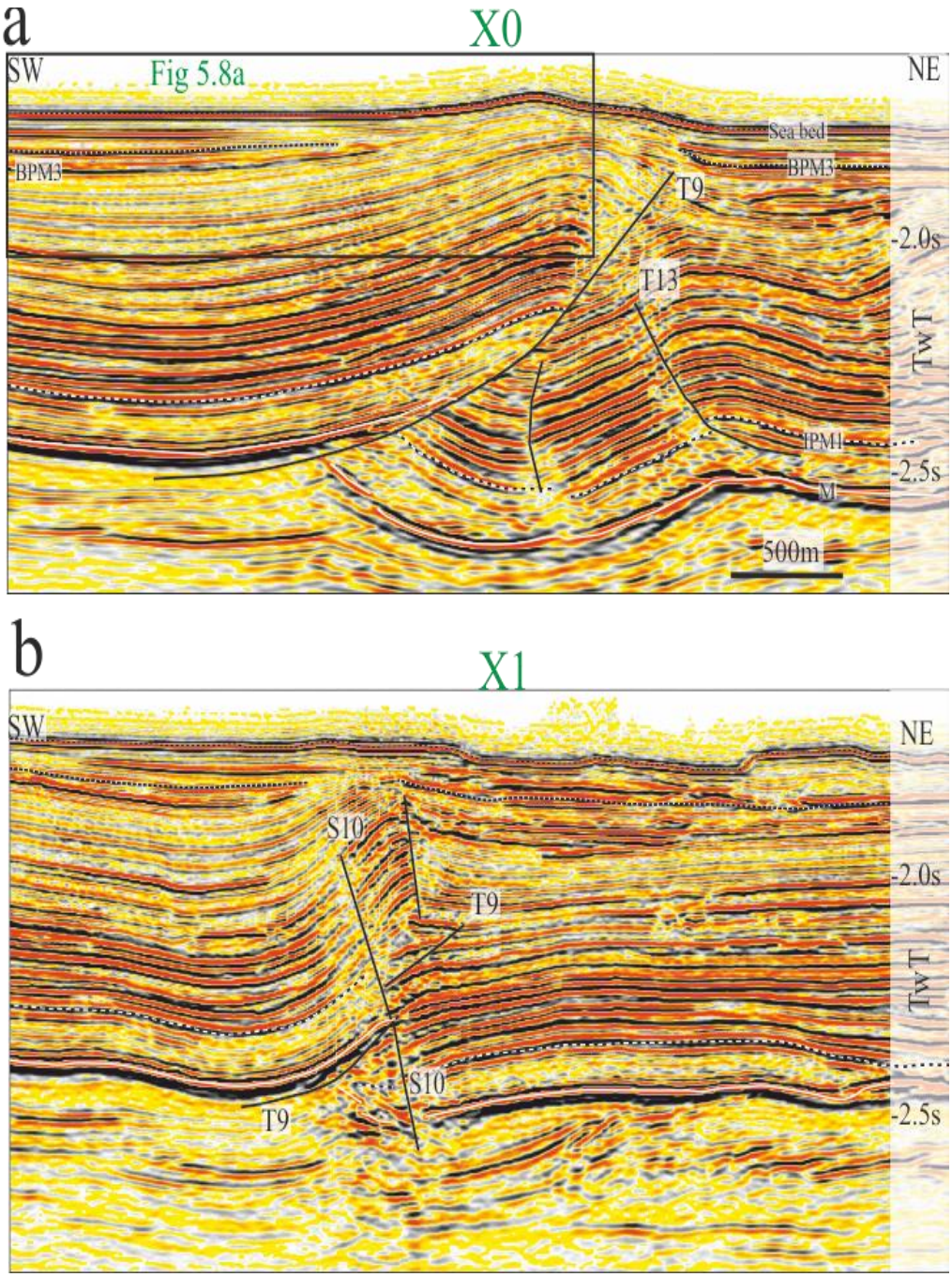


Figure 5.6: Selected seismic sections along the case study structures. Locations of seismic lines (a-f) in Figure 5.5. Vertical exaggeration of 1.5. Horizons M, IPM1, BPM3 are regional stratigraphic horizons. The selected squares in Figure 5.6 a, c, d and e are magnified in Figure 5.7, they show the geometry of the sedimentary kinematic packages above the folds.

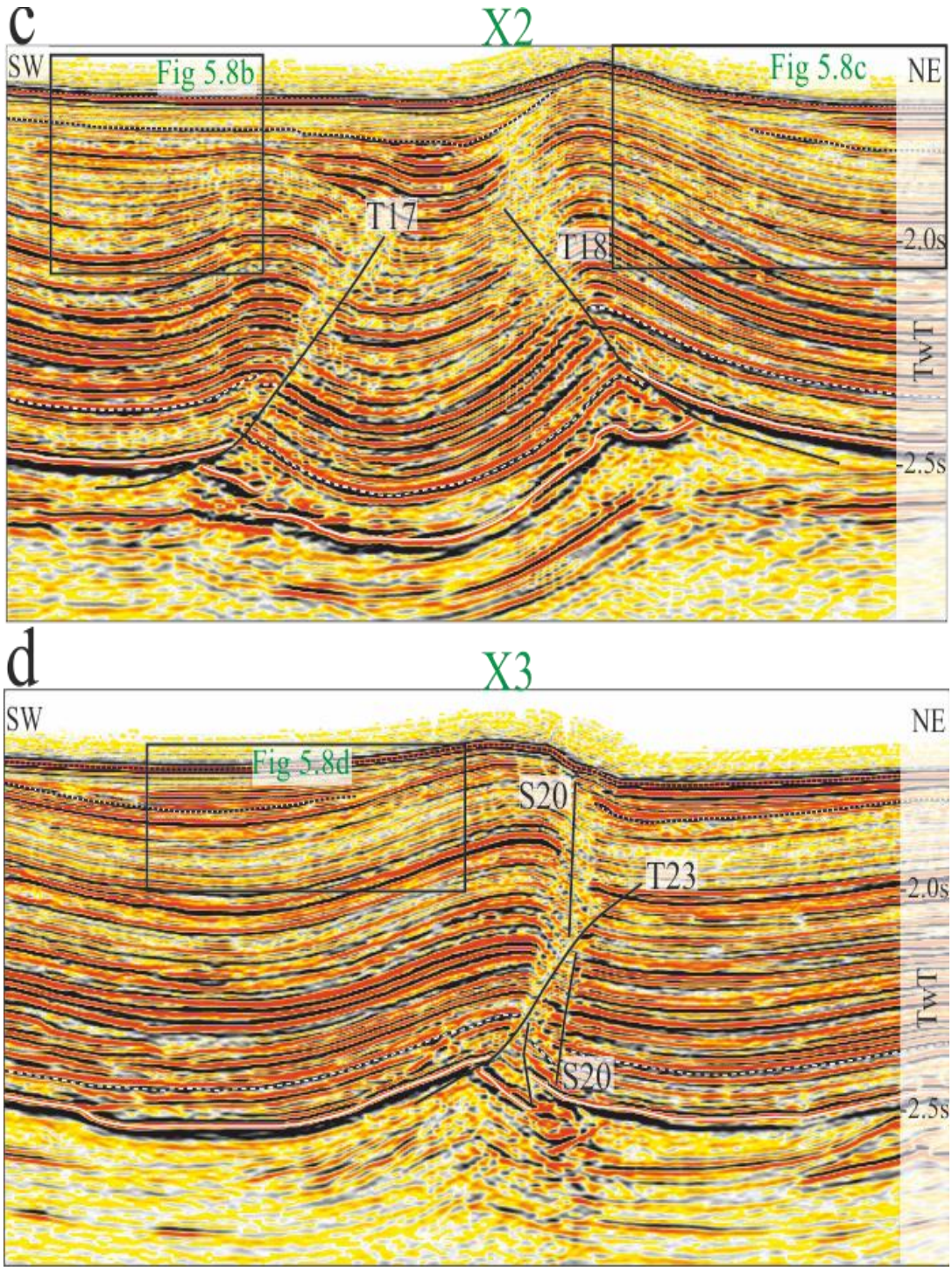


Figure 5.6: Selected seismic sections along the case study structures. Locations of seismic lines (a-f) in Figure 5.5. Vertical exaggeration of 1.5. Horizons M, IPM1, BPM3 are regional stratigraphic horizons. The selected squares in Figure 5.6 a, c, d and e are magnified in Figure 5.7, they show the geometry of the sedimentary kinematic packages above the folds.

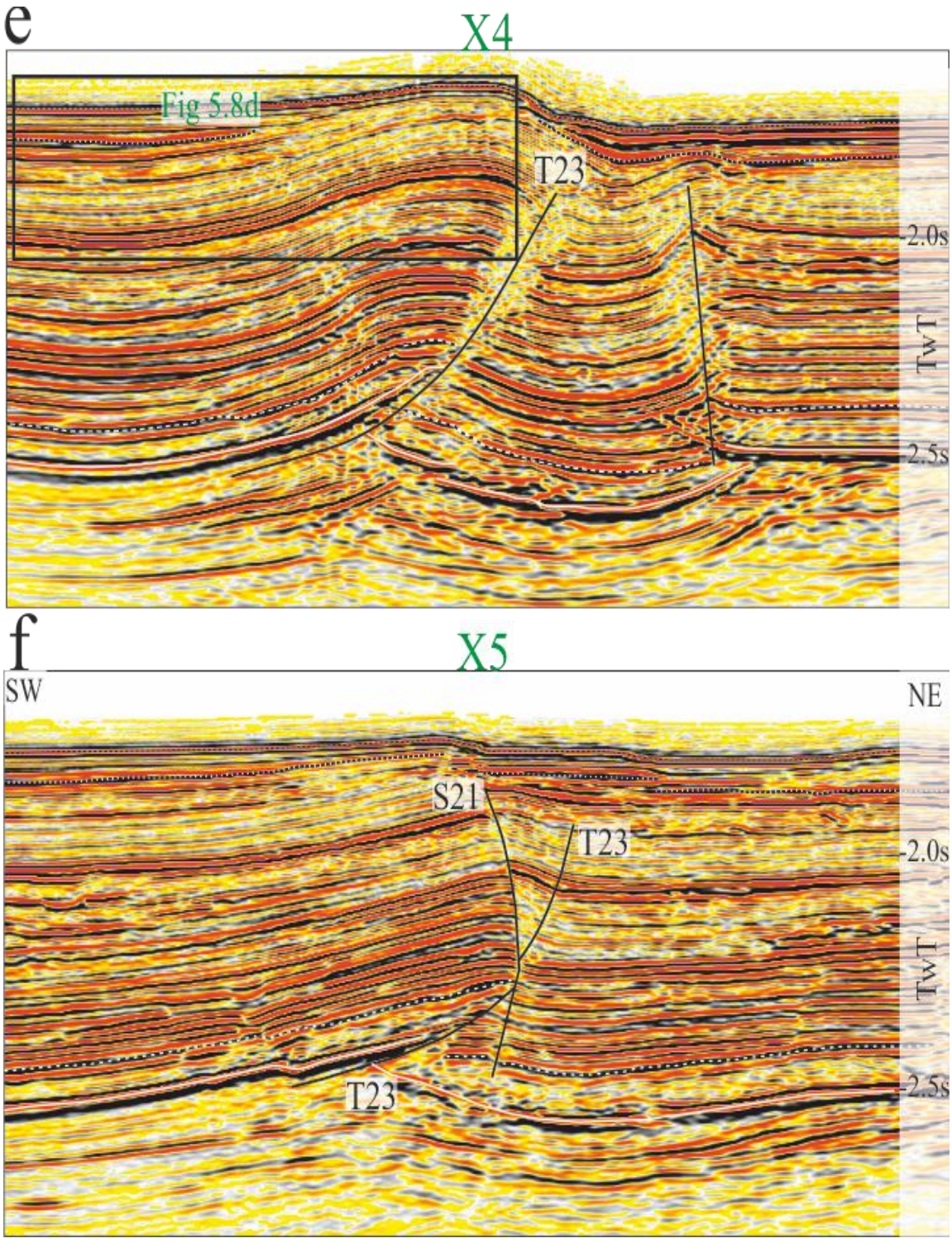


Figure 5.6: Selected seismic sections along the case study structures. Locations of seismic lines (a-f) in Figure 5.5. Vertical exaggeration of 1.5. Horizons M, IPM1, BPM3 are regional stratigraphic horizons. The selected squares in Figure 5.6 a, c, d and e are magnified in Figure 5.7, they show the geometry of the sedimentary kinematic packages above the folds.

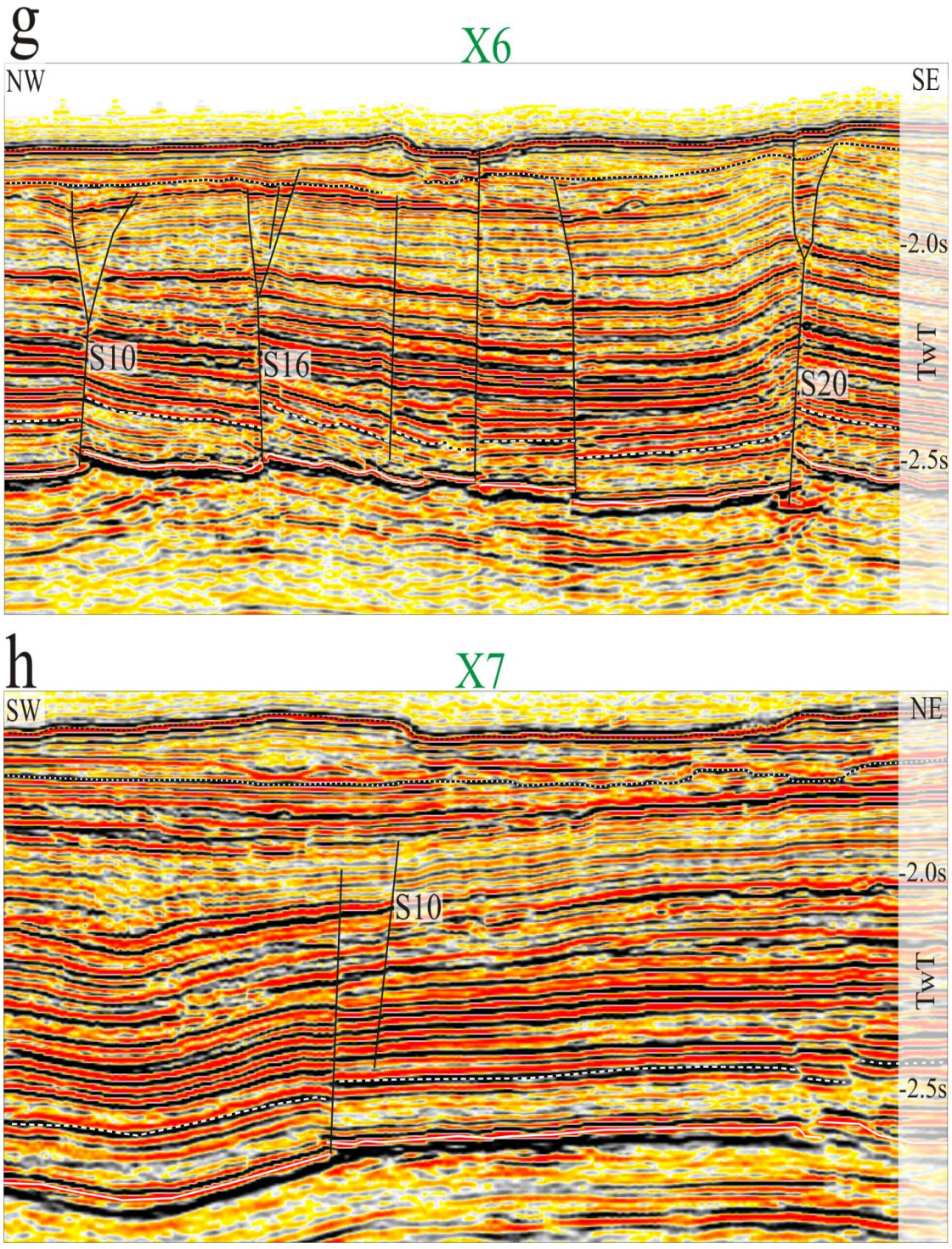


Figure 5.6: Selected seismic sections along the case study structures. Locations of seismic lines (a-h) in Figure 5.5. Vertical exaggeration of 1.5. Horizons M, IPM1, BPM3 are regional stratigraphic horizons. The selected squares in Figure 5.6 a, c, d and e are magnified in Figure 5.7, they show the geometry of the sedimentary kinematic packages above the folds.

The stratal reflections above the back limb of the case study folds are well displayed in Figure 5.7. The folds overlying faults T9, T18 and T23 are mainly overlain by syn kinematic stratal reflections (Figure 5.7a, c and d); this indicates that sedimentation is contemporaneous with deformation (Poblet and Lisle 2011).According to Clark and Cartwright (2011), Horizon BPM3 represents the base of syn-kinematic sedimentation. In this study, the first apparent stratal onlap on the limbs of T9, T18 and T23 is observed at the horizon immediately below BPM3, this horizon is termed X. Horizon X corresponds to the time majority of the thrust related folds in the study area initiated. Generally, the thickness between reflections thins towards the fold crest and is characterized by pinch outs represented as onlaps and offlaps. Fold (T9) shows more consistent onlapping units which tend to be the most flat lying compared to folds of T18 and T23 (Figure 5.7a). For folds (T18 and T23), onlapping reflections are at least separated by a single layer of offlap and overlap respectively (Figure 5.7c and d). Generally, the deposition rates above T9, T18 and T23 are lower than fold and fault uplift rates; this is inferred from the positive bathymetric relief directly above the folds and pattern of reflections above their limbs (Poblet et al. 1997).

In contrast to the folds overlying faults T9, T18 and T23, that of fault T17 is mainly overlain by a localised post-kinematic sedimentary unit (Zoetemeijer 1993) (Figure 5.7b). Horizon X above T17 is flat lying and it onlaps close to the fold crest, whilst, Horizon BPM3 clearly overlaps the fold crest and it shows constant thickness with younger sediment over T17 (Figure 5.7b).

In summary, all the main thrust related folds (T9, T17, T18 and T23) are interpreted to have initiated when Horizon X was deposited, probably in the early Pleistocene (Gradmann et al. 2005). Shortly afterwards, fault T17 became inactive, while T9, T18 and T23 remained active.

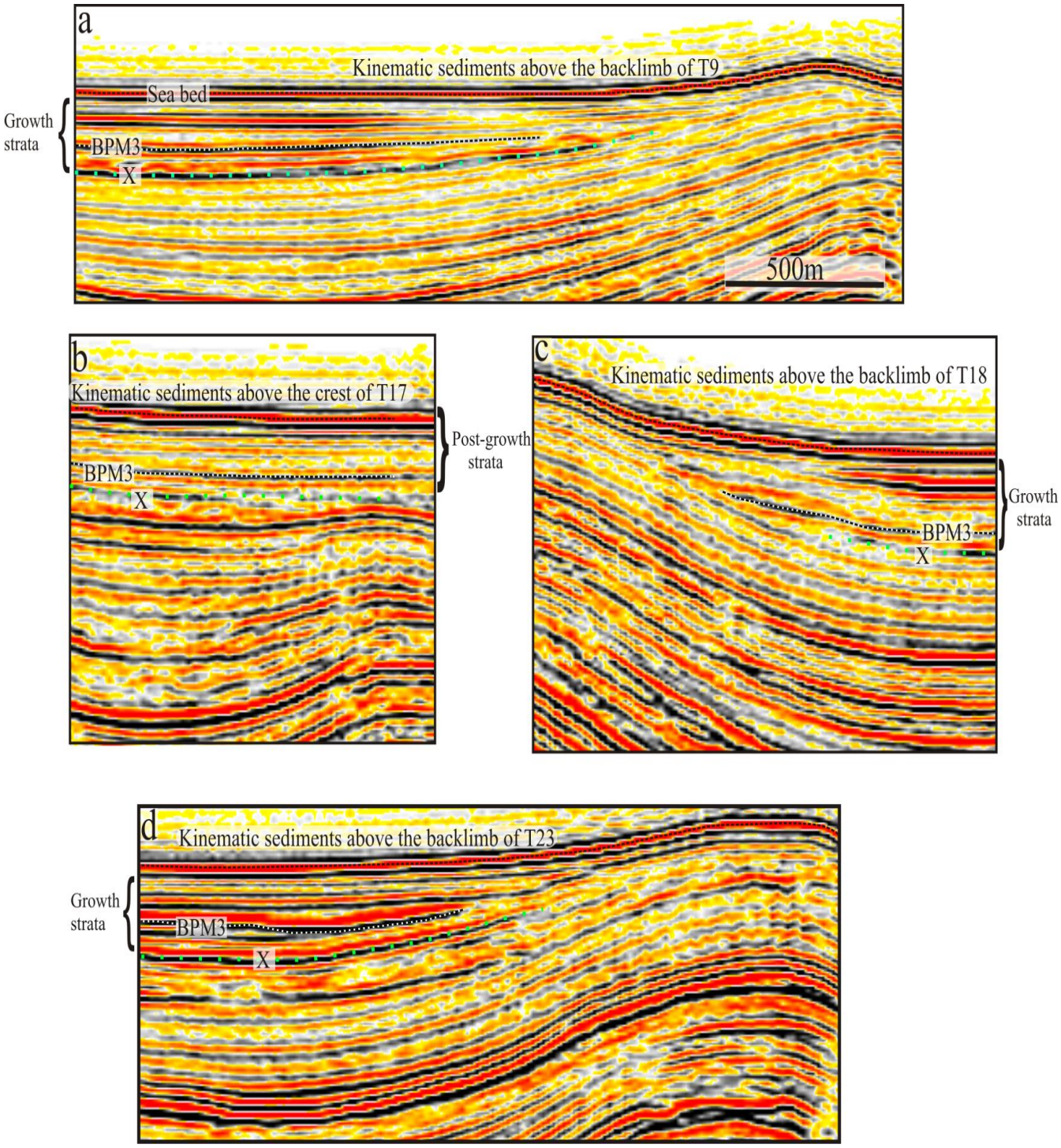


Figure 5.7: Magnified sections (see Figure 5.6 for location), showing the kinematic sediments above the back limbs of the thrust related folds. (a) T9, (b) T17, (c) T18 and (d) T23.

### 5.3.4 Individual Fault Dip-Slip Profiles

Individual dip-slip profiles of the thrust faults in structures A, B and C are shown in Figure 5.8 and 5.9a-g**.** For easy description, the structures are described with reference to the length of the structures. Clearly, the majority of the profiles do not resemble those of the isolated faults described in this study (T6 and T44, Figure 5.4). The profiles mainly show a high gradient change which corresponds to zone of strike slip fault intersection. Some of the faults are characterized by minor irregularities and multiple maxima which may be the result of segment by linkage or lithological contrast (Peacock and Sanderson 1991; Scholz et al. 1993; Cartwright et al. 1995; Willemse and Pollard 2000). In the absence of these irregularities, the profiles show a wide variety of shapes relative to the number of intersection along the thrust fault width (Figure 5.9a-g).

The majority of the profiles intersected by strike slip fault at one end tend to be asymmetric (Figure 5.9a-c), except for fault T13 which has its maximum dip-slip close to the centre (Figure 5.9d). Beyond this difference, profiles for the single end intersected faults characteristically have their elevation close to strike slip fault intersection where they show a rapid decrease. The gradient change close to the intersection is 0.3, 0.12 and 0.26 for faults T9, T19 and T24 respectively (Figure 5.9a-c).

Thrust faults T17, T18 and T23 show different profile geometries different from faults intersected at one end (Figure 5.9e-g). Profiles for faults T17 and T18 are characterized by a central decrease in dip-slip which increases towards both lateral ends (Figure 5.9e and f). T17 reached its maximum displacement (c. 513 m) at c. 6,500 m of the profile length close to fault S20 intersection where it rapidly decreases in slip with a gradient of 0.37 (Figure 5.9e). From the point of maximum displacement at c. 6,500 m (along strike), it shows an abnormal decrease close to fault S16 intersection at c. 5,700 m (along strike) with a gradient of 0.21. At this zone of displacement decrease, the profile shows no notable change in displacement

between c. 4,800 to c. 5,700m (along strike). At c. 5,800 m (along strike), it increases to its maximum value at c. 6,800 m close to where it intersects S10 before an abnormal decrease in elevation (gradient of 0.37).

For fault T18, the displacement profile increases from S16 intersection with a gradient of 0.6 to its maximum elevation at 5,000 m (along strike). In the absence of minor displacement variations, the profile shows no significant change between 5,000 m to the end of the profile length close to S20 intersection (Figure 5.9f). Towards the non-intersected end, the profile shows a local maximum elevation (at 3,000m along strike) before decreasing to zero.

Fault T23 shows a dip-slip profile characterized by several maxima and minima (Figure 5.9g). The most distinct irregularity is observed close to the south-eastern end of the fault (between 4,200-4,800 m along strike), where displacement reached a maximum value of c. 400 m. The maximum displacement is followed by a local irregular minimum and maximum towards the S21 intersection. The average gradient from the maximum displacement (at c. 4,800 m) to the displacement minimum close to S21 intersection (at 5,800 m) is 0.3. No notable change in displacement is observed from 4400 m to 3300 m along the profile length, it decreases with an average gradient of 0.06 from 3300 m to S20 intersection.

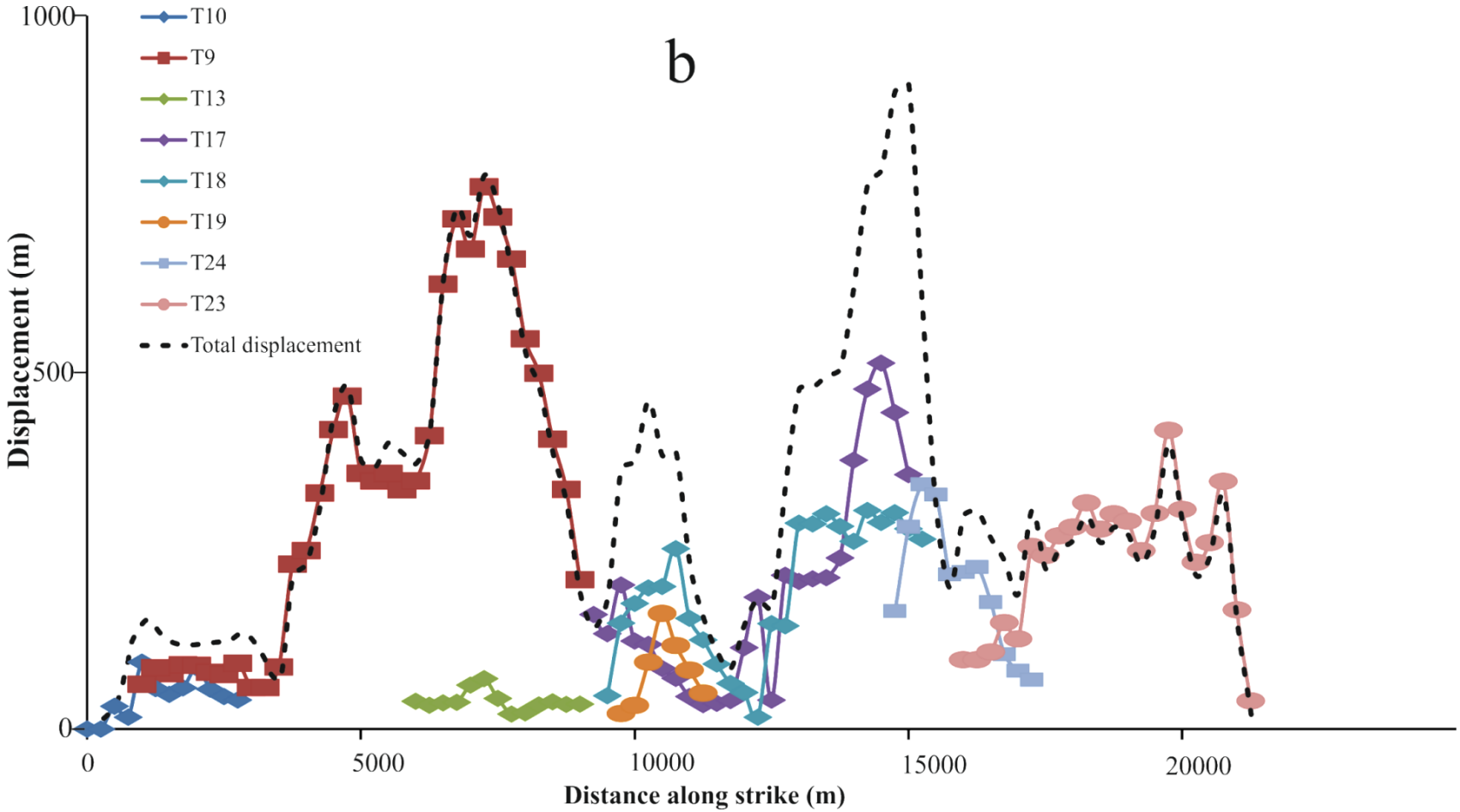


Figure 5.8: Profiles for Individual thrust fault displacement and summed displacement of the thrust faults along Horizon IPM1.

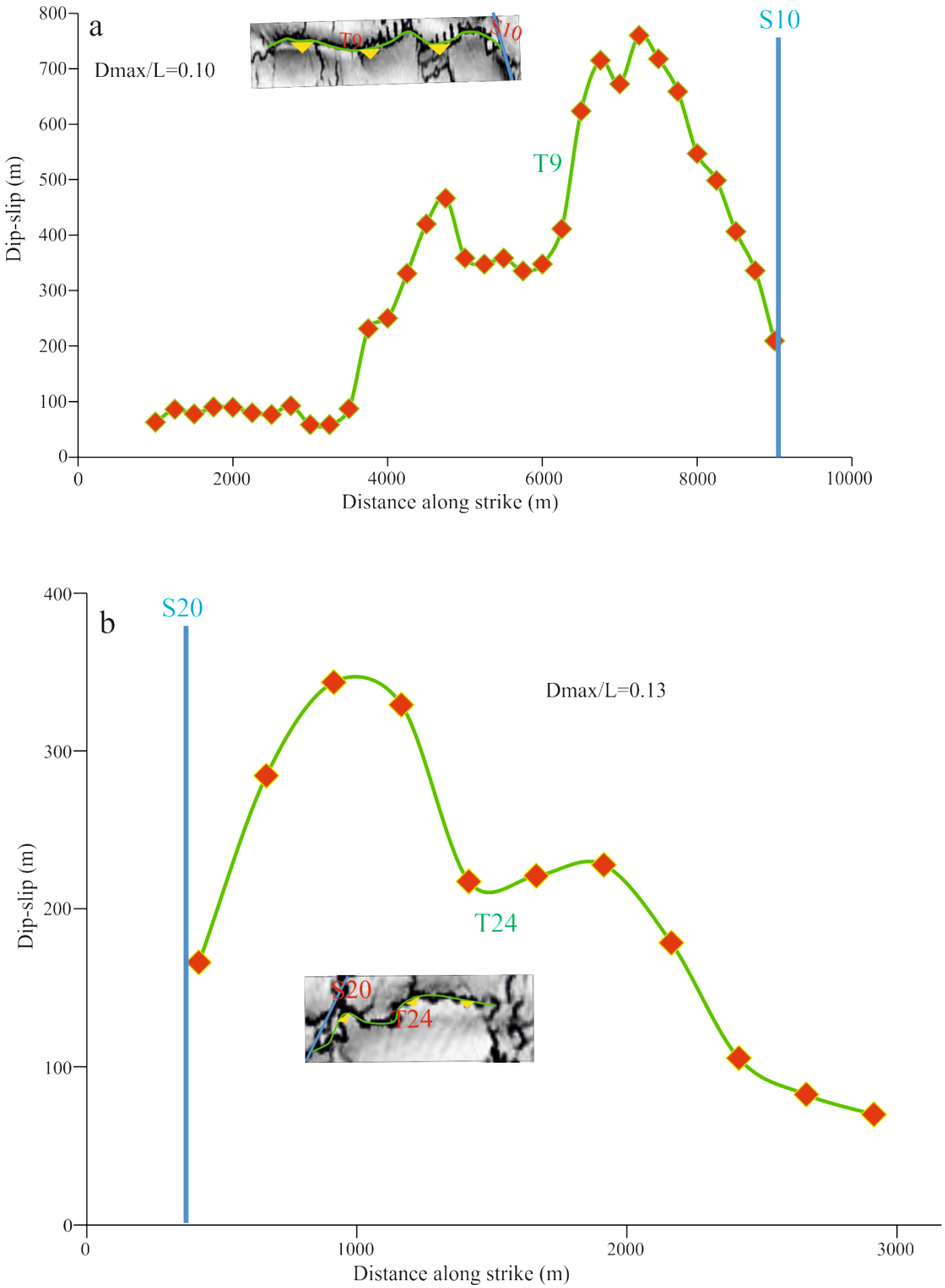


Figure 5.9**:** Dip-slip distribution along strike for the intersected thrust faults.(a) T9, (b) T19, (c) T24, (d) T13, (e) T17, (f) T18 and (g) T23. Figure inset represents time dip structural map showing traces of the intersected faults. The blue vertical line represents strike slip fault.

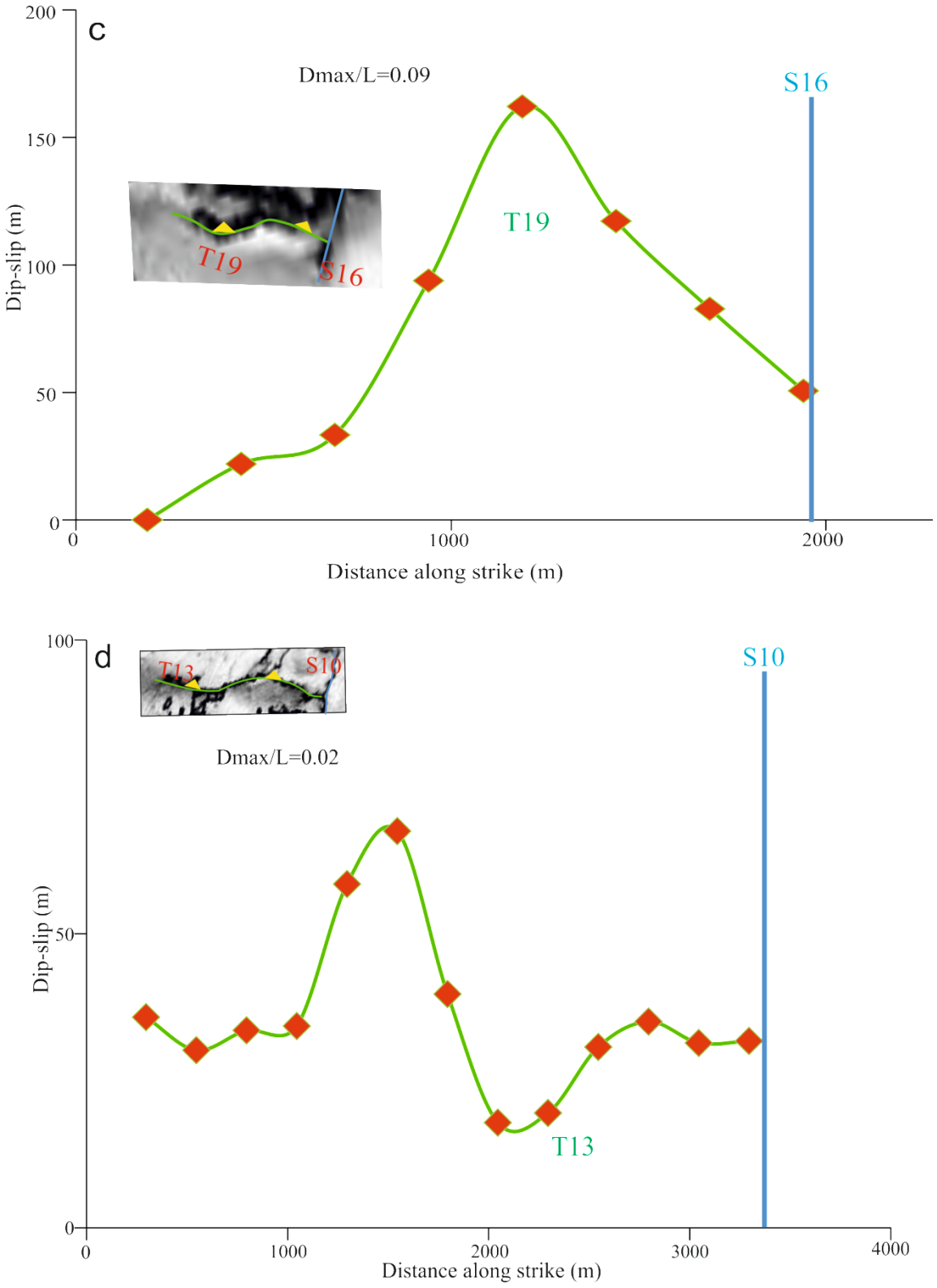


Figure 5.9: Dip-slip distribution along strike for the intersected thrust faults.(a) T9, (b) T19, (c) T24, (d) T13, (e) T17, (f) T18 and (g) T23. Figure inset represents time dip structural map showing traces of the intersected faults. The blue vertical line represents strike slip fault.

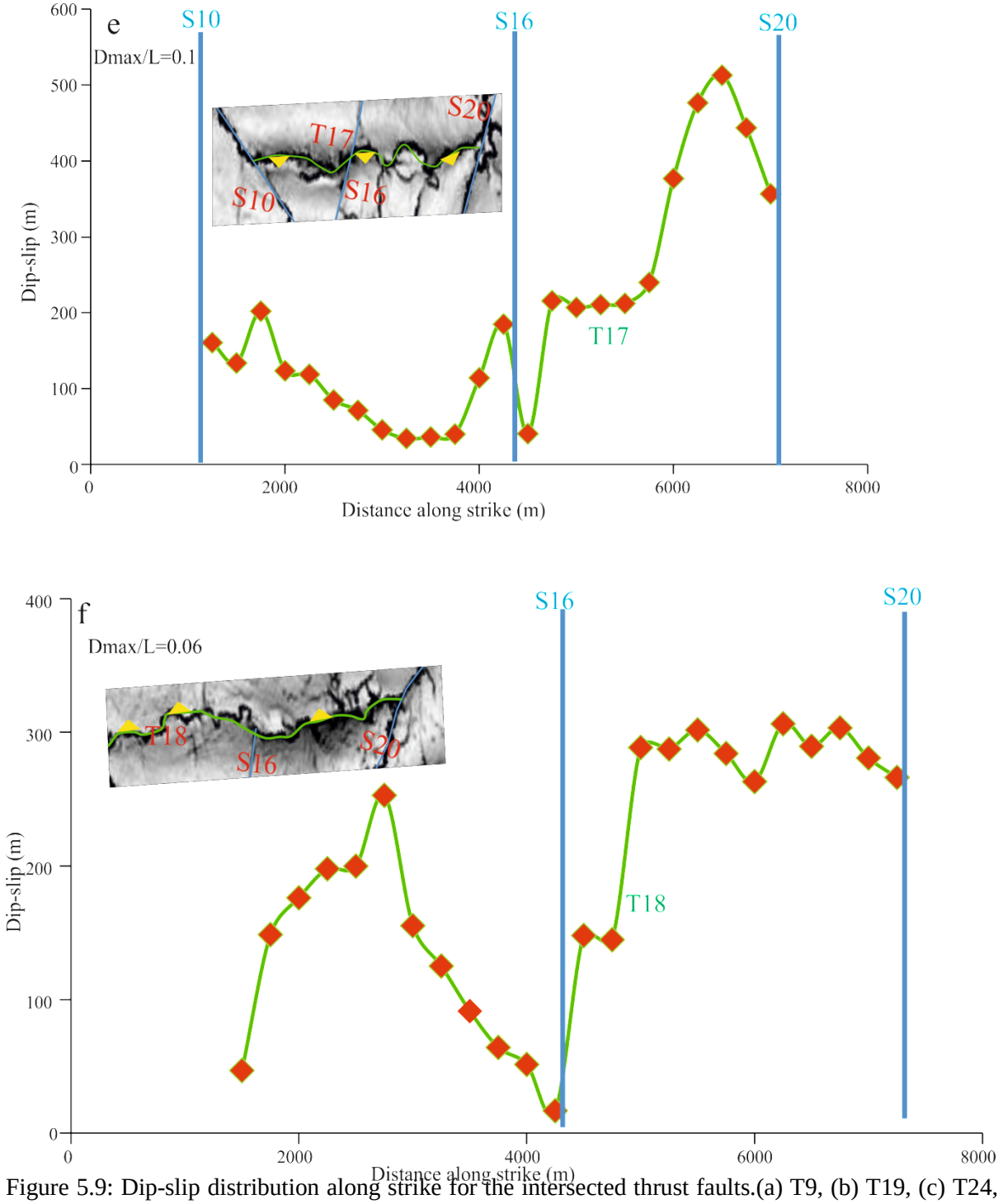


Figure 5.9: Dip-slip distribution along strike for the intersected thrust faults.(a) T9, (b) T19, (c) T24, (d) T13, (e) T17, (f) T18 and (g) T23. Figure inset represents time dip structural map showing traces of the intersected faults. The blue vertical line represents strike slip fault.

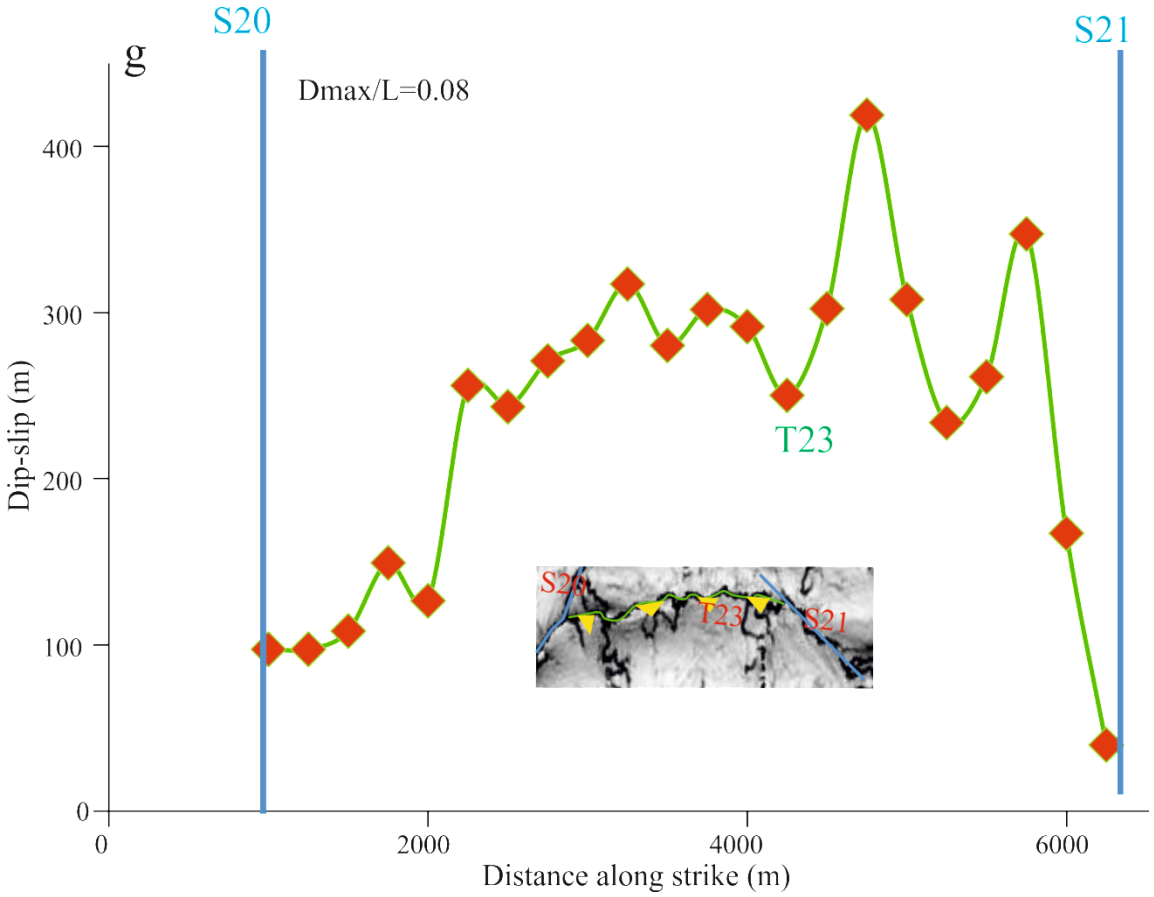


Figure 5.9: Dip-slip distribution along strike for the intersected thrust faults. (a) T9, (b) T19, (c) T24, (d) T13, (e) T17, (f) T18 and (g) T23. Figure inset represents time dip structural map showing traces of the intersected faults. The blue vertical line represents strike slip fault.

### 5.3.5 Relationship Between Displacement and Shortening

One of the main purposes of this section is to compare the pattern of shortening and summed displacement distribution, particularly close to strike slip fault intersections. Aggregate displacement of the faults and total shortening along profiles Horizon IPM1 are shown in Figure 5.10. Both profiles show similar geometry along strike and they both respond to similar anomaly at zones of strike slip fault intersections (Figure 5.10). The profiles increase from zero at both lateral tips of the structure as a whole, with local variations which may be attributed to segment by linkage (Cartwright et al. 1995) or minor fault intervention(Baudon and Cartwright 2008b). Beyond these irregularities, both profiles commonly, but not exclusively, show local peaks, accompanied by rapid decease in elevation close to intersections (Figure 5.10c).

The shortening profile generally has a higher elevation and steeper gradients close to intersection zones than the summed displacement profile. A notable local peak exhibited by both profiles is close to Fault S10 intersection zone between 7000 -7300 m of the profile length. At this zone (7000 -7300 m), the summed displacement profile elevates to 800 m while that of shortening reaches 2450 m. The profiles commonly decrease rapidly with gradient of 0.4 and 2.2 for the summed displacement and shortening, respectively at the zone of intersection (S10). From S10 intersection at c. 10000 m along strike, the shortening profile increases to a value of 1650m at c. 11000 m with gradient of 2.1, while the displacement profile increases to 500 m with a gradient of 0.5. From this local peak (1100 – 1150m), the profiles decrease gradually towards the S16 intersection, followed by an increase towards the S20 intersection. The profiles reached their maximum elevation close to the S20 intersection at c. 2800 m and c. 900 m for shortening and summed displacement, respectively (Figure

5.10c). At this zone, shortening profile decreases rapidly with gradient of 2.8, while the displacement decreases with a gradient of 0.7.

In contrast to other parts of the fold length, the profiles (summed displacement and shortening), exhibit a slightly different in geometry between the intersection zone of S20 and S21 (Figure 5.10c). In the absence of some irregularities attributed to linkage as aforementioned, the shortening profile increases to a local maximum of 1250m at 18000m along strike with an average gradient of 0.04. From this zone of local maxima, the shortening plot shows a decrease followed by increases to S21 intersection zone, to a value of 1100 m, before decreasing with a high gradient of 0.7. The summed displacement profile at this zone (between S20 and S21), also shows a increase to 400m at c. 16000 m and it shows an almost steady gradient to the S21 intersection zone. Multiple maxima separated by minima are observed close to the S21 intersection zone before decreasing abruptly (Figure 5.10c).

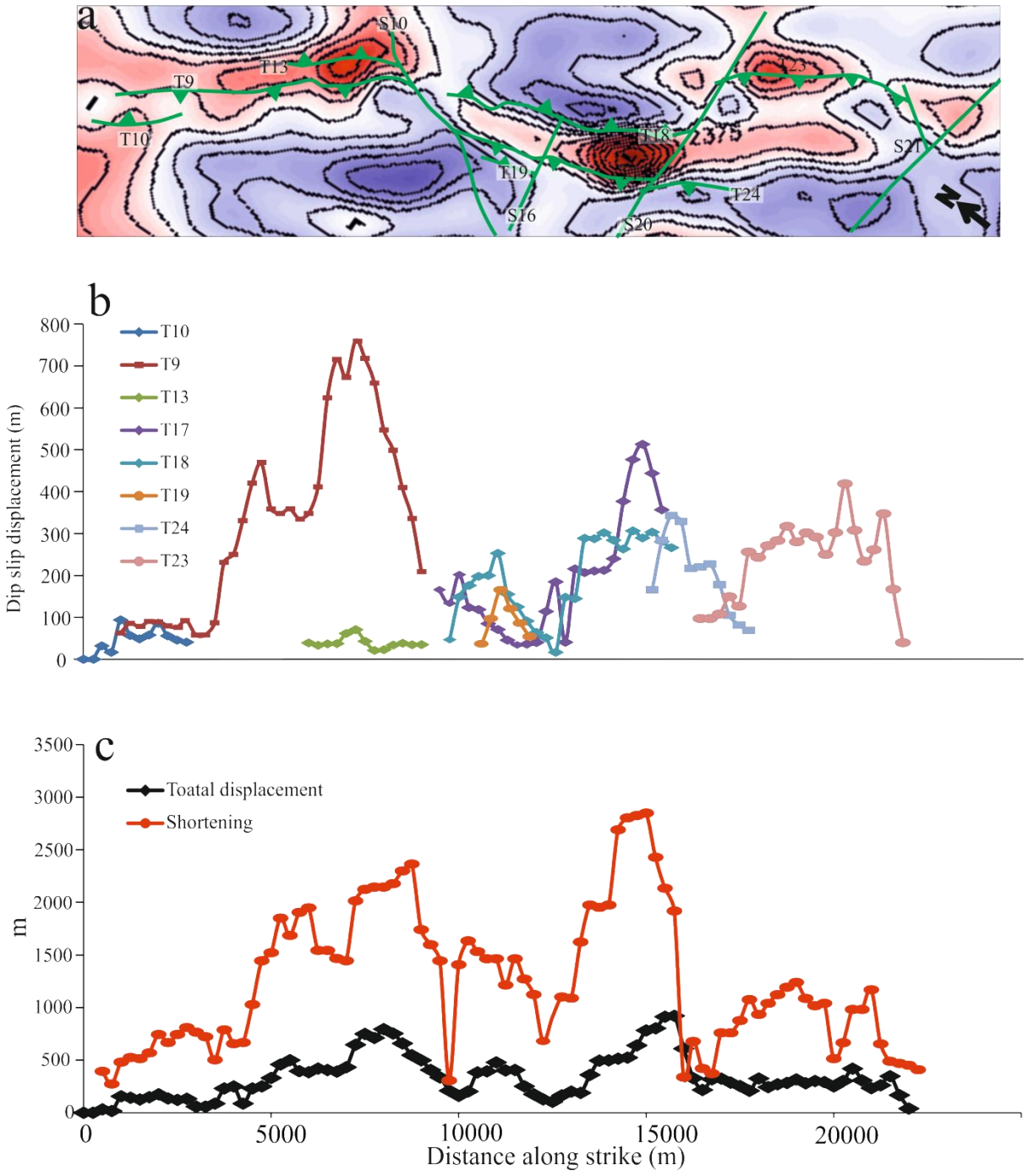


Figure 5.10: Aggregate values of fault dip slip and shortening along Horizon IPM1. (a) Structural time dip map in two travel time showing traces of the case study structural elements. (b) Horizontal dip slip distribution for each faults (c) Lateral dip-slip displacement distribution and fold shortening distribution.

## 5.4 INTERPRETATION

It has been shown in this study and in Chapter 4 that the thrust faults in Structures A, B and C either cross-cut or are themselves transected by strike slip faults (Figure 5.6 b and d). In some cases, intersection zones show notable changes in fault shape compared to isolated zones (Figure 5.6 f). Fault cross-cut, and change in fault shape at intersection zones indicates fault interaction. The effect of fault interaction or interruption to propagation is best examined by analysing their displacement distribution (Ellis and Dunlap 1988; Davis *et al.* 2005). The displacement distribution of thrust faults described in this study shows some striking similarities to those of interacting faults described in other studies (Nicol et al. 1995; Davis et al. 2005). This section mainly focuses on the interpretation of displacement characteristics of thrust faults bounded or segmented by strike slip faults.

### 5.4.1 Displacement Analysis

Clearly it can be observed within the results presented here, that intersecting thrust faults have different tip line surface and dip slip displacement profile geometries from isolated faults. Profiles for the majority of the intersected faults are asymmetric having maximum displacement close to zones of intersection as opposed to central maximum displacement exhibited by isolated faults (Muraoka and Kamata, 1983). Faults with maximum displacement at lateral tip or tips are commonly interpreted as a product of barrier to propagation (Nicol et al. 1995; Davis et al. 2005). Barriers may be changes in material strength due to lithology or fracture density or overlapping faults (Muraoka and Kamata 1983; Larsen 1988; Kim and Sanderson 2005). Here displacement decreases abruptly at intersection zones (Figure 5.8 - 5.10). The average displacement gradient close to intersection zones is 0.27; this value is much higher than the gradients close to isolated tips, which are less than 0.05.

Intersecting faults generally have higher Dmax/L than isolated faults in this study. The D.max/L ratios of the 2 non-intersected faults described here are 0.02 and 0.04 for T6 and T44 respectively (Figure 5.4). According to Shumin and Dixon (1991) model of fault development and propagation, isolated faults should have D.max/L values averaging 0.04 which is almost in agreement with the examples of non-intersected faults described in this study. Although, natural examples of faults characterized by central maximum displacement have D.max/L of 0.07 (Elliott, 1976). This disparity in D.max/L between natural examples of isolated faults and the ones analysed here may be attributed to factors such as linkage and mechanical barriers which are beyond the scope of this chapter. Nevertheless, Manighetti et al (2004), interpreted faults with D.max/L ratio as high as 0.07 to be restricted faults, since their lateral profiles are either asymmetric or quasi-elliptical with lateral tip/tips characterized with very high gradients. Here, intersecting faults have D.max/L ratios as high as 0.1, which is clearly an indication of restriction to propagation

#### *5.4.1.1 Displacement geometry of restricted faults*

The variation in displacement geometry exhibited by restricted faults may be influenced by the region, and number of zones restricted. The interaction between thrust faults and strike slip faults has been classified into several end member interactions (class A-F) in chapter 4. The classification of the end members is based on the zone or number of zones intersected. Each of the end members shows distinctive thrust fault displacement geometry from the other.

Thrust fault displacement geometry of the Class B type end member interaction is similar to that of the single tip restricted faults (Nicol et al., 1995). They mainly have their maximum displacement and high gradient close to the intersected tip. Those restricted half way along the fault length have been termed half restricted fault (Nicol et al., 1995). T9 and T24 are

typical examples of thrust faults in class B interaction. Their displacement profiles (T9 and T24) are asymmetric, having their maximum elevation close to intersection zone. It should be noted that Fault T9 shows some other irregularities, particularly at zones where it overlaps Faults T10 and T13, this may be as a result of linkage or other forms of fault restriction.

Other examples of thrust faults in the Class B interaction end member include Faults T13 and T19, these faults do not have high gradient and maximum slip close their intersected tips as may be expected for a fault restricted at tip. This may be as a result of distance from the initiation distance of the thrust faults (T13 and T19), to the strike slip faults acting as barrier to fault propagation. Faults initiated closer to barrier would display a steeper displacement profile gradient than faults initiated farther away. (See Chapter 7, Section 7.23 for details).

Profiles for faults restricted at both lateral tips have been termed Double tip restricted faults (Manighetti et al. 2001a; Manighetti et al. 2004). Double tip restricted faults normally show high gradients at both lateral ends, with maximum slip at one end or few meters to the centre (see Figure 3 d-f of Manighetti et al 2001). However, the slip profile for the thrust faults restricted at both tips in this study (Class C and D end members), show some contrasting geometry from the Double tip restricted faults of Manighetti et al., (2001). For example, Thrust fault T23 is an example of a Class D end member; it displays flat dip-slip distribution at the centre, separating a zone of maximum slip and steep gradient at one end from the other end characterized by gentle decrease in displacement (Figure 5.9g). The gradual slip decrease may indicate that the faults initiated at some distance away from the barrier (strike slip faults) as demonstrated in Figure 7.7 in Chapter 7

Another example of thrust fault restricted at both ends by strike slip faults is Fault T17, this fault shows an increase in slip towards both ends of intersection from the centre of minimum displacement. This profile geometry displayed by Fault T17 is not a simple double restricted

fault similar to those observed in other studies (Manighetti et al., 2001; 2004). This is because it has a central intersection zone and therefore can be interpreted as a combination of class D, and E or F end members (see 4.22 c-f in Chapter 4).

Similar to Fault T17, T18 shows a displacement minimum at the centre (Figure 5.9e and f). The central displacement minimum displayed by the thrust faults (T17 and T18) is interpreted to be a function of S16 intersection zone, as aforementioned. It is difficult to ascertain whether the central zone of T17 and T18 propagated past S16 as in the case of class E end member or S16 is the cross-cutting faults such as the Class F end member (see Chapter 4, Figure 4.22). The displacement geometry displayed by Faults T17 and T18 resembles that seen on faults in Afar and have been termed elliptical with taper (Manighetti et al., 2001). The elliptical with taper type profile suggests that the fault is restricted at one end, while towards the other end, it propagates past the barrier. In this case, the barrier breaks as the slip extends beyond it; the zone of barrier break is reflected by a displacement deficit as that observed in the central zone of the fault profiles (T17 and T18). The increase in displacement beyond the barrier would therefore suggest the renewal of the propagation of the previously locked and possibly dormant fault (Manighetti et al., 2001) Although, T17 is further restricted by strike slip fault S10 after it propagates past through S16 (Figure 5.9e). Alternatively, Thrust faults T17 and T18 may have been crosscut by Fault S16, such a scenario will show a notable thrust fault deflection at the zone of intersection.

#### *5.4.1.2 Folding and faulting at intersection zone*

In some studies of displacement transfer, it has been observed that the decrease in displacement at transfer zones is usually compensated by greater fold strain (Davis et al. 2005). Here, fault displacement and fold shortening responds similarly at the zone of strike slip fault intersection (Figure 5.10). They commonly reached their highest values close to

intersection zone followed by an abrupt decrease. This decrease and increase in both parameters at intersection zone indicates that shortening and displacement transfers were similarly accommodated by strike slip faults.

The profiles for shortening and displacement generally show striking similarities in geometry such as that seen in intersection zones. They display similar variation pattern which may be attributed to other factors such as linkage and lithological contrast (Figure 5.10). Such resemblance in profile geometry can be interpreted as folding and thrust faulting are contemporaneous.

## 5.5 DISCUSSION

This is the first time the interactions of thrust faults with strike slip faults is analysed and documented in details. In most tectonic areas where thrust faults and strike slip faults co-exist, the origin of thrust faults and folds are mainly associated with transpressional deformation (McClay and Bonora 2001). Here, both fault types (thrust faults and strike slip faults) are formed independently, the thrust related folds do not splay off the sub-vertical strike-slip faults, are not steeply dipping and not arranged in an echelon manner comparable to those formed by transpression (El-Motaal and Kusky 2003). Thus far, it has been argued in this study that thrust fault geometry and propagation are influenced by strike slip faults. The 5 classes of thrust faults and strike slip fault interaction described in Chapter 4 are based on static observations, but have not addressed the timing interaction of the faults. Until this is determined, it may be difficult to conclude the root cause of fold and thrust bounding and segmentation.

Two conceptualized models are proposed to give the mode of interaction and bounding relationship between thrust fault and strike slip fault examples described in this study (Figure

5.11). (a) A thrust related fold segmented by a strike slip fault (Figure 5.11a), (b) Two independently propagating thrust faults restricted by an active strike slip fault (Figure 5.11b).

The first model shows a pre-existing or propagating thrust fault and folds cross cut and segmented by a strike slip fault (Figure 5.11a). At t1, the strike slip fault propagates perpendicularly to the strike direction of the thrust related fold which appears as a single thrust structure. At t2, the strike slip fault intersects the surface of the propagating thrust faults and cross-cuts it into two segments. Offset of the thrust related fold increases through time from t2 to t3 (Figure 5.11a). The folds continue to grow appearing as a compartmentalized structure.

The second model shows that the thrust related folds individually propagated towards a strike slip fault surface where they become restricted (Figure 5.11b). All the faults systematically increase in displacement through time (t1-t3). At time t1, each of the thrust faults initiated and propagated towards the strike slip fault surface. The separation distance between the thrust faults perpendicular to strike increases as the strike slip fault systematically increases in displacement through time. At time t3, the thrust faults are restricted to propagate as they increase in separation distance (Figure 5.11b).

These models are end members that may occur in contractional settings where thrust faults co-exist with strike slip faults. One could call the first model; Tear fault (Mueller and Tailing 1997), while the second; Restricted fault system (Manighetti *et al.* 2001b). Although, the first model does not exactly corresponds to the conventional tear fault model described by Dahlstrom (1970). However, it is easier to use the term tear fault in this case.

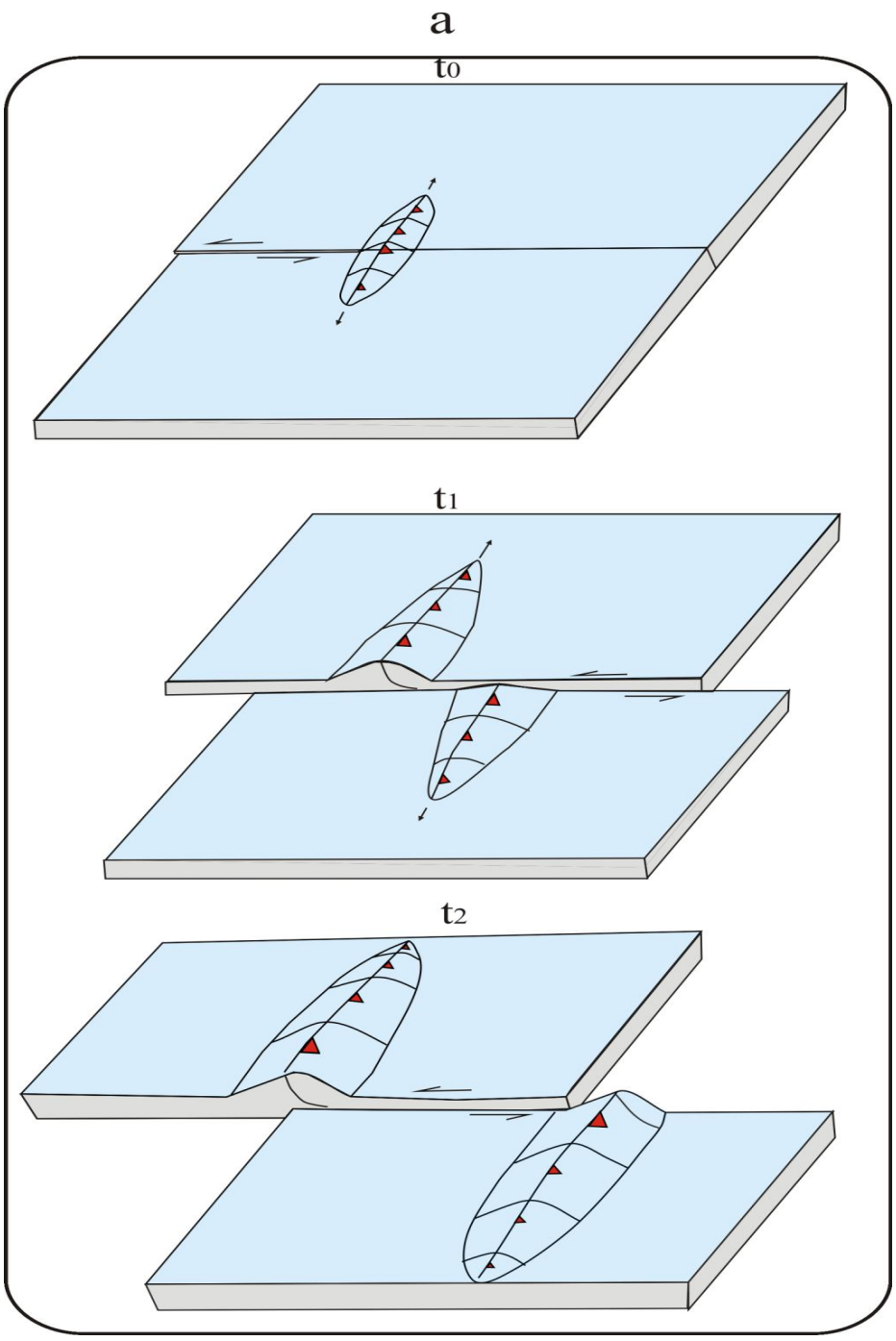


Figure 5.11: Conceptual models showing the evolution of thrust related fold and strike slip fault development and interaction. (a) Thrust related folds cross-cut into two segments by a strike slip fault (b) Two thrust related folds individually propagated towards an active strike slip fault. t0 – t2 represent progressive time of development.

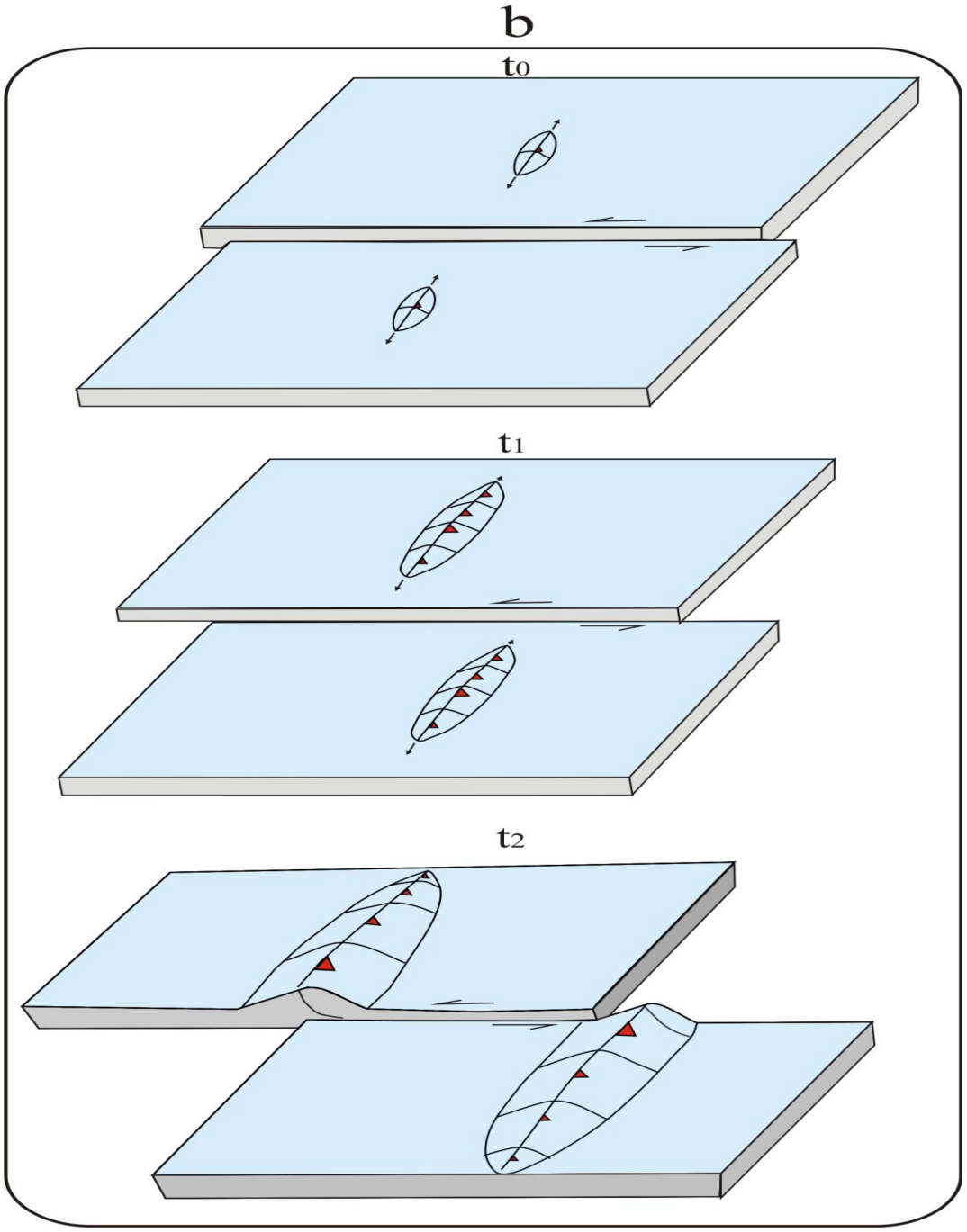


Figure 5.11: Conceptual models showing the evolution of thrust related fold and strike slip fault development and interaction. (a) Thrust related folds cross-cut into two segments by a strike slip fault (b) Two thrust related folds individually propagated towards an active strike slip fault. t0 – t2 represent progressive time of development.

These models are end members that may occur in contractional setting where strike slip faults co-exist with thrust faults. The distinction between these two end member models for the formation of compartmentalized thrust related fold is important, if conclusions are to be drawn regarding their evolution and interaction. Although the final results of both models are similar on plan view, however, this study uses the observation set from seismic data to determine the exact model which reflects the fault interaction of the case study structures.

Focusing on the result presented here (Figure 5.2-5.9), there are several striking observations which makes the first model an unlikely mode of interaction of the case examples. One of the result observations which do not support the first model is the high displacement close to the tip of fault S10, measured from the proposed offset distance between thrust faults T9 and T17 (Figure 5.5). A fault with displacement as high as 2000 m close to tip should have its tip terminating onto a displacement accommodating medium (e.g folds and faults) in terms of displacement transfer (Dahlstrom 1970). The tip region for fault S10 has maximum amplitude less than 0.05s TWT (c. 50 m) (Figure 5.6h); this value is improbable to reflect a displacement transfer of 2000 m. Although, the evolution of thrust fault T13 may be associated with the displacement transfer of S10, assuming this model is the true scenario of the interaction of the case study structure. This sort of displacement transfer is rare in the concept of displacement transfer; it would be more suitable if the tip of S10 terminates on the surface of T13 as in the case of lateral ramp or transfer faults (Pohn 2000).

Another line of evidence not in support of the Cross-cut fault model is the unmatched strike slip fault displacement from proposed fold offset (fold separation) and channel offset (Figure 5.1). For example the apparent offset distance between T17 and T23 along S20 which is measured to be c. 2800 m, as opposed to the segment of channel offset (c.134 m) adjacent to the thrust faults. The distance between the offset thrust faults and the channel offset point is

less than 500 m and too small to account for such a change in displacement for strike slip fault with a width larger than 12000 m. Unless fault S20 is a through-going fault segment formed by the linkage of smaller faults (Cartwright et al. 1995). However, the segment of fault S20 within the case study region is almost straight, and shows no notable jog or bend which may indicate linkage (Higgins et al. 2007).

Consequently, if the thrust related folds were one and the same (Cross-cut model), there should be an almost equal rate of uplift relative to sedimentation rate between the cross-cut folds. Here, thrust related fold T9 and T23 are still active relative to deposition of the present seabed, as opposed to T17 which became passive earlier than the deposition of Horizon BPM3. Such an anomaly may also be attributed to fault linkage as have been demonstrated in some studies (Higgins et al. 2007; Higgins et al. 2009). If the folds were one and same folds formed by process of fold linkage, this would indicate that the strike slip faults preferentially cuts through linkage sites. Such possibility is unrealistic and therefore rules out the proposition of fold offset by strike slip fault. Another probable cause, that may result to variation in character or kinematic sediment, is the interaction between channel segments and deformation within the study area (Clark and Cartwright 2009). Folds overlain by an active channel will have higher deposition rate than uplift rate such as fault T17. However, folds with higher sedimentation rate are characterized with thin sedimentary layers, in some case may have combination of onlapping and overlapping reflections (Poblet et al. 1997), this is not the case with T17.

The second model is consistent with the result from this study. The model suggests that the tip of thrust faults is restricted as the faults propagates and approach the strike slip fault surface: this corresponds to displacement geometries seen on the thrust faults. The cross cutting effect observed at intersection zones may be caused by either of the faults, since the

interacting fault types were both active at the time of interaction. In the case of the thrust faults, they tend to break or shear through the strike slip fault as they transfer displacement (Dahlstrom 1970).

## 5.6 CONCLUSION

This study uses 3D seismic data from the fold and thrust belt in the Levant Basin to examine the interaction between thrust related folds and strike slip faults. The data and analysis support the following conclusions:

(1) Dip slip displacement along a compartmentalized thrust faults are complex, unsystematic, and dissimilar to those of an uninteracted thrust faults.

(2) Along strike shortening profile respond similar to that of dip slip at intersection zone, suggesting thrust faulting and folding are contemporaneous.

(3)Two end member models where proposed to explain the timing interaction between thrust faults and strike slip fault: (a) Cross-cut fault model- A strike slip fault crosscut a thrust related fold into two fold segments, and (b) Restricted fault model- two thrust related folds individually propagated towards an active strike slip fault. Analysis of the case study examples supports the second model.

# CHAPTER SIX

# 6 THE SEGMENTATION AND DEVELOPMENT OF A SINGLE FOLD

## 6.1 INTRODUCTION

A single fold system could appear simple on map view but it is internally complex with faults of similar and opposing dips, termed synthetic and antithetic faults, respectively (Peacock et al. 2000). Such folds are said to be segmented and have been documented in many studies (Rowan 1997; Mitra et al. 2006; Higgins et al. 2007)). The occurrence of segmented thrust related folds raises important questions regarding their mode of evolution. Although analogue modelling provides useful indications as to how thrust fault and fold systems may initiate and progressively interact along strike (e.g Liu and Dixon, 1991). However, the along strike interaction and development of segmented thrust related folds have not been fully understood. This chapter presents an example of a single superficial fold within the Gal C survey to build on studies of segmented thrust related folds (Figure 6.1). The fold is termed Structure X, it is made up of strike slip faults, and thrust faults in synthetic and antithetic relationship (Figure 6.2).

The research into the evolution of extensional faults have provided insight into the along strike interaction of faults (Walsh and Watterson 1987; Larsen 1988; Walsh *et al.* 2003). Thrust faults have been shown to link or transfer displacement along strike similar to extensional faults (Higgins et al. 2009). This can take place between thrust faults in synthetic and antithetic relationship (O'Keefe and Stearns 1982; Higgins et al. 2007). In a broad sense, the region where fault overlap, is termed overlapping zone (Larsen 1988). This zone can be divided into transfer zone or a linkage zone depending on the geometry of the aggregate displacement of the overlapping faults (Walsh et al. 2003). Summed displacement profile

which shows smooth curve at the zone of overlap, such that it's similar to that of a single fault, the fault segments are said to be geometrically related. Faults that are geometrically coherent are interpreted to have linked since inception. Whereas aggregate displacement of fault pairs characterized by a displacement minima between two maxima are said to be initially isolated (Walsh et al. 2003).

Additionally, models of vertical propagation of fold and thrust systems suggests that thrust faults ramp up from detachment and propagate upward, leaving the footwall a passive partner of the development (Rich 1934; Suppe 1983). In contrast, thrust faults initiate at some point above their detachment layer and propagate up towards the surface and down dip to where they detach (Ellis and Dunlap 1988). In this case the footwall is a vital part of deformation.

The main aims of this chapter is to (1) describe in details the internal geometry and segmentation of Structure X using high resolution 3D seismic data, (2) examine the along strike interaction between the thrust faults and strike slip faults, and thrust faults of similar and opposing dips in Structure X, (3) investigate the lateral and vertical propagation of thrust faults in Structure X.

The methodology and geology of the area has been addressed in Chapters 2 and 3, respectively. This chapter starts with a brief summary of the methodology used to obtain the results. This is accompanied by the description of the geometry and structural arrangement of the thrust faults with their associated folds, and strike slip faults using structural maps of key horizons and seismic sections. The chapter continues with the description of the horizontal and vertical displacement distribution of the thrust fault planes, followed by the comparison of summed fault displacement and fold shortening along strike. After this, the results were interpreted and discussed before the chapter was concluded.

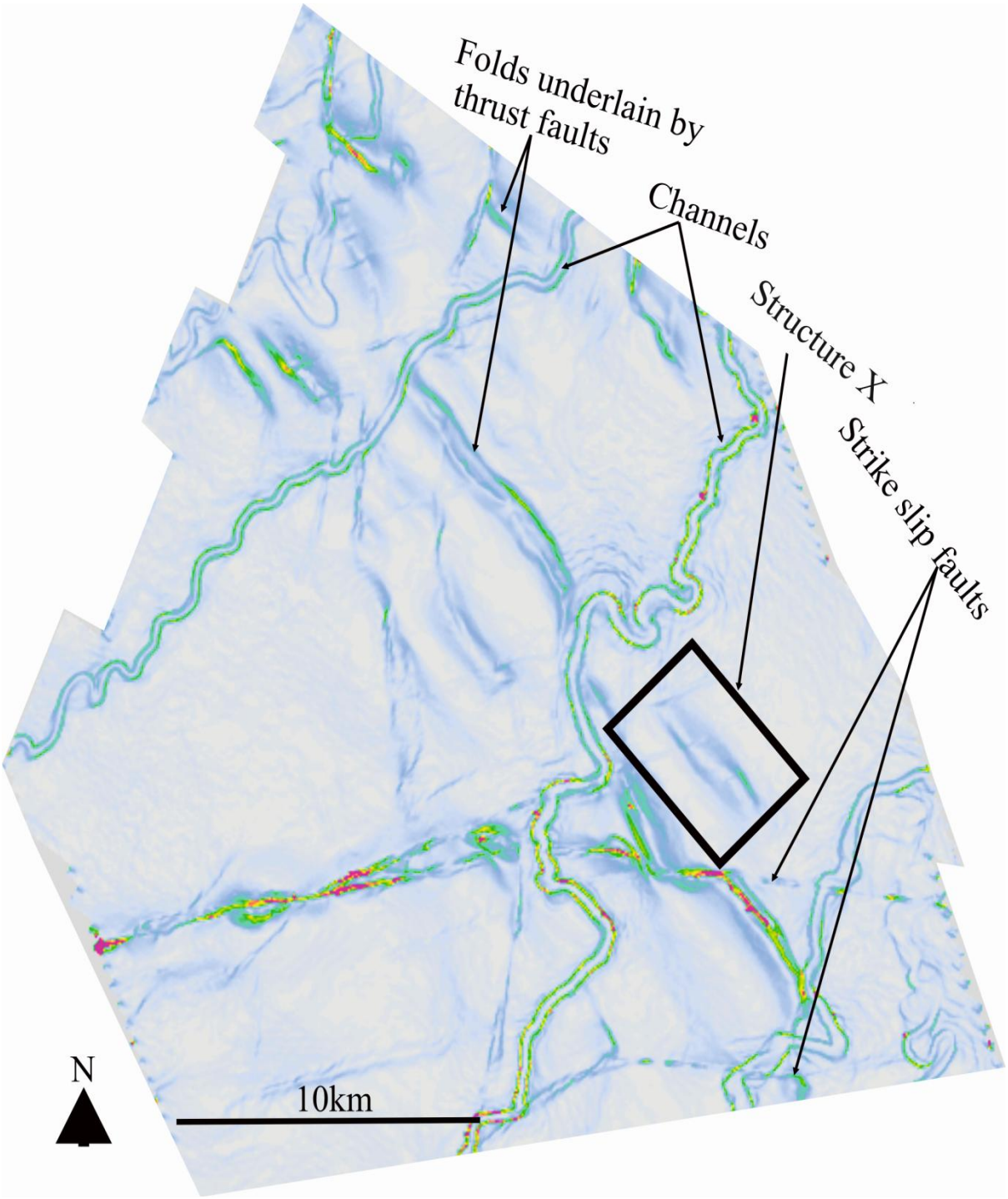


Figure 6.1: Time dip attribute maps of the northern half of the seabed horizon showing the case study fold (Structure X).

## 6.2 METHODOLOGY

The methods used to obtain the results presented in this study have been discussed in Chapter 2 of this thesis. The fold shape is described by using interpreted structural maps of key horizons (Figure 6.2) and seismic sections along strike of the case study structure (Figure 6.3). In this chapter throw is used as a proxy to heave and dip slip, for analysing the faults. This is because, it is representative, easier and faster, and it limits error when comparing throw and depths in two way travel time. For more detailed explanation, see Chapter 2 (section 2.4.1.1-24.1.3) of this thesis.

## 6.3 RESULTS

Structure X is located towards the north-eastern part of the 3D dataset used for this thesis (Figure 6.1). It is fully contained within the dataset and it is isolated from other thrust related folds. Surrounding strata are undeformed at a minimum lateral distance of c. 1000 m away from the case study fold (Figure 6.1). The anticline appears simple on the seabed, but consists of blind thrust fault and strike slip faults, thrust faults dipping towards and away from each other.

### 6.3.1 Fold Geometry and Segmentation

Four key seismic horizons (Seabed, IPM2a, IPM1 and M) were mapped in the survey area (Figure 6.2) and 8 selected seismic sections almost perpendicular to the structure (Figure 6.3) are also used to illustrate the internal geometry of the fold.

Structure X, has an along strike distance of c. 5.5 km, measured between two reference points (R0 and R1), where fold amplitude decreases to zero (Figure 6.2). The fold has an arcuate to linear axial trace, striking between $110^{o}$- $150^{o}$. On the seabed horizon elevation map (Figure 6.2a), it appears as a single and simple structure, whereas the deeper horizon maps show that it is internally deformed by thrust faults (T20, T21, T22 and T25) and strike slip faults ( S13,

S14 and S17) (Figure 6.2b-d). The style of thrusting and interaction between the faults can be seen to influence the shape of Structure X (Figure 6.3). Seismic sections along the fold show that it reverses in vergence from SW to NE, passing through a central zone where the fold is symmetrical (Figure 6.3). This change in vergence exhibited by the internal geometry of the fold indicates that the fold is irregular in shape.

For better illustration of Structure X, this study divides the fold into 3 main segments based on the change in fold vergence and where the thrust faults overlap each other. Each segment is characterized by its own distinctive structural style based on fault interaction (Figure 6.2 and 6.2). Segment 1 is characterized by strike slip fault intersections, Segment 2 displays overlapping of converging thrust faults, and Segment 3 exhibits overlapping of faults in synthetic relationship. The fold is described along strike distance using a reference scale ranging from 0-6 km (R0-R1, Figure 6.2).

#### *6.3.1.1 Segment 1*

This segment laterally extends c. 3.4km (Figure 6.2) and it represents a zone where the fold is asymmetric with a strong south-western vergence (Figure 6.3 a-c). Profiles along this segment show that the fold reaches a structural relief of 2.7km (Figure 6.2c). The amplitude and wavelength of the fold at this zone, is c. 0.8s TWT (~800m) and c. 150m respectively, measured on horizon IPM2a (Figure 6.3 c). This segment of the fold is characterized by a shorter and steeper forelimb than the backlimb, with an inter-limb angle of $80^{o}$-$110^{o}$.

This segment is underlain by a major thrust fault that extends beyond the north-western limit of the fold (Figure 6.2). Thrust fault T20 has an along strike length of approximately 3.7 km and its maximum height reaches c. 0.7s (~700 m) measured from zone of detachment to vertical tip (Tearpock and Bischke 1991). T20 is almost planar in plan view, striking c. $135^{o}$ but tends to change in strike towards Segment 2 (Figure 6.2). It is planar to listric, dipping c.

37$^{o}$NE, having its main site of detachment at the Upper Messinian interval, immediately below Horizon M (Figure 6.3 a-c). Thrust fault T20 and the north-western section of the anticline are intersected by 3 sinistral strike-slip faults (S13, S14 and S17) trending ENE (Figure 6.2). Fault T20 intersects Fault S13 at c. 1.8 km, profile section close to this zone of intersection shows that both faults run through each other without any notable change in dip (Figure 6.3 b). Whereas, in the zone of intersection at 2.7 km, T20 crosscuts S14 into two parts dipping at different angles.

T20, at this zone of crosscut, steepens with depth and is almost concave downwards at its centre. Faults of this shape have been termed anti-listric (Ferrill and Morris 1997; Grasemann *et al.* 2005; Soliva *et al.* 2008). This change in fault shape and dip at the crosscutting zone indicates fault interaction (Davis et al. 2005; Higgins et al. 2009) . This zone marks the south eastern-limit of Segment 1.

#### *6.3.1.2 Segment 2*

Segment 2 has an along strike length of 1 km and it is characterized by the overlap of T20 and T21 (Figure 6.2 and 6.3 d and e). The footwall of T20 is cut by S17, as it (T20) decreases in scale (vertical height and throw) along strike (Figure 6.3d and e).

Fault T21 has an along strike length of c. 2.2km measured from the central region of Segment 2 to the end of Segment 3 along Horizon IPM2a. It decreases in strike length at depth (Figure 6.2). It is planar dipping c. 38$^{o}$ SW, opposite to the dip direction of Fault T20, forming an antithetic convergent zone (Morley et al. 1990). This convergent overlapping zone marks the position where displacement at the north-eastern and south-western segments of T20 and T21 respectively, decrease to zero. The transition along T20 and T21 occur within a transfer zone (Dahlstrom 1970; McClay 2002; Higgins et al. 2007). Both thrust faults are almost linear, striking in the same direction but a considerable change in strike occurs within the

overlapping zone as their lateral tips curve towards each other (Figure 6.2). This change in strike within the overlapping zone is indicative of fault interaction and has also been observed in the results of other studies on relay faults (Larsen 1988; Walsh *et al.* 1999).

Seismic sections along the strike of the overlapping zone in Segment 2, shows how the faults increases and decreases in dimension (Figure 6.3d and 6.2e). At c. 3.7 km (Figure 6.3d), T20 is observed to detach below Horizon M, while the basal tip of T21 is in Unit PM1. Along strike, at c. 4 km, T21 increases in vertical height and displacement, detaching within the Messinian unit, whilst in the same region of the overlap T20 decreases in dimension so that the tips of the faults are located within the Unit PM1. Both oppositely dipping faults (T20 and T21) are observed to have their ramps intersect within the base of Unit PM1, forming a branch point (McClay 1992a; Walsh et al. 1999) (Figure 6.3d).

Segment 2 displays no vergence direction above the branch point (Figure 6.3e). It is almost symmetrical having both limbs equal in dip and length, resembling a pop-up structure (Harrison and Bally 1988; Buchanan and McClay 1991; Higgins et al. 2007). The fold in this segment is broad having an inter-limb angle of more than 150$^{o}$, maximum fold amplitude is roughly the same to that of Segment 1.

#### *6.3.1.3 Segment 3*

Segment 3 defines the south-eastern limit of the fold as a whole structure and it has a lateral distance of c. 2.5 km (Figure 6.2). The fold in Segment 3 is asymmetrical, verging northeast, with the forelimb slightly longer and steeper than the back limb (Figure 6.3f-h). Here, the fold is broader than that of Segment 1; its inter-limb angle reaches 130$^{o}$. The maximum fold amplitude of this segment is less than 0.05s TwT (~0.5 km) and has a wavelength of approximately 0.5 km.

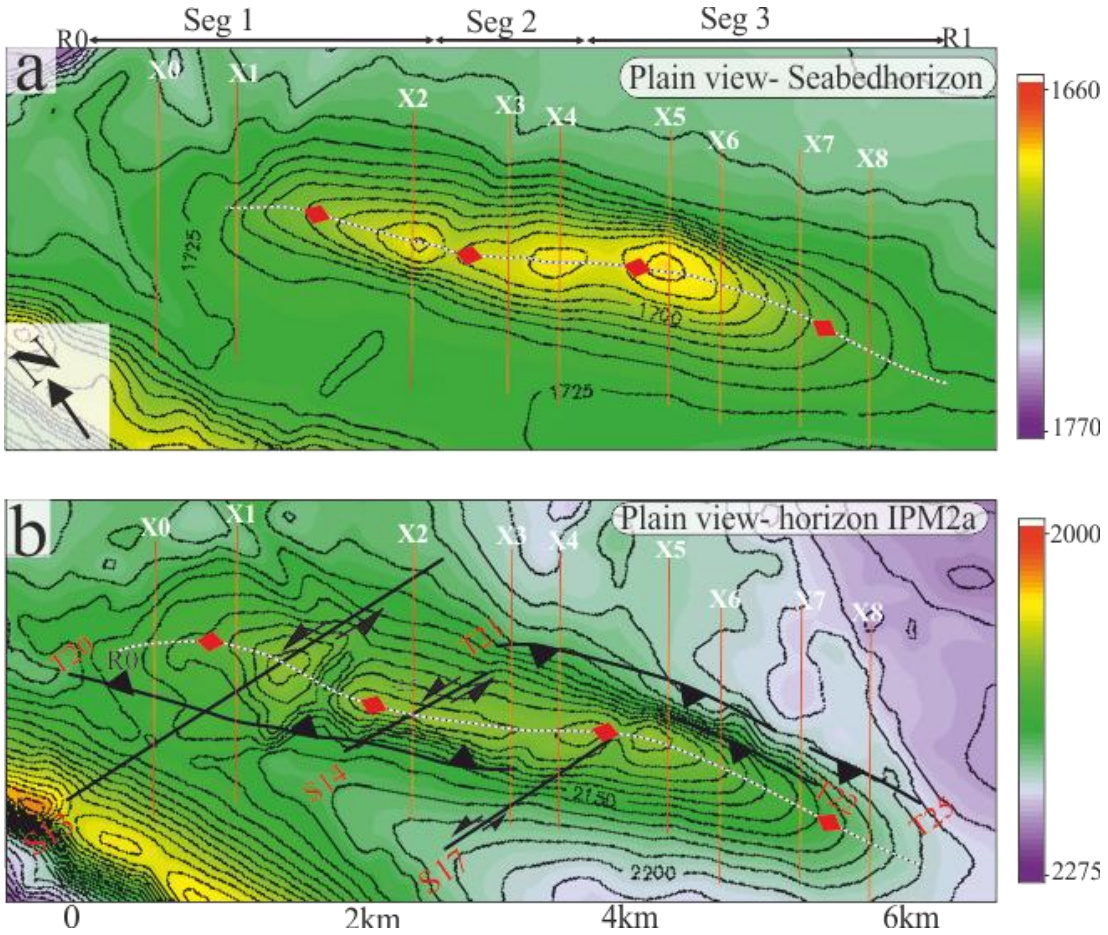


Figure 6.2: Maps of horizon elevation in two-way –time (ms) along Structure X. (a) Horizon seabed (b) Horizon IPM2a (c) Horizon IPM1 (d) Horizon M. Traces of the fold divided in 3 segments (seg), and the 3 major thrust faults labelled T20, T21, T22 and strike slip faults S13, S14 and S17 (as labelled in Figure 4.2). Thrust fault trace is denoted by black triangles in the hanging walls. Line X0- X8 show locations of the 8 sections in Figure 6.3. R0 and R1 represent the limits of the fold. Red/Yellow colours represent structural high. Purple/green colour represents structural low. Contour interval: 25ms.

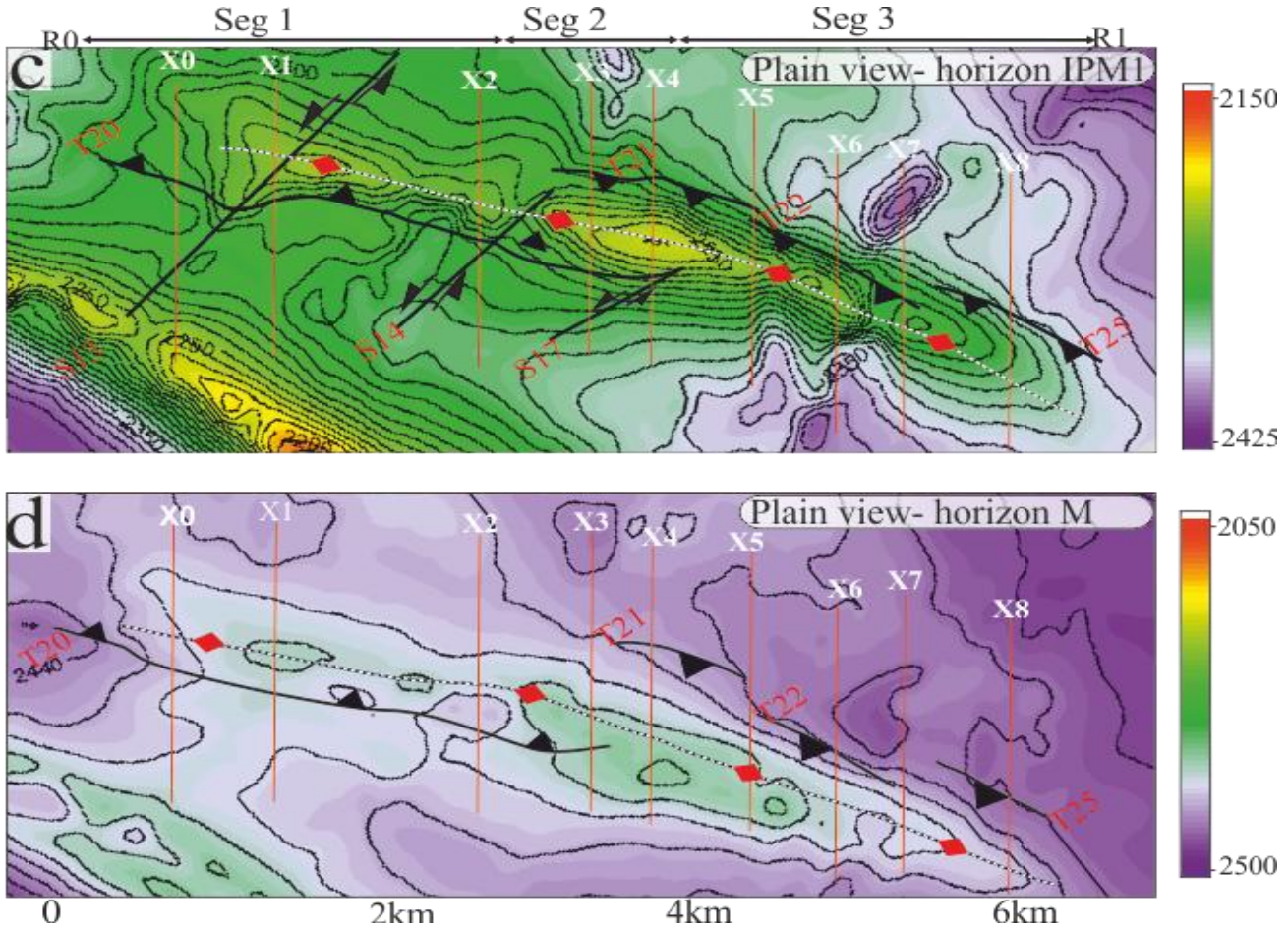


Figure 6.2: Maps of horizon elevation in two-way –time (ms) along Structure X. (a) Horizon seabed (b) Horizon IPM2a (c) Horizon IPM1 (d) Horizon M. Traces of the fold divided in 3 segments (seg), and the 3 major thrust faults labelled T20, T21, T22 and strike slip faults S13, S14 and S17 (as labelled in Figure 4.2). Thrust fault trace is denoted by black triangles in the hanging walls. Line X0- X8 show locations of the 8 sections in Figure 6.3. R0 and R1 represent the limits of the fold. Red/Yellow colours represent structural high. Purple/green colour represents structural low. Contour interval: 25ms.

Segment 3 is characterized at the south-eastern limit by Faults T21, T22 and T25, they all dip south west (Figure 6.3f-h). On map view the thrust faults are almost linear, striking between $140^{o}$-$145^{o}$ within this segment (Figure 6.2). Fault T21 extends from 3.8 - 4.6 km along this segment in horizon IPM2a and is overlapped by Fault T22 which has a lateral width of more than 1km. The overlapping zone between the thrust faults is well defined along Horizon IPM2a (Figure 6.2b) and it extends along strike from c. 4.2 km to c. 5 km along the fold. Fault T21 has its vertical tip terminating slightly above Horizon IPM2a, it dies out along strike towards the central zone of Segment 3 as T22 increases in dimension. At this zone, T22 appear to ramp up from detachment (below the M reflection) to the upper section of unit PM2 (4.7-5 km, Figure 6.3 g). The dimension polarity displayed between both faults at the overlapping zone is indicative of fault interaction (Morley et al. 1990).

T22 is more listric than its counterpart faults in sectional view. It increases in dip to c. $65^{o}$ towards the upper tip from detachment layer where it is sub-horizontal. Fault T22 branches Fault T21 immediately below Horizon IPM1 towards the north-western end of the segment (Figure 6.3 f), whereas, towards the south-eastern zone of the segment, the branching occurs at a higher stratigraphic level: between Horizon IPM1 and BPM2 (Figure 6.3 g).

Towards the south-eastern end of Segment 3, Fault T22 overlaps Fault T25 as it dies out (Figure 6.2). Fault T25 is linear in map view with maximum length of c. 0.75km, measured on Horizon IPM1 (Figure 6.2c). It has similar characteristics to that of Fault T21. It ramps up from a detachment layer (Upper Messinian unit), towards the seabed, having its upper tip at the same stratigraphic level as T21 IPM2a). It is planar, with a dip of $37^{o}$ (Figure 6.3i).

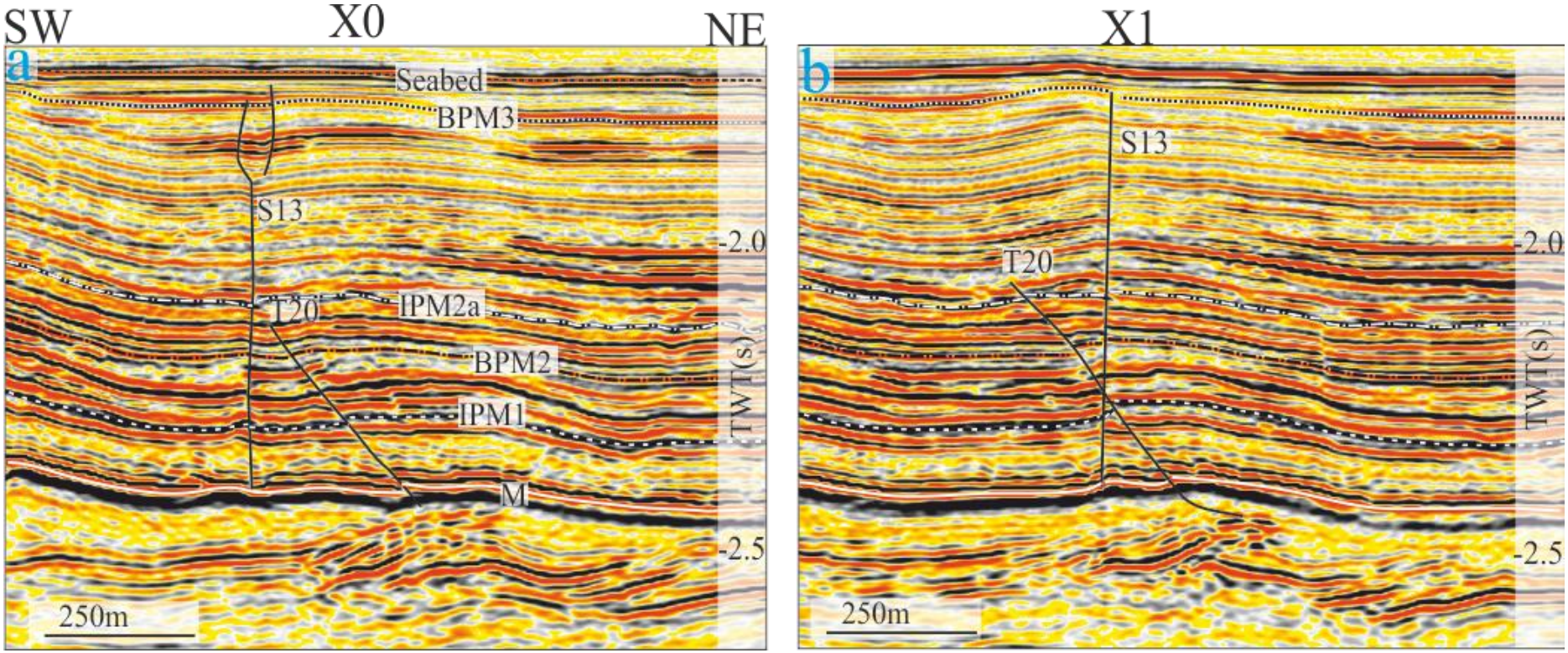


Figure 6.3: Selected seismic sections perpendicular to Structure X, illustrating change in fold vergence, fault geometry and fault interactions along strike. Location of seismic lines in Figure 6.2. All sections are viewed looking north. Sections have an approximate vertical exaggeration of 2. *M, IPM1, BPM2, IPM2 and BPM3 are* regional stratigraphic horizons.

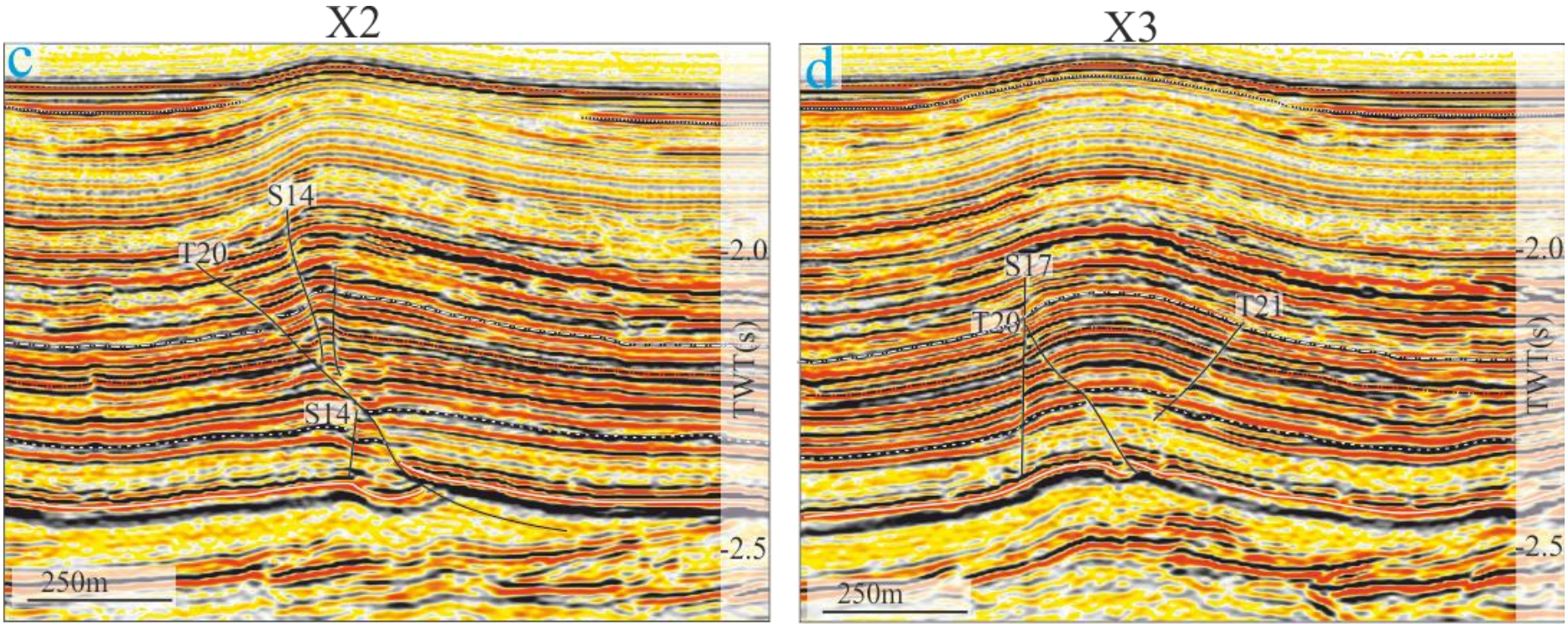


Figure 6.3: Selected seismic sections perpendicular to Structure X, illustrating change in fold vergence, fault geometry and fault interactions along strike. Location of seismic lines in Figure 6.2. All sections are viewed looking north. Sections have an approximate vertical exaggeration of 2. *M, IPM1, BPM2, IPM2 and BPM3 are* regional stratigraphic horizons.

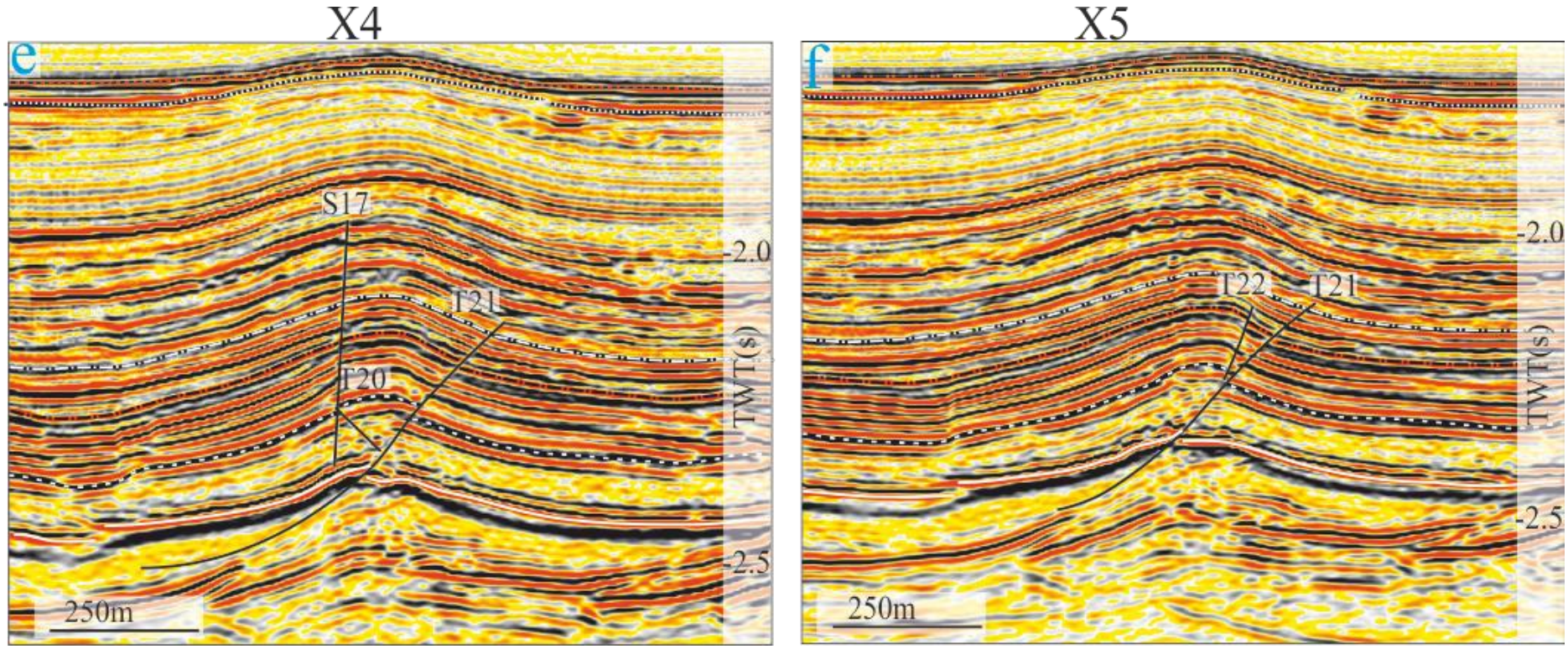


Figure 6.3: Selected seismic sections perpendicular to Structure X, illustrating change in fold vergence, fault geometry and fault interactions along strike. Location of seismic lines in Figure 6.2. All sections are viewed looking north. Sections have an approximate vertical exaggeration of 2. *M, IPM1, BPM2, IPM2 and BPM3 are* regional stratigraphic horizons.

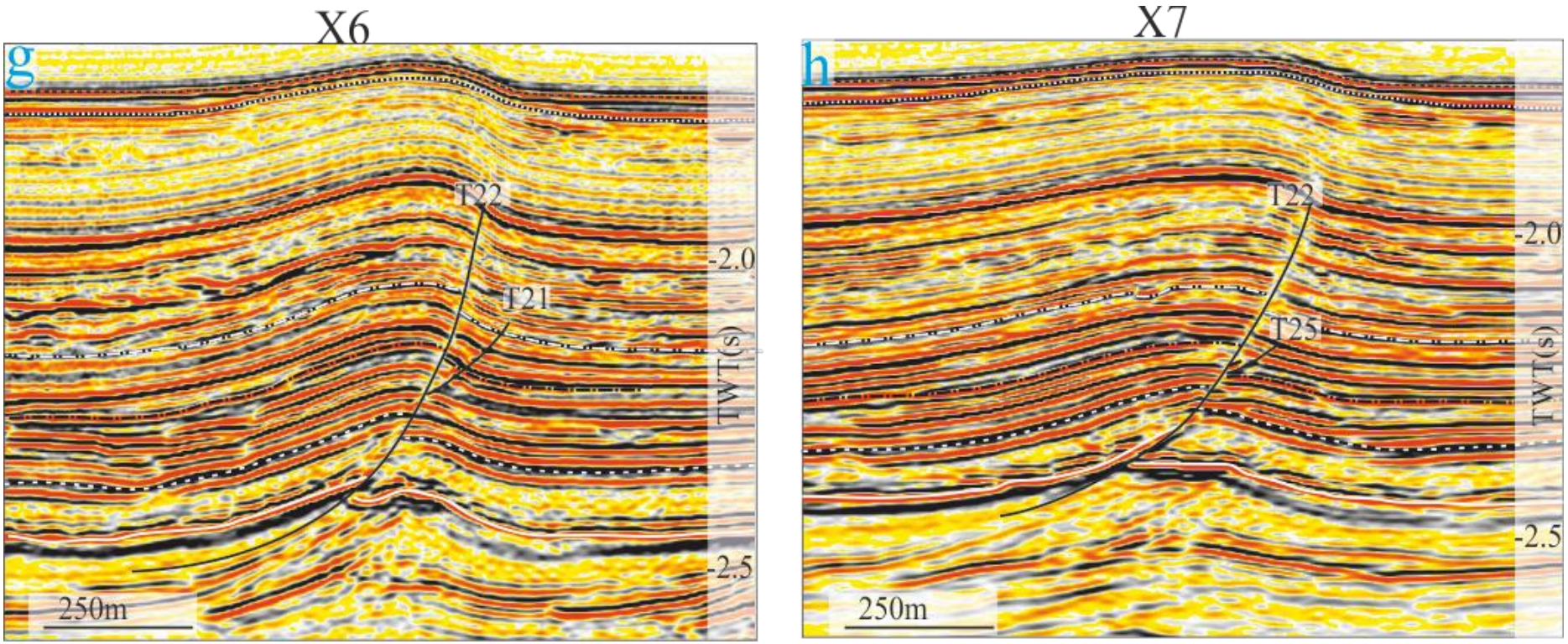


Figure 6.3: Selected seismic sections perpendicular to Structure X, illustrating change in fold vergence, fault geometry and fault interactions along strike. Location of seismic lines in Figure 6.2. All sections are viewed looking north. Sections have an approximate vertical exaggeration of 2. *M, IPM1, BPM2, IPM2 and BPM3 are* regional stratigraphic horizons.

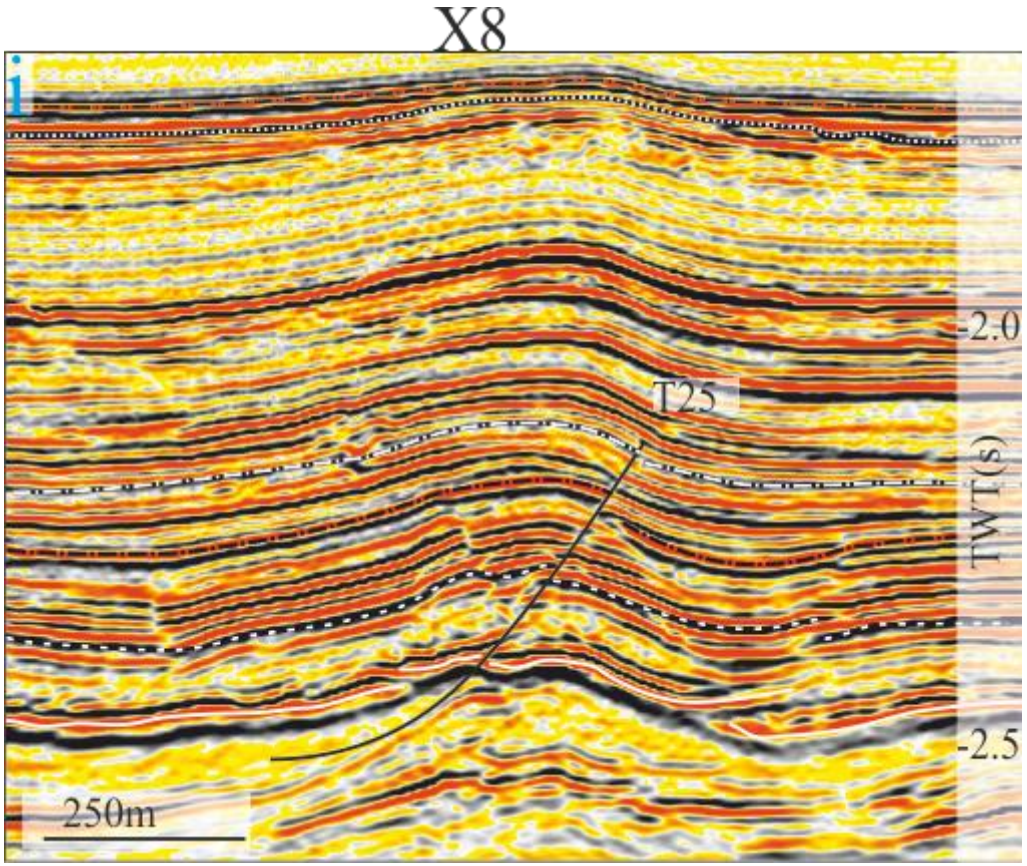


Figure 6.3: Selected seismic sections perpendicular to Structure X, illustrating change in fold vergence, fault geometry and fault interactions along strike. Location of seismic lines in Figure 6.2. All sections are viewed looking north. Sections have an approximate vertical exaggeration of 2. *M, IPM1, BPM2, IPM2 and BPM3 are* regional stratigraphic horizons.

### 6.3.2 Dating the Fold

The temporal evolution of the fold can be interpreted from the growth strata that were deposited on the limbs of the structure (see Figure 6.3d and e). The different strata mapped along the fold have been defined in chapter 3 (Figure 3.5). Horizon BPM3 corresponds to the seabed at the time of the fold onset as it is immediately overlies the first evident onlapping reflection. Horizon BPM3 was deposited in late Pliocene to early Pleistocene which corresponds to the time of fold onset predicted by previous studies (Cartwright and Jackson 2008; Clark and Cartwright 2011; Cartwright et al. 2012). The growth strata are flat lying, thinning towards both limbs which may suggest fold development by component of limb migration (Storti and Poblet 1997a; Suppe *et al.* 2004). These onlapping kinematic packages onto the limbs of the fold and the positive bathymetric relief formed by the emergence of the fold crest suggest a high uplift rate compared to sedimentation rate (Storti and Poblet, 1997b). The similarity in geometry of the growth sediment along the fold and the un-segmentation appearance on the seabed may suggest that recent development of the fold occurred as a single structure.

### 6.3.3 Throw Analysis

This section uses throw in place of dip-slip and heave to analyse the thrust faults in Structure X. Chapter 2 (Section 2.4.1.1) already sets out how throw was obtained. Throw presentation in this study is similar to that of Baudon and Cartwright (2008b) (Figure 6.4-6.9) . Throw values at different stratigraphic levels along strike of the thrust faults were contoured at every 5ms (TWT) to illustrate the throw distribution on a fault plane. In order to clearly depict throw gradient changes, particularly across overlapping or intersection zones, lateral throw distribution plots along key horizons (M, IPM1, BPM and IPM2a) were presented. Furthermore, as a separate means for analysing throw distribution, vertical throw distribution along strike were plotted.

Generally the throw plots of the thrust faults are characterized by several maxima and minima some of which may be attributed to the effect of linkage, lithological contrast and measurement error (Childs et al. 1995; Mansfield and Cartwright 1996). However, many of the irregularities observed on the plots correspond to where the thrust faults interact with each other or with a strike-slip fault (Figure 6.4-6.9). The profiles are described using their length distance as a reference.

#### *6.3.3.1 Fault T20*

The throw contour and horizontal plots for T20 are generally symmetric in shape, and exhibiting several maxima and minima (Figure 6.4 a and b). These irregularities are most distinct at 600m, 1000m and 2400m, all of which correspond to where the thrust fault intersects strike slip faults. The throw contour pattern for T20 varies in geometry from symmetric to semi-elliptical to those that are shapeless.

The contours for T20 centre between 1700 m- 2200 m of the fault plane, with all the contours reaching their maximum at this zone (Figure 6.4a). The tip line contour reaches its maximum elevation at the centre between 1,800 m and 2,100 m, and decreases towards both ends. Generally, contour spacing decreases upward, indicating steeper gradient towards the seabed (Figure 6.4 a and c)

The horizontal throw distribution along key horizons also attains their maximum close to the zone where the contours centres (Figure 6.4b). The plots are roughly asymmetrical with exception of horizon M which tends to be symmetric (Figure 6.4b). Generally, individual horizontal profiles show very high gradients between 2300m to 2600m along the profile length.

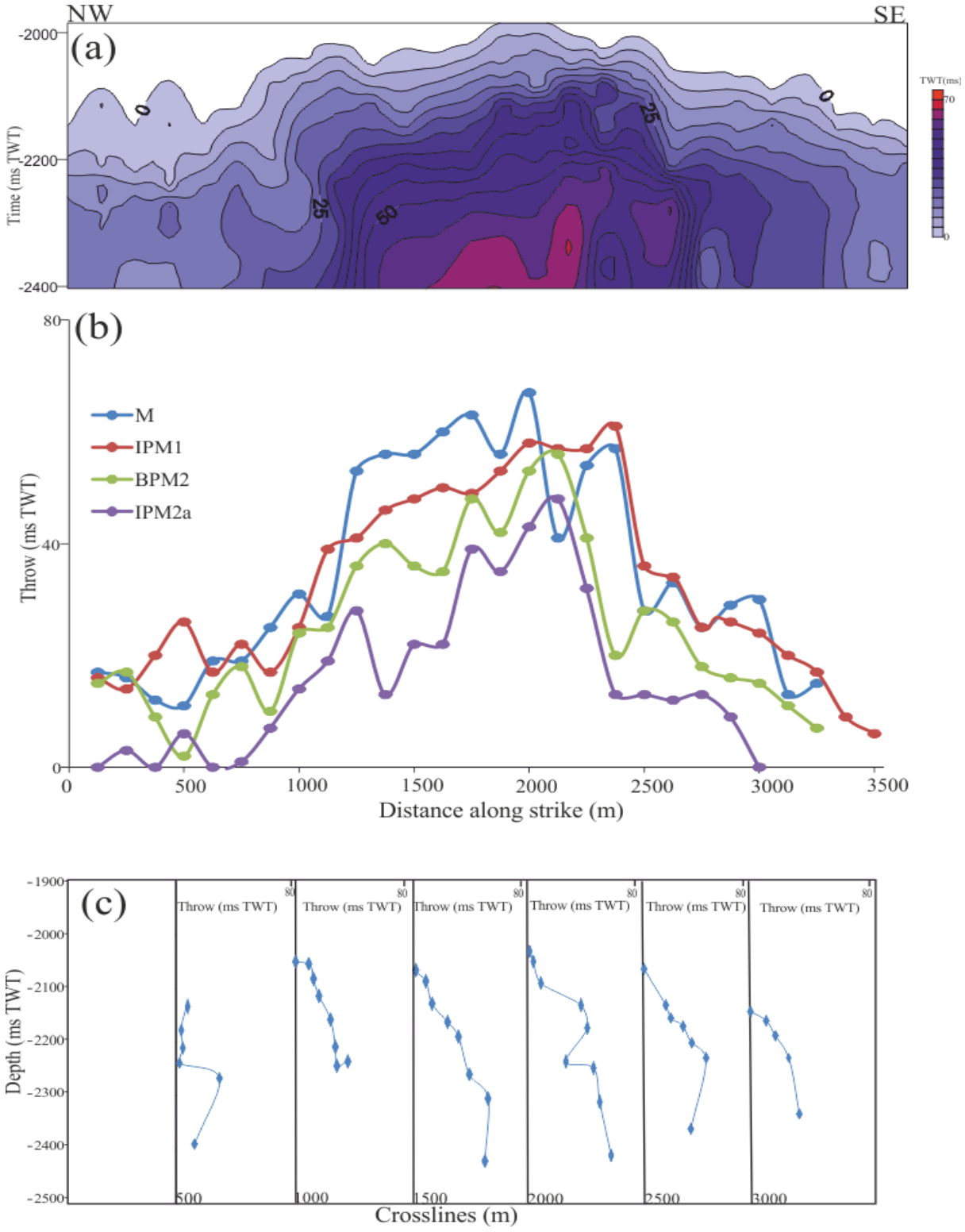


Figure 6.4: Throw distribution for Fault T20.(a) Throw contour along fault length. Interval throw contours are spaced every 5ms TWT. Red colours represent high throw values while blue colours represent low throw values. (b) Horizontal throw distribution graph of the key stratigraphic horizons at every 125 meters along fault length (Cartwright et al. 1995).

The vertical plots along T20 generally show an increase in displacement towards the detachment with exception of the profile at c.500m which show a decrease at the centre, which may indicate dip linkage (Mansfield and Cartwright 1996). Beyond these irregularities, the vertical throw profiles along the fault plane generally exhibit an increase in throw towards the detachment layer or basal tip (Figure 6.4c).

#### *6.3.3.2 Fault T21*

The throw contours for T21 vary in shape along strike, with the tip line contour displaying several irregularities (Figure 6.5a). The fault plane exhibit contours with a long axis along strike towards the upper part of the plane, and centres at the lower part, where they decrease in spacing. The tip line contour reached its maximum elevation close to the north-western end of the fault plane at c. 2,900 m (Figure 6.5a).

The lateral throw distributions along the main horizons are generally characterized by multiple maxima separated by localised minima (Figure 6.5b). They generally have their maximum close to where the contours centre (Figure 6.5a and b). With the exception of Horizon IPM2a, the profiles show high throw gradients close to both ends, similar to those of multiple tip restricted faults (Nicol et al. 1995; Manighetti et al. 2001a). The lateral profile for IPM2a extends beyond 3750m, where most of the profiles decrease to zero. Beyond this zone (3750m), Horizon IPM2a tends to be almost flat towards the south-eastern end of the fault plane (Figure 6.5b).

Vertical throw plots along T21 also show several minima and maxima (Figure 6.5c). These irregularities may be attributed to dip linkage and have been observed in other studies (e.g Mansfield and Cartwright, 1996, Baudon and Cartwright, 2008). Generally, the profiles are characterized by increase in throw from detachment towards the fault tip, with an exception of the profile at 4250m, which corresponds to edge of the fault plane (Figure 6.5c).

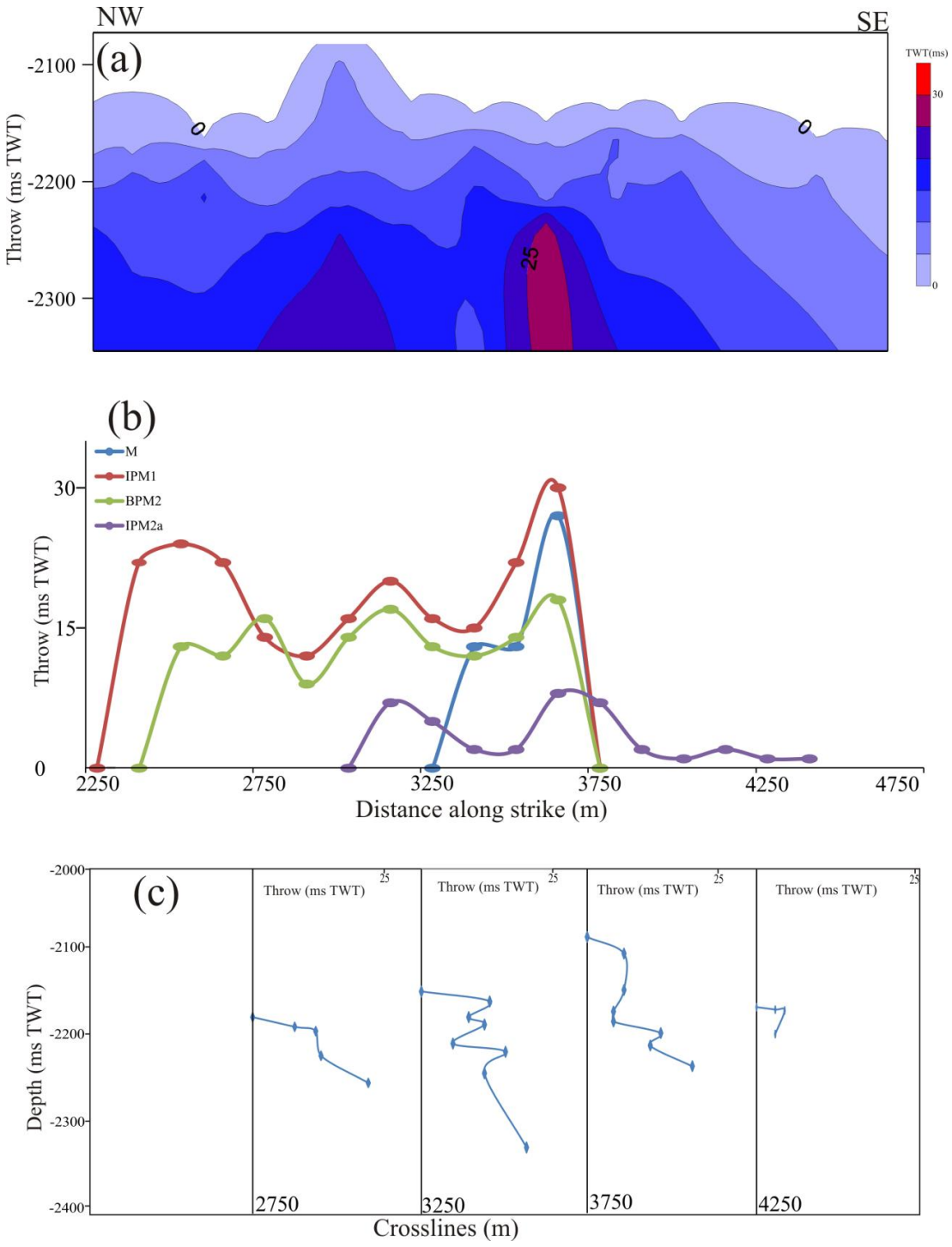


Figure 6.5: Throw distribution for Fault 21 . (a) Throw contour along fault length. Interval throw contours are spaced every 5ms TWT. Red colours represent high throw values while blue colours represent low throw values. (b) Horizontal throw distribution graph of the key stratigraphic horizons at every 125 meters along fault length. (c) Vertical throw distribution graph at every 500m along fault length.

#### *6.3.3.3 Fault T22*

The tip line contour for T22 tends to show less maxima and minima compared to T20 and T21. The middle contours tend to be the most irregular in shape with some exhibiting the shape of a mushroom (Figure 6.6a). Contour lines of high throw values tend to be symmetric and they centre towards the south eastern part of the faults plane (4000 – 4080m). Contours are most widely spaced at the central zone of the faults plane compared to the upper and basal regions (Figure 6.6a).

Horizontal throw distributions of key horizons are symmetric to weakly asymmetric having their maximum throw close to the south-eastern end of the plot. Horizon M shows the steepest gradient close to the south-eastern zone (4000m - 4125m), while other horizons tend to show a small decrease with low gradient (less than 0.8) followed by increase at this zone (Figure 6.6b).

The vertical throw profiles mainly increase from the upper tip towards the decollement layer, with several minor throw variations (Figure 6.6c). The throw gradient ranges between (0.18 - 2.3), with the steepest gradients observed towards the upper tip of the fault plane (Figure 6.6a and c).

#### *6.3.3.4 Fault T25*

The contour for the Fault T25 is characterized by an elliptical outline which approximately centres on a large maximum throw zone close to the north-western end of the fault plane (Figure 6.7a). The lateral throw distribution along key horizons is mainly asymmetric, having their maximum throw north-ward; only the pattern on Horizon IPM2a exhibits a symmetric trend (Figure 6.7b). The gradient towards the north-western end of the profiles tend to be greater compared to the south-eastern end.

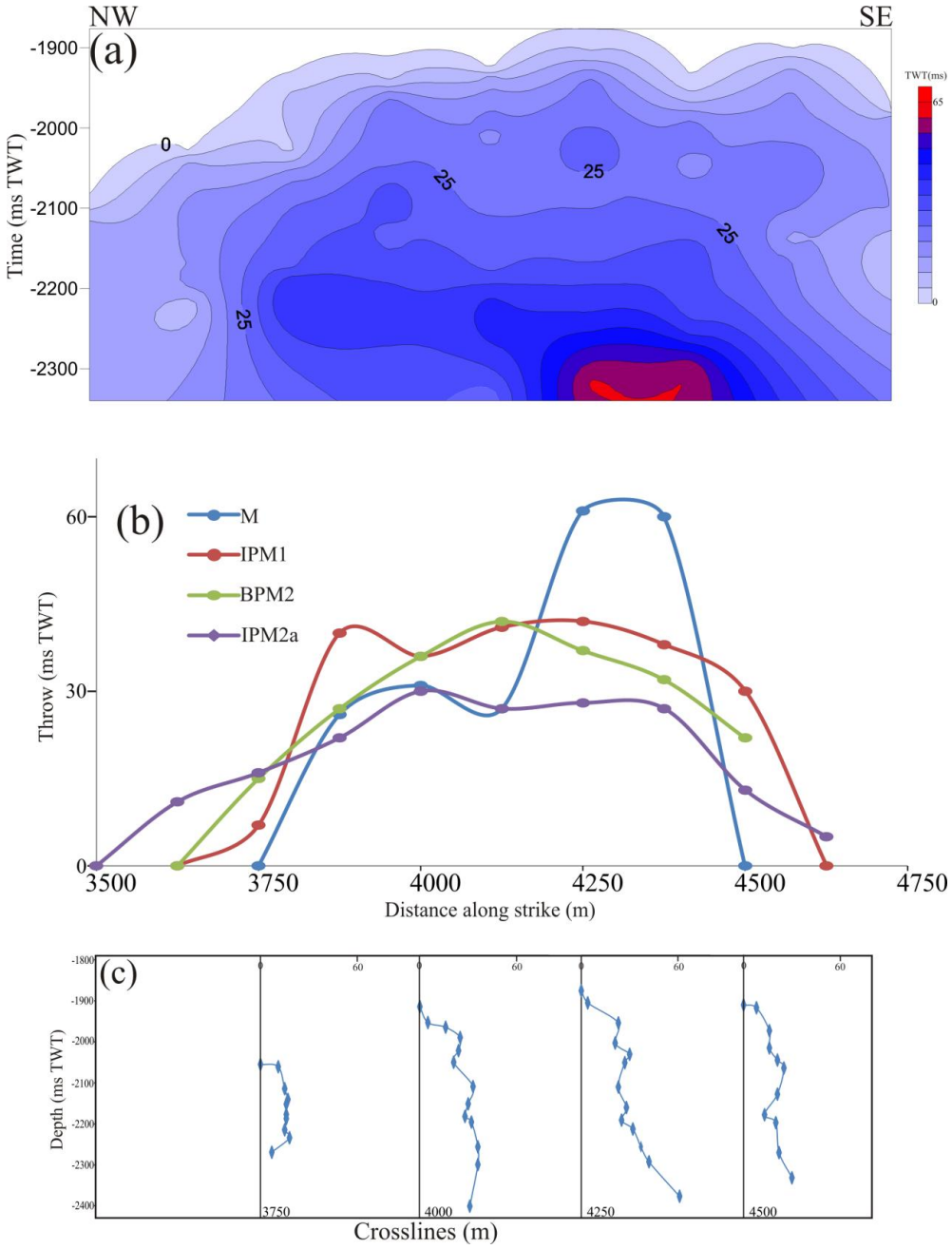


Figure 6.6: Throw distribution for thrust fault 21a (T22). (a) Throw contour along fault length. Interval throw contours are spaced every 5ms TWT. Red colours represent high throw values while blue colours represent low throw values. (b) Horizontal throw distribution graph of the key stratigraphic horizons at every 125 meters along fault length. (c) Vertical throw distribution graph at every 250m along fault length.

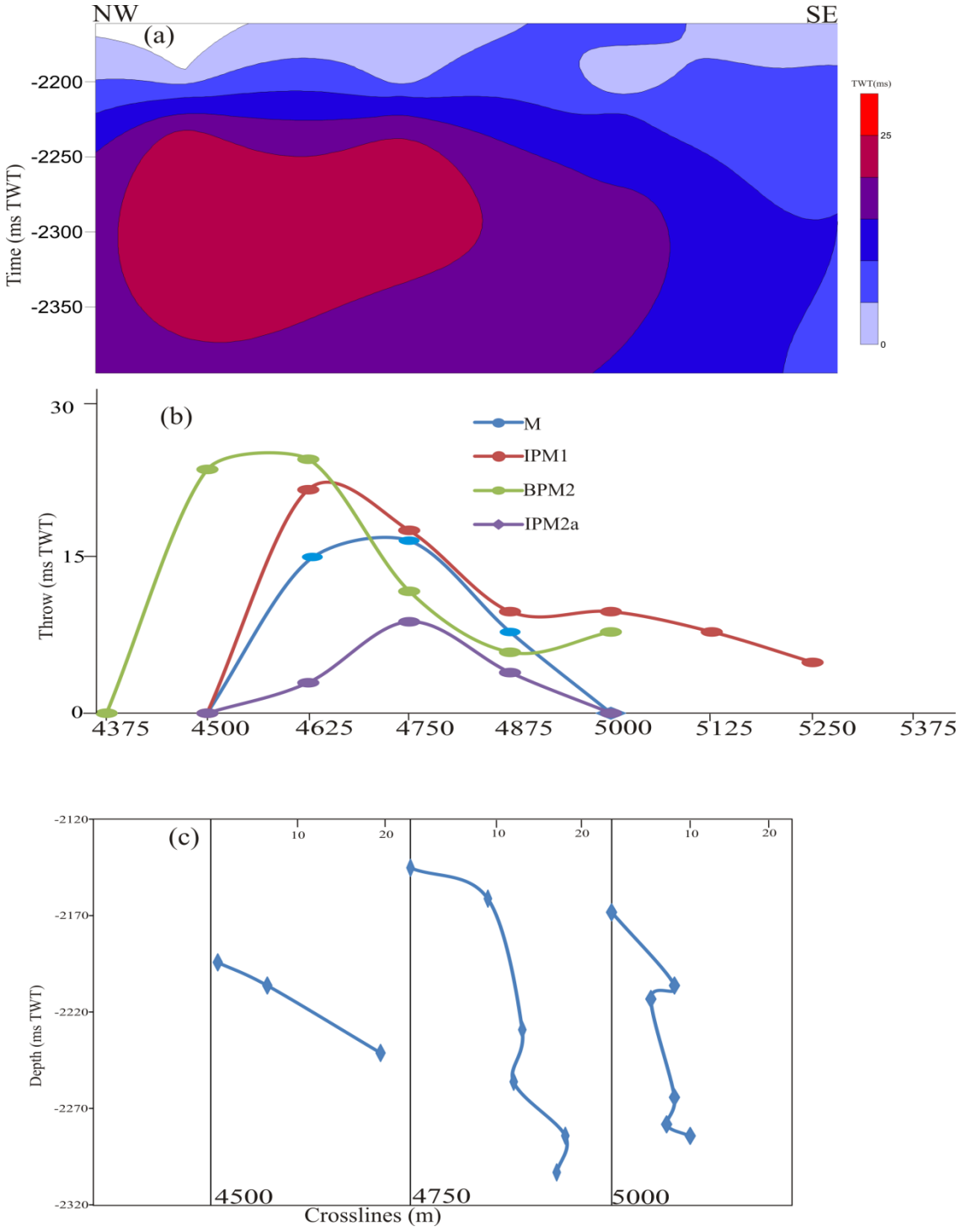


Figure 6.7: Throw distribution for thrust fault 21a (T22). (a) Throw contour along fault length. Interval throw contours are spaced every 5ms TWT. Red colours represent high throw values while blue colours represent low throw values. (b) Horizontal throw distribution graph of the key stratigraphic horizons at every 125 meters along fault length. (c) Vertical throw distribution graph at every 250m along fault length.

Both the horizontal and vertical plots for T25 tends to show less irregularity compared to the other thrust faults described in this study. The vertical plots also show increase in throw downwards with increase in gradient up dip (Figure 6.7c).

### 6.3.4 Cumulative Throw and Shortening Profiles

Summed throw and shortening distribution along strike of the thrust related folds in Structure X are compared in this section. The comparisons of both parameters have previously been used to determine the timing relationship between faulting and folding (Rowan 1997; Higgins et al. 2009). The summed throw profile was also compared to that of each of the faults, in order to determine the kinematic relationship of the thrust faults.

In order to compare throw and shortening distribution in this study, throw values are converted to meters using a velocity of 2000m/s, as the internal velocity of the post-Messinian overburden. This velocity value (c. 2000m/s) was determined from a check shot of a nearby exploration well (Frey Martinez et al. 2005), and it is assumed to be constant throughout the study area.

The throw distribution for each of the thrust faults and their summed values, and fold shortening profiles along 2 key horizons (IPM1 and IPM2a) are presented in Figure 6.8 and 6.9. The profiles for shortening and throw generally vary in geometry and gradient along strike as expected in most complex thrust related systems (Rowan 1997; Higgins et al. 2009). The summed displacement profiles for the 4 faults as whole, tend to be irregular showing multiple peaks and deficits along strike, whereas shortening distribution profiles tend to be roughly symmetrical (Figure 6.8 and 6.9). The profiles for shortening and dip-slip generally vary in geometry and gradient along strike as expected in most complex thrust related systems (Rowan 1997; Higgins et al. 2009).

#### *6.3.4.1 Horizon IPM1*

Throw and shortening profiles along Horizon IPM1 in Segment 1 are almost similar in geometry. Throw profile and shortening for Fault T20 are characterized by the same local irregularity close to Strike slip fault S13 intersection zone between 700 m to 1000 m of Structure X (Figure 6.8). Both profiles show a systematic increase in elevation to their maximum point at approximately the south eastern end of Segment 1.

In Segment 2, where Fault T20 and T21 overlap, throw profile for T20 decreases abruptly with a gradient of 0.05. Similarly, in this zone throw profile for Fault T21 decreases from its maximum with a gradient of 0.06, and it displays several throw maxima and minima towards the south-eastern end of Segment 2. Whereas, the summed throw profile for the overlapping faults is smoother and it decreases with a gentler average gradient (0.03) than faults at the zone of overlap (Figure 6.8 b). In contrast to the geometry of summed throw distribution in Segment 2, the shortening profile displays an almost flat geometry, but with several irregular maxima and minima (Figure 6.8 c).

In Segment 3, the profile for Fault T21 also decreases in elevation with gradient of 0.07 close to the north-western end of the segment where it overlaps Fault T22 (Figure 6.8 b). Profile for Fault T22 decreases from its maximum elevation towards its north-western and south-eastern ends with gradients of 0.2 and 0.08, respectively. Fault T25 also shows a high throw profile gradient of 0.2 at the zone where it overlaps T22, however, its south eastern end, shows a gradual decrease from its maximum elevation (Figure 6.8 b). The summed throw profile for the synthetic faults is characterized by a notable throw minimum at the zone of overlap at c. 3,800m of the profile length, and it does not show significant decrease in gradient when compared to that of the each of the faults. Whereas, the shortening profile show a flat

geometry from Segment 2 to the mid zone of Segment 3 where it decreases with an average gradient of 0.3(Figure 6.8 c).

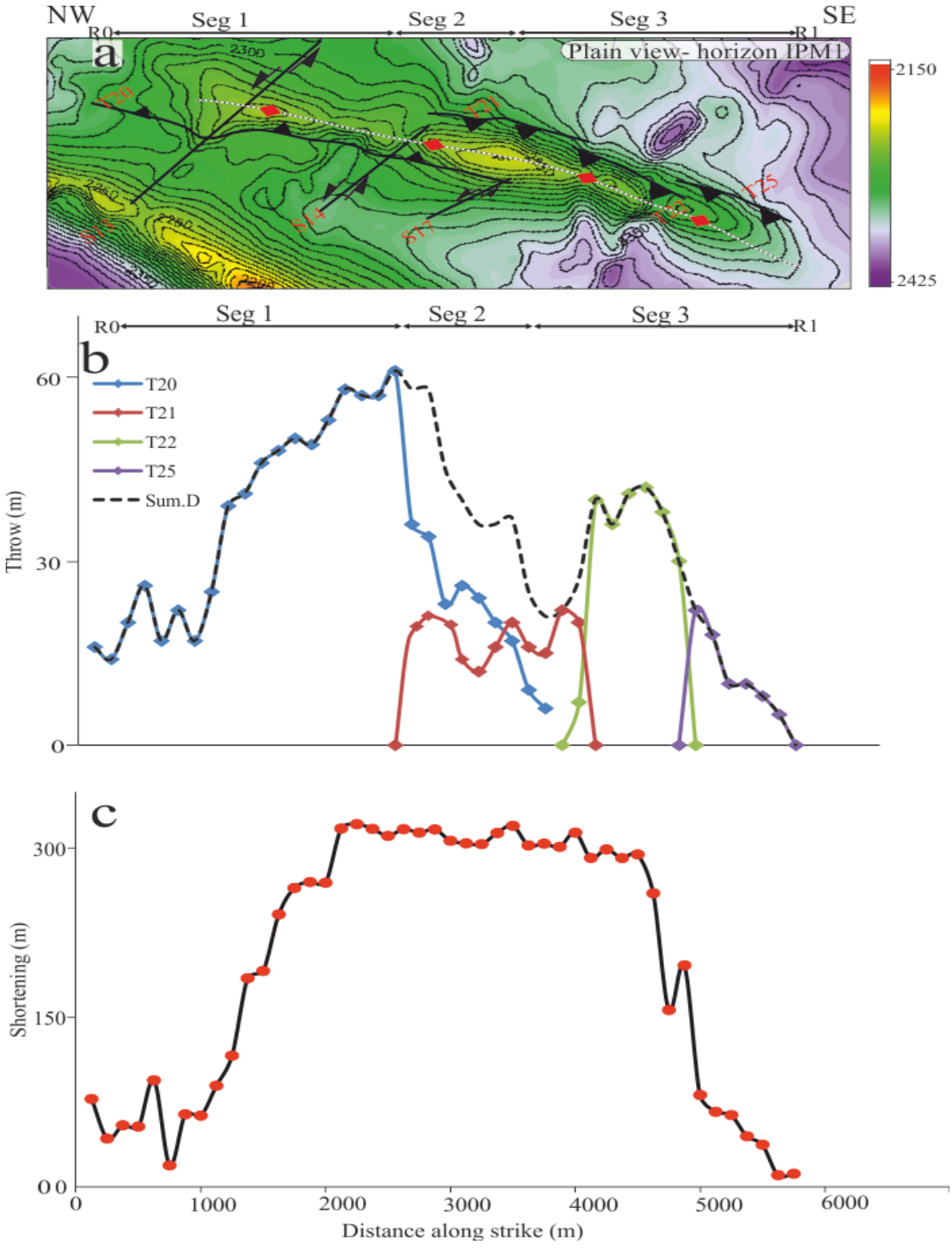


Figure 6.8: Summed throw and fold shortening distribution along Horizon IPM1. (a) Horizontal throw (b) Lateral fold shortening.

#### *6.3.4.2 Horizon IPM2a*

The throw and shortening profiles for Fault T20 along IPM2a within Segment 1 also show similar irregularity of minima and maxima. These irregularities correspond to Strike slip faults S13 and S14 intersection zones (Figure 6.9). In the absence of these irregularities, profile for Fault T20 increases systematically from the north-western end of Structure X to the end of Segment 1, where it attains its maximum elevation (Figure 6.9b). Whereas, the shortening profile increases towards the end of Segment 2, from Segment 1 (Figure 6.9 c).

In Segment 2 throw profile for T20 decreases with an average gradient of 0.05. The thrust faults do not overlap Fault T21 in this horizon (IPM2a) as that of Horizon IPM1. The shortening profile in Segment 2 decreases in profile gradient compared to Segment 1.

In Segment 3, throw profile for Fault T21 displays two maxima separated by a minimum between 3,500 m to 4,500 m of the profile length, this is followed by an almost flat geometry towards the south-eastern part of the segment (Figure 6.9 c). The throw decrease of Fault T21, at c. 4000 corresponds to the lateral tip of Fault T22 or the north western end of the overlapping zone between T21 and T22. Throw profile for Fault T22 is characterized by a minimum at the centre separated by two maxima. The average gradient towards both ends for T22 is c. 0.09. The throw profile for T25 is symmetric within this segment, with an average gradient of 0.03. The profile for the summed throw of Fault T21, T22 and T25, is characterized by notable minima, particular, close to zones of overlap. While the shortening profile in Segment 3, shows only minor irregularities (Figure 6.9 c). It decreases in elevation towards the south eastern end of Segment 3, from its maximum at c. 4100 m from its maximum at 4100 m.

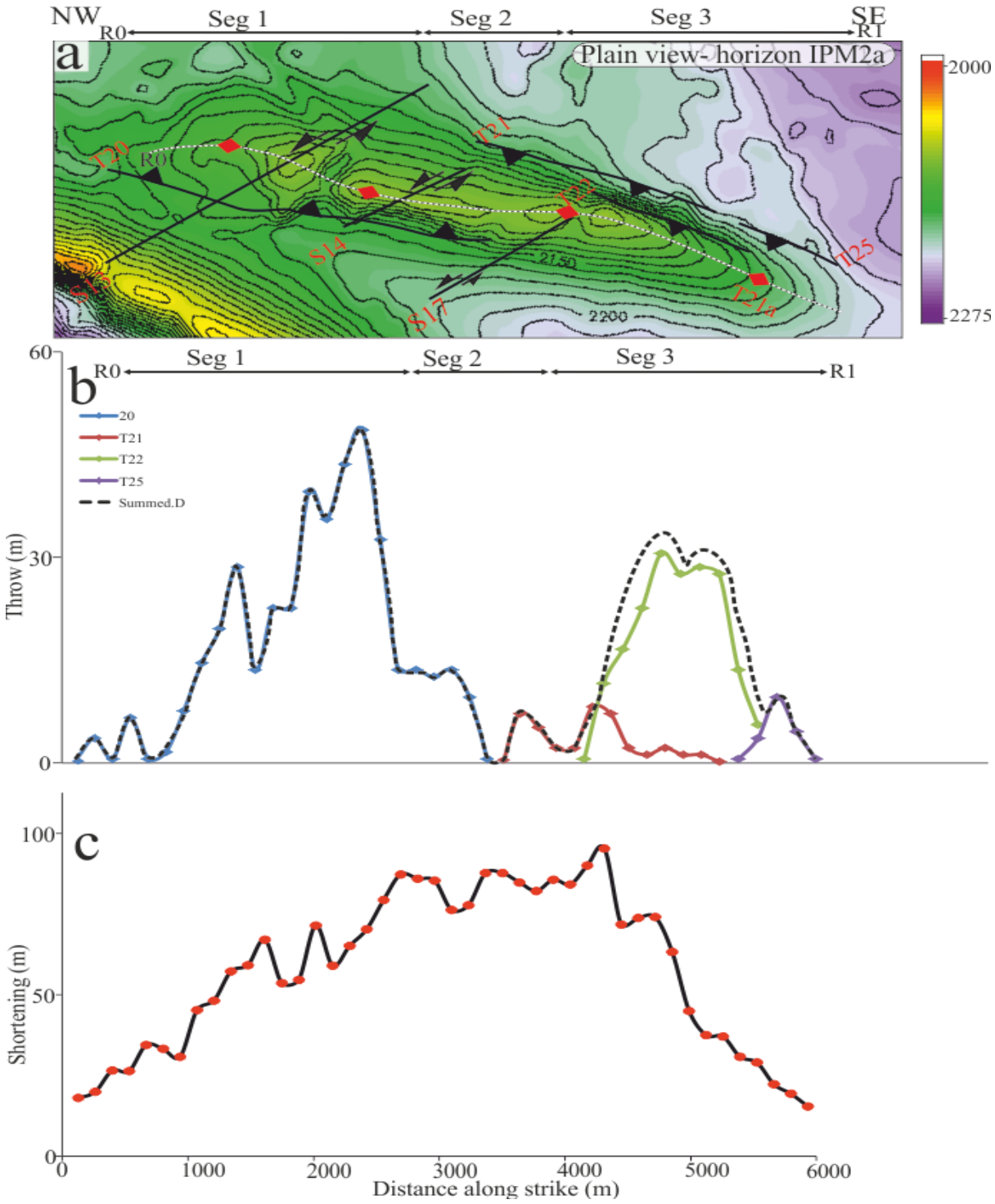


Figure 6.9: Summed dip-slip and fold shortening distribution along Horizon IPM2a. (a) Horizontal dip-slip. (b) Lateral fold shortening.

## 6.4 INTERPRETATION

### 6.4.1 Lateral Fault Interaction

The fold described in this study can be interpreted as a structure which appears simple on the seabed but is internally complex along strike as illustrated in Figure 6.1 - 6.9. The zones of fold vergence reversal, which defines the fold segments, coincide with region of fault overlap. It has also been shown that each segment in Structure X is defined by its own unique fault interaction, based on the pattern of the throw profiles. In this section, the throw geometries are interpreted based on examples of documented throw profiles (Muraoka and Kamata 1983; Nicol *et al*. 2002; Rowan et al. 2004).

Clearly, the thrust faults in Structure X does not exhibit the classical displacement pattern normally associated with an idealised isolated fault, which is characterized by the C type or asymmetric geometry (Muraoka and Kamata, 1983, Nicol et al., 1996). The majority of the displacement profiles along horizons cut by the thrust faults show notable anomalies, particularly at zones where they intersects strike-slip faults or overlap neigbouring faults (Figure 6.8 and 6.9).

The irregular maxima seperated by minima exhibited by the throw profile for Fault T20 (in Segment 1), particularly between 1,000 m and 2000 m of the fold length(Figure 6.9 and 6.10), can be interpreted an expression of strike slip fault intersection. Although, this irregularity can not be exclusively differentiated from the effects caused by fault linkage (Cartwright et al. 1995). However, the zones almost correspond to where the strike slip faults (Faults S13 and S14) intersect Fault T20. More also, the cross cutting relationship between Faults T20 and S14 implies fault interaction (Figure 6.3 c). Fault T20 is the cross cutting fault, this indicates S14 is acting as a barrie to fault propagation. The change in shape

exhibited by T20 at the region of cross-cut from listrict to anti-listric may imply a zone of intense deformation during fault propagation.

The presence of overlapping faults in Structure X implies displacement transfer between faults and therefore invokes an evidence for fault kinematic interaction (Larsen 1988; Nicol et al. 2002). Although, it may be difficult to ascertain the major cause of the abrupt change in throw profile displayed by Fault T20 and T21 in Segment 2. This is because the zone of fault overlap is close to where Fault S17 intersects Structure X, which is also capable of modifying displacement geometry. However, the summed dip-slip distribution in Segment 2 (T20 and T21) is less variable compared to that of each thrust fault (Figure 6.8b), and it displays a symmetric curve as would be expected for a single isolated fault. Such faults (T20 and T21) can be said to be geometrical coherent (Walsh and Watterson, 1991). Pairs of faults that are geometrically coherent are interpreted to have been kinematically linked since inception, such faults are termed relay faults (Larsen 1988; Nicol et al. 2002).In this case, the overlapping zone formed by the relay faults has been established from onset (Nicol et al. 2002)

Conversely, the summed throw profile in Segment 3 involving T21, T22 and T25 is characterized by an irregularly maxima and minima (Figure 6.8 b and 6.9 b). The minima are most notable at lateral ends of the overlapping region  This throw pattern reflects evidence of accidental or soft linkage (Cartwright et al. 1995), and such faults are not kinematically related, as interpreted in other studies (Nicol et al. 2002; Higgins et al. 2007). In summary, the case study fold is interpreted as a structure which contains both kinematically linked thrust faults, and thrust faults that are kinematically separated from onset.

Another form of interaction that may have occurred in Structure X is fault and fold transfer (Dahlstrom 1970; Gardner and Spang 1973). Vertical throw profiles of the thrust faults most

commonly show high gradient close to their upper tip (Figure 6.4 c – 6.7 c). This may indicate displacement transfer from the faults to their associated folds.

### 6.4.2 Initiation of Thrust Ramp

In the theory fault ramp development, zone of maximum displacement always corresponds close to the exact site of fault nucleation (Williams and Chapman 1983; Barnett et al. 1987; Baudon and Cartwright 2008b). The four faults examined in this study mainly show a systematic increase in throw from the upper tip downwards to the detachment layer (Figure 6.4 c - 6.7 c). However, some profiles show a maximum displacement at the centre, for example Fault T21 at 3000m and 4500m (Figure 6.5 c), suggesting several initiation zones, which may be interpreted as function of dip linkage (King and Yielding 1984; Mansfield and Cartwright 1996). Generally, the vertical throw distribution pattern of the faults suggests that they ramp upward from some point close to the detachment layer.

## 6.5 DISCUSSION

### 6.5.1 Fold Segmentation and Lateral Development

The similarity in geometry of the growth sediment, combined with the non-segmentated appearance on the seabed may suggest that recent development of the fold occurred as a single structure. The complexity of the internal geometry of the fold can be explained by considering the lateral development.

The lateral growth of thrust related folds is commonly dependent on the lateral propagation of their associated thrust faults (Rich 1934; Boyer and Elliott 1982; Briggs et al. 2006). Models of thrust related folds in three dimensions have been shown to vary in geometry along strike corresponding to displacement gradients (Scott *et al.* 1991; Rowan 1997; Higgins et al. 2009). The zones or points of change in geometry, represents sites of linkage or displacement transfer. This suggests that such thrust folds develop from different small structures which

propagate towards each other as has been demonstrated in many studies (Shumin and Dixon 1991; Dixon and Liu 1992; Higgins et al. 2007). Employing the same criterion, this study proposes that Structure X is a through growing fold formed by both thrust faults that are kinematically linked from onset, and faults that are kinematically isolated.

The formation of Structure X is illustrated in Figure 6.10 a-c. As shortening increases in time t1, the relay faults (Fa and Fb) are restricted within the relay zone, as they tend to propagate pass each other, thus forming a symmetric pop fold (McClay 1992a). Whereas, the free tipping ends of the faults laterally propagate asymmetrically (Figure 6.10 b). At t3, the (Fb and Fc) propagated towards each other and merge to form a through going segment. (Figure 6.10c).

It can be argued, however, that Structure X initiated from a single point source and become complex through time. This is inferred from both the shortening profile geometry and syn-kinematic package which appear as that of a single structure. In this case, as shortening increases, the fold increases in length, thereby propagating into the surrounding zones of previously undeformed layering and triggering the formation of secondary thrust related structures. The formation of a new thrust fault would depend on the lateral friction, sense of shear and basal friction (Costa and Vendeville 2002), which has not been determined in this study.

It is important to note that strike slip faults were also acting as intervening faults or barriers during the fold formation process. However, there were only 2 zones where strike slip fault were observed to offset thrust faults and these zone do not show notable change displacement gradient as may be expected for a restricted fault. Although, the strike slip faults in Structure X are small in length, the longest is 3,000 m. It is possible that the strike slip faults are too small to restrict thrust fault propagation. However, a more detailed study between thrust fault and strike slip fault interaction is described in Chapter 5, and the gradient change of thrust

faults interacting with strike slip fault is compared with that of relay thrust faults Chapter 7 of this thesis.

There have been few documented examples of internally segmented folds along strike similar to the fold described in this study, that have been proposed to have been formed by the process of linkage. Higgins (2007, 2009), Documented a single fold in the Niger Delta, as having developed by the linkage of synthetic and antithetic faults within the thrust related folds. These authors showed that the change in fold vergence occurs through a symmetric pop-up zone along strike, and they characterized the fault interactions into antithetic Type 1, 2 and 3 interactions (Higgins 2007). They observed a symmetric pop-up structure below converging faults similar to the fold geometry in Segment 2. Although the tip line geometry and summed displacement distribution within the pop-up zone tend be characterized by upwards tapering and deficit respectively differing to the fault interaction pattern observed between T20 and T21. The formation of pop-up structure have been demonstrated by Harrison and Bally (1988), using numerous case studies from the Parry Island Fold and Thrust Belt (Canadian Arc). They showed converging thrust faults cross cutting each other below the pop-up zone, which is not compatible to the fault interaction observed in Segment 2, although the style of fold vergence reversal is the same.

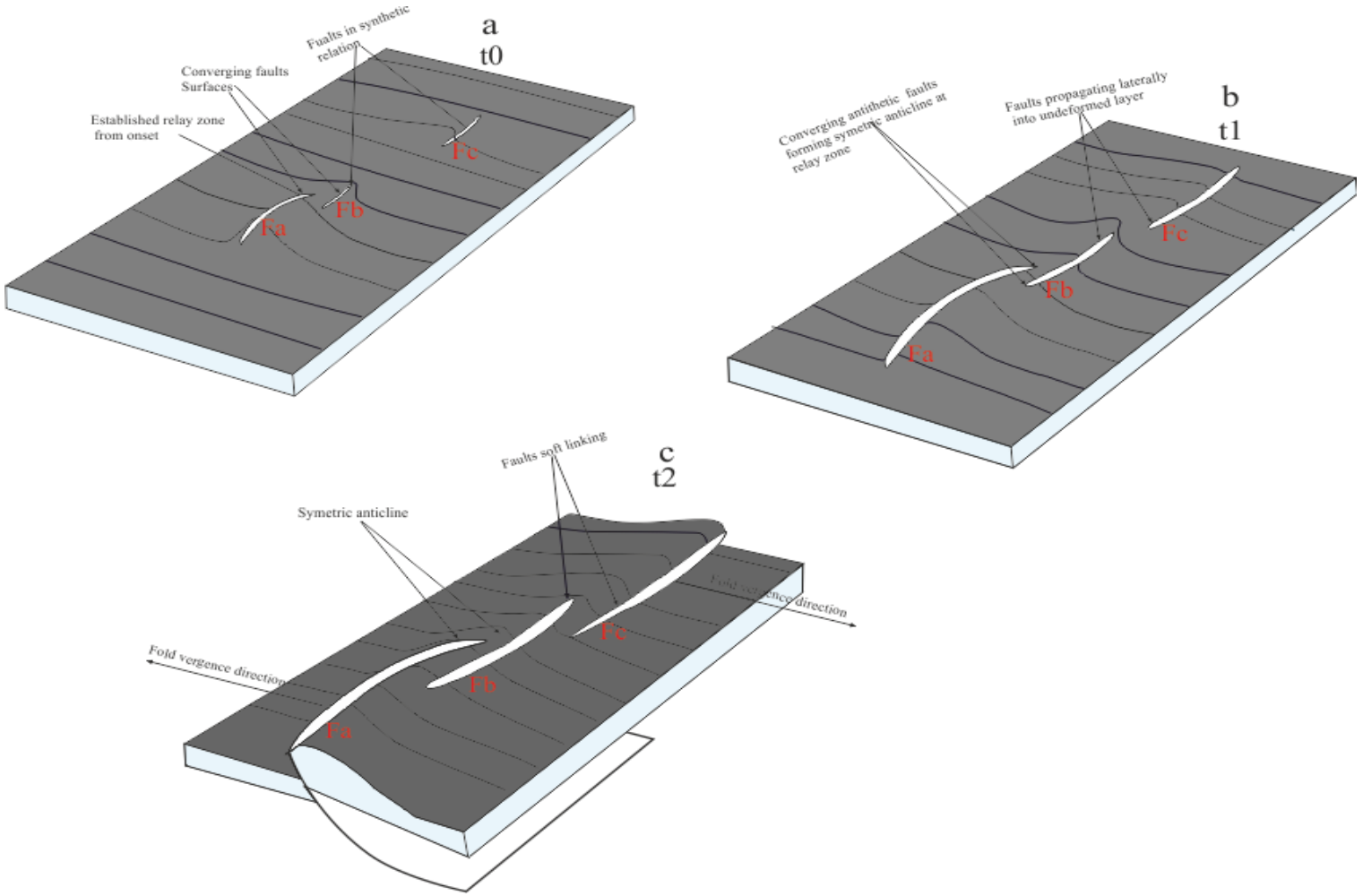


Figure 6.10. Hypothetical model of the evolution of the case study segmented fold at different times (t0-t2). (a) Relay zone (Fa and Fb)) already established at t0, kinematically separated from Fc. (b) The converging faults (Fa and Fb) are restricted at the relay zone and propagate freely at their opposite end, and the Fc increases in length. (c) Fb and Fc overlap (soft link) forming a through growing fold.

Another typical example of fold which varies in style perpendicular to transport direction is the fold of the deepwater Mississippi Fan fold and thrust belt in northern Gulf of Mexico (DeBalko and Buffler 1992). Rowan (1997) described the 3 dimensional geometry of this structure, it consist of three main compartments. Each compartment is characterized by a noticeable culmination and displays a different structural style and kinematic packages from the other. The displacement and shortening distribution along the Mississippian fold tend to be incoherent in geometry (Rowan 1996, their Figure 12), as observed in this study (Figure 6.8 and Figure 6.9). Although, the incoherency in geometry between the profile geometries of shortening and displacement was interpreted as folding preceeding faulting, which is compatible to a fault break fold (Willis 1893, Fisher et al., 1992). However, in this study its best to say both structures (fold, and thrust faults), formed at different times (see Chapter 7)

Mitra et al., (2006) described the Ku-Zaap-Maloob fold and thrust belt offshore Campeche Bay, Mexico as internally segmented structural system. The structure consists of series of complex thrust related folds, which change orientation from east-west to north-west-south-southeast along strike. The major structures are interpreted to be related to a series of nested thrust faults all merging into the principal thrust fault. The authors also show that the thrust faults are characterized by small displacement relative to fold wavelength and amplitude. They interpreted the structures as faulted detachment folds, formed by a transition in deformational behaviour from detachment folding to progressive fault propagation (Mitra 1990, 2002).

### 6.5.2 Thrust Ramp Development

Recent studies of thrust ramp development suggest central nucleation point or some point above the decollement layer, and propagate both upward and downward (Eisenstadt and De Paor 1987; Ellis and Dunlap 1988). The vertical throw distribution of faults presented in this

study does not corroborate with the central nucleation theory, but rather supports the models of Rich, (1934), Suppe, (1983). These authors suggest that thrust faults step off a basal decollement to cut up section. However, a limitation to this model has been pointed out by Ellis and Dunlap (1988), such as leaving the footwall of the thrust fault undeformed and inactive during deformation. The thrust faults described here and in Chapter 4 show variation in geometry in the footwall from anticline to syncline verging at different orientation; this indicates that footwall is an integral part of the deformation. It is proposed here that thrust fault initiated close to the detachment and ramp up towards the sea surface.

Deformation of the footwall is probably caused by friction during hanging wall thrusting above footwall. It is suggested here, that the geometry of the footwall depends on the angle at which the hangingwall thrust above the footwall. If the thrust fault, is ramping with a low angle, the footwall will be concave downward forming an anticline, while steep angle ramping will result in concave upward geometry (footwall syncline).

The mechanism of central initiation, and radial propation is not excluded here and is widely observed in other studies (Muraoka and Kamata 1983; Barnett et al. 1987; Baudon and Cartwright 2008b). However, the fault analysis presented in this study does not agree with the inference of Ellis and Dunlap, (1988), that thrust faults do not propagate from detachment layer. An alternative interpretation is that thrust ramps can either propagate from the centre and propagate both upward and downward, or step up from detachment and propage towards the seabed. As interpreted by Briggs (2006), faults characterized by central iniiation are most likely fault detachment folds (Mitra 2002), while those which display maximum displacement close to detachment similar to the faults described here are fault propagation folds (Suppe 1985).

## 6.6 CONCLUSION

This study provides an example of a periclinal thrust related fold within the Levant deepwater fold and thrust belt, for studying the three dimensional geometry of folds, and fault interactions. The major conclusion drawn from the data and analysis is listed below.

- The fold appears simple on seabed but internally compartmentalised into 3 fold segments verging at different directions, by strike slip faults, and thrust faults of similar and opposing dips. Segment 1 is characterized by strike slip fault acting as only a subtle barrier to thrust propagation, Segment 2 comprises of convergent antithetic thrust fault which have been linked since inception, and segment 3 is made of synthetic thrust faults that are kinematically isolated.
- The fold is formed laterally as either a through going structure formed by linkage of smaller thrust related folds, or fold that developed as a simple thrust that becomes complex through time. Several models that are compatible with the result of this study support the formation by linkage.
- The thrust ramp initiated upward close to the detachment layer and propagates upward towards the sea bed.

# CHAPTER SEVEN

## 7 DISCUSSION

This thesis has documented examples of thrust related folds from a 3D seismic dataset in the contractional domain of the Levant Basin, which has been used to expand on the knowledge of fold and thrust fault segmentation and development. Detailed analysis improves the understanding of the inter-relationships between thrust faults, thrust related folds and strike slip faults within the study area. Whilst the study is focused on one geographic area it is believed that the results are relevant to other fold and thrust belts in the world, particularly where strike slip faults and thrust related folds co-exist.

The major findings in this thesis have been addressed in Chapters 4, 5 and 6 and therefore will not be discussed further in this chapter. The focus of this chapter is to expand upon and address the main points that were raised in preceding chapters that are currently unanswered. The main points to be addressed include the: (1) inter-relationship between thrust faults and associated folds, (2) influence of mechanical stratigraphy on the inter-relationship between thrust faults and their associated folds (3) factors influencing the propagation of restricted faults and (4) the wider implications of the research.

### 7.1 RELATIONSHIP BETWEEN FOLDS AND THRUST FAULTS

The geometries and timing relationship of the main types of thrust related folds have been addressed in Chapter 1 (Section 1.3.3). Fault bend folds, form passively over pre-existing faults with ramp flat trajectories (Rich 1934). In fault propagation folds (Suppe 1985a), folding and faulting are contemporaneous with folds growing as faults progressively propagates. In fold detachment thrust, initially unfaulted detachment folds are modified by thrust faults or reverse faults cutting fold limbs (Mitra 2002). The majority of the thrust

related folds in the Gal C survey are either thrust propagation folds or thrust detachment folds; this is inferred from the geometry of the structures (absence of upper detachment layer).

Fold detachment thrust faults, initiate as a detachment fold above a weak ductile layer (e.g salt) underlain by a competent unit (Jamison 1987; Mitra 2002) (Figure 7.1). A detachment fold (Figure 7.1 a), is formed as the weak strata are distributed into the fold core (Jamison 1987; Stewart 1996). In theory, if there was insufficient material to fill the core, deformation would be accommodated by faulting (Figure 7.1 b and c). The fault would probably nucleate within the more competent units, which will eventually propagate downwards toward the weak layer where it detaches or connects with the basal detachment (Figure 7.1 c). The idea of fault nucleation within the competent unit agrees with the model demonstrated by Mitra (2002).

In a fault propagation fold (Figure 7.2), the fold develops coevally with thrust faulting and it has been described in many studies (Suppe 1985a; McClay 1992b). In Chapter 4, the thrust related folds are described as pure fault propagation folds, which evolve from shear thrust faults (Willis 1893), as demonstrated in Figure 7.2 a). The mechanical model for the development of shear thrust faults has not been documented in any study. It is inferred from the illustration of Willis (1893) that there are faults with minimal amplitude and shortening. The thrust fault and fold developed as shortening increases through time (Figure 7.2 a and b).

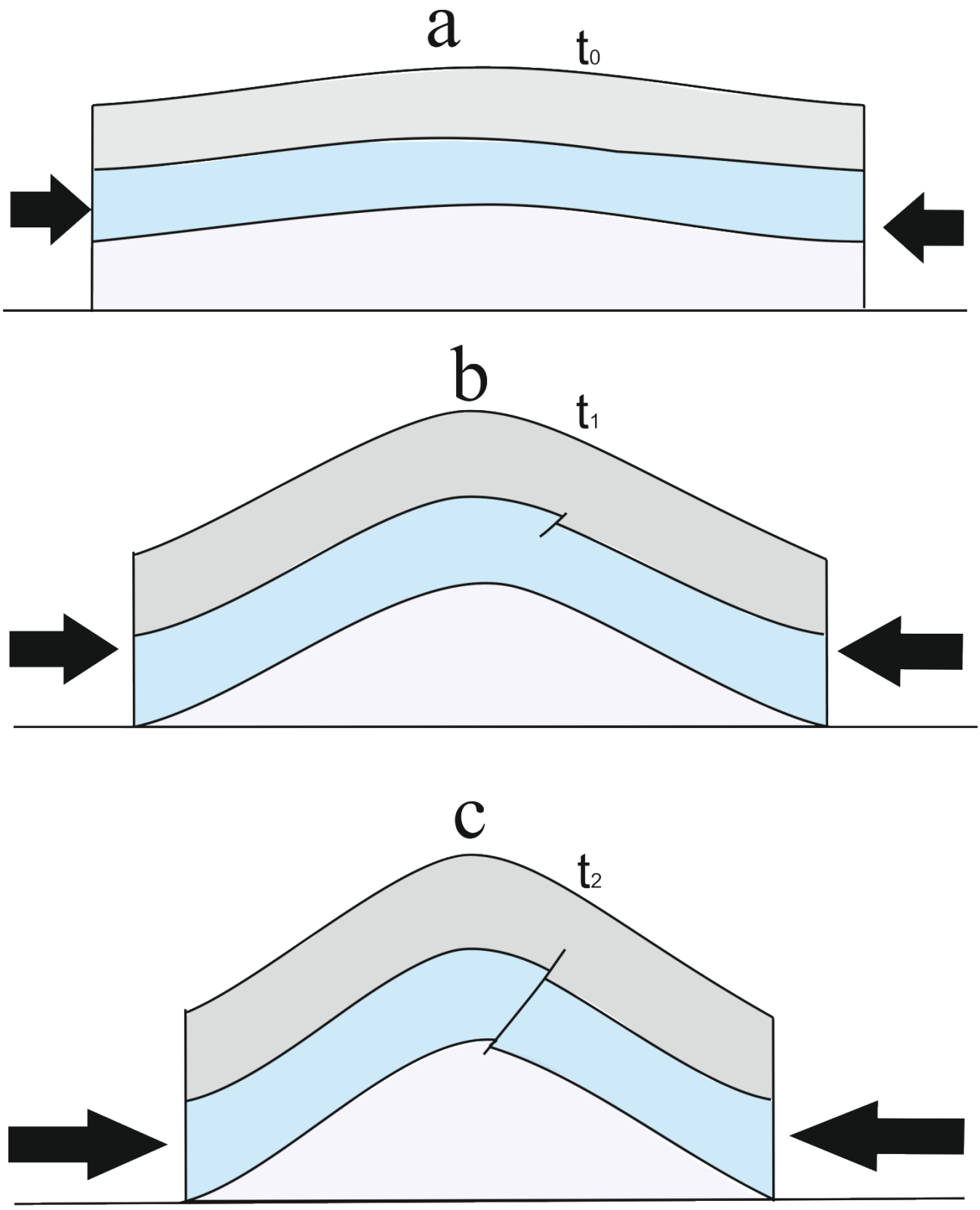


Figure 7.1: Conceptual model of the development of a thrust detachment fold. t0 – t2 represent progressive time of development.

Geometrically, it is difficult to determine whether the thrust related folds described in this study are fault propagation folds or fault detachment folds, even though they have different evolutionary paths. A criterion which may be used to distinguish between fault propagation fold and fault detachment fold is the interplay between their hinge and limb (Storti and Poblet 1997). According to published literature on geometric-kinematic models, fault propagation folds are likely to form with a non-rotating backlimb and at least a migrating hindward syncline. As pointed out by Wallace and Homza (2004), some detachment folds have been shown to form with rotating limbs, and even fixed synclinal hinges.

Fault propagation fold may be characterized by an upward decrease in fault displacement (Suppe and Medwedeff 1990; Hedlund 1997). However, this condition alone does not uniquely establish the origin of a fold as a fault propagation fold because they could also be met by a pre-existed fold that has been modified by a propagation of a ramp tip, similar to fault detachment fold (Wallace and Homza 2004). These characteristics to some extent may be useful guides towards a preferred interpretation. However, they certainly should not be used as a diagnostic tool, because they are based on models and have only limited support from observation. Since a wide range of overlapping kinematic similarities can be envisioned for fault propagation fold, and fault detachment fold, the mechanical stratigraphy of the area and perhaps the local structural style are the most likely criterion.

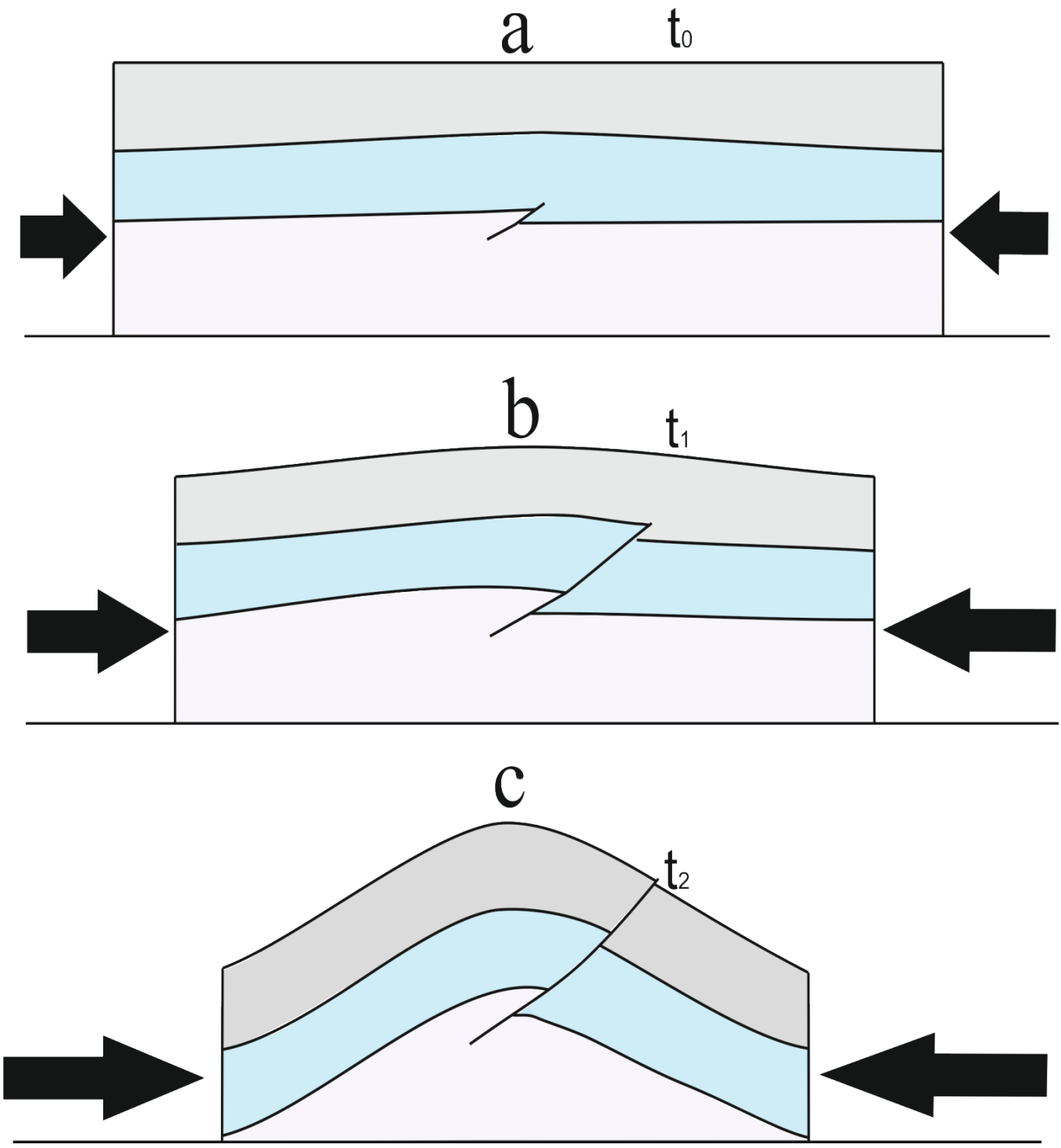


Figure 7.2: Conceptual model of the development of a thrust propagation fold. $t_0 - t_2$ represent progressive time of development.

### 7.1.1 Influence of Mechanical Stratigraphy on Fault and Fold Interaction

The dynamic evolution and final geometry of fold and thrust fault is strongly dependant Mechanical stratigraphy (Davis and Engelder 1985a; Pfiffner 1993; Hardy and Finch 2007; Vidal-Royo *et al.* 2009; Vergés *et al.* 2011). One possible factor controlling the development of thrust related folds formed above a detachment layer, similar to those in the Gal C survey is the thickness and strength ratios of incompetent to competent layers.

According to Woodward and Rutherford (1989), mechanical weak layers will act as detachment layer for thrust faults if the thickness of the incompetent layer exceeds a critical value. Pfiffner (1992) used the symbol "n" to define the thickness ratio of detachment layer (incompetent unit) to overburden layer (competent unit). In his study, it was observed that high n (greater than 0.5) values favour disharmonic folding, while low n-values (less than 0.5) adjacent layers interfere with each other and lead to harmonic folding or thrust ramping from the incompetent layer (Pfiffner 1993). Given the thickness difference between decollment layer, and its overburden in the Gal C survey, the thrust faults can be said to have ramp up from detachment. The Messinian salt is characterized by several prominent reflections (M to M6, Chapter 3, Figure x). The upper unit (between M and M6 or package T7), is a detachment site for the majority of the post-Messinian thrust related folds (Chapters 4-6). The average ratio thickness of package T7 and post-Messinian overburden is 0.28. This ratio is less than 0.5, which is characterized by Pfiffner (1992) as low n values, and therefore favours fault erupting from detachment, which may corresponds to fault propagation fold.

Similar to thickness ratio, strength contrast between the stratigraphic layers is another important factor controlling the development of thrust related fold. Erickson (1996), discussed this aspect and concluded that folding will exceed faulting, similar to fault detachment fold (Jamison 1987), or fault break fold (Willis 1893), if the there is a high

strength difference between the decollment layer, and its overburden. Therefore, if the strength contrast is low faulting will either proceed folding or both processes (faulting and folding) will be coeval. The mechanical strength of the Messinian evaporate may be difficult to determine, since the origin of its internal layering is not clear due to the absence of well data (See Figure 3.6, of Chapter 3). However, the prominent internal reflections, and brittle deformation at the upper Messinian unit contains impurity of cataclastic origin within the evaporite units, as suggested elsewhere (Bertoni and Cartwright 2006; Cartwright et al. 2012). It is suggested here that this impurities within the salt implies low strength contrast between evaporate unit and its Plio-Quaternary overburden, and therefore corresponds to early development of thrust fault in the detachment.

Thrust ramp propagation through a stratigraphic cover is also dependant on the mechanical characteristics of the layer. According to Hardy and Firch (2007), faults in a weak and poor mechanical layering tend have a broad upward widening monocline with limb dips increasing towards the fault tip similar to that of a trishear fault propagation fold (Erslev 1991).Whereas, bedding parallel mechanical layering in the cover display narrower, kink-like fold geometries with more constant limb width and dips. The folds described study show some evidence of kink band style. For instance in structure A (Chapter 4, Figure 4.12c), the central zone of Fault T9 tends to display sharp and angular hinges similar to a kink band style. Although, this geometry is not consistent along strike, the folds are generally characterized by rounded hinges. Evidence of kink band style is common in well layered heterogeneous units (Hardy and Finch 2007). Similarly, the post-Messinian overburden is well layered, and can be differentiated into mud dominated, and sand dominated units, as inferred from seismic sections (Figure 3.6, Chapter 3). The variation in sand content may result to the kink style geometry observed in this study.

Another type of fault propagation geometry which may resemble the fault and fold pair in the study is the double edge fault propagation folds (Tavani and Storti 2011). This type of fold is also expected to occur in well layered materials. The main difference between the double edge propagation fold and the thrust related folds described in this study is that the latter increases in deformation intensity upward (Tavani and Storti 2011). Whereas, the former have been shown to decrease in shortening upward (Cartwright et al. 2012). Such decrease may be a reflection of syn-kinematic deformation, whereby older overburden sediment has shortened for longer time than the younger sediments.

### 7.1.2 Other Evidences Supporting Early Development of Thrust Faults

There are four supporting lines of evidence in favour of the interpretation of the thrust related folds in the Gal C survey as fault propagation folds instead of fault detachment folds.

(1) The absence of detachment folds and the presence of thrust faults associated with low amplitude folds (Type A thrust related fold) indicates faulting initiated early in the development of the structures in Gal C. The Type A thrust related folds, as interpreted in Chapter 4, are considered as the early development stage of the Type B folds. As demonstrated in Figure 7.2, the structure at t0 and t2 are representative of Type A and Type B thrust related folds respectively.

(2) It is also observed that the difference between shortening and displacement values are commonly smaller for the Type A thrust related folds than the Type B. For example Faults T46 and T49 (Chapter 4), have displacement values either higher or equal to their shortening values (Figure 7.3 and 7.4). Whereas, the thrust related folds in Structure X (Chapter 6, Figure 6.8), and Structures A, B and C (Chapter 5, Figure 5.9) clearly have higher shortening values than displacement (Figure 5.9). Higher displacement than shortening values of the Type A thrust fold implies faulting is an integral process in the early stages of development (Figure

7.2). While the increase in shortening than dip-slip exhibited by Type B thrust related folds may indicate that folding became more dominant than faulting at a later stage of development.

(3) Profiles for dip-slip displacement and shortening distribution commonly, although not exclusively, show a similar geometry. Both types of profiles display a systematic increase close to any strike slip fault intersection, and in some cases they similarly show similar maxima and minima at the same intersection zone. These similarities in geometry indicate a contemporaneous relationship between the thrust faults and their associated folds Figure 7.3 and 7.4.

(4) Fault propagation folds are suggested to have relatively higher amplitude to displacement ratios than thrust detachment folds (Mitra et al., 2006). Fault displacement of thrust related folds in Gal C are relatively higher than amplitude. The average ratio of the maximum displacement and amplitude (D/A) for the Type B thrust related folds is 1.6 at Horizon IPM1, 1.3 for the Type A.

(5) The majority of the faults have their maximum displacement close to the detachment layer (Chapter 6, Figure 6.4c -6.7c). This may imply that the faults erupted from detachment, which is compatible to physical models of a fault propagation fold (Suppe 1985).

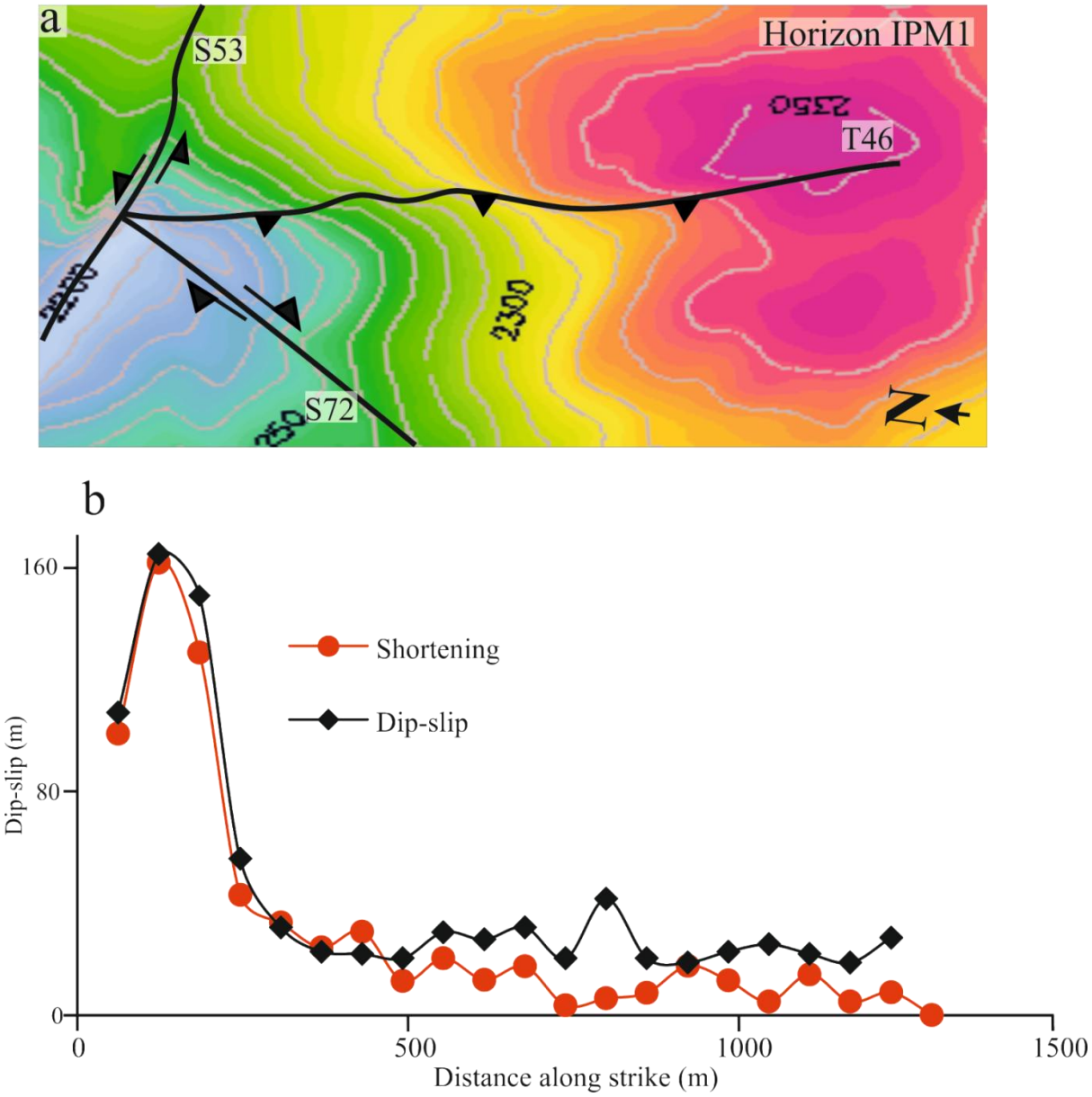


Figure 7.3: Fault dip slip and shortening distribution for Fault T46 along horizon IPM1. (a) Structural time dip map in two way travel time showing traces of the case study structural elements. (b) Profile for dip slip and shortening.

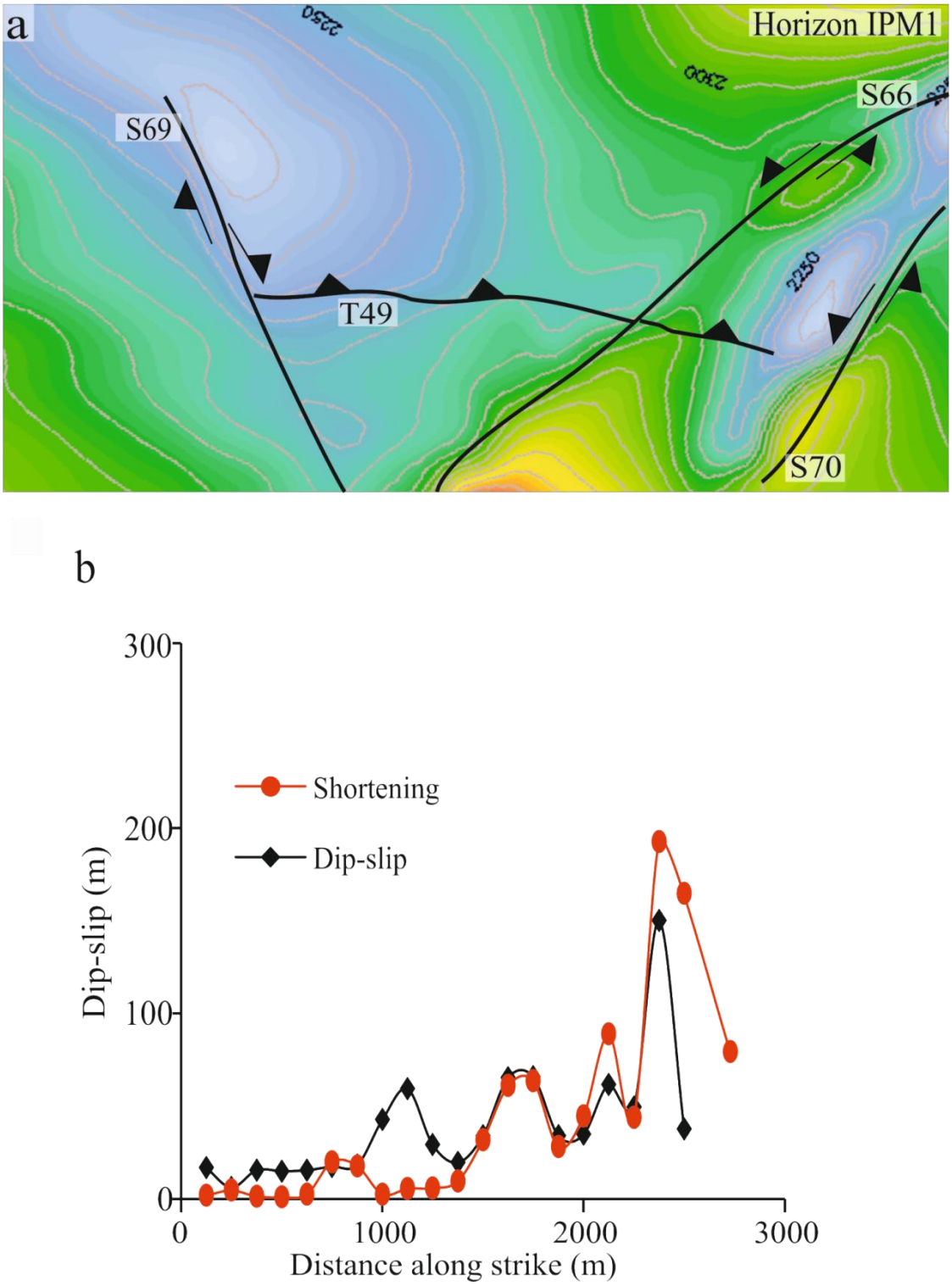


Figure 7.4: Fault dip slip and shortening distribution for Fault T49 along horizon IPM1. (a) Structural time dip map in two way travel time showing traces of the case study structural elements. (b) Profile for dip slip and shortening.

### 7.1.3 Development of Fold and Thrust Fault Pairs

The development of the thrust related folds in the study area can be inferred from the nature of the stratigraphy, result analysis from Chapters 4, 5 and 6, and from previous literature. The development of the folds is illustrated in Figure 7.5. This model is based on the deformation subsequent to the deposition of Horizon M (Figure 7.5a). The model shows two fault propagation folds (F1 and F2), illustrating possible development of the fault and fold pairs in Gal C.

In the early to middle Pliocene after the deposition of unit PM1 and PM2, F1 ramps up from detachment (Figure 7.5b), as that of a classical fault propagation fold (Suppe 1985b; Jamison 1987). Whereas, F2 initiates as ramp close to detachment, similar to that of a double edge fault propagation fold (Tavani and Storti 2011) . The basal ramp initiation illustrated here is inferred from the nature of stratigraphy, and maximum throw close to detachment (Chapter 6.9c – 6.12c, Figure x). Both faults formed with minimal folds as that of the Type A thrust related folds described in Chapter 4. In the Pleistocene, during the deposition of unit PM3, the thrust faults propagated with their associated folds (Figure 7.5c). F1 propagated up-dip as it increases in flat within the detachment layer. While F2 ramp connects the basal flat as it propagates both upward and downward (Figure 7.5c).

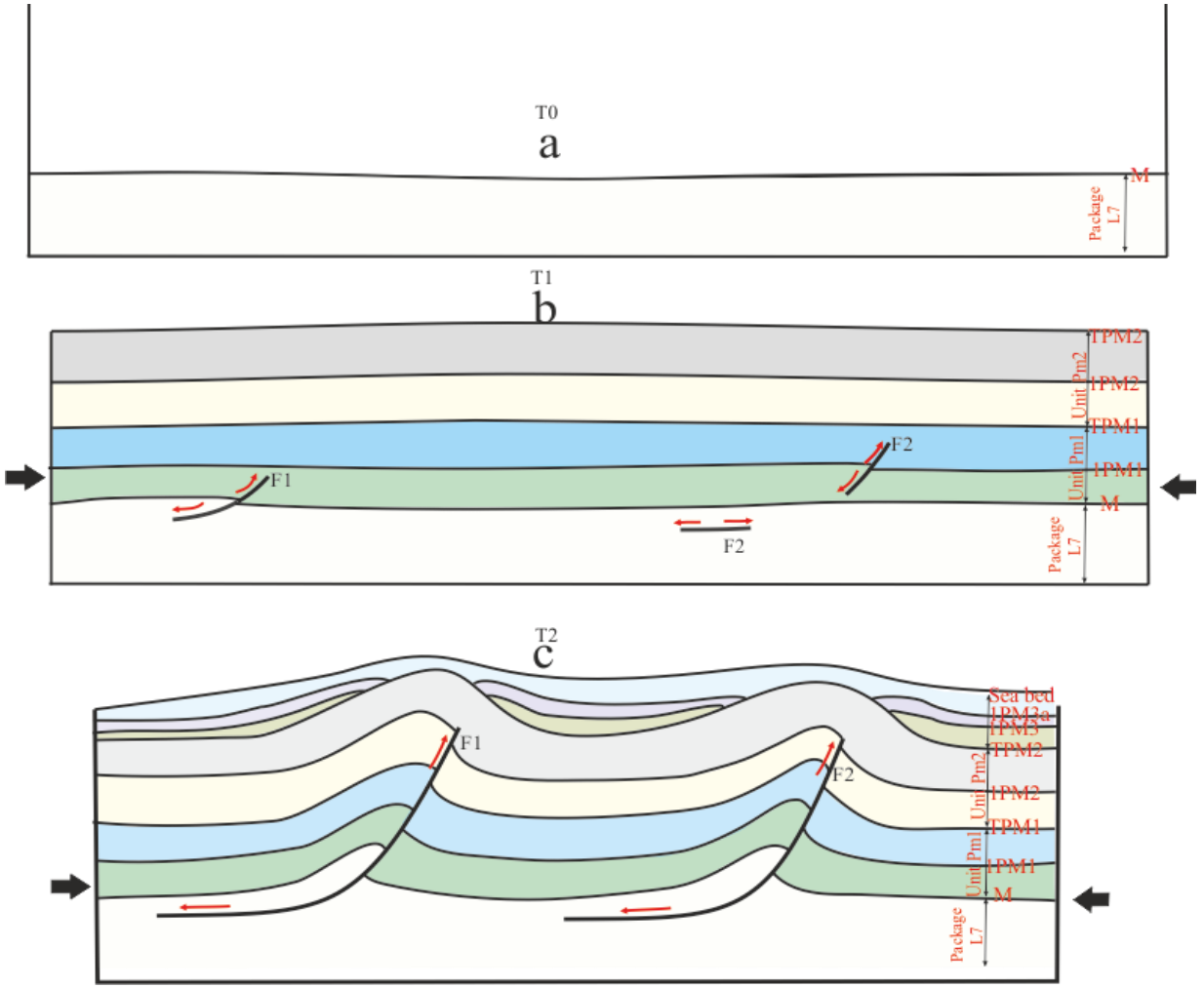


Figure 7.5: A conceptual model illustrating the development of thrust related folds in the study area through time (t0-t2). The model uses the same stratigraphic units of the study area (See Chapter 3, Figure 3.6) for nomenclature. The red arrows represent direction of propagation.

## 7.2 INFLUENCE ON BARRIER TO FAULT RESTRICTION

Two main types of physical barriers limiting thrust fault propagation are observed in this study. These are: (1) the 'overlapping thrust fault barrier' and, (2) the 'strike slip fault barrier'. It has been shown in previous chapters that the geometry of the displacement distribution of restricted thrust faults do not resemble those of isolated faults (Chapters 5 and 6). The majority of the restricted thrust faults show a high displacement gradient close to barrier, which may either be related to the development of fault overlapping zones (Chapter 6), or strike slip fault intersection zones (Chapter 5). Despite the studies in previous chapters, it still remains unclear what controls the inconsistency in displacement distribution with respect to barrier. For instance, some faults show no notable change at zones of restrictions, while some display higher displacement gradients than others. This section highlights the possible factors capable of influencing displacements at restricted zones.

The 3 main factors controlling fault restriction with respect to barrier include: (1) type of barrier, (2) barrier size, (3) distance of barrier to fault initiation. Each of these factors is described below.

### 7.2.1 Barrier Type

The two (2) main types of barriers described in this thesis include overlapping thrust fault (Chapter 5 and 6), and strike slip fault barriers (Chapter 5). Throw was used in Chapter 5, while dip slip in Chapter 6. In order to compare the influence of both types of barriers to fault displacement distribution, it is imperative to use the same displacement type (Figure 7.6 and 7.7). The throw values for the faults in Chapter 6, is converted to dip-slip (Figure 7.5) (see chapter 2, Section 2.3.1, for the difference between throw and dip-slip).

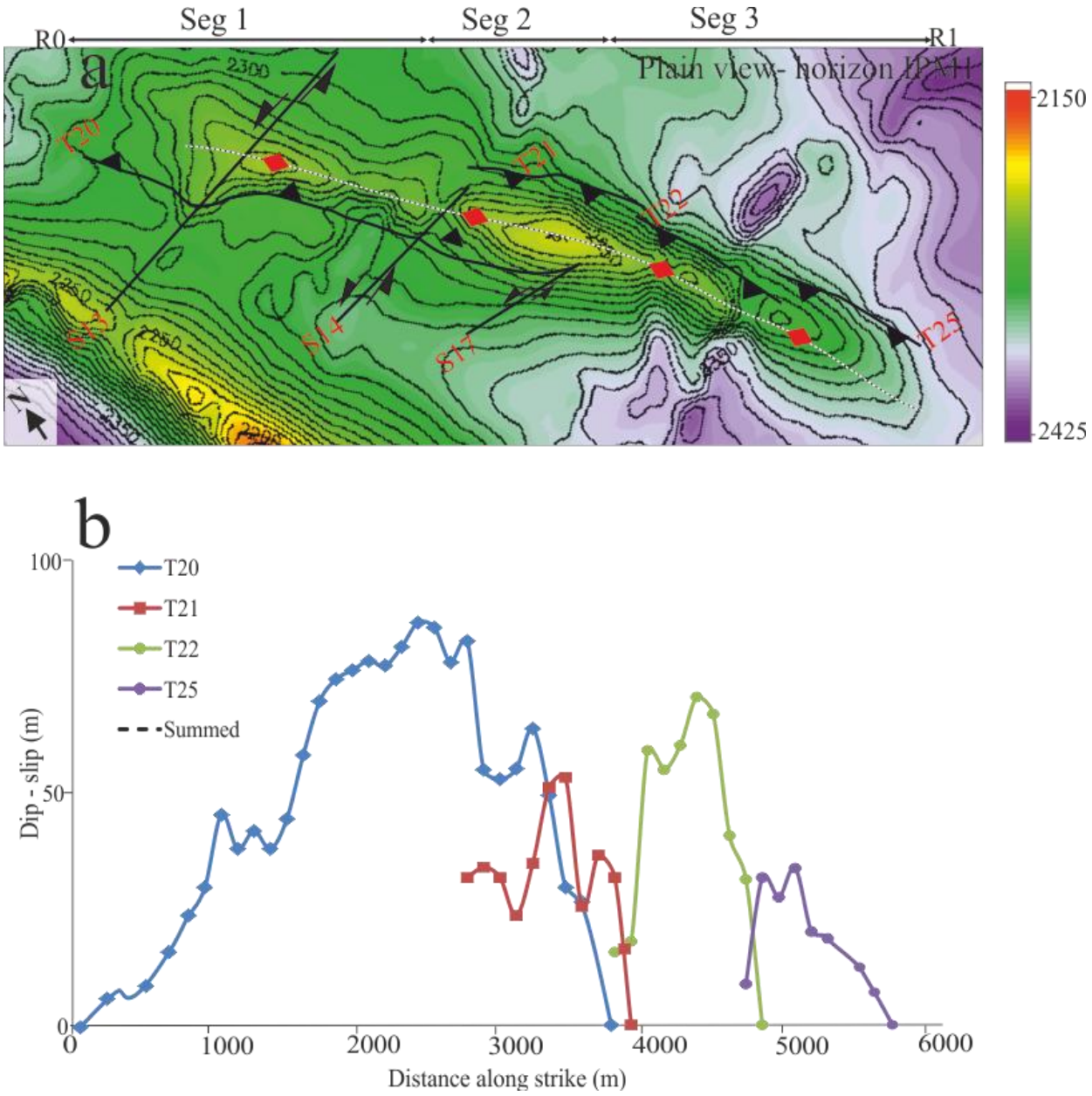


Figure 7.6: Dip-slip distribution along strike of the thrust faults in Structure X.

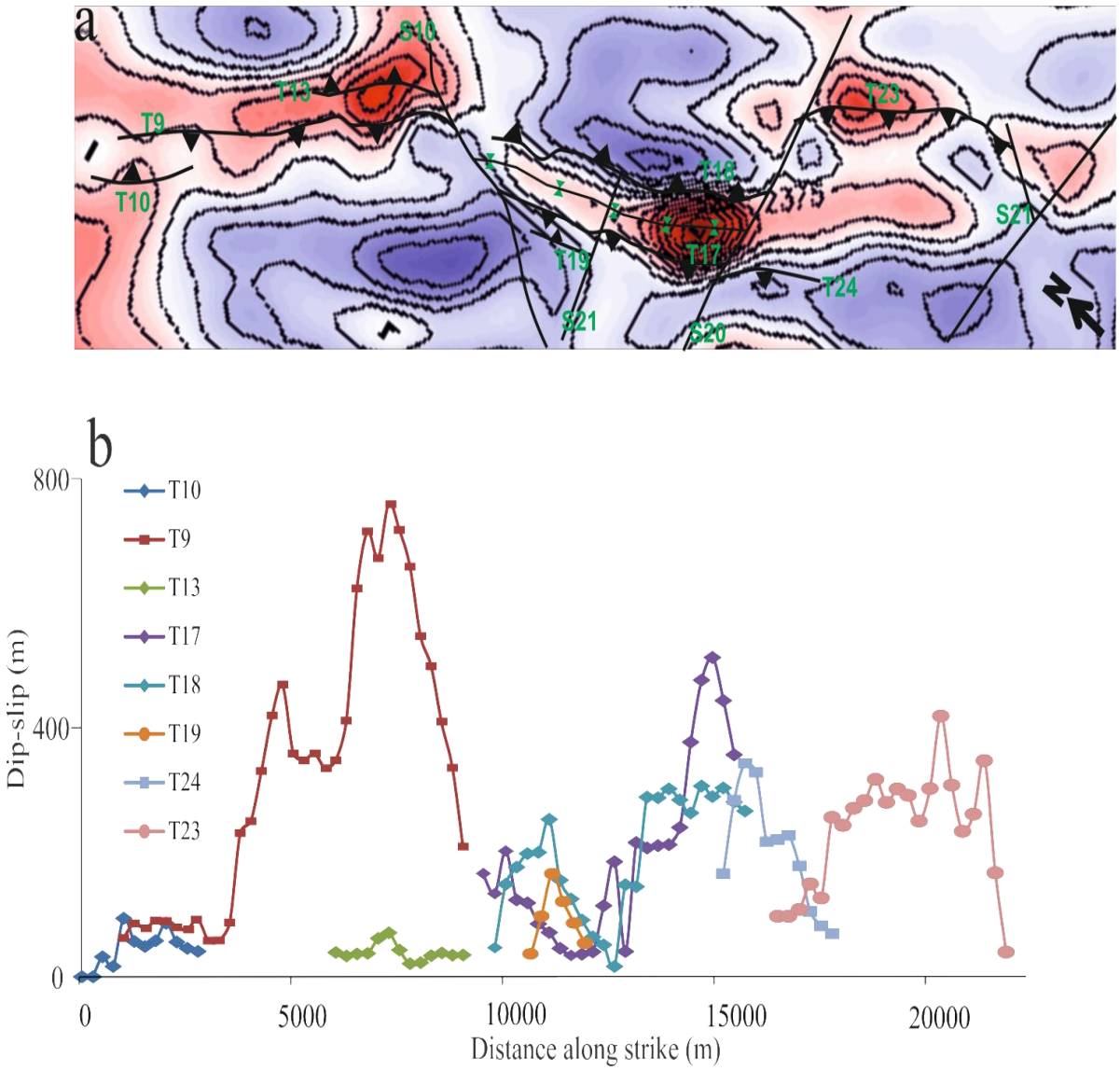


Figure 7.7: Dip-slip distribution along strike of the thrust faults in Structure A, B and C.

Manighetti et al (2004) modelled several faults restricted by different barriers in conjunction with their slip profiles. From the model, steepness of slip distribution profile at the tip was interpreted to be dependent on the barrier type (Manighetti et al., 2004). The thrust faults in Structure X have dip-slip gradients ranging from 0.06 to 0.45, close to the zone of overlap along Horizon IPM1 (Figure 7.6). Whereas, thrust faults restricted by strike slip faults, however, have dip slip gradients greater than 0.8, close to the zone of restriction (Figure 7.7). This gradient value exceeds the gradient range of those of overlapping faults described in Chapter 6. Therefore, barriers caused by parallel to sub-parallel thrust faults (such as overlapping faults) may have a lower restrictive effect comparable to faults oblique to intersecting faults.

### 7.2.2 Barrier Size

The size of barrier is one probable cause for displacement profile modification. It is observed that the zones where small strike slip faults intersect thrust faults, display less impact on displacement profiles compared to intersections with large strike slip faults. Examples of small strike slip fault intersecting thrust fault are observed in Structure X (Figure 7.6). The throw and dip slip profile for Fault T20, displayed only subtle changes at the zones of strike slip fault intersections. Whereas, large strikes slip faults in Structures A, B and C such as Faults S10, S20 and S23 modify displacement patterns of thrust faults significantly at intersections (Figure 7.7)

Additionally, it is observed that the majority of the strike slip fault barriers bounding thrust faults at lateral tips are larger in length size than the thrust faults. Examples are strike slip faults (S10, or S20) bounding the tips of Thrust faults T9, T17, T18 etc (Chapter 4, Figure 4.3). Whereas, small strike slip faults are most commonly cut or propagated through by thrust faults that are lengthier in size. An example of such interaction is presented in Structure B

(Chapters 4 and 5). In this structure, Fault S16 which is less than 2000 m in length intersects Faults T17 and T18. Fault S16 can be interpreted as a small barrier not capable of bounding the thrust faults (T17 and T18) as inferred from the pattern of their displacement distribution geometry (Figure 5.9e and f, Chapter 5).

### 7.2.3 Distance between Fault Initiation and Barrier

The distance between fault initiation and barrier is a probable influence to displacement geometry. It is observed in this study that some tip restricted faults show a similar geometry to those of isolated faults, an example is Fault T19 (Figure 5.9c), whilst others show maximum slip away from restriction zone such as Fault T13 (Figure 5.9d). In other words, why do some restricted faults do not have a maximum displacement and steep gradient close to the intersections? Such inconsistency may be attributed to the fault nucleation distance from the barrier: faults which initiated closer to barrier will show a steeper gradient than faults that initiated further way from barrier, as conceptualized in Figure 7.8. The model assumes the common theory which stipulates that the faults initiate at their zone of maximum displacement and increases in length as displacement increases in accordance with models of Watterson (1986). Each plot is made up of 4 curves (t1-t4) representing the time it takes the faults to initiate and propagate length along strike (A-I).

The first schematic displacement profile represents an unrestricted fault (Figure 7.8 a). The fault initiates at point E, at time t1 and with the successive increases in slip, the fault laterally elongates without intersecting a barrier to point A and I from E (Figure 7.8 a). Modifications to the unrestricted model are shown in Figure 7.8 b and c, with profiles showing fault restrictions at points H and G, respectively. In Figure 7.8, the barrier is situated close to a point of initiation. In this case, the fault only propagates freely in time t1, the curves t2-t4 resemble a half restricted fault similar to slip profile for T9 and T24.

Additionally, maximum slip away from the restricted zone can also be explained as a result of shifting in maximum displacement as suggested by Ellis and Dunlap (1988). In this case, as the fault is restricted at a lateral tip, close to maximum slip (Figure 7.8e). The zone of maximum slip close to restriction becomes displaced with time, (Figure 7.8e). The migration of maximum slip from point E to D is as a result of intense stress at the restricted zone. It should be noted that this model (Figure 7.8e) may not be valid for barriers that easily accommodate displacement such as folds but refers to barriers that limits displacement transfer.

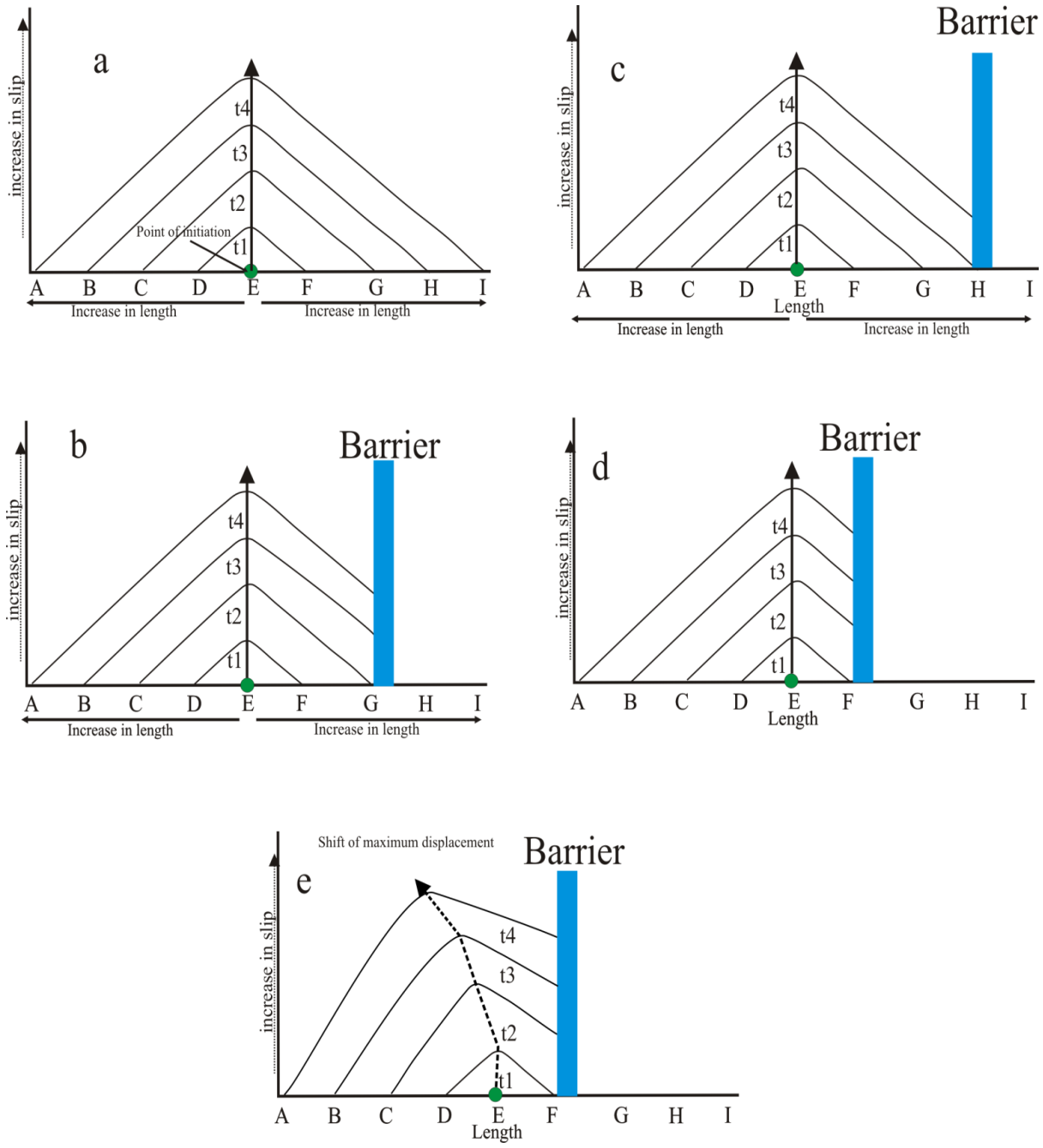


Figure 7.8: Schematic scenario for evolution of restricted faults. (a-d) changes in geometry relative to distance between points of initiation to barrier. (e) Shift in maximum slip from barrier.

## 7.3 STRUCTURAL DEFORMATION

In many compressional settings, thrust faults and thrust related folds are the most dominant structures, regardless of whether deformation is linked to either intracratonic rift systems or passive margins (Cunningham and Mann, 2007, Damuth, 1994, Santanach et al., 2005, Corredor et al., 2005). In the contractional domain of the Levant Basin, however, strike slip faults are in competing population with thrust related folds, and both types of structures are active till data. Although, the occurrence of thrust related folds and strike slip faults have been observed in the same compressional settings such as the South Trinidad Thrust Belt (Russo and Speed 1992) and in the South Wales Variscan (Gayer and Jones 1989). The development of folds and thrust faults in these settings are directly associated with transpressional ranges at either oblique plate boundaries where strike-slip movement is added to the overall convergence, or at restraining bends where reverse slip is added onto strike-slip movement (McClay and Bonora 2001; Cunningham and Mann 2007).

Conversely, the juxtaposition of thrust folds and conjugate strike-slip faults in the study area respectively shows traditional geometries expected for pure compression, and pure strike-slip movement. The thrust faults do not splay off the sub-vertical strike-slip faults, exhibit low angles of dip fault plane, and are not arranged in an echelon manner as may be expected for those formed by transpressional tectonics (Cunningham *et al.* 2003; El-Motaal and Kusky 2003). This suggests that the deformation resulting to the formation of the thrust-related folds and conjugate strike slip faults in the study area are to a large extent independent of each other, except as regards their intersection. However, the interactions between the deformations through time produce the complex fold and fault geometries described in this thesis.

Formation of the structures in the study area as speculated in Chapter 4 is associated with the gravity driven systems of the Levant Margin and the Nile Delta (Netzeband et al., 2006b, Cartwright et al., 2012). The maximum principal stress (σ1) directions towards the study area from both margins are almost perpendicular to each other; this is inferred from the direction of salt flow (Figure 4.1). The competing σ1 directions probably cause highly variable and localised changes to the stress field, which affect the bearing of the intermediate ($\sigma_2$) and minimum ($\sigma_3$) stresses. The formation of the thrust faults or the strike slip faults are dictated by the vertical and horizontal direction of these two stresses ($\sigma_2$ and $\sigma_3$).

## 7.4 IMPLICATIONS FOR HYROCARBON EXPLORATION

The research presented in this thesis includes novel kinematic and geometric observations that are useful for hydrocarbon exploration and this section will explore this implication. Faults are either baffles or barriers to fluid flow and can prevent communication in the case of the latter (Hulten 2010). One way of categorizing these extremes is to understand fault interactions as they relate to fold segmentation (Chapter 6). For instance a thrust related folds that seal reservoirs may be segmented by other faults into compartments that then behave as a collection of smaller reservoirs. Each compartment may have its own pressure and fluid characteristics, hampering efficient and effective field development and subsequent hydrocarbon recovery (Larue and Friedmann 2005).

The correct interpretation of fold and fault compartmentalization and interaction is useful in determining the strategy for hydrocarbon exploration, which may in turn reduce cost. Fold and faults with different structural geometries and displacement patterns may require a diverse set of techniques for exploration. Furthermore, determining the relative timing between thrust faults and their associated fold may aid in predicting seal integrity. For instance, the early developments of faults that do not seal, may not prevent oil and gas from accumulating as hydrocarbon form and migrate through structures in the subsurface. Open

and permeable faults within an established reservoir may also cause loss of circulation during drilling operations resulting in expensive losses in drilling mud (Hearn *et al.* 1984). This may be dangerous and lead to well abandonment.

An understanding of fault damage zones is crucial in modelling fault behaviour and its impact on reservoir performance. Zones of fault interactions may give rise to intensively fractured or damaged zones (Peacock et al. 2000). Also, an understanding of the interplay between local deformation and deposition is helpful to infer the position of subtle pinch-outs that may provide hydrocarbon prospects. It has been suggested that these features can exist beyond the imaging resolution of typical seismic reflection data (Clark and Cartwright 2009). These types of trap commonly occur on the crest and limbs of fold structures.

## 7.5 PROJECT LIMITATION AND FUTURE WORK

The work presented in this thesis is a comprehensive study, on the geometry and interaction of the main structural elements in a 3D seismic data within the contractional domain of a deepwater fold and thrust belt in the Levant Basin. The utilization of 3D seismic data has produced high definition mapping, and measurement of strain within a fold belt that was previously unattainable. However, whilst this project provides new insights into fold belt characteristics and development, some of the interpretations and findings may have been partially hindered by a number of limitations. This section is focused on the project limitation with reference to future work of this research that may overcome these difficulties.

One of the limitations in this research is the incomplete coverage of the study area by the seismic surveys. The 3D data set used for this study only covers an area of 1450 $km^2$ of the compression domain of the Levant Basin. Therefore deformation of the entire contractional domain was assumed based on extrapolation. More extensive, regional 2D seismic datasets are unsuitable for high resolution mapping of faults due to wide spacing of seismic lines. The

acquisition of 3D seismic data of this part of the Levant Basin is driven by pioneering oil and gas exploration in deep waters, and hence for future work to provide a more complete study of deformation in the area is dependent on the production and release of more data.

Another significant limitation of this study is the unavailability of well data in the study area. This is partly due to the cost of drilling boreholes in such settings. The well data used in describing the lithology of the study area, is located in the Levant margin c. 100 km from the Gal C survey (Chapter 2, Section 2.5). More also, there is little information available on the nature of detachment in this part of the basin. As more well data becomes available from ongoing exploration, the additional information on displacement, mechanical and lithological heterogeneities, the characteristics of the detachment layer will enable clearer conclusions to be drawn of the development.

Furthermore, a limiting factor in this research is time constraint. For instance, it is interpreted in this chapter that thrust faulting is an early process to the development of thrust related folds. One of the main reasons for this inference is the ratio of fault displacement to fold amplitude (D/A). It is proposed here that D/A values for fault propagation folds are higher than those of fault detachment thrust which have not been documented in any study. It would be valuable to characterize in details fault detachment thrust from fault propagation folds based on their D/A values. More also a subject that requires further study is a detailed study of stress field in the study area. It has been suggested that deformation in the area is associated to the thin-skin response of the Nile Delta, and the Levant Margin, and other far field tectonic boundaries in the study area (Chapter 4, Section 4.3.1). It would be interesting to know the stress distribution of the study area, and statistically quantify how much stress is contributed by each regional boundary.

Additionally, it has been demonstrated in this study on how strike slip faults, and thrust faults barriers influence the displacement distribution geometry of thrust faults. Expansion of the database collated herein to include how thrust faults influence the displacement distribution of strike slip faults and normal faults at all scales would produce a robust dataset and enable comparison of fault interaction types.

# CONCLUSIONS

## 8 GENERAL CONCLUSIONS

This study is one of the first where 3D seismic data is used to analyze and describe the distribution of strain within thrust related folds compartmentalized by strike slip faults, and thrust faults. The preceding chapters have demonstrated that this novel approach has provided important insight into the geometry, interaction and kinematic relationship of compartmentalized structures that accommodate shortening in the contractional domain of the Levant Basin. Although, this project is focused in one geographic area, it is anticipated that the findings are relevant and applicable to fold and thrust belts worldwide. The primary conclusions of this project, and specific summarizing statements drawn from each result Chapters 4, 5 and 6 are listed below.

### 8.1 THE STRUCTURES IN GAL C

- The Gal C survey is mainly deformed by thrust fault, and fold pairs and strike slip faults. The possible interactions and origin of these structural elements provide basis for this research.
- Deformation in the Gal C area is mainly associated with two phase systems; a Messinian phase which occurred immediately after the deposition of the evaporite layer, and a Plio-Quaternary phase involving the thin skin response of the Levant Margin and the Nile cone.
- The relationship between thrust faults and folds closely resembles that of a pure fault propagation fold, which originated as fault with low amplitude, other than a fault detachment fold which evolved from a detachment fold.

- The thrust related folds are bounded or segmented by thrust faults, and or strike slip faults. 3 main end member thrust fault and strike slip fault interactions were identified.
- Single end type (Class B) are thrust faults bounded at one end by strike slip faults
- Double end (Class C or D) are thrust faults bounded at both ends by strike slip faults. Those bounded by strike slip faults with different sense of shear are termed Class C, while those bounded by strike slip faults with the same sense of shear are termed Class D.
- Cross cutting faults (Class E or F) are faults shearing through preexisted faults. Class E is defined by thrust faults that shear through strike slip faults while Class F are thrust faults sheared by strike slip faults.

## 8.2 THE INTERACTIONS BETWEEN THRUST FAULTS AND STRIKE SLIP FAULTS

- This is the first time a combination of growth sequence and, dip slip displacement and shortening distribution analysis were used to examine the propagation of thrust related folds compartmentalized by strike slip faults.
- Dip slip displacement along a compartmentalized thrust faults are almost systematic, and dissimilar to those of an uninterested thrust faults.
- Isolated faults have a symmetric dip slip distribution geometry, while intersected thrust most commonly display asymmetric profile geometry, with maximum slip and steep gradient close to intersection zone.
- Thrust faults bounded by strike slip faults generally have higher Dmax/L values than non-intersected faults.
- Along strike shortening profile respond similar to that of dip slip at intersection zone, suggesting thrust faulting and folding are contemporaneous.

- Two end member models where proposed to explain the timing interaction between thrust faults and strike slip fault: (a) Cross-cut fault model- A strike slip fault crosscut a thrust related fold into two fold segments, and (b) Restricted fault model- two thrust related folds individually propagated towards an active strike slip fault. Syn kinematic study and dip slip distribution analysis of the case study folds supports the second model.

## 8.3 THE SEGMENTATION AND DEVELOPMENT OF A SINGLE FOLD

- The use of 3D seismic data is used to investigate the development, and lateral interaction of a single fold in the study area.
- Detailed seismic interpretation and analysis showed that the fold appears simple on seabed but internally compartmentalized into 3 segments verging at different direction, and each segment is characterized by a different fault interactions.
- Segment 1 is characterized by strike slip fault acting as a barrier to thrust propagation, Segment 2 comprises of convergent antithetic thrust fault which have been linked since inception, and segment 3 is made of synthetic thrust faults that are kinematically isolated.
- The fold is formed laterally as either a through going structure formed by linkage of smaller thrust related folds, or fold that developed as a simple thrust that becomes complex through time. Several models that are compatible with the result of this study support the formation by linkage.
- The thrust ramp initiated upward close to the detachment layer and propagates upward towards the sea bed.

## 8.4 INTER-RELATIONSHIP BETWEEN THE STRUCTURAL ELEMENTS

- Detailed seismic interpretation and analysis in this thesis reveals the inter-relationship and interaction of the structural elements in the study area.
- Thrust faulting is an integral process in the development of the thrust related folds.
- The main factors influencing thrust faults propagation includes barrier type, size, and initiation distance of the propagating fault to the barrier.
- The formation of the structural elements is dependent on the orientation of the minimal and intermediate stresses which is largely influenced by the interaction between the thin skin response of the Levant margin and Nile Delta.

# 9 REFERENCES

Almagor, G. (1984). Salt-controlled slumping on the Mediterranean slope of central Israel. *Marine Geophysical Research* **6:**227-243.

Baby, P., Hérail, G., Salinas, R. and Sempere, T. (1992). Geometry and kinematic evolution of passive roof duplexes deduced from cross section balancing: Example from the foreland thrust system of the southern Bolivian Subandean Zone. *Tectonics* **11:**523-536.

Bacon, M., Simm, R. and Redshaw, T. (2003). 3-D seismic interpretation. Cambridge Univ Pr.

Badawy, A. and Horváth, F. (1999). The Sinai subplate and tectonic evolution of the northern Red Sea region. *Journal of Geodynamics* **27:**433-450.

Ball, M. W. and Ball, D. (1953). Oil prospects of Israel.

Bally, A. W., Gordy, P. L., Stewart, G. A., Keating, L. F. and Alberta Society of Petroleum, G. (1970). Structure, seismic data, and orogenic evolution of southern Canadian Rocky Mountains. Alberta Society of Petroleum Geologists.

Barnett, J. A. M., Mortimer, J., Rippon, J. H., Walsh, J. J. and Watterson, J. (1987). Displacement geometry in the volume containing a single normal fault. *American Association of Petroleum Geologists Bulletin* **71:**925-937.

Baudon, C. and Cartwright, J. (2008a). Early stage evolution of growth faults: 3D seismic insights from the Levant Basin, Eastern Mediterranean. *Journal of Structural Geology* **30:**888-898.

Baudon, C. and Cartwright, J. A. (2008b). 3D seismic characterisation of an array of blind normal faults in the Levant Basin, Eastern Mediterranean. *Journal of Structural Geology* **30:**746-760.

Ben-Avraham, Z. (1978). The structure and tectonic setting of the Levant continental margin, eastern Mediterranean. *Tectonophysics* **46:**313-331.

Ben-Avraham, Z. and Ginzburg, A. (1990). Displaced terranes and crustal evolution of the Levant and the eastern Mediterranean. *Tectonics* **9:**613-622.

Ben-Gai, Y., Ben-Avraham, Z., Buchbinder, B. and Kendall, C. G. S. C. (2005). Post-Messinian evolution of the Southeastern Levant Basin based on two-dimensional stratigraphic simulation. *Marine Geology* **221:**359-379.

Berger, P. and Johnson, A. M. (1982). Folding of passive layers and forms of minor structures near terminations of blind thrust faults—application to the central Appalachian blind thrust. *Journal of Structural Geology* **4:**343-353.

Bertoni, C. and Cartwright, J. A. (2005). 3D seismic analysis of circular evaporite dissolution structures, Eastern Mediterranean. *Journal of the Geological Society* **162:**909-926.

Bertoni, C. and Cartwright, J. A. (2006). Controls on the basinwide architecture of late Miocene (Messinian) evaporites on the Levant margin (Eastern Mediterranean). *Sedimentary Geology* **188-189:**93-114.

Bond, G. C. and Kominz, M. A. (1984). Construction of tectonic subsidence curves for the early Paleozoic miogeocline, southern Canadian Rocky Mountains: Implications for subsidence mechanisms, age of breakup, and crustal thinning. *Geological Society of America Bulletin* **95:**155-173.

Boyer, S. E. and Elliott, D. (1982). Thrust systems. *AAPG Bulletin* **66:**1196-1230.

Briggs, S. E., Davies, R. J., Cartwright, J. A. and Morgan, R. (2006). Multiple detachment levels and their control on fold styles in the compressional domain of the deepwater west Niger Delta. *Basin Research* **18:**435-450.

Brown, A. R. (1999). Interpretation of three dimensional seismic data. *AAPG Memoir, SEG Investigation in Geophysics* **42**.

Buchanan, P. G. and McClay, K. R. (1991). Sandbox experiments of inverted listric and planar fault systems. *Tectonophysics* **188:**97-115.

Buchbinder, B. and Zilberman, E. (1997). Sequence stratigraphy of Miocene-Pliocene carbonate-siliciclastic shelf deposits in the eastern Mediterranean margin (Israel): Effects of eustasy and tectonics. *Sedimentary Geology* **112:**7-32.

Burchfiel, B., Quidong, D., Molnar, P., Royden, L., Yipeng, W., Peizhen, Z. and Weiqi, Z. (1989). Intracrustal detachment within zones of continental deformation. *Geology* **17:**748-752.

Cartwright, J., Bouroullec, R., James, D. and Johnson, H. (1998). Polycyclic motion history of some Gulf Coast growth faults from high-resolution displacement analysis. *Geology* **26:**819-822.

Cartwright, J., Jackson, M., Dooley, T. and Higgins, S. (2012). Strain partitioning in gravity-driven shortening of a thick, multilayered evaporite sequence. *Geological Society, London, Special Publications* **363:**449-470.

Cartwright, J. and Mansfield, C. (1998). Lateral displacement variation and lateral tip geometry of normal faults in the Canyonlands National Park, Utah. *Journal of Structural Geology* **20:**3-19.

Cartwright, J. A. and Jackson, M. P. A. (2008). Initiation of gravitational collapse of an evaporite basin margin: The Messinian saline giant, Levant Basin, eastern Mediterranean. *Geological Society of America Bulletin* **120:**399-413.

Cartwright, J. A., Trudgill, B. D. and Mansfield, C. S. (1995). Fault growth by segment linkage: an explanation for scatter in maximum displacement and trace length data from the Canyonlands Grabens of SE Utah. *Journal of Structural Geology* **17:**1319-1326.

Childs, C., Watterson, J. and Walsh, J. J. (1995). Fault overlap zones within developing normal fault systems. *Journal of the Geological Society* **152:**535-549.

Cita, M. B. and Ryan, W. B. F. (1978). Messinian erosional surfaces in the Mediterranean. Elsevier Scientific Publishing Company.

Clark, I. R. and Cartwright, J. A. (2009). Interactions between submarine channel systems and deformation in deepwater fold belts: Examples from the Levant Basin, Eastern Mediterranean sea. *Marine and Petroleum Geology* **26:**1465-1482.

Clark, I. R. and Cartwright, J. A. (2011). Key controls on submarine channel development in structurally active settings. *Marine and Petroleum Geology* **28:**1333-1349.

Cobbold, P. R., Szatmari, P., Demercian, L. S., Coelho, D. and Rossello, E. A. (1996). Seismic and experimental evidence for thin-skinned horizontal shortening by convergent radial gliding on evaporites, deep-water Santos Basin, Brazil. *Salt Tectonics: A Global Perspective* **65:**305-321.

Cohen, H. A. and McClay, K. (1996). Sedimentation and shale tectonics of the northwestern Niger Delta front. *Marine and Petroleum Geology* **13:**313-328.

Cohen, Z., Flexer, A. and Kaptsan, V. (1988). THE PLESHET BASIN: A NEWLY-DISCOVERED LINK IN THE PERIPHERAL CHAIN OF BASINS OF THE ARABIAN CRATON. *Journal of Petroleum Geology* **11:**403-414.

Cooper, M. (2007). Structural style and hydrocarbon prospectivity in fold and thrust belts: a global review. *SPECIAL PUBLICATION-GEOLOGICAL SOCIETY OF LONDON* **272:**447.

Corredor, F., Shaw, J. H. and Bilotti, F. (2005). Structural styles in the deep-water fold and thrust belts of the Niger Delta. *AAPG Bulletin* **89:**753-780.

Costa, E. and Vendeville, B. C. (2002). Experimental insights on the geometry and kinematics of fold-and-thrust belts above weak, viscous evaporitic decollement. *Journal of Structural Geology* **24:**1729-1739.

Coward, M. P. (1983). Thrust tectonics, thin skinned or thick skinned, and the continuation of thrusts to deep in the crust. *Journal of Structural Geology* **5:**113-123.

Cross, T. A. (1986). Tectonic controls of foreland basin subsidence and Laramide style deformation, western United States. *Foreland basins* 13-39.

Cunningham, D., Davies, S. and Badarch, G. (2003). Crustal architecture and active growth of the Sutai Range, western Mongolia: a major intracontinental, intraplate restraining bend. *Journal of Geodynamics* **36:**169-191.

Cunningham, W. D. and Mann, P. (2007). Tectonics of strike-slip restraining and releasing bends. *Geological Society, London, Special Publications* **290:**1-12.

Dahlstrom, C. D. A. (1969). Balanced cross sections. *Canadian Journal of Earth Sciences* **6:**743-757.

Dahlstrom, C. D. A. (1970). Structural geology in the eastern margin of the canadian rocky mountains. *Bulletin of Canadian Petroleum Geology* **18:**332-406.

Damuth, J. E. (1994). Neogene gravity tectonics and depositional processes on the deep Niger Delta continental margin. *Marine and Petroleum Geology* **11:**320, IN321-IN310, 321-346.

Davies, R. J., Simon. A. Stewart, Joseph. A. Cartwright, Mark. Lappin, Rodney . Johnston, Fraser, S. I. and Brown, A. R. (2004). 3D Seismic Technology: Are We Realising Its Full Potential? *Geological Society, London, Memoirs* **29:**1-10.

Davis, D. M. and Engelder, T. (1985a). The role of salt in fold-and-thrust belts. *Tectonophysics* **119:**67-88.

Davis, D. M. and Engelder, T. (1985b). The role of salt in fold-and-thrust belts. *Tectonophysics* **119:**67-88.

Davis, K., Burbank, D. W., Fisher, D., Wallace, S. and Nobes, D. (2005). Thrust-fault growth and segment linkage in the active Ostler fault zone, New Zealand. *Journal of Structural Geology* **27:**1528-1546.

DeBalko, D. A. and Buffler, R. T. (1992). Seismic stratigraphy and geologic history of Middle Jurassic through Lower Cretaceous rocks, deep eastern Gulf of Mexico.

DeCelles, P. G. and Giles, K. A. (1996). Foreland basin systems. *Basin Research* **8:**105-123.

Dixon, J. M. and Liu, S. (1992). Centrifuge modelling of the propagation of thrust faults.*Thrust tectonics*. Springer, pp. 53-69.

Dooley, T. and McClay, K. (1997). Analog modeling of pull-apart basins. *AAPG bulletin* **81:**1804-1826.

Druckman, Y., Buchbinder, B., Martinotti, G. M., Tov, R. and Aharon, P. (1995). The buried Afiq Canyon (eastern Mediterranean, Israel): a case study of a Tertiary submarine canyon exposed in Late Messinian times. *Marine Geology* **123:**167-185.

Eaddy, M., Zimmermann, T., Sherwood, K. D., Garg, V., Murphy, G. C., Nagappan, N. and Aho, A. V. (2008). Do crosscutting concerns cause defects? *Software Engineering, IEEE Transactions on* **34:**497-515.

Eigen, J. T. (1960). Velocity analysis using prestack depth migration: applying the linear theory.

Eisenstadt, G. and De Paor, D. G. (1987). Alternative model of thrust-fault propagation. *Geology* **15:**630-633.

El-Motaal, E. A. and Kusky, T. M. eds. (2003). *Tectonic evolution of the intraplate s-shaped Syrian Arc fold-thrust belt of the Middle East region in the context of plate tectonics*. The 3rd International Conference on the Geology of Africa.

Elliott, D. (1976). The Motion of Thrust Sheets. *J. Geophys. Res.* **81:**949-963.

Elliott, D. and Johnson, M. R. W. (1980). Structural evolution in the northern part of the Moine thrust belt, NW Scotland. *Transactions of the Royal Society of Edinburgh: Earth Sciences* **71:**69-96.

Ellis, M. A. and Dunlap, W. J. (1988). Displacement variation along thrust faults: implications for the development of large faults. *Journal of Structural Geology* **10:**183-192.

Erickson, S. G. (1996). Influence of mechanical stratigraphy on folding vs faulting. *Journal of Structural Geology* **18:**443-450.

Erslev, E. A. (1991). Trishear fault-propagation folding. *Geology* **19:**617-620.

Ferrill, D. A. and Morris, A. P. (1997). Geometric considerations of deformation above curved normal faults and salt evacuation surfaces. *The Leading Edge* **16:**1129-1133.

Folkman, Y. and Mart, Y. (2008). Newly recognized eastern extension of the Nile deep-sea fan. *Geology* **36:**939-942.

Fort, X., Brun, J.-P. and Chauvel, F. (2004). Salt tectonics on the Angolan margin, synsedimentary deformation processes. *AAPG bulletin* **88:**1523-1544.

Frey Martinez, J., Cartwright, J. and Hall, B. (2005). 3D seismic interpretation of slump complexes: examples from the continental margin of Israel. *Basin Research* **17:**83-108.

Gallup, W. B. (1951). Geology of Turner Valley oil and gas field, Alberta, Canada. *Bull. Am. Ass. Petrol. Geol* **35:**797-821.

Gardner, D. A. C. and Spang, J. H. (1973). Model studies of the displacement transfer associated with overthrust faulting. *Bulletin of Canadian Petroleum Geology* **21:**534-552.

Gardosh, M., Reches, Z. and Garfunkel, Z. (1990). Holocene tectonic deformation along the western margins of the Dead Sea. *Tectonophysics* **180:**123-137.

Gardosh, M. A. and Druckman, Y. (2006). Seismic stratigraphy, structure and tectonic evolution of the Levantine Basin, offshore Israel. *Geological Society, London, Special Publications* **260:**201-227.

Gardosh, M. A., Druckman, Y., Buchbinder, B. a. and Rybakov, M. (2008). The levant Basin Offshore Israel: Stratigraphy, Structure, Tectonic Evolution and Implication for Hydrocarbon Exploration. Jerusalem Israel:

Garfunkel, Z. (1998). Constrains on the origin and history of the Eastern Mediterranean basin. *Tectonophysics* **298:**5-35.

Garfunkel, Z., A. , Arad, a. G. and Almagor. (1979). The Palmachim disturbance and its region setting. *Geological Survey of Israel Bulletin 72:1–56.*

Garfunkel, Z. and Almagor, G. (1984). Geology and structure of the continental margin off northern Israel and the adjacent part of the Levantine Basin. *Marine Geology* **62:**105-131.

Gayer, R. and Jones, J. (1989). The Variscan foreland in South Wales. *Proceedings of the Ussher Society* **7:**177-179.

Ginzburg, A. and Gvirtzman, G. (1979). Changes in the crust and in the sedimentary cover across the transition from the Arabian platform to the Mediterranean basin: evidence from seismic refraction and sedimentary studies in Israel and in Sinai. *Sedimentary Geology* **23:**19-36.

Girdler, R. W. (1990). The Dead Sea transform fault system. *Tectonophysics* **180:**1-13.

Gradmann, S., Hübscher, C., Ben-Avraham, Z., Gajewski, D. and Netzeband, G. (2005). Salt tectonics off northern Israel. *Marine and Petroleum Geology* **22:**597-611.

Grasemann, B., Martel, S. and Passchier, C. (2005). Reverse and normal drag along a fault. *Journal of Structural Geology* **27:**999-1010.

Groshong, R. H. (2006). Three-D structural geology. Springer Verlag.

Groshong , R. H. and Epard, J.-L. (1994). The role of strain in area-constant detachment folding. *Journal of Structural Geology* **16:**613-618.

Hardy, S. and Finch, E. (2007). Mechanical stratigraphy and the transition from trishear to kink-band fault-propagation fold forms above blind basement thrust faults: a discrete-element study. *Marine and Petroleum Geology* **24:**75-90.

Hardy, S., Poblet, J., McClay, K. and Waltham, D. (1996). Mathematical modelling of growth strata associated with fault-related fold structures. *Geological Society, London, Special Publications* **99:**265-282.

Harrison, J. C. and Bally, A. W. (1988). Cross-sections of the Parry Islands fold belt on Melville Island, Canadian Arctic Islands: implications for the timing and kinematic history of some thin-skinned decollement systems. *Bulletin of Canadian Petroleum Geology* **36:**311-332.

Hart, B. S. (1999). Definition of subsurface stratigraphy, structure and rock properties from 3-D seismic data. *Earth-Science Reviews* **47:**189-218.

Hearn, C., WJ, E., Tye, R. and Ranganathan, V. (1984). Geological factors influencing reservoir performance of the Hartzog Draw field, Wyoming. *Journal of Petroleum Technology* **36:**1335-1344.

Hedlund, C. A. (1997). Fault-propagation, ductile strain, and displacament-distance relationships. *Journal of Structural Geology* **19** 243–248.

Hesse, S., Back, S. and Franke, D. (2009). The deep-water fold-and-thrust belt offshore NW Borneo: Gravity-driven versus basement-driven shortening. *Geological Society of America Bulletin* **121:**939-953.

Higgins, S., Clarke, B., Davies, R. J. and Cartwright, J. (2009). Internal geometry and growth history of a thrust-related anticline in a deep water fold belt. *Journal of Structural Geology* **31:**1597-1611.

Higgins, S., Davies, R. J. and Clarke, B. (2007). Antithetic fault linkages in a deep water fold and thrust belt. *Journal of Structural Geology* **29:**1900-1914.

Hills, E. S. and Hills, E. S. (1972). Elements of structural geology. Chapman and Hall London.

Hirsch, F. (1984). The Arabian sub-plate during the Mesozoic. *Geological Society, London, Special Publications* **17:**217-223.

Hsü et al., K. J. H., L. Monadert, D. Bernoulli, B.C. Cita, A. Erickson and R.E. Garrison et al., . (1978). History of the Mediterranean Salinity Crisis. *In: K.J. Hsü and L. Montadert, Editors, Init. Repts. DSDP, 42 I, US Govt. Printing Office, Washington, DC (1978), pp. 1053–1078.*

Hsü et al., K. J. H., M.B. Cita and W.B.F. Ryan, . (1973). The origin of the Mediterranean Evaporites. *In: W.B.F. Ryan and K.J. Hsü, Editors, Init. Repts. DSDP, 13, US Govt. Printing Office, Washington, DC (1973), pp. 1203–1232.*

Huggins, P., Watterson, J., Walsh, J. J. and Childs, C. (1995). Relay zone geometry and displacement transfer between normal faults recorded in coal-mine plans. *Journal of Structural Geology* **17:**1741-1755.

Ingram, G. M., Chisholm, T. J., Grant, C. J., Hedlund, C. A., Stuart-Smith, P. and Teasdale, J. (2004). Deepwater North West Borneo: hydrocarbon accumulation in an active fold and thrust belt. *Marine and Petroleum Geology* **21:**879-887.

Jamison, W. R. (1987). Geometric analysis of fold development in overthrust terranes. *Journal of Structural Geology* **9:**207-219.

Jamison, W. R. (1997). Quantitative evaluation of fractures on the Monkswood Anticline : a detachment in the foothills of Western canada. *American Association of Petroleum Geologists* **81:**1110-1132.

Kearney, P., Brooks, M. and Hill, I. (2002 ). An Introduction to Geophysical Exploration. *Blackwell Science, 3rd Ed.*

Kim, Y. S. and Sanderson, D. J. (2005). The relationship between displacement and length of faults: a review. *Earth-Science Reviews* **68:**317-334.

King, G. and Yielding, G. (1984). The evolution of a thrust fault system: processes of rupture initiation, propagation and termination in the 1980 El Asnam (Algeria) earthquake. *Geophysical Journal International* **77:**915-933.

Klinger, Y., Avouac, J. P., Abou Karaki, N., Dorbath, L., Bourles, D. and Reyss, J. L. (2000). Slip rate on the Dead Sea transform fault in northern Araba valley (Jordan). *Geophysical Journal International* **142:**755-768.

Larsen, P. H. (1988). Relay structures in a Lower Permian basement-involved extension system, East Greenland. *Journal of Structural Geology* **10:**3-8.

Larue, D. and Friedmann, F. (2005). The controversy concerning stratigraphic architecture of channelized reservoirs and recovery by waterflooding. *Petroleum Geoscience* **11:**131-146.

Livnat, A. and Kronfeld, J. (1985). Paleoclimatic implications of U-series dates for lake sediments and travertines in the Arava Rift Valley, Israel. *Quaternary Research* **24:**164-172.

Loncke, L., Gaullier, V., Mascle, J., Vendeville, B. and Camera, L. (2006). The Nile deep-sea fan: an example of interacting sedimentation, salt tectonics, and inherited subsalt paleotopographic features. *Marine and Petroleum Geology* **23:**297-315.

MacDonald, J., Holford, S. and King, R. Structure and Prospectivity of the Ceduna Delta—Deep-Water Fold-Thrust Belt Systems, Bight Basin, Australia.

Makris, J., Abraham, Z. B., Behle, A., Ginzburg, A., Giese, P., Steinmetz, L., Whitmarsh, R. B. *et al.* (1983). Seismic refraction profiles between Cyprus and Israel and their interpretation. *Geophysical Journal of the Royal Astronomical Society* **75:**575-591.

Malik, J. N., Shah, A. A., Sahoo, A. K., Puhan, B., Banerjee, C., Shinde, D. P., Juyal, N. *et al.* (2010). Active fault, fault growth and segment linkage along the Janauri anticline (frontal foreland fold), NW Himalaya, India. *Tectonophysics* **483:**327-343.

Manighetti, I., King, G. and Sammis, C. G. (2004). The role of off-fault damage in the evolution of normal faults. *Earth and Planetary Science Letters* **217:**399-408.

Manighetti, I., King, G. C. P. and Gaudemer, Y. (2001a). Slip accumulation and lateral propagation of active. *Journal of Geophysical Research* **106:**13,667-613,696.

Manighetti, I., King, G. C. P., Gaudemer, Y., Scholz, C. H. and Doubre, C. (2001b). Slip accumulation and lateral propagation of active normal faults in Afar, *J. Geophys. Res.* **106**.

Mansfield, C. S. and Cartwright, J. A. (1996). High resolution fault displacement mapping from three-dimensional seismic data: evidence for dip linkage during fault growth. *Journal of Structural Geology* **18:**249-263.

Mascle, J., Zitter, T., Bellaiche, G., Droz, L., Gaullier, V. and Loncke, L. (2001). The Nile deep sea fan: preliminary results from a swath bathymetry survey. *Marine and petroleum geology* **18:**471-477.

McClay, K. and Bonora, M. (2001). Analog models of restraining stepovers in strike-slip fault systems. *AAPG bulletin* **85:**233-260.

McClay, K. and Khalil, S. (1998). Extensional hard linkages, eastern Gulf of Suez, Egypt. *Geology* **26:**563-566.

McClay, K. R. (1992a). *Glossary of thrust tectonics terms* 419-433.

McClay, K. R. (1992b). Thrust tectonics. Chapman & Hall.

McClay, K. R. (2002). Recent advances in analogue modelling: uses in section interpretation and validation. *Extensional Tectonics: Faulting and related processes* **2:**185.

McClay, K. R. (2004). Thrust tectonics and hydrocarbon systems; Introduction.

McClay, K. R., Dooley, T. and Lewis, G. (1998). Analog modeling of progradational delta systems. *Geology* **26:**771-774.

McClay, K. R. and Ellis, P. G. (1987). Geometries of extensional fault systems developed in model experiments. *Geology* **15:**341-344.

McCulloh, R. P. (1988). Differential fault-related early Miocene sedimentation, Bayou Hebert area, southwestern Louisiana. *AAPG Bulletin* **72:**477-492.

McGrath, A. G. and Davison, I. (1995). Damage zone geometry around fault tips. *Journal of Structural Geology* **17:**1011-1024.

McNeill, L. C., Piper, K. A., Goldfinger, C., Kulm, L. V. and Yeats, R. S. (1997). Listric normal faulting on the Cascadia continental margin.

Meneses-Rocha, J. and Yurewicz, D. A. (1999). Petroleum exploration and production in fold and thrust belts; ideas from a Hedberg research symposium. *AAPG Bulletin* **83:**889-897.

Mitchum, R. M. and Van Wagoner, J. C. (1991). High-frequency sequences and their stacking patterns: sequence-stratigraphic evidence of high-frequency eustatic cycles. *Sedimentary Geology* **70:**131-160.

Mitra, S. (1986). Duplex structures and imbricate thrust systems; geometry, structural position, and hydrocarbon potential. *AAPG Bulletin* **70:**1087-1112.

Mitra, S. (1990). Fault-propagation folds: geometry, kinematic evolution, and hydrocarbon traps. *AAPG Bulletin* **74:**921-945.

Mitra, S. (2002). Structural models of faulted detachment folds. *AAPG bulletin* **86:**1673-1694.

Mitra, S., Gonzalez, J. A. D., Hernandez, J. G., Garcia, S. H. and Banerjee, S. (2006). Structural geometry and evolution of the Ku, Zaap, and Maloob structures, Campeche Bay, Mexico. *AAPG bulletin* **90:**1565-1584.

Morley, C. K. and Guerin, G. (1996). Comparison of gravity-driven deformation styles and behavior associated with mobile shales and salt. *Tectonics* **15:**1154-1170.

Morley, C. K., King, R., Hillis, R., Tingay, M. and Backe, G. (2011). Deepwater fold and thrust belt classification, tectonics, structure and hydrocarbon prospectivity: A review. *Earth-Science Reviews* **104:**41-91.

Morley, C. K., Nelson, R. A., Patton, T. L. and Munn, S. G. (1990). Transfer zones in the East African rift system and their relevance to hydrocarbon exploration in rifts. *American Association of Petroleum Geologists Bulletin* **74:**1234-1253.

Morozov, I., Chubak, G. and Blyth, S. (2009). Interactive 3D/2D visualization for geophysical data processing and interpretation. *Computers & Geosciences* **35:**1397-1408.

Mueller, J. P., Guzofski, C., Rivero, C., Plesch, A., Shaw, J. H., Muron, P., Bilotti, F. *et al.* eds. (2005). *New Approaches to 3D Structural Restoration in Fold-And-Thrust Belts Using Growth Strata*. AAPG Annual Meeting Program. Calgary, Canada: AAPG Annual Meeting.

Müller, D. W. and Mueller, P. A. (1991). Origin and age of the Mediterranean Messinian evaporites: implications from Sr isotopes. *Earth and Planetary Science Letters* **107:**1-12.

Muraoka, H. and Kamata, H. (1983). Displacement distribution along minor fault traces. *Journal of Structural Geology* **5:**483-495.

Needham, D., Yielding, G. and Freeman, B. (1996a). Analysis of fault geometry and displacement patterns. *Geological Society, London, Special Publications* **99:**189-199.

Nemcok, M., Schamel, S. and Gayer, R. (2009). Thrustbelts: Structural architecture, thermal regimes and petroleum systems. Cambridge Univ Pr.

Netzeband, G. L., Gohl, K., Hübscher, C. P., Ben-Avraham, Z., Dehghani, G. A., Gajewski, D. and Liersch, P. (2006a). The Levantine Basin--crustal structure and origin. *Tectonophysics* **418:**167-188.

Netzeband, G. L., Hübscher, C. P. and Gajewski, D. (2006b). The structural evolution of the Messinian evaporites in the Levantine Basin. *Marine Geology* **230:**249-273.

Nicol, A., Gillespie, P. A., Childs, C. and Walsh, J. J. (2002). Relay zones between mesoscopic thrust faults in layered sedimentary sequences. *Journal of Structural Geology* **24:**709-727.

Nicol, A., Watterson, J., Walsh, J. J. and Childs, C. (1995). The shapes, major axis orientations and displacement patterns of fault surfaces. *Journal of Structural Geology* **18:**235-248.

O'Keefe, F. X. and Stearns, D. W. (1982). Characteristics of displacement transfer zones associated with thrust faults.

Peach, B. N., Horne, J., Gunn, W., Clough, C. T., Hinxman, L. W. and Teall, J. J. H. (1907). The geological structure of the North-West Highlands of Scotland. Printed for HM Stationery off., by J. Hedderwick & sons, ltd.

Peacock, D. C. P., Knipe, R. J. and Sanderson, D. J. (2000). Glossary of normal faults. *Journal of Structural Geology* **22:**291-305.

Peacock, D. C. P. and Sanderson, D. J. (1995). Strike-slip relay ramps. *Journal of Structural Geology* **17:**1351-1360.

Perry, W. J. (1979). The Wills Mountain Anticline: a study in complex folding and faulting in eastern West Virginia. West Virginia Geological and Economic Survey.

Pfiffner, O. A. (1993). The structure of the Helvetic nappes and its relation to the mechanical stratigraphy. *Journal of structural Geology* **15:**511-521.

Pfiffner, O. A. (2006). Thick-skinned and thin-skinned styles of continental contraction. *Geological Society of America Special Papers* **414:**153-177.

Philip, K. and Brooks, M. (1991). An introduction to geophysical exploration. Blackwell Science.

Pickering, G., Bull, J. M. and Sanderson, D. J. (1996). Scaling of fault displacements and implications for the estimation of sub-seismic strain. *Geological Society, London, Special Publications* **99:**11-26.

Platt, J. P., Leggett, J. K., Young, J., Raza, H. and Alam, S. (1985). Large-scale sediment underplating in the Makran accretionary prism, southwest Pakistan. *Geology* **13:**507-511.

Poblet, J. and Lisle, R. J. (2011). Kinematic evolution and structural styles of fold-and-thrust belts. *Geological Society, London, Special Publications* **349:**1-24.

Poblet, J., McClay, K., Storti, F. and Muñoz, J. A. (1997). Geometries of syntectonic sediments associated with single-layer detachment folds. *Journal of Structural Geology* **19:**369-381.

Pohn, H. A. (2000). Lateral ramps in the folded Appalachians and in overthrust belts worldwide: a fundamental element of thrust-belt architecture. US Dept. of the Interior, US Geological Survey.

Price, R. A. (1981). The Cordilleran forelarid thrust and fold belt in the southern'Canadian Rocky Mountains.

Rich, J. L. (1934). Mechanics of low-angle overthrust faulting as illustrated by Cumberland thrust block, Virginia, Kentucky, and Tennessee. *AAPG Bulletin* **18:**1584-1596.

Rowan, M. G. (1997). Three-dimensional geometry and evolution of a segmented detachment fold, Mississippi Fan foldbelt, Gulf of Mexico. *Journal of Structural Geology* **19:**463-480.

Rowan, M. G., Peel, F. J. and Vendeville, B. C., in press. (2004). Gravity driven foldbelts on passive margins. In: K.R. McClay (Ed.), . *AAPG Memoir on Thrust Tectonics.*

Russo, R. and Speed, R. (1992). Oblique collision and tectonic wedging of the South American continent and Caribbean terranes. *Geology* **20:**447-450.

Ryan, W. B. F. (1973). Geodynamic implications of the Messinian crisis of salinity. *Messinian events in the Mediterranean* 26-38.

Ryan, W. B. F. and Cita, M. B. (1978). The nature and distribution of Messinian erosional surfaces—Indicators of a several-kilometer-deep Mediterranean in the Miocene. *Marine Geology* **27:**193-230.

Sass, E. and Bein, A. (1982). The Cretaceous carbonate platform in Israel. *Cretaceous Research* **3:**135-144.

Schlagenhauf, A., Manighetti, I., Malavieille, J. and Dominguez, S. (2008). Incremental growth of normal faults: Insights from a laser-equipped analog experiment. *Earth and Planetary Science Letters* **273:**299-311.

Scott, W. M., Medwedeff, D. A. and Marshak, S. (1991). Geometrical modeling of fault-related folds: a pseudo-three-dimensional approach. *Journal of Structural Geology* **13:**801-812.

Shaw, J. H., Novoa, E. and Connors, C. D. (2004). Structural controls on growth stratigraphy in contractional fault-related folds. *Thrust tectonics and hydrocarbon systems: AAPG Memoir* **82:**400-412.

Sheriff, R. E. (1997). Seismic Resolution a key element. *AAPG Explorer*.

Sherkati, S., Molinaro, M., Frizon de Lamotte, D. and Letouzey, J. (2005). Detachment folding in the Central and Eastern Zagros fold-belt (Iran): salt mobility, multiple detachments and late basement control. *Journal of Structural Geology* **27:**1680-1696.

Shumin, L. and Dixon, J. M. (1991). Centrifuge modelling of thrust faulting: structural variation along strike in fold-thrust belts. *Tectonophysics* **188:**39-62.

Soliva, R., Benedicto, A., Schultz, R. A., Maerten, L. and Micarelli, L. (2008). Displacement and interaction of normal fault segments branched at depth: Implications for fault growth and potential earthquake rupture size. *Journal of Structural Geology* **30:**1288-1299.

Stearns, D. W. (1978). Faulting and forced folding in the Rocky Mountains foreland. *Geological Society of America Memoir* **151:**1-38.

Stewart, S. A. (1996). Influence of detachment layer thickness on style of thin-skinned shortening. *Journal of Structural Geology* **18:**1271-1274.

Storti, F. and Poblet, J. (1997a). Growth stratal architectures associated to decollement folds and fault-propagation folds. Inferences on fold kinematics. *Tectonophysics* **282:**353-373.

Suppe, J. (1983). Geometry and Kinematics of Fault Bend Fold. *Am. Jour.Sci* **283:** 684-721.

Suppe, J. (1985a). Principles of structural geology. Prentice-Hall New York.

Suppe, J., Connors, C. D. and Zhang, Y. (2004). Shear fault-bend folding.

Suppe, J. and Medwedeff, D. A. (1984). *Fault-propagation folding* **16:**670.

Suppe, J. and Medwedeff, D. A. (1990). Geometry and kinematics of fault-propagation folding. *Eclogae Geologicae Helvetiae* **83:**409-454.

Tavani, S. and Storti, F. (2011). Layer-parallel Shortening Templates Associated with Double-edge Fault-propagation Folding.

Tearpock, D., J. and Bischke, R., E. . (1991). Applied Subsurface Geological Mapping. U.S.A: Printice Hall.

Thorsen, C. E. (1963). Age of growth faulting in Southeast Louisiana. *Transactions, Gulf Coast Association of Geological Societies* **13:**103-110.

Tibor, G. and Ben-Avraham, Z. (1992). Late Tertiary seismic facies and structures of the Levant passive margin off central Israel, eastern Mediterranean. *Marine Geology* **105:**253-273.

Tibor, G., Ben-Avraham, Z., Steckler, M. and Fligelman, H. (1992). Late Tertiary Subsidence History of the Southern Levant Margin, Eastern Mediterranean Sea, and Its Implications to the Understanding of the Messinian Event. *J. Geophys. Res.* **97:**17593-17614.

Tonghe, W. (1999). Structural Styles of Fronts of Thrust-Detachment Faults in Petroleum-bearing Areas of Western China. *Acta Geologica Sinica - English Edition* **73:**371-383.

Trudgill, B. and Cartwright, J. (1994). Relay-ramp forms and normal-fault linkages, Canyonlands National Park, Utah. *Geological Society of America Bulletin* **106:**1143-1157.

Trudgill, B. D., Rowan, M. G., Fiduk, J. C., Weimer, P., Gale, P. E., Korn, B. E., Phair, R. L. *et al.* (1999). The Perdido fold belt, northwestern deep Gulf of Mexico, part 1: structural geometry, evolution and regional implications. *AAPG Bulletin* **83:**88-113.

Tucker, P. M. (1982). Pitfalls revisited. Society of Exploration Geophysicists.

Van der Flier-Keller, E. and Goodarzi, F. (1992). Regional variations in coal quality in the Canadian Cordillera. *Controls on the Distribution and Quality of Cretaceous Coals* 165-175.

Van Hulten, F. (2010). Geological factors effecting compartmentalization of Rotliegend gas fields in the Netherlands. *Geological Society, London, Special Publications* **347:**301-315.

Vergés, J., Goodarzi, M., Emami, H., Karpuz, R., Efstathiou, J. and Gillespie, P. (2011). Multiple detachment folding in Pusht-e Kuh arc, Zagros: Role of mechanical stratigraphy.

Vidal-Royo, O., Koyi, H. A. and Muñoz, J. A. (2009). Formation of orogen-perpendicular thrusts due to mechanical contrasts in the basal décollement in the Central External Sierras (Southern Pyrenees, Spain). *Journal of Structural Geology* **31:**523-539.

Vidal, N., Alvarez-Marron, J. and Klaeschen, D. (2000). Internal configuration of the Levantine Basin from seismic reflection data (eastern Mediterranean). *Earth and Planetary Science Letters* **180:**77-89.

Wallace, W. K. and Homza, T. X. (2004). Detachment folds versus fault-propagation folds, and their truncation by thrust faults.

Walsh, J., Watterson, J. and Yielding, G. (1991). The importance of small-scale faulting in regional extension. *Nature* **351:**391-393.

Walsh, J. J., Bailey, W. R., Childs, C., Nicol, A. and Bonson, C. G. (2003). Formation of segmented normal faults: a 3-D perspective. *Journal of Structural Geology* **25:**1251-1262.

Walsh, J. J. and Watterson, J. (1987). Distributions of cumulative displacement and seismic slip on a single normal fault surface. *Journal of Structural Geology* **9:**1039-1046.

Walsh, J. J. and Watterson, J. (1988). Analysis of the relationship between displacements and dimensions of faults. *Journal of Structural Geology* **10:**239-247.

Walsh, J. J. and Watterson, J. (1991). Geometric and kinematic coherence and scale effects in normal fault systems. *Geological Society, London, Special Publications* **56:**193-203.

Walsh, J. J., Watterson, J., Bailey, W. R. and Childs, C. (1999). Fault relays, bends and branch-lines. *Journal of Structural Geology* **21:**1019-1026.

Walton, G. G. (1972). Three -dimenasional seismic method:Geophysics,V.37,p.417-430

Watters, T. R. and Maxwell, T. A. (1983). Crosscutting relations and relative ages of ridges and faults in the Tharsis region of Mars. *Icarus* **56:**278-298.

Wickham, J. (1995). Fault displacement-gradient folds and the structure at Lost Hills, California (U.S.A.). *Journal of Structural Geology* **17:**1293-1302.

Widess, M. B. (1973). How thin is a thin bed? *Geophysics* **38:**1176.

Williams, G. and Chapman, T. (1983). Strains developed in the hangingwalls of thrusts due to their slip/propagation rate: A dislocation model. *Journal of Structural Geology* **5:**563-571.

Willis, B. (1893). The mechanics of Appalachian structure. *U.S. Geological Survey 13th Annual Report, pp. 212–281*. 212–281.

Wiltschko, D. V. and Chapple, W. M. (1977). Flow of weak rocks in Appalachian Plateau folds. *AAPG Bulletin* **61:**653-670.

Woodcock, N. H. and Fischer, M. (1986). Strike-slip duplexes. *Journal of Structural Geology* **8:**725-735.

Yilmaz, Ö. (2001). Seismic data analysis: processing, inversion, and interpretation of seismic data. SEG Books.

Zoetemeijer, B. P. (1993). Tectonic modelling of foreland basins: thin skinned thrusting, syntectonic sedimentation and lithospheric flexure.

# 10 APPENDICES

Appendice 1: Supplementary figures

Figure AP 1.1- 1.9 provides examples of maps used for producing structural maps.

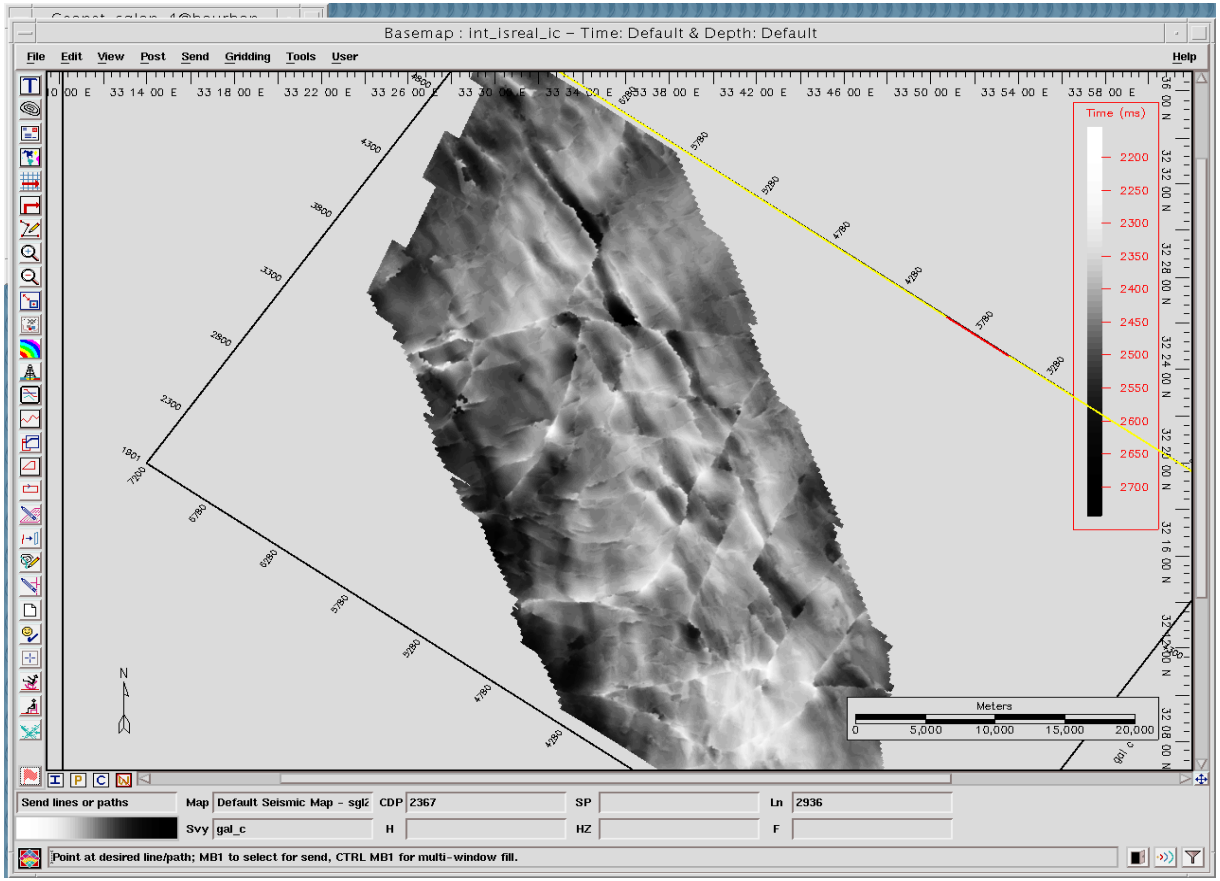


Figure AP 1.1. Gal C Survey. Seismic time map (TWT, ms) of Horizon M

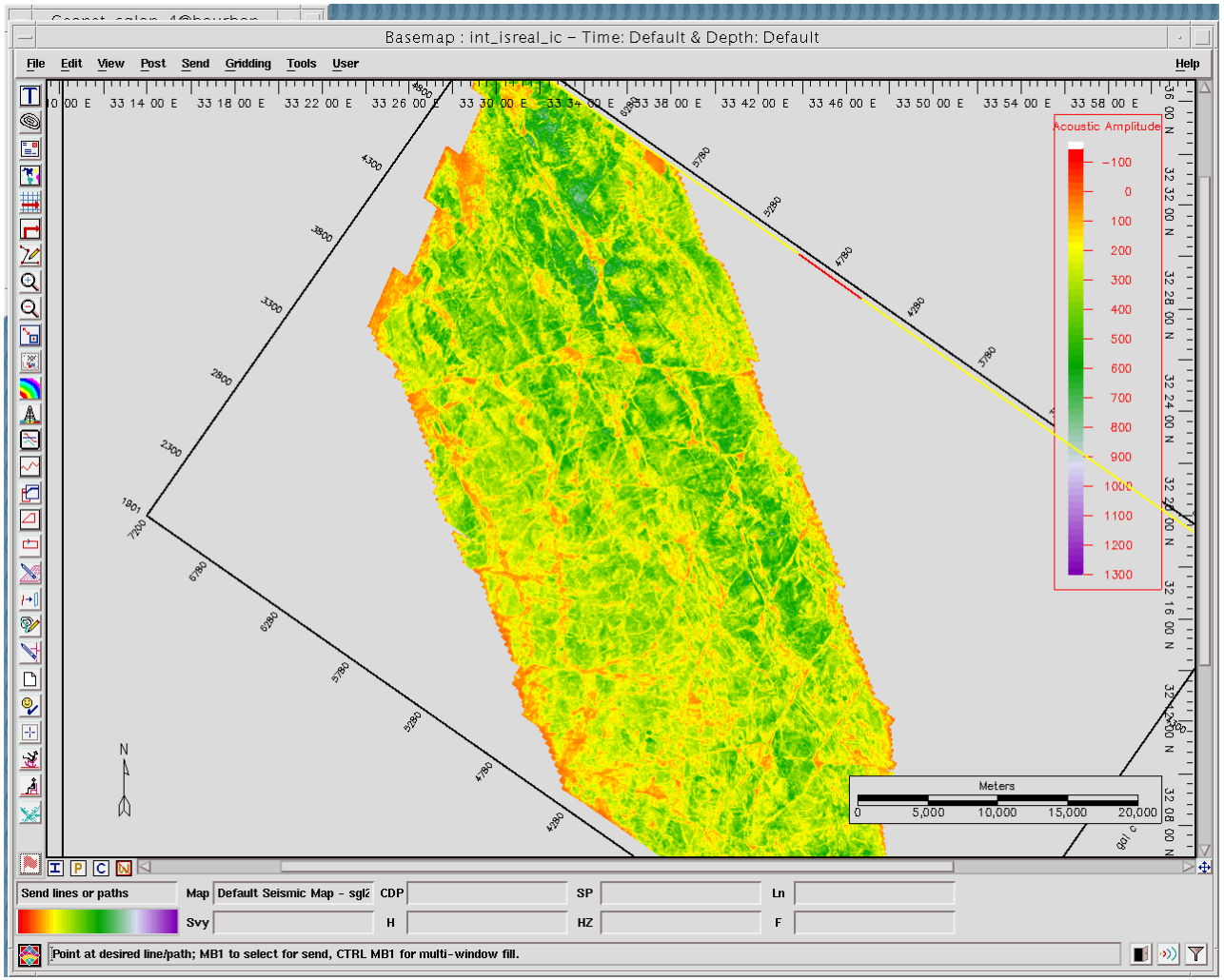


Figure AP 1.2. Gal C Survey. Time amplitude map (TWT, ms) of Horizon M.

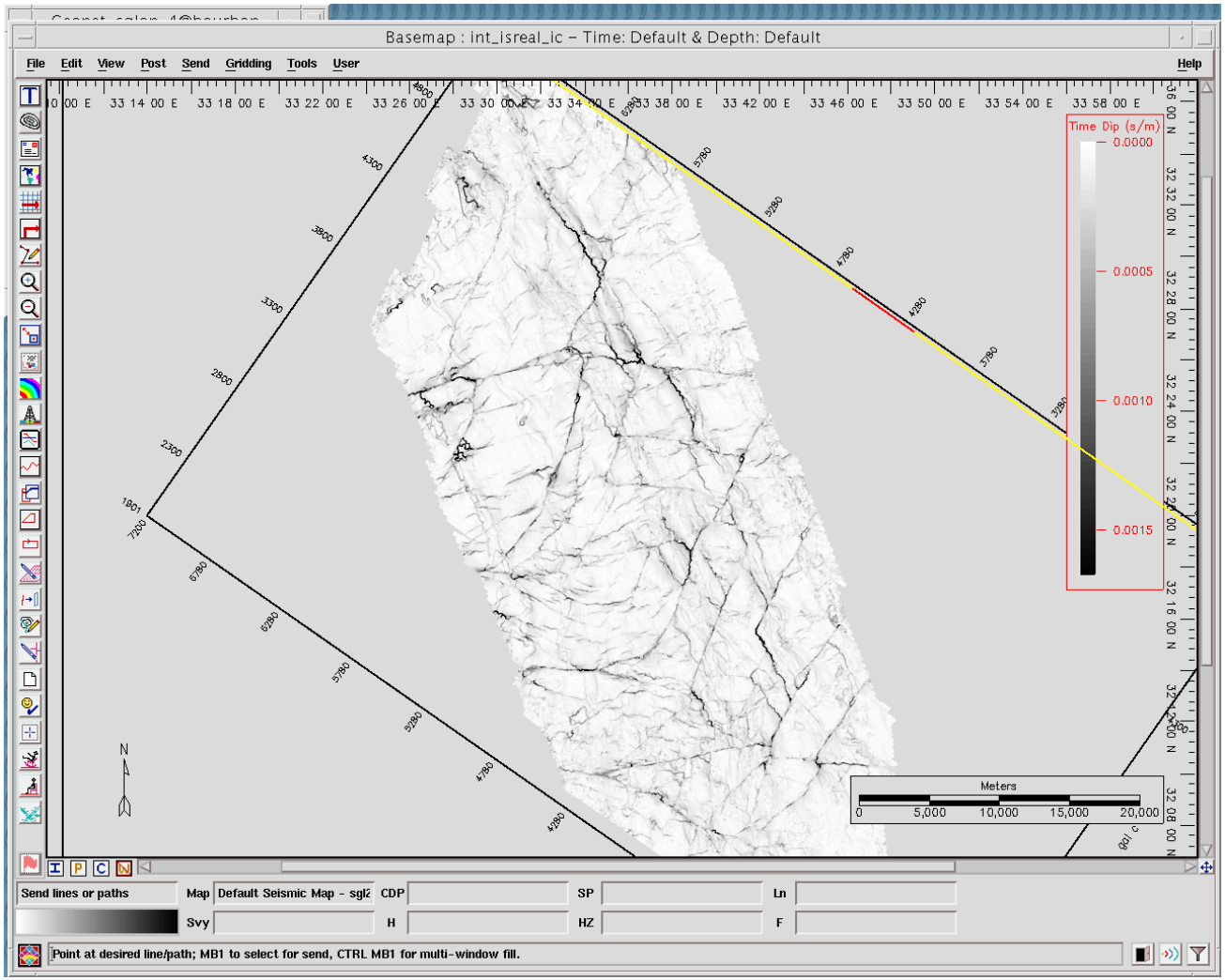


Figure AP 1.3. Gal C Survey. Time dip (TWT, ms) map of Horizon M.

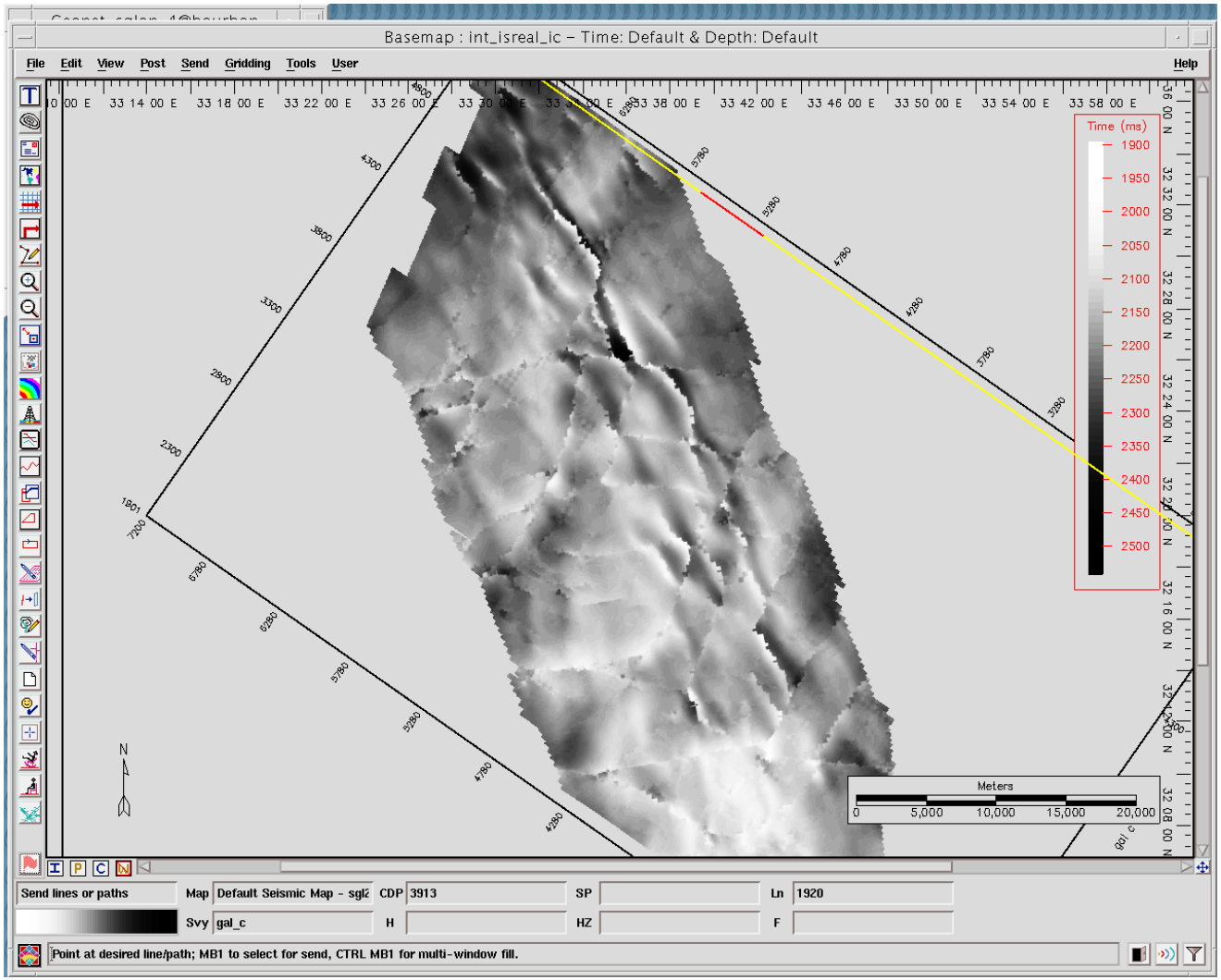


Figure AP 1.4. Gal C Survey. Seismic time map (TWT, ms) of Horizon BPM2

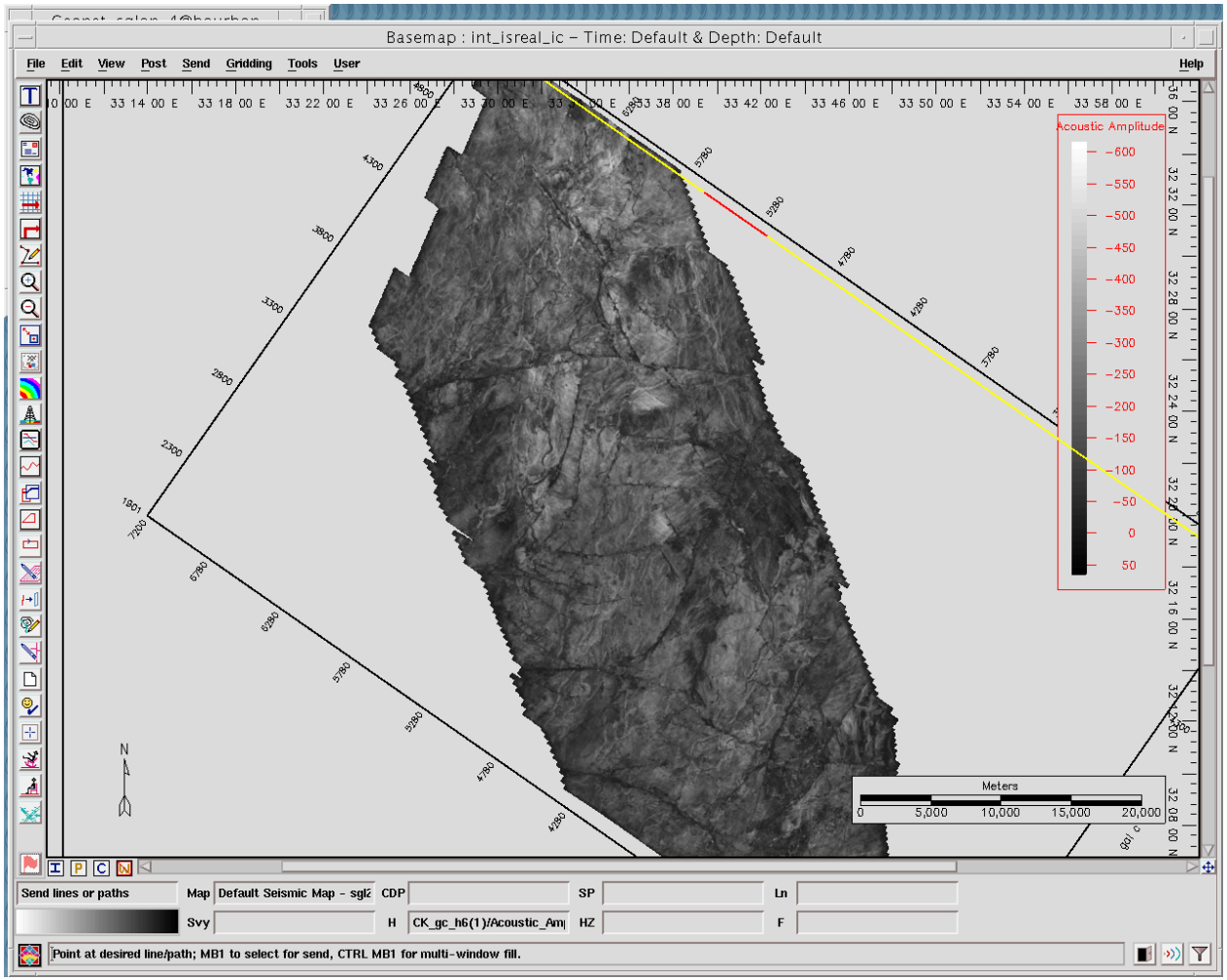


Figure AP 1.5. Gal C Survey. Time amplitude map (TWT, ms) of Horizon BPM2.

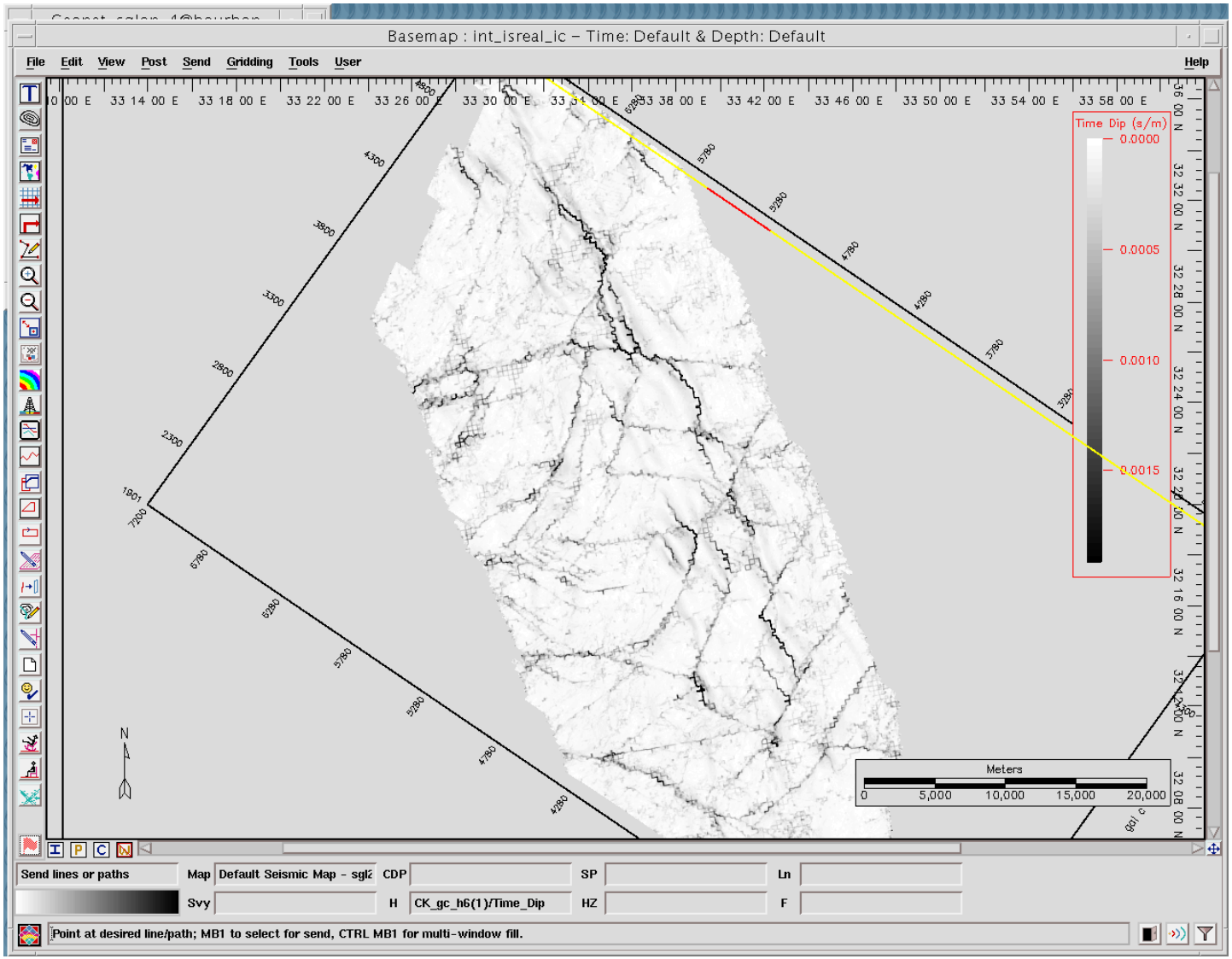


Figure AP 1.6. Gal C Survey. Time dip (TWT, ms) map of Horizon BPM2.

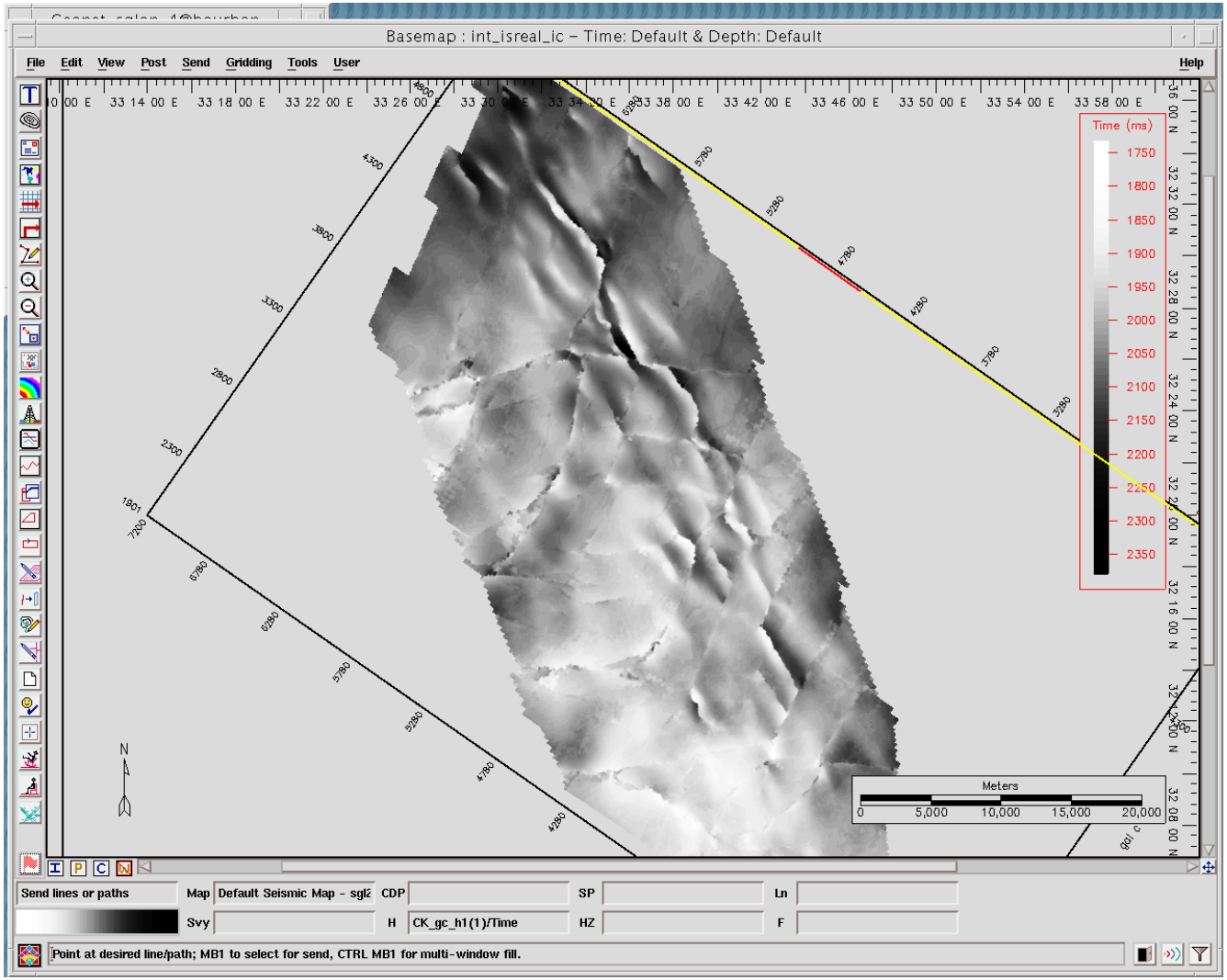


Figure AP 1.7. Gal C Survey. Seismic time map (TWT, ms) of Horizon 1PM2

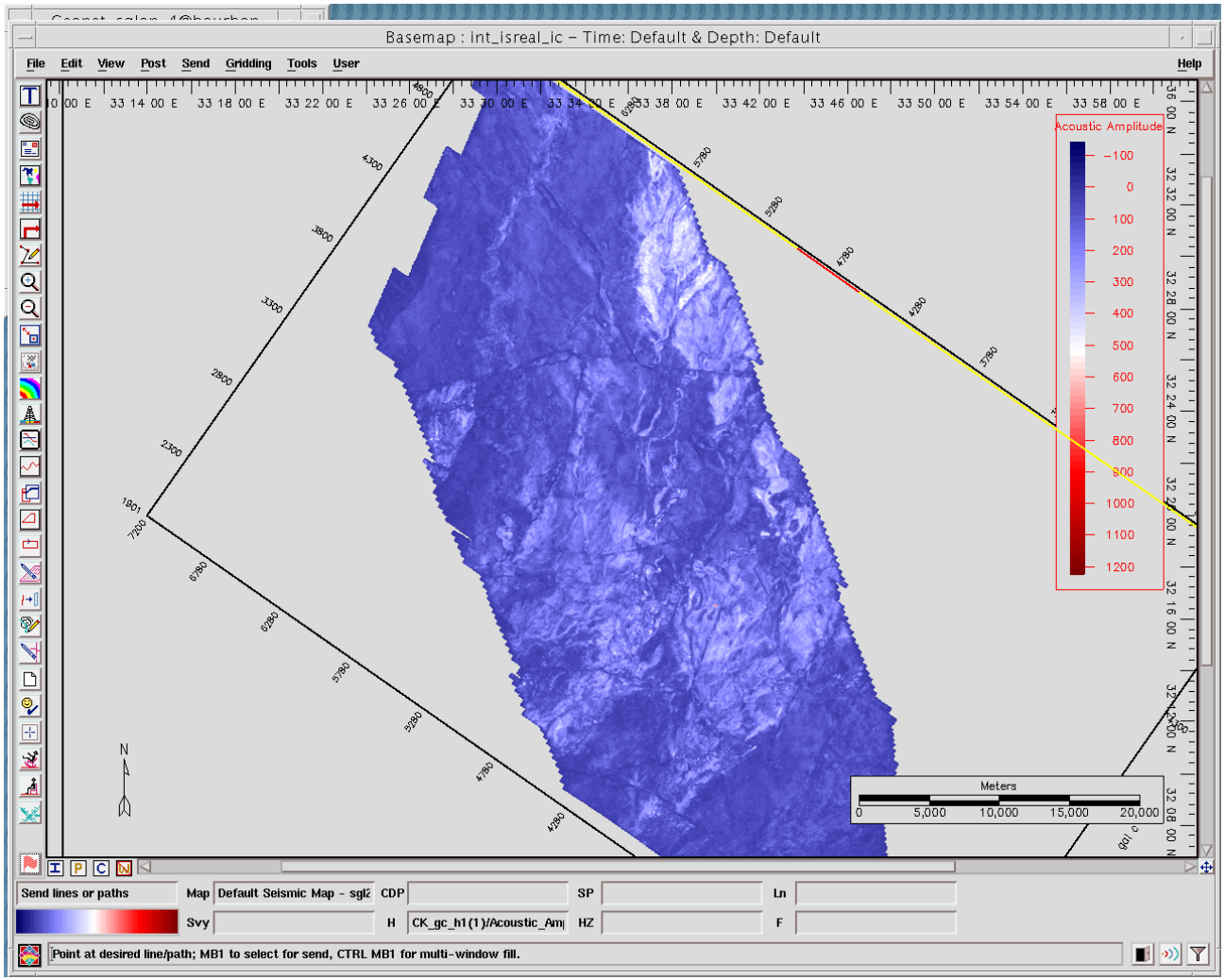


Figure AP 1.8. Gal C Survey. Time amplitude map (TWT, ms) of Horizon 1PM2.

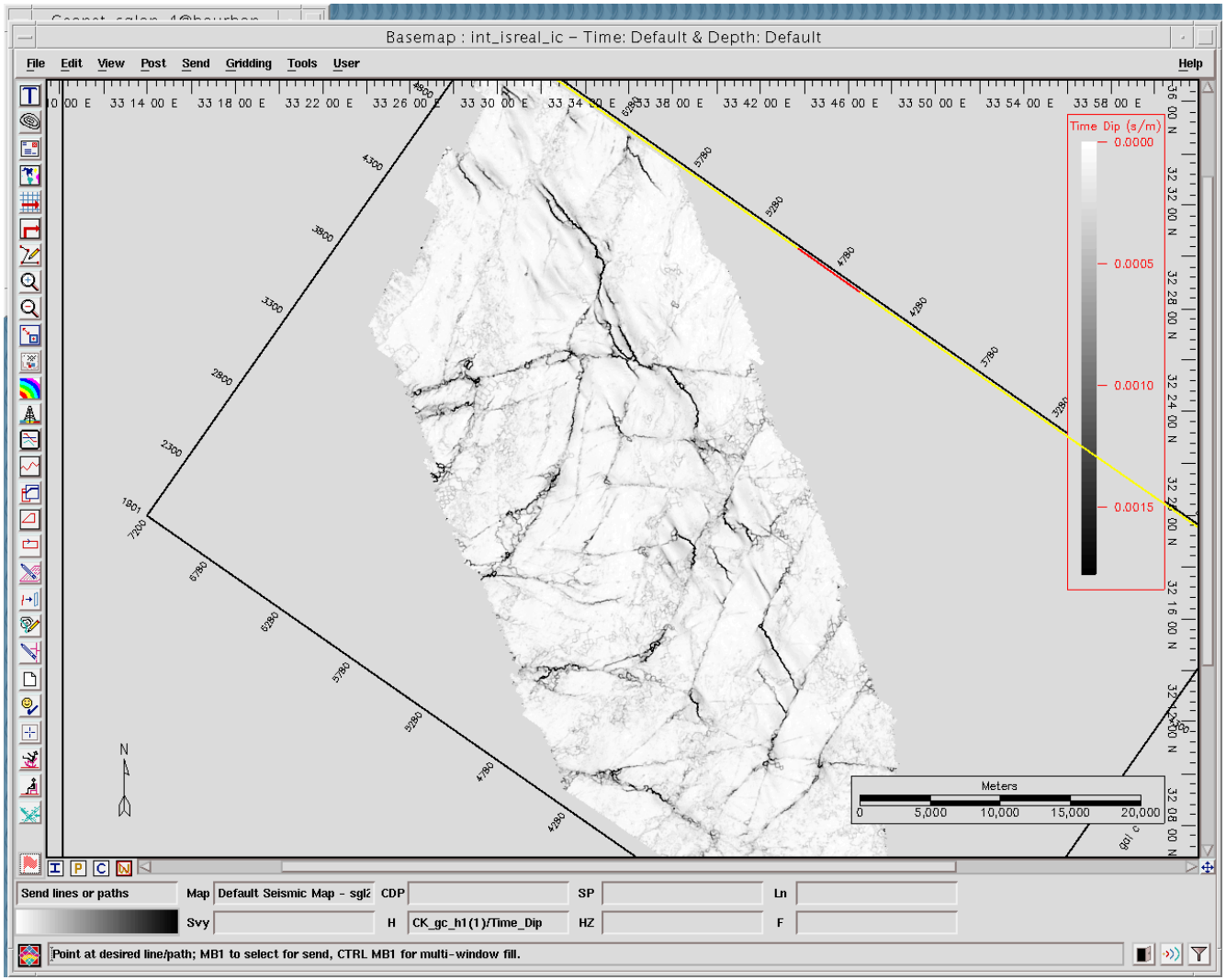


Figure AP 1.9. Gal C Survey. Time dip (TWT, ms) map of Horizon 1PM2.

Appendice 1.10 and 1.11- Zoomed maps showing kinematic markers for determining the sense of shear and displacement of strike slip faults in Gal C

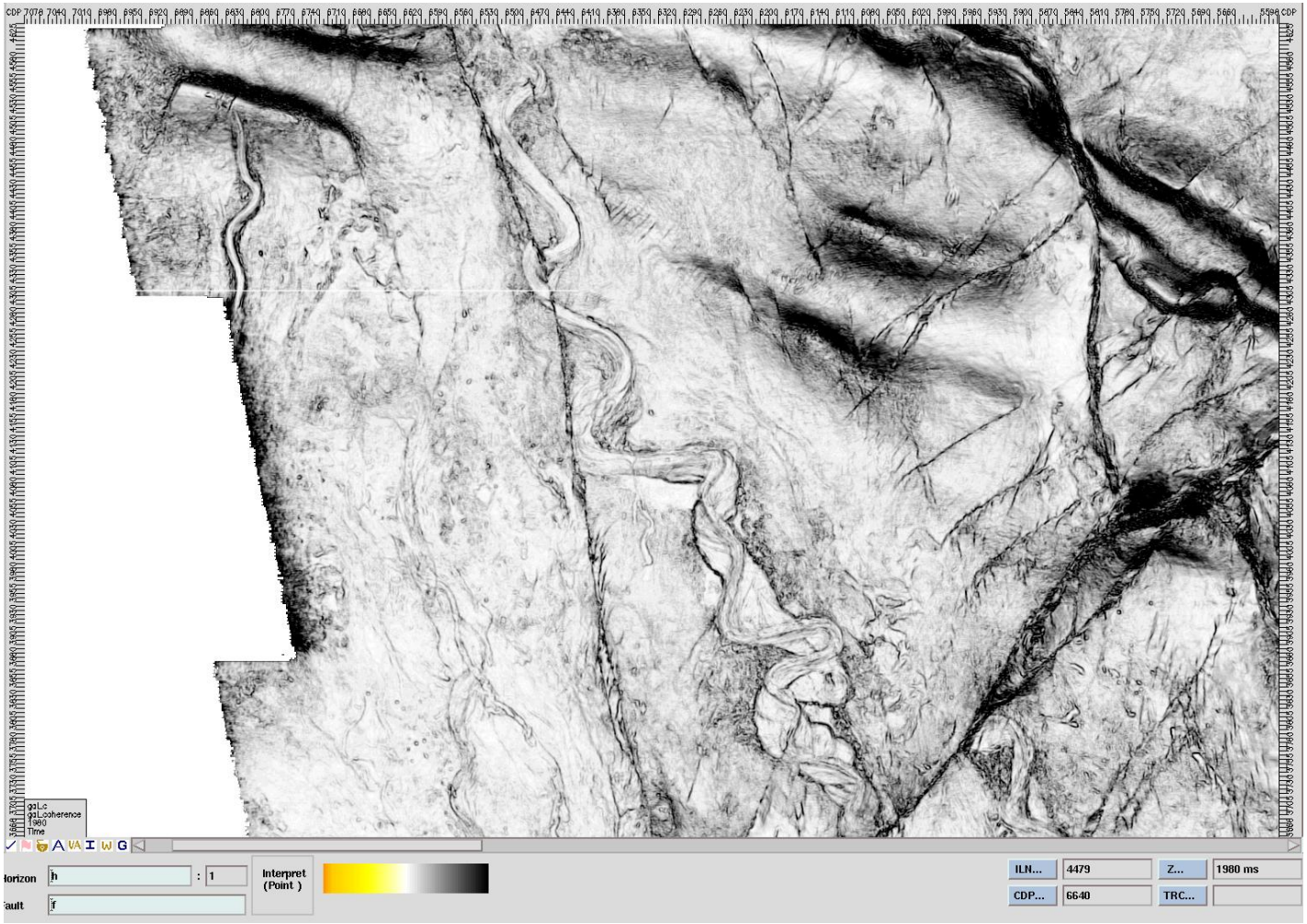


Figure AP 1.10. Gal C Survey.  Time dip (TWT, ms) map of parts of Horizon BP3.

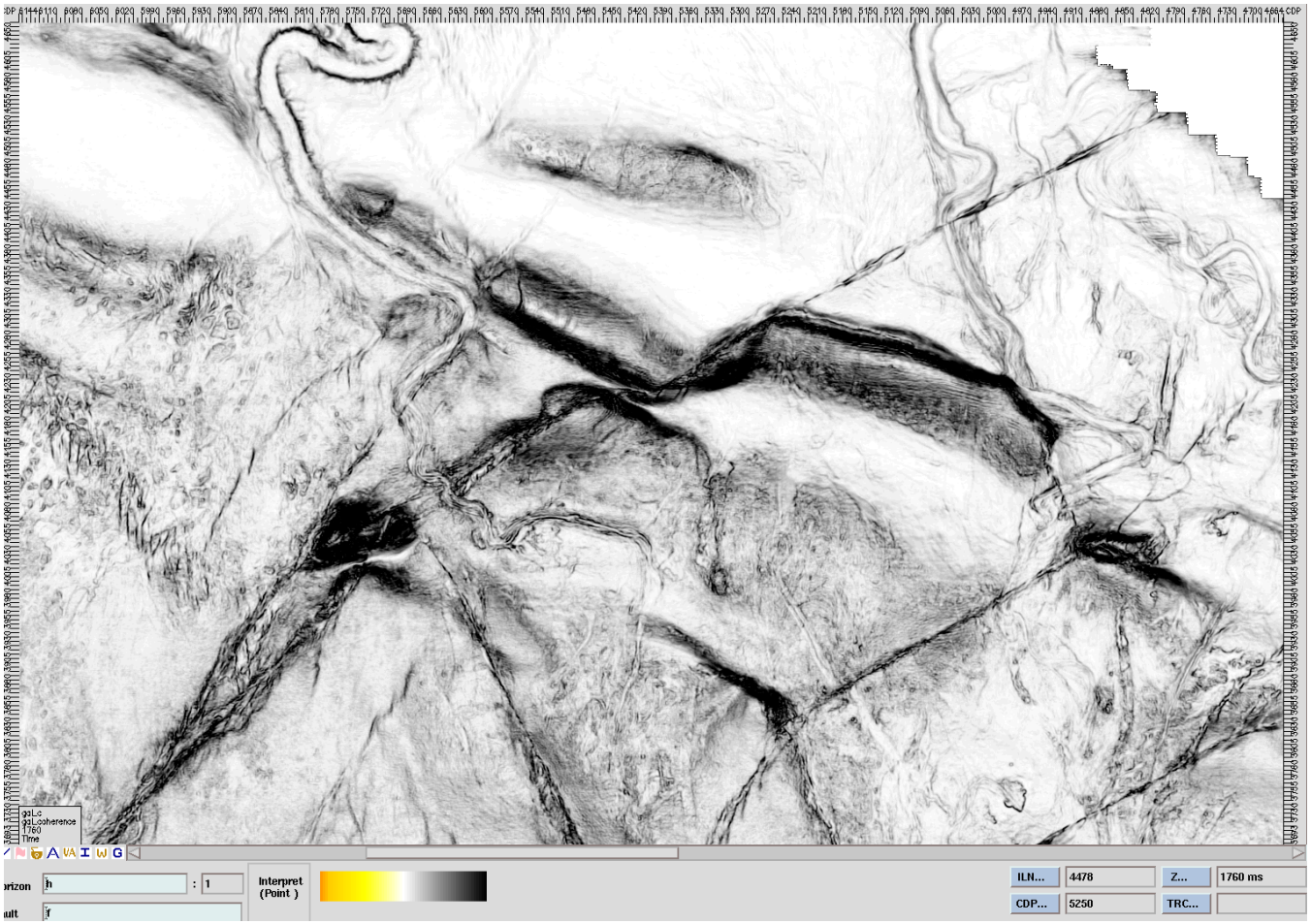


Figure AP 1.11. Gal C Survey.  Time dip (TWT, ms) map of parts of Horizon IPM2

Appendice 2- Fault dip slip and shortening values along strike for the main thrust faults in Structures A, B and C. Measurements were made on sequential inlines oriented perpendicular to fault and fold strike . Spacing between lines: 250m

| | | Fault dip-slip | | | | | | | | | |
|---|---|---|---|---|---|---|---|---|---|---|---|
| No | Line No(m) | T10 | T9 | T13 | T17 | T19 | T18 | T24 | T23 | shortening | Total displacement |
| 0 | 0 | 0 | 0 | 0 | 0 | 0 | 0 | 0 | 0 | 0 | 0 |
| 1 | 250 | 0 | 0 | 0 | 0 | 0 | 0 | 0 | 0 | 0 | 0 |
| 2 | 500 | 32.0156 | 0 | 0 | 0 | 0 | 0 | 0 | 0 | 90.2474 | 32.0156212 |
| 3 | 750 | 16.6508 | 0 | 0 | 0 | 0 | 0 | 0 | 0 | 132.363 | 16.6508258 |
| 4 | 1000 | 93.8736 | 62.8013 | 0 | 0 | 0 | 0 | 0 | 0 | 78.2144 | 156.674859 |
| 5 | 1250 | 56.8243 | 85.9593 | 0 | 0 | 0 | 0 | 0 | 0 | 90.2474 | 142.783583 |
| 6 | 1500 | 48.6544 | 77.6032 | 0 | 0 | 0 | 0 | 0 | 0 | 132.363 | 126.257551 |
| 7 | 1750 | 57.8122 | 90.1388 | 0 | 0 | 0 | 0 | 0 | 0 | 180.495 | 147.950978 |
| 8 | 2000 | 85.9593 | 89.4553 | 0 | 0 | 0 | 0 | 0 | 0 | 198.544 | 175.414589 |
| 9 | 2250 | 55.9017 | 79.6492 | 0 | 0 | 0 | 0 | 0 | 0 | 192.528 | 135.55093 |
| 10 | 2500 | 45.6317 | 76.5768 | 0 | 0 | 0 | 0 | 0 | 0 | 198.544 | 122.208436 |
| 11 | 2750 | 40.7707 | 92.3594 | 0 | 0 | 0 | 0 | 0 | 0 | 174.478 | 133.130053 |

| | | | | | | | | | | | |
|---|---|---|---|---|---|---|---|---|---|---|---|
| 12 | 3000 | 0 | 58.3095 | 0 | 0 | 0 | 0 | 0 | 0 | 180.495 | 58.3095189 |
| 13 | 3250 | 0 | 58.3095 | 0 | 0 | 0 | 0 | 0 | 0 | 180.495 | 58.3095189 |
| 14 | 3500 | 0 | 86.954 | 0 | 0 | 0 | 0 | 0 | 0 | 150.412 | 86.9540108 |
| 15 | 3750 | 0 | 231.206 | 0 | 0 | 0 | 0 | 0 | 0 | 192.528 | 231.205536 |
| 16 | 4000 | 0 | 250.16 | 0 | 0 | 0 | 0 | 0 | 0 | 150.412 | 250.160449 |
| 17 | 4250 | 0 | 330.879 | 0 | 0 | 0 | 0 | 0 | 0 | 180.495 | 86.9540108 |
| 18 | 4500 | 0 | 419.91 | 0 | 0 | 0 | 0 | 0 | 0 | 300.825 | 231.205536 |
| 19 | 4750 | 0 | 466.476 | 0 | 0 | 0 | 0 | 0 | 0 | 312.858 | 250.160449 |
| 20 | 5000 | 0 | 358.504 | 0 | 0 | 0 | 0 | 0 | 0 | 439.204 | 330.879132 |
| 21 | 5250 | 0 | 347.693 | 0 | 0 | 0 | 0 | 0 | 0 | 487.336 | 458.960762 |
| 22 | 5500 | 0 | 358.402 | 0 | 0 | 0 | 0 | 0 | 0 | 571.567 | 499.901441 |
| 23 | 5750 | 0 | 335.394 | 0 | 0 | 0 | 0 | 0 | 0 | 571.567 | 395.300574 |
| 24 | 6000 | 0 | 347.816 | 39.0512 | 0 | 0 | 0 | 0 | 0 | 571.567 | 385.229401 |
| 25 | 6250 | 0 | 411.286 | 33.4253 | 0 | 0 | 0 | 0 | 0 | 421.155 | 420.105275 |
| 26 | 6500 | 0 | 623.647 | 36.7967 | 0 | 0 | 0 | 0 | 0 | 391.072 | 406.104477 |
| 27 | 6750 | 0 | 715.055 | 37.5366 | 0 | 0 | 0 | 0 | 0 | 457.254 | 390.79569 |
| 28 | 7000 | 0 | 672.619 | 61.7029 | 0 | 0 | 0 | 0 | 0 | 559.534 | 432.386737 |

| | | | | | | | | | | | |
|---|---|---|---|---|---|---|---|---|---|---|---|
| 29 | 7250 | 0 | 760.021 | 70.7107 | 0 | 0 | 0 | 0 | 0 | 631.732 | 646.390467 |
| 30 | 7500 | 0 | 717.692 | 42.9796 | 0 | 0 | 0 | 0 | 0 | 770.111 | 749.025818 |
| 31 | 7750 | 0 | 658.775 | 21.1009 | 0 | 0 | 0 | 0 | 0 | 818.243 | 710.907142 |
| 32 | 8000 | 0 | 546.955 | 22.7431 | 0 | 0 | 0 | 0 | 0 | 854.342 | 794.676664 |
| 33 | 8250 | 0 | 498.554 | 33.9706 | 0 | 0 | 0 | 0 | 0 | 734.012 | 752.692309 |
| 34 | 8500 | 0 | 406.517 | 38.2884 | 0 | 0 | 0 | 0 | 0 | 794.177 | 658.77462 |
| 35 | 8750 | 0 | 335.92 | 34.6554 | 0 | 0 | 0 | 0 | 0 | 679.864 | 546.955437 |
| 36 | 9000 | 0 | 209.452 | 35 | 0 | 0 | 0 | 0 | 0 | 559.534 | 498.55416 |
| 37 | 9250 | 0 | 0 | 0 | 160.59 | 0 | | 0 | 0 | 421.155 | 406.51722 |
| 38 | 9500 | 0 | 0 | 0 | 133.701 | 21.9146 | 46.8001 | 0 | 0 | 439.204 | 335.920005 |
| 39 | 9750 | 0 | 0 | 0 | 202.006 | 33.3017 | 148.544 | 0 | 0 | 511.402 | 209.452262 |
| 40 | 10000 | 0 | 0 | 0 | 123.406 | 93.8416 | 176.086 | 0 | 0 | 222.61 | 160.589539 |
| 41 | 10250 | 0 | 0 | 0 | 118.697 | 162.18 | 197.841 | 0 | 0 | 90.2474 | 202.415873 |
| 42 | 10500 | 0 | 0 | 0 | 85 | 117.219 | 199.81 | 0 | 0 | 90.2474 | 383.850985 |
| 43 | 10750 | 0 | 0 | 0 | 71.1495 | 82.801 | 252.834 | 0 | 0 | 228.627 | 393.333373 |
| 44 | 11000 | 0 | 0 | 0 | 45.6317 | 50.6063 | 155.21 | 0 | 0 | 463.27 | 478.717623 |
| 45 | 11250 | 0 | 0 | 0 | 34.3548 | 16.0078 | 125 | 0 | 0 | 469.287 | 402.028722 |

| | | | | | | | | | | | |
|---|---|---|---|---|---|---|---|---|---|---|---|
| 46 | 11500 | 0 | 0 | 0 | 36.225 | 0 | 91.2634 | 0 | 0 | 409.122 | 406.784889 |
| 47 | 11750 | 0 | 0 | 0 | 40.0031 | 0 | 64.0312 | 0 | 0 | 457.254 | 251.448342 |
| 48 | 12000 | 0 | 0 | 0 | 114.11 | 0 | 51.2957 | 0 | 0 | 373.023 | 175.362577 |
| 49 | 12250 | 0 | 0 | 0 | 184.835 | 0 | 16.6508 | 0 | 0 | 354.973 | 127.488347 |
| 50 | 12500 | 0 | 0 | 0 | 40.6079 | 0 | 147.872 | 0 | 0 | 336.924 | 104.034367 |
| 51 | 12750 | 0 | 0 | 0 | 215.641 | 0 | 144.697 | 0 | 0 | 228.627 | 165.405308 |
| 52 | 13000 | 0 | 0 | 0 | 206.858 | 0 | 288.628 | 0 | 0 | 246.676 | 201.485887 |
| 53 | 13250 | 0 | 0 | 0 | 210.623 | 0 | 287.49 | 0 | 0 | 138.379 | 188.479447 |
| 54 | 13500 | 0 | 0 | 0 | 212.191 | 0 | 301.763 | 0 | 0 | 282.775 | 360.338003 |
| 55 | 13750 | 0 | 0 | 0 | 239.835 | 0 | 284.152 | 0 | 0 | 282.775 | 495.486264 |
| 56 | 14000 | 0 | 0 | 0 | 376.808 | 0 | 263.137 | 0 | 0 | 336.924 | 498.113044 |
| 57 | 14250 | 0 | 0 | 0 | 476.509 | 0 | 306.383 | 0 | 0 | 559.534 | 513.954104 |
| 58 | 14500 | 0 | 0 | 0 | 512.886 | 0 | 289.51 | 0 | 0 | 559.534 | 523.987168 |
| 59 | 14750 | 0 | 0 | 0 | 443.635 | 0 | 303.332 | 165.602 | 0 | 559.534 | 639.94449 |
| 60 | 15000 | 0 | 0 | 0 | 356.598 | 0 | 280.78 | 283.82 | 0 | 547.501 | 782.891704 |
| 61 | 15250 | 0 | 0 | 0 | 0 | 0 | 266.228 | 342.965 | 0 | 848.326 | 802.396127 |
| 62 | 15500 | 0 | 0 | 0 | 0 | 0 | 0 | 328.672 | 0 | 842.309 | 912.569113 |

| | | | | | | | | | | | |
|---|---|---|---|---|---|---|---|---|---|---|---|
| 63 | 15750 | 0 | 0 | 0 | 0 | 0 | 0 | 216.816 | 0 | 1040.85 | 921.198247 |
| 64 | 16000 | 0 | 0 | 0 | 0 | 0 | 0 | 220.411 | 97.2677 | 1197.28 | 609.193193 |
| 65 | 16250 | 0 | 0 | 0 | 0 | 0 | 0 | 227.297 | 97.2677 | 439.204 | 328.671569 |
| 66 | 16500 | 0 | 0 | 0 | 0 | 0 | 0 | 177.975 | 108.24 | 270.742 | 216.81559 |
| 67 | 16750 | 0 | 0 | 0 | 0 | 0 | 0 | 104.977 | 149.323 | 180.495 | 317.678652 |
| 68 | 17000 | 0 | 0 | 0 | 0 | 0 | 0 | 81.9466 | 126.516 | 180.495 | 324.564834 |
| 69 | 17250 | 0 | 0 | 0 | 0 | 0 | 0 | 69.3109 | 256.125 | 300.825 | 286.215893 |
| 70 | 17500 | 0 | 0 | 0 | 0 | 0 | 0 | 0 | 243.282 | 300.825 | 254.300016 |
| 71 | 17750 | 0 | 0 | 0 | 0 | 0 | 0 | 0 | 270.888 | 300.825 | 208.462438 |
| 72 | 18000 | 0 | 0 | 0 | 0 | 0 | 0 | 0 | 283.212 | 300.825 | 325.435863 |
| 73 | 18250 | 0 | 0 | 0 | 0 | 0 | 0 | 0 | 317.16 | 300.825 | 243.28173 |
| 74 | 18500 | 0 | 0 | 0 | 0 | 0 | 0 | 0 | 280.203 | 385.056 | 270.887892 |
| 75 | 18750 | 0 | 0 | 0 | 0 | 0 | 0 | 0 | 301.84 | 360.99 | 283.211935 |
| 76 | 19000 | 0 | 0 | 0 | 0 | 0 | 0 | 0 | 291.548 | 373.023 | 317.15966 |
| 77 | 19250 | 0 | 0 | 0 | 0 | 0 | 0 | 0 | 250.16 | 336.924 | 280.203497 |
| 78 | 19500 | 0 | 0 | 0 | 0 | 0 | 0 | 0 | 302.335 | 457.254 | 301.839775 |
| 79 | 19750 | 0 | 0 | 0 | 0 | 0 | 0 | 0 | 418.852 | 330.907 | 291.547595 |

| | | | | | | | | | | | |
|---|---|---|---|---|---|---|---|---|---|---|---|
| 80 | 20000 | 0 | 0 | 0 | 0 | 0 | 0 | 0 | 307.825 | 312.858 | 250.160449 |
| 81 | 20250 | 0 | 0 | 0 | 0 | 0 | 0 | 0 | 233.754 | 294.808 | 302.334666 |
| 82 | 20500 | 0 | 0 | 0 | 0 | 0 | 0 | 0 | 261.369 | 336.924 | 418.852301 |
| 83 | 20750 | 0 | 0 | 0 | 0 | 0 | 0 | 0 | 347.311 | 276.759 | 307.825031 |
| 84 | 21000 | 0 | 0 | 0 | 0 | 0 | 0 | 0 | 167.126 | 180.495 | 233.754144 |
| 85 | 21250 | 0 | 0 | 0 | 0 | 0 | 0 | 0 | 39.6894 | 138.379 | 261.36947 |
| 86 | 21500 | 0 | 0 | 0 | 0 | 0 | 0 | 0 | 0 | 409.122 | 347.3111 |
| 87 | 21750 | 0 | 0 | 0 | 0 | 0 | 0 | 0 | 0 | 451.237 | 167.126449 |
| 88 | 22000 | 0 | 0 | 0 | 0 | 0 | 0 | 0 | 0 | 469.287 | 39.6894192 |
| 89 | 22250 | 0 | 0 | 0 | 0 | 0 | 0 | 0 | 0 | 469.287 | 0 |

**Appendice 3, vertical throw distribution along strike. These values were used in plotting the contours and vertical profiles for Faults T20, T21, T22, and T25.**

| Distance (m) | Depth (TWT, s) | Throw (TWT, s) | |
|---|---|---|---|
| X | Y | Z | |
| 125 | -2149 | 0 | |
| 125 | -2184 | 4 | |
| 125 | -2245 | 15 | |
| 125 | -2289 | 16 | |
| 125 | -2404 | 17 | |
| 250 | -2100 | 0 | |
| 250 | -2138 | 3 | |
| 250 | -2180 | 2 | |
| 250 | -2233 | 17 | |
| 250 | -2284 | 14 | |
| 250 | -2401 | 16 | |
| 375 | -2150 | 0 | |
| 375 | -2181 | 1 | |
| 375 | -2237 | 9 | |
| 375 | -2269 | 20 | |
| 375 | -2394 | 12 | |
| 500 | -2130 | 0 | |
| 500 | -2136 | 6 | |
| 500 | -2177 | 3 | |
| 500 | -2240 | 2 | |
| 500 | -2268 | 26 | |
| 500 | -2390 | 11 | |

**Fault T20**

| | | |
|---|---|---|
| 625 | -2170 | 0 |
| 625 | -2224 | 13 |
| 625 | -2265 | 17 |
| 625 | -2380 | 19 |
| 750 | -2138 | 1 |
| 750 | -2164 | 13 |
| 750 | -2218 | 18 |
| 750 | -2257 | 22 |
| 750 | -2373 | 19 |
| 875 | -2060 | 0 |
| 875 | -2065 | 7 |
| 875 | -2122 | 7 |
| 875 | -2164 | 8 |
| 875 | -2214 | 10 |
| 875 | -2257 | 17 |
| 875 | -2370 | 25 |
| 1000 | -2054 | 0 |
| 1000 | -2060 | 9 |
| 1000 | -2116 | 14 |
| 1000 | -2160 | 21 |
| 1000 | -2210 | 24 |
| 1000 | -2208 | 25 |
| 1000 | -2239 | 13 |
| 1125 | -2021 | 0 |
| 1125 | -2057 | 11 |
| 1125 | -2114 | 19 |

**Fault T20**

| | | |
|---|---|---|
| 1125 | -2206 | 26 |
| 1125 | -2205 | 25 |
| 1125 | -2232 | 39 |
| 1125 | -2318 | 27 |
| 1250 | -2060 | 0 |
| 1250 | -2126 | 28 |
| 1250 | -2152 | 21 |
| 1250 | -2198 | 36 |
| 1250 | -2236 | 41 |
| 1250 | -2341 | 53 |
| 1375 | -2021 | 0 |
| 1375 | -2060 | 4 |
| 1375 | -2128 | 13 |
| 1375 | -2154 | 20 |
| 1375 | -2198 | 40 |
| 1375 | -2238 | 46 |
| 1375 | -2337 | 56 |
| 1500 | -2041 | 0 |
| 1500 | -2058 | 8 |
| 1500 | -2122 | 22 |
| 1500 | -2145 | 29 |
| 1500 | -2204 | 36 |
| 1500 | -2242 | 48 |
| 1500 | -2340 | 56 |
| 1625 | -2020 | 0 |
| 1625 | -2054 | 8 |

**Fault T20**

| | | | |
|---|---|---|---|
| 1625 | -2122 | 22 | |
| 1625 | -2145 | 32 | |
| 1625 | -2205 | 35 | |
| 1625 | -2246 | 50 | |
| 1625 | -2326 | 60 | |
| 1750 | -1984 | 0 | |
| 1750 | -2008 | 6 | |
| 1750 | -2065 | 8 | **Fault T20** |
| 1750 | -2106 | 39 | |
| 1750 | -2146 | 36 | |
| 1750 | -2201 | 48 | |
| 1750 | -2256 | 49 | |
| 1750 | -2335 | 63 | |
| 1875 | -1986 | 0 | |
| 1875 | -2005 | 9 | |
| 1875 | -2048 | 14 | |
| 1875 | -2105 | 35 | |
| 1875 | -2140 | 40 | |
| 1875 | -2193 | 42 | |
| 1875 | -2252 | 53 | |
| 1875 | -2345 | 56 | |
| 2000 | -2006 | 0 | |
| 2000 | -2028 | 5 | |
| 2000 | -2097 | 43 | |
| 2000 | -2133 | 48 | |
| 2000 | -2196 | 53 | |

| | | | |
|---|---|---|---|
| 2000 | -2250 | 58 | |
| 2000 | -2334 | 67 | |
| 2125 | -2036 | 0 | |
| 2125 | -2058 | 10 | |
| 2125 | -2088 | 48 | |
| 2125 | -2109 | 28 | |
| 2125 | -2198 | 56 | |
| 2125 | -2253 | 57 | |
| 2125 | -2360 | 41 | |
| 2250 | -2077 | 0 | |
| 2250 | -2092 | 32 | |
| 2250 | -2132 | 32 | **Fault T20** |
| 2250 | -2205 | 41 | |
| 2250 | -2261 | 57 | |
| 2250 | -2320 | 54 | |
| 2375 | -2066 | 0 | |
| 2375 | -2132 | 13 | |
| 2375 | -2157 | 15 | |
| 2375 | -2212 | 20 | |
| 2375 | -2256 | 61 | |
| 2375 | -2340 | 57 | |
| 2500 | -2065 | 0 | |
| 2500 | -2132 | 13 | |
| 2500 | -2156 | 16 | |
| 2500 | -2200 | 28 | |
| 2500 | -2237 | 36 | |

| | | |
|---|---|---|
| 2500 | -2362 | 28 |
| 2625 | -2077 | 0 |
| 2625 | -2130 | 12 |
| 2625 | -2157 | 15 |
| 2625 | -2202 | 26 |
| 2625 | -2238 | 34 |
| 2625 | -2349 | 33 |
| 2750 | -2098 | 0 |
| 2750 | -2129 | 13 |
| 2750 | -2156 | 13 |
| 2750 | -2186 | 18 |
| 2750 | -2238 | 30 |
| 2750 | -2352 | 25 |
| 2875 | -2875 | 0 |
| 2875 | -2129 | 9 |
| 2875 | -2156 | 14 |
| 2875 | -2186 | 16 |
| 2875 | -2238 | 26 |
| 2875 | -2344 | 29 |
| 3000 | -2142 | 0 |
| 3000 | -2160 | 10 |
| 3000 | -2185 | 15 |
| 3000 | -2234 | 24 |
| 3000 | -2346 | 20 |
| 3125 | -2146 | 0 |
| 3125 | -2186 | 11 |

**Fault T20**

| | | | |
|---|---|---|---|
| 3125 | -2236 | 20 | **Fault T20** |
| 3125 | -2349 | 13 | |
| 3250 | -2185 | 7 | |
| 3250 | -2237 | 17 | |
| 3250 | -2350 | 15 | |

| Distance (m) | Depth (TWT, s) | Throw (TWT, s) | **Fault T21** |
|---|---|---|---|
| X | Y | Z | |
| 2625 | -2254 | 0 | |
| 2625 | -2253 | 24 | |
| 2750 | -2181 | 0 | |
| 2750 | -2192 | 8 | |
| 2750 | -2197 | 12 | |
| 2750 | -2225 | 13 | |
| 2750 | -2256 | 22 | |
| 2875 | -2186 | 0 | |
| 2875 | -2182 | 6 | |
| 2875 | -2190 | 12 | |
| 2875 | -2264 | 14 | |
| 3000 | -2166 | 0 | |
| 3000 | -2174 | 6 | |
| 3000 | -2180 | 10 | |
| 3000 | -2206 | 16 | |

| | | |
|---|---|---|
| 3000 | -2254 | 12 |
| 3125 | -2158 | 0 |
| 3125 | -2172 | 8 |
| 3125 | -2182 | 6 |
| 3125 | -2208 | 4 |
| 3125 | -2213 | 9 |
| 3125 | -2248 | 16 |
| 3250 | -2082 | 0 |
| 3250 | -2102 | 7 |
| 3250 | -2146 | 7 |
| 3250 | -2172 | 5 |
| 3250 | -2184 | 5 |
| 3250 | -2198 | 14 |
| 3250 | -2213 | 12 |
| 3250 | -2238 | 20 |
| 3375 | -2137 | 0 |
| 3375 | -2143 | 7 |
| 3375 | -2148 | 5 |
| 3375 | -2176 | 5 |
| 3375 | -2204 | 9 |
| 3375 | -2148 | 5 |
| 3375 | -2240 | 16 |
| 3500 | -2148 | 0 |
| 3500 | -2152 | 2 |
| 3500 | -2170 | 14 |
| 3500 | -2180 | 10 |

**Fault T21**

| | | |
|---|---|---|
| 3500 | -2196 | 13 |
| 3500 | -2210 | 18 |
| 3500 | -2241 | 15 |
| 3500 | -2345 | 13 |
| 3625 | -2150 | 0 |
| 3625 | -2158 | 2 |
| 3625 | -2178 | 10 |
| 3625 | -2190 | 4 |
| 3625 | -2206 | 7 |
| 3625 | -2221 | 7 |
| 3625 | -2233 | 29 |
| 3625 | -2341 | 27 |
| 3750 | -2149 | 0 |
| 3750 | -2161 | 13 |
| 3750 | -2180 | 9 |
| 3750 | -2189 | 12 |
| 3750 | -2212 | 6 |
| 3750 | -2222 | 16 |
| 3750 | -2248 | 12 |
| 3750 | -2338 | 20 |
| 3875 | -2155 | 0 |
| 3875 | -2161 | 7 |
| 3875 | -2188 | 10 |
| 4000 | -2134 | 0 |
| 4000 | -2162 | 2 |
| 4125 | -2170 | 0 |

**Fault T21**

| | | | |
|---|---|---|---|
| 4125 | -2173 | 3 | **Fault T21** |
| 4125 | -2202 | 6 | |
| 4125 | -2205 | 5 | |
| 4250 | -2169 | 0 | |
| 4250 | -2172 | 2 | |
| 4250 | -2173 | 3 | |
| 4250 | -2202 | 2 | |

| Distance (m) | Depth (TWT, s) | Throw (TWT, s) | |
|---|---|---|---|
| X | Y | Z | |
| 3625 | -2086 | 0 | **Fault T22** |
| 3625 | -2112 | 8 | |
| 3625 | -2118 | 11 | |
| 3625 | -2130 | 12 | |
| 3625 | -2140 | 13 | |
| 3750 | -2033 | 0 | |
| 3750 | -2038 | 11 | |
| 3750 | -2085 | 15 | |
| 3750 | -2108 | 17 | |
| 3750 | -2118 | 16 | |
| 3750 | -2140 | 16 | |
| 3750 | -2149 | 16 | |
| 3750 | -2173 | 15 | |
| 3750 | -2190 | 18 | |
| 3750 | -2221 | 7 | |

| | | |
|---|---|---|
| 3875 | -1934 | 0 |
| 3875 | -1936 | 2 |
| 3875 | -1962 | 6 |
| 3875 | -1984 | 6 |
| 3875 | -2032 | 4 |
| 3875 | -2052 | 16 |
| 3875 | -2076 | 22 |
| 3875 | -2110 | 26 |
| 3875 | -2150 | 28 |
| 3875 | -2169 | 27 |
| 3875 | -2193 | 39 |
| 3875 | -2224 | 40 |
| 3875 | -2340 | 26 |
| 4000 | -1910 | 0 |
| 4000 | -1944 | 5 |
| 4000 | -1954 | 16 |
| 4000 | -1976 | 25 |
| 4000 | -2004 | 24 |
| 4000 | -2029 | 21 |
| 4000 | -2081 | 33 |
| 4000 | -2118 | 30 |
| 4000 | -2145 | 28 |
| 4000 | -2157 | 32 |
| 4000 | -2210 | 36 |
| 4000 | -2248 | 36 |
| 4000 | -2337 | 31 |

**Fault T22**

| | | |
|---|---|---|
| 4125 | -1933 | 0 |
| 4125 | -1934 | 13 |
| 4125 | -1961 | 16 |
| 4125 | -1994 | 23 |
| 4125 | -2006 | 18 |
| 4125 | -2040 | 22 |
| 4125 | -2085 | 21 |
| 4125 | -2122 | 27 |
| 4125 | -2148 | 30 |
| 4125 | -2158 | 24 |
| 4125 | -2218 | 42 |
| 4125 | -2261 | 41 |
| 4125 | -2338 | 27 |
| 4250 | -1876 | 0 |
| 4250 | -1902 | 4 |
| 4250 | -1945 | 23 |
| 4250 | -1988 | 21 |
| 4250 | -2012 | 30 |
| 4250 | -2030 | 27 |
| 4250 | -2082 | 23 |
| 4250 | -2126 | 28 |
| 4250 | -2153 | 25 |
| 4250 | -2172 | 32 |
| 4250 | -2210 | 37 |
| 4250 | -2242 | 42 |
| 4250 | -2316 | 61 |

**Fault T22**

| | | |
|---|---|---|
| 4375 | -1937 | 0 |
| 4375 | -1962 | 7 |
| 4375 | -1989 | 20 |
| 4375 | -2012 | 24 |
| 4375 | -2045 | 17 |
| 4375 | -2089 | 24 |
| 4375 | -2130 | 27 |
| 4375 | -2148 | 33 |
| 4375 | -2185 | 32 |
| 4375 | -2222 | 32 |
| 4375 | -2254 | 38 |
| 4375 | -2300 | 60 |
| 4500 | -1906 | 0 |
| 4500 | -1912 | 8 |
| 4500 | -1961 | 16 |
| 4500 | -1998 | 16 |
| 4500 | -2024 | 21 |
| 4500 | -2041 | 25 |
| 4500 | -2097 | 21 |
| 4500 | -2141 | 13 |
| 4500 | -2158 | 20 |
| 4500 | -2222 | 22 |
| 4500 | -2276 | 30 |
| 4625 | -1978 | 0 |
| 4625 | -1985 | 12 |
| 4625 | -2008 | 13 |

**Fault T22**

| | | | |
|---|---|---|---|
| 4625 | -2032 | 13 | **Fault T22** |
| 4625 | -2048 | 14 | |
| 4625 | -2106 | 15 | |
| 4625 | -2149 | 5 | |
| 4625 | -2180 | 6 | |

| Distance (m) | Depth (TWT, s) | Throw (TWT, s) | |
|---|---|---|---|
| x | y | z | |
| 4375 | -2187 | 0 | |
| 4375 | -2192 | 1 | |
| 4500 | -2194 | 0 | |
| 4500 | -2206 | 8 | |
| 4500 | -2241 | 24 | |
| 4625 | -2194 | 0 | |
| 4625 | -2178 | 3 | |
| 4625 | -2206 | 8 | **Fault T25** |
| 4625 | -2213 | 12 | |
| 4625 | -2254 | 25 | |
| 4625 | -2264 | 24 | |
| 4625 | -2298 | 22 | |
| 4625 | -2394 | 15 | |
| 4750 | -2195 | 0 | |
| 4750 | -2161 | 9 | |
| 4750 | -2229 | 13 | |
| 4750 | -2256 | 12 | |

| | | | |
|---|---|---|---|
| 4750 | -2284 | 18 | **Fault T25** |
| 4750 | -2303 | 17 | |
| 4875 | -2166 | 0 | |
| 4875 | -2170 | 2 | |
| 4875 | -2178 | 3 | |
| 4875 | -2213 | 5 | |
| 4875 | -2264 | 6 | |
| 4875 | -2284 | 10 | |
| 4875 | -2388 | 8 | |
| 4875 | -2168 | 0 | |
| 4875 | -2206 | 8 | |
| 4875 | -2213 | 5 | |
| 4875 | -2264 | 8 | |
| 4875 | -2278 | 7 | |
| 4875 | -2284 | 10 | |